UNIVERSITÀ
DEGLI STUDI
DI PADOVA

Sede Amministrativa: Università degli Studi di Padova

Dipartimento di Fisica e Astronomia "Galileo Galilei"

SCUOLA DI DOTTORATO DI RICERCA IN: ASTRONOMIA
INDIRIZZO: UNICO
CICLO: XXVII

ENVIRONMENTAL EFFECTS ON THE EVOLUTION OF DWARF AND SPIRAL GALAXIES: DYNAMICS AND STELLAR POPULATIONS

Direttore della Scuola: Prof. Giampaolo Piotto

Supervisori: Dr. Enrico V. Held
Prof. Enrico M. Corsini

Dottorando: Marco Parmiggiani

Sommario

L'obiettivo del lavoro presentato in questa tesi è la caratterizzazione osservativa delle proprietà fisiche delle galassie, per vincolarne gli scenari di formazione ed evoluzione. In particolare mi sono concentrato nel determinare come l'ambiente, in cui evolvono le galassie, influisca sulle loro proprietà strutturali e cinematiche e sulle loro popolazioni stellari.

La prima parte della tesi è focalizzata sulle proprietà delle galassie nane dei primi tipi morfologici negli ammassi di galassie del Centauro e di Perseo.

Per l'Ammasso del Centauro, ho analizzato gli spettri ottenuti con X-Shooter di un campione di 8 galassie ellittiche nane e 2 galassie ellittiche compatte. Gli spettri nella banda ottica ad alta risoluzione sono stati utilizzati per ricavare la dispersione di velocità interna delle galassie, insieme alla stima della loro massa dinamica e del rapporto massa/luminosità. Ho utilizzato le dispersioni di velocità per calcolare la prima stima della relazione di Faber-Jackson per le galassie nane dell'Ammasso di Centaurus. Ho sfruttato gli spettri nella banda ultravioletta e blu a media risoluzione per caratterizzare le popolazioni stellari delle galassie nane e delle galassie compatte.

Successivamente ho effettuato l'analisi di spettroscopia da fibre ottiche di galassie ellittiche a bassa luminosità nell'Ammasso di Perseuo. La mia indagine della cinematica globale dell'ammasso ha confermato la diversa origine della popolazione di galassie a bassa brillanza rispetto a quelle ad alta brillanza. La misura delle proprietà delle popolazioni stellari è stata condotta su tutte le galassie ellittiche e lenticolari dell'ammasso, ed ha permesso di ricavare la prima stima della relazione massa-metallicità per l'Ammasso di Perseo.

Nella seconda parte della tesi ho analizzato le popolazioni stellari di un campione di sferoidi in 12 galassie a disco isolate ed in 4 galassie a spirale di alta brillanza superficiale. Ho derivato i parametri strutturali degli sferoidi attraverso la decomposizione fotometrica. Ho analizzato spettroscopia di fenditura per ricavare l'età, la metallicità, il rapporto [α/Fe] nella parte centrale degli sferoidi ed in corrispondenza del raggio dove lo sferoide contribuisce la stessa frazione di brillanza superficiale rispetto alle altre componenti della galassia. Gli sferoidi delle galassie isolate sono caratterizzati da età intermedie ed elevate, da una metallicità molto varia e da alti valori di del rapporto [α/Fe], che indicano come i tempi scala di formazione stellare siano più corti rispetto a quelli delle galassie in ambienti più densi. Tutti gli sferoidi del campione presentano anche gradienti del rapporto [α/Fe] negativi, in accordo con le previsioni del modello di formazione per collasso dissipativo. Confrontando la mia analisi con campioni selezionati dalla letteratura, ho potuto confermare che i processi di interazione con l'ambiente hanno un ruolo importante nell'evoluzione degli sferoidi in ambienti ad alta densità. In particolare, interazioni ripetute e fusioni con altre galassie tendono a cancellare i gradienti nelle popolazioni stellari degli sferoidi e prolungano i tempi di formazione stellare.

Abstract

The work presented in this thesis is aimed at the observational characterization of the physical properties of galaxies to place constraints on their scenarios of formation and evolution. In particular, I have focused on the determination of how the environment in which galaxies evolve affects their structural and kinematic properties, and their stellar populations.

In the first part of my thesis I studied the properties of the dwarf early-type galaxy population in two nearby galaxy clusters: Centaurus and Perseus.

For the Centaurus Cluster, I analysed X-Shooter spectroscopy of a sample of eight dwarf elliptical galaxies and two compact elliptical galaxies. The visible arm high-resolution spectra were employed to derive the internal velocity dispersion of the galaxies, together with an estimate of their dynamical mass and their mass-to-light ratios. I used the internal velocity dispersion measurements to compute the first estimate of the Faber-Jackson relation of dwarf galaxies in the Centaurus Cluster. I used the medium resolution optical spectra to characterize the stellar populations of the dwarf and compact galaxies.

In addition, I analysed fibre spectroscopic data of low-luminosity ellipticals in the Perseus Cluster. My investigation of the global cluster kinematics confirmed the different origin of the faint galaxy population with respect to the bright galaxies. Measurements of the properties of the stellar populations were performed on all the cluster early-type galaxies, and were used to derive the first estimate of the mass-metallicity relation for the Perseus Cluster.

In the second part of my thesis I analysed the stellar populations of a sample of bulges in twelve isolated disc galaxies and in four spiral galaxies with a high surface brightness disc. I derived the structural parameters of the bulges by performing two-dimensional photometric decomposition of galaxy images. I analysed long-slit spectroscopy to derive the age, metallicity, and [α/Fe] enhancement in the central part of the bulge and at the radius where the bulge contributes the same surface brightness as the other galaxy components. The bulges of isolated galaxies are characterized by intermediate and old ages, a large spread in metallicities ranging from sub- to super-solar values, and super-solar [α/Fe] enhancements. The high [α/Fe] ratios indicates shorter star formation timescales with respect to galaxies in denser environments. All the sample bulges also show a negative gradient for the [α/Fe] enhancement, in agreement with the predictions of the dissipative collapse formation scenario. By comparing our analysis with those of selected samples from the literature, I was able to confirm that environment-driven processes play an important role in the evolution of bulges in high density environments. In particular, repeated interactions and merging with other galaxies tend to erase the stellar population gradients of the bulges and prolong their star formation histories.

Contents

Chapter 1

Introduction

The dependence of galaxy properties on the environmental conditions in which they have evolved and currently reside is a well established result of the extragalactic astronomical studies of the past decades. One of the first and most evident examples of such dependence is the relation between the morphology of the galaxies and local density (Dressler 1980; Dressler et al. 1997), in the sense that the fraction of early-type galaxies (ellipticals and S0s) increases with increasing density. Results from photometric surveys have confirmed that indeed the spatial distributions of galaxies belonging to different types show different trends as one moves from low-density environment to high-density ones (Blanton & Moustakas 2009). Spectroscopic studies have revealed further differences in the stellar population properties of the galaxies belonging to different environments: for example, low redshift early-type galaxies show systematic variations in their star formation histories in relation to the local density (Thomas et al. 2005).

The effects of environment are also dependent on two other parameters. The first (intrinsic) parameter is the galaxy mass: galaxies of different mass react differently to environment-driven processes, because of the depth of the gravitational potential well (Thomas et al. 2010). The second parameter is the evolutionary phase (both of the galaxy and its environment) at which the interaction is observed. The time information is encoded in the galaxy age or cosmological look-back time (i.e., the redshift) of the galaxy, depending on the type of scientific question under investigation. Since every observation has some a magnitude limit, the two parameters are correlated: for example, a medium-high redshift galaxy survey will not be able to probe the environmental effects on the lowest mass passive galaxies.

As with all other astrophysical phenomena, the interaction of galaxies with environment is driven by the intertwined action of gas-dynamical and gravitational forces. While the former interaction is mainly of local nature and affects the baryonic component of galaxies and intergalactic material, the latter affects also the "unseen" components of galaxies, it is less localized and is therefore more dependent on the assumed cosmology

and initial conditions. We briefly review in the next section the cosmological framework on which the analyses presented in this thesis are based, and we will subsequently elaborate on the main physical processes which constitute the focus of our work.

1.1 Galaxy formation in the ΛCDM model

The cosmology assumed in this work is the "Standard Model" cold dark matter (CDM) Universe with cosmological constant Λ, or ΛCDM cosmology. The model describes a flat ($\Omega_0 \simeq 1$) and expanding universe which is homogeneous and isotropic on large scales. The main components of the Universe are the baryonic matter (protons, electrons, neutrinos etc.), a "cold" (non-relativistic) dark matter component (DM) and a dark energy component given by the cosmological constant Λ and responsible for the accelerated expansion of the universe (Riess et al. 1998; Perlmutter et al. 1999). Baryonic matter, which contributes a mass-energy budget which is only $\simeq 5\%$ of the total content of the Universe, is the only component that interacts through electro-magnetic forces and is therefore the only "visible" component that is possible to study through direct observations. Since there is as of now no direct proof of the existence of dark matter (e.g., the results of the decay of a DM particle) and dark energy, their presence can instead only be inferred indirectly by the effects they produce on the structure of galaxies and galaxy clusters or on the expansion of the universe, respectively.

The way in which the various components interact to generate the large- and small-scale structure of the universe is a complex topic. We give only a very brief outline of the most established results which are meaningful to the following analysis.

In the standard ΛCDM model, the main driver of galaxy formation is the DM component which accounts for $\simeq 25\%$ of the mass-energy budget. The process of structure formation starts at the epoch of hydrogen recombination ($z \simeq 10^3$) when the Universe is practically homogeneous and isotropic and its geometry is well described by a Robertson-Walker metric. There are small fluctuations in the density field of the order of $\delta\rho/\rho \sim 10^{-5}$ which correspond to primordial quantum fluctuations amplified by the inflationary (Guth 1981) period of accelerated expansion. The observable evidence of the existence of these density anisotropies comes from the cosmic microwave background (CMB) radiation. The inhomogeneities undergo gravitational instability, giving rise to DM haloes which are the first bound structures in the universe. Baryons subsequently follow the gravitational pull of DM haloes and, after energy dissipation via radiative losses and contraction, stars and galaxies are formed (White & Rees 1978). The assembly of gravitationally bound structures proceeds then in a hierarchical fashion, with progressively massive structures being generated via the aggregation of smaller units (Press & Schechter 1974; Lacey & Cole 1993). This process ends up producing the so called "cosmic web" large-scale structure of the universe seen in redshift surveys and

cosmological simulations: massive clusters and superclusters connected by filaments of smaller structures, and large voids in between. The accretion of smaller structures is in fact a continuous process which is still ongoing at $z = 0$.

Galaxy clusters are therefore the largest ($R \sim$ few Mpc) and most massive ($M \sim 10^{14}$–$10^{15}\,\mathrm{M}_{\odot}$) gravitationally-bound structures in the Universe. Typical galaxy numbers in clusters are of the order of several hundred, although deep survey of low redshift clusters show that even thousands of low-surface brightness galaxies may populate evolved clusters (Ferrarese et al. 2012; Koda et al. 2015). Besides the stellar component visible in galaxies, clusters contain a prominent hot ($T \simeq 10^7\,\mathrm{K}$) gas halo, which is visible in the X-rays because of thermal bremsstrahlung emission. The dominant mass component of clusters is however in the form of dark matter, which is necessary to resolve the discrepancy between the mass accounted for by gas and stars and mass inferred through dynamical tracers. These tracers include, for example, gravitational lensing, kinematics of galaxies, and hydrostatic equilibrium analysis of the hot gas.

Proceeding down the structure hierarchy we find galaxy groups and loose groups, which usually contain no more than a hundred galaxies, and have hot gas and DM haloes which are associated with the group most massive galaxy and hence are less extended and evolved than in galaxy clusters. At the small mass end of the list of gravitationally-bound structures are isolated galaxies. Note that, in practice, there is no discrete transition between isolated galaxies, galaxy groups and clusters; and bound structures form a continuous sequence in mass. Depending on the environment in which a galaxy evolves, it will therefore experience a different evolution caused by its interaction with the surrounding material. The degree of interaction will depend on the intrinsic properties of the galaxy itself such as mass and morphology.

1.2 The components of galaxies and their interactions

The main components of a galaxy which we consider in this work are:

- the **stellar** component, that is the material which is locked in stars and emits mainly in the optical region of the spectrum through blackbody radiation. We follow standard astronomical practice and consider all stellar remnants as part of the mass of the stellar component. The behaviour of the stellar component, from the moment of star formation (SF) to the mass-dependent eventual fate of stars, is fully described by the theory of stellar evolution.

- the **gaseous** component, in the form of atomic or molecular gas, which follows the laws of fluid dynamics, and has generally a strong effect on the SF activity. There are many different types of gas in galaxies, each formed in a different way, and with a different influence on the emission and evolution of the galaxy itself. Examples of

gases typically found in galaxies are atomic hydrogen (both neutral and ionized), molecular hydrogen. In addition, the inter-stellar medium (ISM, i.e., all baryonic matter not locked in stars) may contain a dust component. Depending on the size and the morphological type, gas may be present in more or less abundant fractions: late-type galaxies, for example, are much richer in gas with respect to early-type galaxies.

- the **dark matter** halo, which may actually not be present if the galaxy is embedded in the DM halo of an evolved structure.
- an **active galactic nucleus** (AGN), which is characterized by a prominent emission originating in a very small region near the centre of the galaxy. The AGN emission is commonly associated with accretion activity onto a central supermassive black hole (SMBH)

The main constituents of galaxies listed above interact with each other during the evolutionary history of a galaxy, in a way that is mostly evident through their connection with SF. However, each of the components will interact in a particular way with the surrounding environment. With the aid of Figure 1.1, we make a non-exhaustive list of the main processes taking place during the co-evolution of galaxy and environment. Since the interaction picture shown in the figure is complex, we divide the purely environment-driven processes (blue arrows) from the internal processes (red arrows) which are however influenced by the action of the environment. We first list the processes included in the latter group, and give a brief description:

Star formation: SF is the process by which new stars are formed. Since the main sites of SF are molecular clouds, the total amount and rate of SF are directly related to the quantity of gas which is available and is in the right physical conditions (Schmidt 1959; Kennicutt 1989). The star formation rate (SFR) denotes the rate at which gas is converted in to stars (in units of $M_\odot\,yr^{-1}$) and is an important quantity that can be inferred from observations and compared with galaxy evolution models. Another key ingredient in the way SF influences the spectro-photometric evolution of galaxies is the initial mass function (IMF), which is defined as the number density of stars per unit mass which are generated in each SF event.

Winds and supernovae (SNe): The SF activity in a galaxy returns both energy and enriched material to the gas phase in the form of stellar winds and supernova explosions. However, when the mass of the galaxy is small, the gravitational force is not sufficient to contrast the kinetic energy injected into the gas phase by winds and SNe, and the gas is expelled from the galaxy, halting star formation (Dekel & Silk 1986). This introduces a direct relation between the mass of the galaxy and the metal enrichment of its stellar and gas components (Yoshii & Arimoto 1987).

Gas inflow: Galaxies may accrete gaseous material from the intergalactic medium, which may be either primordial or pre-processed and expelled through the process of SF, winds and SNe.

AGN accretion and feedback: Gaseous material in the galaxy ISM is accreted onto the central SMBH. The presence of AGN emission may give an important contribution on the regulation of SF by mitigating the inflow of gas (Bower et al. 2006).

The schematic picture of galaxy formation that emerges from this short list is that of galaxy which is formed inside a DM halo by dissipative collapse of the baryonic component. The cycle of star formation → outflow → inflow then proceeds until all gas is depleted. The main parameter involved in the outcome of galaxy formation is the mass, which determines the size of the final object and regulates both the gas inflow and gas rates, and hence the amount of fuel available for SF.

For low mass galaxies, additional factors come into play. One example is angular momentum (Schroyen et al. 2013), which can, if present, reduce the amount of gas which is funnelled to the centre of the galaxy and smear out possible stellar population gradients. The other factor, which may be predominant for low-mass systems, is the environment.

1.3 The role of environment

Other processes can occur only in the presence of an external environment, in the form of other galaxies or an external gravitational potential.

A galaxy spending its lifetime in a cluster or group will have one or multiple **close encounters** with other galaxies. The outcome of these encounters depends on multiple factors, including the mass ratio between the two galaxies, the relative orbit parameters, energy, and angular momentum. A general result is that the internal energy of the two galaxies is increased at the expense of the orbital energy of the encounter: this increase may result in some of the external galaxy material becoming unbound, and may lead to mass loss. Multiple repeated encounters with other galaxies in a cluster environment have been referred to as "**harassment**" (Moore et al. 1996). The process of "**galaxy merging**", which is a crucial ingredient of the hierarchical assembly scenario for galaxy formation, occurs when the removal of orbital energy is efficient enough to lead to a collision between the two original galaxies. Three-body encounters between galaxies are rare, but are expected theoretically and have been shown to be the plausible cause of the presence of isolated compact galaxies (Chilingarian & Zolotukhin 2015).

A second process which can induce mass loss in galaxies is **tidal stripping**. Tidal stripping refers to the loss of the external stellar material by a galaxy as a consequence

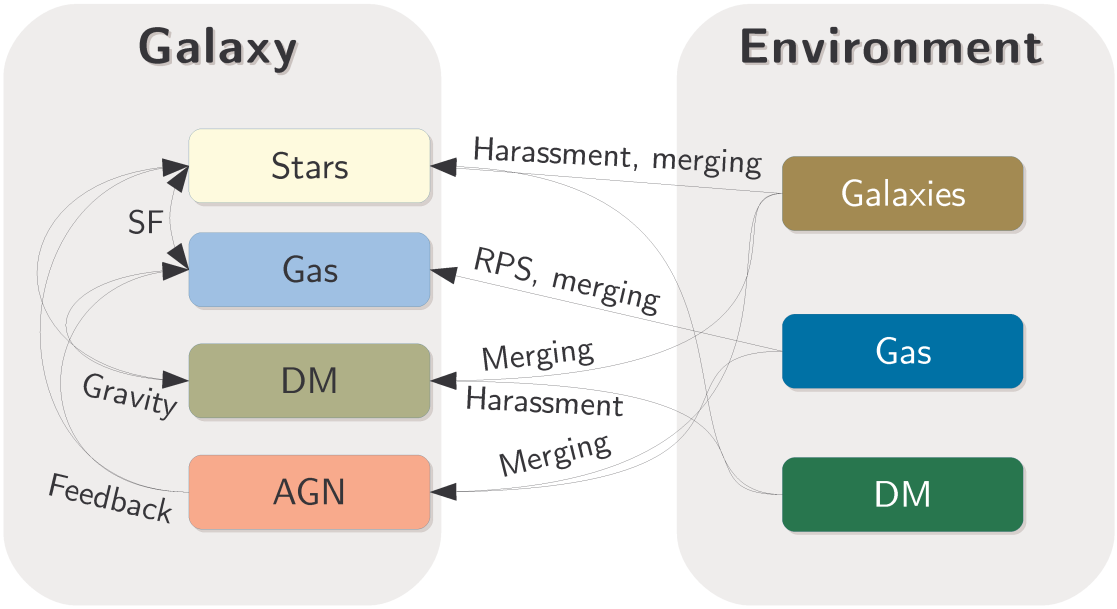

Figure 1.1: Schematic diagram of the components of galaxies, the main components which constitute the environment and the processes which relate all the various components.

of the interaction with a static gravitational potential, such as those of clusters, groups or massive galaxies.

The stripping of the gaseous material of a galaxy may occur as a consequence of the interaction with the hot gas halo of a cluster, and is known as **ram pressure stripping**. The process of **strangulation** (Larson et al. 1980) refers to the removal of only the gas halo surrounding the galaxy, while leaving the gas in the disc in place. While the physical process behind the two events is the same, strangulation differs from ram pressure stripping in the predicted trends of metallicity with galaxy mass (Peng et al. 2015).

The work described in this thesis is aimed at deriving observational constraints on the effects of environment on the formation and evolution of three classes of "hot" stellar systems: dwarf elliptical (dE) galaxies, compact elliptical (cE) galaxies and bulges of disc galaxies. Dwarf and compact galaxies, because of the weak gravitational pull exerted by their low mass, are heavily susceptible to environment-driven transformations. The relative contribution of the various processes on their evolution is not yet fully understood, and since the typical surface brightness of dwarfs is low, observed samples are mostly studied in nearby clusters (e.g., Virgo). The influence of environment on the evolution of the bulges of disc galaxies is also not yet fully understood, and is studied in this work through a consistent analysis of galaxies belonging to different environments.

In the following subsections we first describe in greater detail each of the processes listed above, and in the next sections we discuss how environment-driven evolution affects these types of galaxies.

1.3.1 Galaxy merging

The process of galaxy merging occurs when the removal of energy through dynamical friction is effective enough to cause two interacting galaxies to become bound and to eventually become a single object. The dynamics of mergers is explained in detail in Binney & Tremaine (1987). Since the process of dynamical friction involves an exchange of energy from $E_{\rm orb}$ to the internal energy of the individual galaxies, mergers are expected to be more effective when the relative velocity between two galaxies is close to their internal velocity dispersion ($E_{\rm orb} \sim \sigma^2$). Mergers are therefore expected to be rare in galaxy clusters, where relative velocities often exceed $\sim 1000\,{\rm km\,s^{-1}}$, and more frequent in galaxy groups, where typical velocity dispersions are below ~ 300 $\rm km\,s^{-1}$. However, merger-induced preprocessing in group sized haloes may affect the properties of cluster galaxies because, according to the hierarchical assembly structure formation scenario, group-sized haloes might eventually merge to form clusters.

Since a large number of physical components (stars, gas, DM etc.) and structural and dynamical parameters are involved in the process of merging, in order to disentangle the effects on the evolution of galaxies it is customary to distinguish between different types of merging. The primary factor in the determination of the outcome of merging is the mass ratio between the two interacting galaxies: in "major" mergers the mass of the merging galaxies is similar, while "minor" mergers refer to merging events where one galaxy is much more massive than the other (a common discriminating value is $M_1/M_2 \simeq 4$). Major mergers are typically "destructive" events, in the sense that after the collision the remnant galaxy seldom resembles the original progenitors. As an example, numerical simulations accounting for the evolution of stars, gas and embedded AGNs have shown that major mergers between spiral galaxies can generate spheroidal systems similar to early type galaxies (Springel et al. 2005). During a minor merger, instead, the more massive galaxy usually remains relatively unchanged, although the exact degree of the perturbation will depend on the mass ratio and intrinsic properties of the two galaxies. For example, in minor mergers involving disc galaxies, the interaction with a satellite typically generates a perturbation (heating and thickening of the disc) which makes the original galaxy resemble a galaxy of an earlier type (Walker et al. 1996). Sequential repeated minor mergers could also be responsible for a fraction of the elliptical galaxy population (Bournaud et al. 2007).

Another key ingredient in galaxy mergers is the presence of gas in the interacting galaxies. If there is little or no gas in the progenitor galaxies (the case is named dry merging), the build-up of stellar mass (and/or DM) is the dominant outcome of the

encounter. Another effect is that systematic variations in the stellar population properties between the two galaxies or internal gradients are erased in the mixing process. The case of wet merging, when the progenitors are blue, gas-rich galaxies, has more diverse consequences pertaining to the involved galaxy components: apart from the stellar mass assembly, the interacting gas can trigger star formation, and can also fuel the central AGN triggering feedback (Springel et al. 2005). The renewed star formation activity eventually produces substantial changes in the chemical and stellar population properties of the merged stellar system.

As we have seen, the possible combination of the properties of the interacting galaxies is manifold. In this work, we have concentrated on the determination of the effects of merging on the evolution of the bulges of disc galaxies (see Section 1.5).

1.3.2 Harassment and tidal stripping

Unlike galaxy encounters and merging, which are an important driver of galaxy evolution in groups of galaxies, the phenomena of harassment and tidal stripping play a prominent role in shaping the galaxy populations of the most massive structures: galaxy clusters. Tidally-induced disturbances affecting galaxies in clusters actually refer to two different processes: tidal heating (sometimes also referred to as tidal stripping) refers to the mass loss experienced by a galaxy as it moves through the halo of a more massive object. Tidal fields tend to heat and distort the galaxy in a way that causes the external parts of the stellar material to become unbound. Other than the perturbation of dwarf galaxies moving through the potential of a massive cluster, another example of the effects of tidally-induced mass loss are the tidal streams left by Milky Way satellites (Lynden-Bell & Lynden-Bell 1995) travelling through the DM halo of the Galaxy. The second process which affects galaxies in clusters is the transformation caused by multiple high-speed interactions with other galaxies, which is usually called tidal shocking. Although the two processes in principle cause the same type of effect (i.e., mass loss and morphological transformations), they are have different timescales: tidal shocking is a short-lived interaction between two high speed galaxies, while tidal heating can have a long duration if the infalling galaxy passes close to the cluster centre. The distinction is important also because sometimes the term "tidal stripping" is (confusingly) used to refer to either of the two processes, or both.

The term "harassment" is usually employed to refer to the combined effect of both types of interaction. The harassment scenario for galaxy evolution in clusters was initially proposed (Moore et al. 1996) to explain, on one hand, the deficiency of blue spiral galaxies in low redshift clusters (Butcher & Oemler 1984) and on the other hand the ubiquitous presence in the same clusters of a rich early-type dwarf galaxy population. Numerical simulations showed that indeed multiple encounters (Moore et al. 1996, 1998) could modify the morphology of infalling spiral galaxies to produce low-mass spheroidal

systems resembling the dE population in a cluster. The early simulations showed that multiple encounters caused pressure-support of the galaxy kinematics to be enhanced at the expense of angular momentum and predicted the degree of increase of the internal velocity dispersion to depend on the relative inclination between the disc rotation plane and the orbital plane in the cluster potential. However, Mastropietro et al. (2005) conducted a photometric analysis on simulated cluster galaxies, and found that the disc-like component is never completely destroyed. These authors also showed that systems subject to harassment seldom become completely pressure supported, and usually retain a significant amount of rotational motion. Recent results from hydrodynamical simulations (Smith et al. 2010, 2015) have strengthened these results by considering a wider input parameter space both in the input mass (i.e., extending the analysis to lower masses) and in the orbital properties of the infalling galaxies. The main result of these studies is that harassment caused by high-speed encounters and by the cluster potential is able to significantly perturb late-type galaxies only for the small ($\lesssim 25\%$) fraction of possible orbital parameters that cause the infalling members to pass very close to the cluster centre, where the gravitational potential is deeper and high-speed encounters are more probable because of the increased galaxy density. These authors however, caution against the discrimination of harassed versus non-harassed galaxies based purely on the spatial location, because given the multiple possible orbital eccentricities, it is possible to find also strongly harassed galaxies far from the cluster core (e.g., close to the virial radius). Nevertheless, the predicted influence of tidal stripping on the majority of infalling late-type galaxies is small, resulting in less than 10% of the stellar mass, hence the authors favour a predominant role of ram pressure stripping for the evolution of cluster dwarfs.

1.3.3 Ram pressure stripping

Ram pressure stripping (RPS) was introduced by Gunn & Gott (1972) as one of the physical consequence of the spherical collapse model for density perturbation. RPS denotes the action of the hot intracluster medium (ICM) on the cold gas in galaxies. The pressure P exerted by the ICM on the infalling galaxies is proportional to ρv^2, where ρ is the density of the ICM and v is the velocity of the galaxy. For RPS to be effective, P must exceed the internal gravitational force per unit area, which is proportional to $\Sigma_{\rm g}\Sigma_*$, where $\Sigma_{\rm g}$ and Σ_* represent the surface density of gas and stars, respectively.

Since $P \propto \rho v^2$, it is easy to see that RPS is most effective in the cores of galaxy clusters where 1) the hot gas density is higher (Makino et al. 1998) and 2) the velocity of the galaxy is higher. Condition 2) actually depends on the cluster velocity dispersion profile, but is usually verified for the low redshift clusters where dwarf galaxies are best studied (e.g., Virgo, Coma, see Fadda et al. 1996). Indeed, detailed hydrodynamical simulations (Roediger & Hensler 2005; Tonnesen et al. 2007) have shown that gas strip-

ping of late-type galaxies from the hot intracluster gas can be the dominant process in transforming the galaxy properties at low redshift. However, more recent hydrodynamical simulations (Bekki 2009; Cen et al. 2014) have also shown that RPS can be effective also in lower density environments such as groups or in the outskirts of clusters, and that most of the gas is lost within one orbit through the cluster potential, i.e., gas removal from late-type galaxies starts in the early stages of their evolution and is a relatively fast process.

The consequences of RPS on the SF histories of galaxies are twofold: first, cold gas is removed from the disc, starting from the external regions where the gas is less bound ($\Sigma_{\rm g}$ and Σ_* are lower) resulting in a gradual shut down (or "quenching") of SF. Hence, as the fuel is exhausted, a blue star-forming galaxy is gradually transformed into a red passive galaxy. The second effect, of opposite sign, is that the gas in the disc is compressed, which may actually enhance SF if the high-density regions are able to undergo efficient radiative cooling. The detailed balance of the two effects depends on the intensity of ram pressure (Tonnesen & Bryan 2009), resulting in enhanced SF where the gas density and galaxy velocities are low. This effect might be responsible for the increased number of dwarf post-starburst galaxies found in the outskirts of galaxy clusters (Poggianti et al. 2004).

As opposed to harassment, the ram pressure stripping affects mainly the gaseous components of galaxies. The kinematics of the stellar component are therefore expected to be largely unaffected by the gas removal. The hydrodynamical simulations conducted by Smith et al. (2012b) confirmed this picture. The authors studied the effect of the loss of the gas mass by RPS on the other components of disc galaxies: DM and stars are mainly affected by small and short-lived displacements and the stellar disc is slightly thickened because of the shallower gravitational potential of the disc after gas removal.

1.4 Evolution of low-mass and compact stellar systems in clusters

The fact that the majority of the faint galaxy population in clusters originates from environment-driven transformation of infalling galaxies is supported by various observational evidences. The first indication that low-mass galaxies undergo significant transformations moving from low-density to high-density environments comes from their luminosity function. This is defined as the number of galaxies per magnitude per unit volume, and it is customarily described as a Schechter (1976) function:

$$\phi(L) = \phi^* \left(\frac{L}{L^*}\right)^{\alpha} \exp\left(-\frac{L}{L^*}\right) ,$$

where ϕ^* is a normalization constant, L is the galaxy luminosity, α is the slope of the faint-end power-law and L^* is the characteristic luminosity of the exponential cut-off. A change in the faint-end slope as a function of local density has been reported in several studies (Popesso et al. 2006; Robotham et al. 2010; Zandivarez & Martínez 2011), although the degree of variations usually depends on how the sample is selected and separated. For example, the recent study by McNaught-Roberts et al. (2014) finds variation of the faint-end slope with local density only when passive ("red") and star-forming ("blue") galaxies are considered separately. Nevertheless, systematic changes in the slope and the other Schechter function parameters are observed. This finding implies that some degree of transformation is indeed taking place.

Other evidence for the late infall of the low-luminosity galaxy population in clusters stems from the analysis of their kinematics: for example, the analysis of the velocity dispersion of the dwarf galaxy population in the Fornax (Held & Mould 1994), Virgo (Conselice et al. 2001) and Perseus (Penny & Conselice 2008) clusters has shown that faint galaxies possess higher velocity dispersions with respect to other types of galaxies. If the velocity dispersion of each galaxy population is related to the mass of the cluster at the moment of the "turn-around" from the Hubble flow, then dwarf galaxies must have become bound to the cluster at later times. The velocity distribution of dwarf galaxies in the Virgo Cluster was also found by Lisker et al. (2007) to show variations *among* the different dE types: nucleated dE galaxies are found preferentially close to the cluster centre, and have a velocity distribution which narrower with respect to both non-nucleated dE galaxies and discy dE galaxies. This may suggest that the red dEs near the cluster core have been accreted at earlier times with respect to discy, blue dEs, and have therefore spent a longer time under the influence of the harsh cluster environment.

Which of the processes described above ultimately drives the evolution of dwarf galaxies in clusters? The answer must be sought in the observational properties of galaxies, but it is probably not possible to isolate a *single* mechanism.

The possibility that dE galaxies and giant ellipticals share a common evolution scenario, dominated by merging, is supported by the evidence that some of the scaling relations between the galaxy structural parameters form a continuous sequence from faint to bright magnitudes (Graham & Guzmán 2003; Ferrarese et al. 2006). Similar conclusions based on the kinematic and stellar population profiles were presented by Chilingarian (2009). Despite the low number of expected progenitors of low-mass galaxies predicted by semi-analytic modelling ($\lesssim 2$, De Lucia et al. 2006), high resolution hydro-dynamical simulations of the merger sequence that leads to the formation of a dwarf galaxies have also been shown to reproduce correctly some of the scaling relations of dE galaxies (Cloet-Osselaer et al. 2014). Starting from realistic orbital parameters from cosmological simulations, the authors recover the relations between magnitude and Sérsic index n, surface brightness and internal velocity dispersion σ. The observed scaling relations

of the galaxy internal kinematics, however, show significant differences with respect to those of giant elliptical galaxies: the slope of the Faber & Jackson (1976, FJ) relation is typically lower for dE samples ($\simeq$2–3, see Held et al. 1992; de Rijcke et al. 2005; Kourkchi et al. 2012) with respect to giant elliptical samples ($\simeq 4$). The "fundamental planes" (Djorgovski & Davis 1987; Bender et al. 1992) of dwarf and giant ellipticals are also offset one from the other (Toloba et al. 2012), which may reflect a diversity in formation mechanisms. This diversity is also hinted at by the fact that scaling relations of dEs often show considerable scatter that is not explained by random errors caused by the low signal-to-noise ratio of the observations (de Rijcke et al. 2005; Ferrarese et al. 2006).

Early spectroscopic studies of extended kinematics of dE galaxies in the Fornax and Virgo clusters(de Rijcke et al. 2001; Geha et al. 2002) found that most of these objects showed modest degrees of rotational support, thereby favouring a scenario of galaxy transformation by harassment. Shortly after, however, the major limitation (i.e., small statistics) of these studies was overcome by enlarging the samples of observed galaxies, and soon other galaxies were found which showed 1) a high degree of rotational motion (Geha et al. 2003; van Zee et al. 2004) and 2) residual disc-like features in their structure (de Rijcke et al. 2003; Lisker et al. 2006). At about the same time, multiwavelength observations clearly revealed the interactions occurring between the gas phase of late-type galaxies and the cluster ICM. Both atomic hydrogen (Kenney et al. 2004) and Hα narrow-band imaging (Kenney et al. 2008) allowed RPS to be "caught in the act" in Virgo late-type galaxies.

Recent studies of the internal kinematics of dE galaxies in the Virgo Cluster have not yet been able to completely resolve the issue. Toloba et al. (2011, 2012) found a significant numbers of fast rotating galaxies in the Virgo Cluster, which also roughly follow the extension of the Tully & Fisher (1977) relation at lower magnitudes, supporting the RPS scenario. On the other hand, Ryś et al. (2014) have shown, using 3D kinematical data of Virgo dEs, that the rotation curves of dE galaxies are not consistent with those of their expected late type progenitors, favouring a scenario in which harassment is mainly responsible for the galaxy final shape and kinematics. Toloba et al. (2015) find a dependence of the specific angular momentum on the projected distance from the centre of the cluster, which can be also interpreted as evidence that the centremost galaxies have undergone more substantial tidal interactions with the cluster potential and with other galaxies, with respect to the outermost galaxies.

Using medium-high resolution data, Toloba et al. (2012), Ryś et al. (2014), and Penny et al. (2015) have been able to determine the DM content in dE galaxies in nearby groups and clusters. The mass-to-light (M/L) ratio (from which the dark matter fraction is derived) can be an important parameter in the evolution of dwarf galaxies in a cluster: a high DM content could make the galaxy less susceptible to, e.g., harassment.

The above studies find that a non-negligible fraction of the galaxy mass is actually in the form of DM ($\gtrsim 40\%$ within the half light radius). The derived M/L ratios for the Virgo dEs are found to be not dependent on the distance from the cluster centre, but mildly dependent on the type of environment, in the sense that dEs in groups have higher M/L ratios (Penny et al. 2015). This result is somewhat at odds with the notion that M/L is higher for more "perturbed" objects, but it must be noted that the above samples of medium-high spectroscopic data of dEs in the group environment are still limited, and not spatially resolved.

These studies on the kinematics of dE galaxies are mostly focused on the Virgo Cluster, because of its proximity and hence of the possibility to obtain large kinematic samples. To find trends in the galaxy properties with varying density, which is what is needed if the various environmental processes are to be successfully disentangled, Ryś et al. (2014) and Penny et al. (2015) correctly resort to deprojected distances. However, these can be relatively uncertain, and it is not guaranteed that a galaxy which is far from the cluster centre has not had at least one passage close to the core, which is usually sufficient to significantly perturb the appearance and kinematics of the galaxy. A first step in the construction of statistically significant samples of internal galaxy kinematics in different environmental conditions has been taken by (Penny et al. 2015), who also studied six dE galaxies in group environments. In Chapter 2, we take a step further by analysing the kinematics of eight more dE galaxies of the Centaurus Cluster using high resolution VLT spectroscopy.

The stellar populations of dE galaxies offer a complementary view on the their evolution in the cluster environment. From the point of view of the galaxy colours, the observed "red sequence" of passive galaxies in cluster has a negative slope, i.e. dE galaxies are on average bluer with respect to bright passive galaxies (Conselice et al. 2003; Misgeld et al. 2009). This implies that stars in dE galaxies have on average younger ages and/or lower metallicities. This has been confirmed in a large number of subsequent spectroscopic studies based on absorption-line index diagnostics, which have uncovered a large diversity in the measured stellar population parameters: both old metal poor, and young metal-rich dE galaxies were found in the Coma (Poggianti et al. 2001) and Perseus (Penny & Conselice 2008) clusters. Smith et al. (2009, 2012a) have studied in a similar manner a large sample of early-type dwarfs in the Coma Cluster. They have been able to characterize the dependence of the age and metallicity of the stellar population on the projected distance from the cluster centre (and hence on the local environmental conditions). The authors confirm a radial trend in age, metallicity, and α-element enhancement with galaxies closer to the cluster core having older ages, higher [Mg/Fe], and lower [Fe/H]. The same trends are not found for more massive ellipticals, favouring a scenario of environmental quenching of SF affecting only galaxies whose mass is not able to contrast the disruptive effects of the cluster environment.

Further advances in the study of the stellar populations of dE galaxies have been achieved using full-spectrum fitting programs (Ocvirk et al. 2006; Chilingarian et al. 2007; Koleva et al. 2009b), which were used to recover detailed SF histories of dE galaxies in the Fornax Cluster (Koleva et al. 2009a) and Virgo Cluster (Chilingarian 2009; Ryś et al. 2015). These studies find, consistently with previous results, intermediate ages and sub-solar metallicities. The results of the fitting procedures are however consistent in most cases with the presence of an old stellar population and a subsequent declining SFH. In many sample galaxies the authors also find evidence for internal age and metallicity gradients. The authors argue that the evidence may indicate that the gas removal process or the tidal effects in the cluster may not be as efficient as is required to transform a late-type spiral in an early-type dwarf. The progenitors of dE galaxies could be in this case also less massive systems, such as dwarf irregular galaxies or blue compact galaxies which have been subject to strangulation by the cluster environment.

In Chapters 2 and 3, we study the stellar populations of two samples of low luminosity galaxies in different cluster environments, to place further constraints on their evolutionary paths. In Chapter 2 we derive ages and metallicities for a sample of eight dE galaxies in the Centaurus Cluster. In Chapter 3, we exploit fibre spectroscopy to derive global trends in the stellar populations of low-luminosity early type galaxies in the Perseus Cluster.

Several studies in the last two decades have uncovered a large variety of new types of dynamically hot stellar systems in clusters, which bridge the gap in the size-luminosity diagram between giant elliptical galaxies and globular clusters (GCs). Among these systems there are the ultra-compact dwarf galaxies (UCDs) (Drinkwater et al. 2000), at the faint end of the "bridge", and the M32-like compact elliptical galaxies (cEs) (Mieske et al. 2005a; Smith Castelli et al. 2008; Price et al. 2009) at the bright end. Different formation scenarios have been proposed for these compact stellar systems (CSS). UCDs, for example, are not a homogeneous population: faint UCDs have similar distributions with respect to GCs, and may represent the bright tail of the GC luminosity function (Mieske et al. 2012). On the contrary, bright UCDs have properties consistent with tidally transformed dwarf galaxies. The brighter cEs appear more homogeneous in terms of observed properties. They usually present higher velocity dispersions and higher metallicities with respect to other early-type galaxies at the same magnitude (Chilingarian et al. 2009; Price et al. 2009; Janz et al. 2016), which is interpreted as evidence for tidally-induced stripping of more massive progenitors. Simple luminosity arguments (Norris et al. 2014) suggest that cEs could be the remnant of bulges of late-type galaxies which have lost most of their stellar mass in tidal interactions.

In Chapter 2 we also study the kinematics and the stellar populations of two cE galaxies in the Centaurus Cluster to determine if their properties are consistent with the formation scenario outlined above.

1.5 The effect of merging on the bulges of disc galaxies

The formation of bulges of lenticular and spiral galaxies in the context of ΛCDM is not yet fully understood. As for massive elliptical galaxies, the relative contribution of pure dissipative collapse (Eggen et al. 1962; Gilmore & Wyse 1998) and merging (Cole et al. 2000) must still be clearly determined. In addition, bulges may also be formed by secular evolution (Kormendy & Kennicutt 2004), for example by transport of disk material driven by a bar.

The dissipative collapse scenario involves a primordial gas cloud contracting under the gravitational pull of itself and DM halo in which it is embedded. As the gas contracts, it is able to radiatively dissipate the thermal energy and stars are formed. While stars are formed at all galactocentric radii and remain on their orbits with little radial migration, the gas dissipates and progressively moves inward. Since the gas itself is enriched in metals by the evolving stellar populations, stars which are formed closer to the centre of the galaxy possess a higher metallicity with respect to the stars in the outskirts. Galactic winds enhance the expected negative gradient in metallicity, by removing gas (the fuel for SF) more effectively in the outer parts of the galaxy (Arimoto & Yoshii 1987).

The effects of merging on the structure and stellar population of bulges is less clear, also because that the different merging scenarios (major/minor, wet/dry) produce different outcomes. For example, while first high-resolution hydrodynamical simulations described the outcome of a wet and major merger as a system resembling elliptical galaxies (Springel et al. 2005), later works have shown that the disc component can survive mergers (Hopkins et al. 2009b) and that SF during mergers may be not only enhanced in the galactic spheroid, but also in the disc (Kannan et al. 2015). Predictions for the effects of merging on the stellar populations of bulges are contradictory: the metallicity gradients might be erased in the clustering and merging process (Bekki & Shioya 1999) or it might be moderately affected by interactions since violent relaxation preserves the position of the stars in the local potential (van Albada 1982). The detailed properties of the interaction outcome possibly depend on the gas fraction and mass ratios of the merging galaxies.

Secular evolution predicts bulge formation by the redistribution of the disc stars due to the instabilities triggered by bars, ovals, and spiral arms. The metallicity gradient could be either amplified since the resulting bulge has either a smaller scalelength than the disc or it is erased as a consequence of disc heating (Moorthy & Holtzman 2006).

From an observational point of view, the stellar populations of bulges present a wide variety of properties: measured ages span from 1 and 15 Gyr, and the timescales of the last major star-formation burst are between 1 to 5 Gyr, as derived from the central values of α/Fe abundance ratio (Thomas & Davies 2006; Zoccali et al. 2008). Most bulges also present a negative metallicity gradient, which is one of the tighter predictions made by theoretical models for the dissipative collapse (Gilmore & Wyse 1998; Pipino et al.

2010). On the other hand, the absence of stellar population gradients measured in some bulges is an indication that mixing caused by internal or external processes does make an important contribution on the overall appearance of the spheroidal component in disc galaxies (Bekki & Shioya 1999; Kobayashi 2004).

Such variety of properties in galaxy bulges prevent the attainment of firm conclusions on their most probable formation scenario. This is most likely not a consequence of incomplete model predictions, but it is the result of the fact that the various processes are all acting at the same time, together with other environment-driven transformations (e.g., harassment, gas stripping). A possible solution to resolve the confusion is to lead consistent analyses of the stellar populations of bulges in well controlled samples belonging to different environments. This is achieved in this thesis in Chapters 4 and 5, where we describe the study of a sample of bulges of isolated galaxies and of galaxies in denser environments. The aim of the study is to highlight possible links between the stellar population of bulges and the environment in which they have evolved.

1.6 Thesis outline

In **Chapter 2** we present X-Shooter spectroscopy for a sample of eight dE and two cE galaxies in the Centaurus Cluster, to place constraints on their possible formation and evolution scenarios. We derived accurate internal kinematics for the sample galaxies by analysing high-resolution ($R \simeq 11000$) from the X-Shooter VIS arm using the full spectrum fitting technique. The measured velocity dispersions of the dE galaxies yield a slope of the FJ relation equal to 2.00 ± 1.20, which is consistent with the relation found for dwarf galaxies in other clusters. The velocity dispersion of the cE galaxies is higher than that of the dwarf galaxies at the same magnitude, but lower than galaxies from other cE samples. We derived population parameters of both the dEs and the cEs using line-strength index analysis and full spectrum fitting with single stellar population models (SSP) on the medium resolution ($R \simeq 3000$) UVB arm spectra. We find intermediate luminosity-weighted ages (4–8 Gyr) for all galaxies in the sample, consistent with prolonged star formation episodes. Dwarf galaxies present low metallicities ([Fe/H] $\simeq -1$) which places them on the mass–metallicity relation for early type galaxies, while cE galaxies are displaced from the same relation towards higher metallicities. This evidence, together with the high velocity dispersions, supports the tidal stripping scenario of more massive progenitors.

In **Chapter 3** we describe our investigation of large-scale trends in the low-luminosity early type galaxy population of the Perseus Cluster. We analysed, using the cross-correlation technique, fibre spectroscopy from the William Herschel Telescope (WHT) in order to increase the confirmed members of the clusters and characterize the stellar populations of galaxies in the magnitude range that represents a transition from the

giant to dwarf regime. We provide new membership confirmation for 16 low luminosity ($M_r \gtrsim -19$) elliptical galaxies. We enlarged the spectroscopic database by adding spectra from the Sloan Digital Sky Survet (SDSS) Data Release 12, and constructed a photometric catalogue of confirmed cluster members totalling 354 galaxies. We used the updated catalogue to derive the cluster velocity dispersion and mass. The validity of the mass estimate was verified by confirming the absence of significant substructure in the cluster. Full spectrum fitting was applied to derive consistent estimates of the SSP-equivalent ages and metallicities for early-type galaxies in the WHT and SDSS spectroscopic samples, and thus obtain the first estimate of the mass-metallicity relation for Perseus early-type galaxies. For the same early-type samples, we provide new and updated absorption line indices in the Lick system.

In Chapter 4 we analyse the photometry and long-slit spectroscopy for 12 isolated S0 and spiral galaxies. The structural parameters of the sample galaxies were derived from the Sloan Digital Sky Survey r-band images by performing a two-dimensional photometric decomposition of the surface brightness distribution, using a bulge, a disc and a bar component. We derived rotation curves and velocity dispersion profiles of the stellar using the spectra obtained along the major axis of galaxies. We also derived radial profiles of the H$\,\beta$, Mg and Fe line-strength indices, and found correlations between the central values of Mg$_2$, $\langle$Fe$\rangle$, H$\,\beta$ and velocity dispersion. We determine the age, metallicity, and [α/Fe] enhancement of the stellar population in the centre and at the radius where bulge and disc give the same contribution to the total surface brightness. The values were obtained using stellar population models with variable element abundance ratios. Two classes of bulges were identified: the intermediate-age bulges ($\sim$ 3 Gyr) with solar metallicity and old bulges ($\sim$ 15 Gyr) with a large spread in metallicity. Most of the sample bulges display super-solar [α/Fe] enhancement, no gradient in age and negative gradients of metallicity and [α/Fe] enhancement. These findings support a formation scenario via dissipative collapse where environmental effects are remarkably less important than in the assembly of bulges of galaxies in groups and clusters.

In **Chapter 5** we provide new measurements of the stellar population properties of the bulges of four spiral galaxies. Both the central values and radial profiles of the line strength of some of the most common Lick indices were measured along the major- and minor- axis of the bulge-dominated region of the sample galaxies. The corresponding age, metallicity, and α/Fe ratio were derived by using the SSP synthesis model predictions. The central values and the gradients of the stellar population properties of three of the sample bulges are consistent with previous findings for bulges of spiral galaxies. On the contrary, the bulge of the fourth galaxy shows peculiar chemical properties possibly due to the presence of a central kinematically-decoupled component. The negative metallicity gradient found in our bulges sample indicates a relevant role for the dissipative collapse in bulge formation. However, the shallow gradients found for the age and α/Fe ratio

suggests that merging can not be completely ruled out for the sample bulges. This is confirmed by the properties of ESO-LV 4500200 which can hardly be explained without invoking the capture of external material.

Chapter 2

Dynamics and stellar populations of Centaurus Cluster dwarf and compact elliptical galaxies

Abstract

We present X-Shooter spectroscopy for a sample of eight dwarf elliptical and two compact elliptical galaxies in the Centaurus Cluster. We derived accurate internal kinematics for the sample galaxies by analysing high resolution ($R \simeq 11000$) spectra from the X-Shooter VIS arm. We provide the first estimate of the Faber-Jackson relation for dwarf galaxies in the Centaurus Cluster by measuring the internal velocity dispersion with the full spectrum fitting technique. The slope of the relation is 2.00 ± 1.20, which is consistent with the relation found for dwarf galaxies in the Coma Cluster. The internal velocity dispersion of the compact elliptical galaxies is higher than that of the dwarf galaxies at the same magnitude, but lower than galaxies from other compact elliptical samples. Stellar population parameters were derived using both a Lick index analysis and full spectrum fitting with single stellar population models on the medium resolution ($R \simeq 3000$) UVB arm spectra. We find intermediate luminosity-weighted ages (4–8 Gyr) for all galaxies in the sample, consistent with prolonged star formation histories. The dwarf galaxies in our sample present low metallicities ([Fe/H] $\simeq -1$) consistent with the mass–metallicity relation for early type galaxies. Compact ellipticals, with slightly super-solar iron abundances, are offset from the early type relation. Their kinematics and metal-rich stellar populations are consistent with formation by tidal stripping of massive progenitors.

2.1 Introduction

The formation of the faint elliptical galaxy population we observe in cluster still lacks a full understanding, because the typically low surface brightness of these objects prevents a direct reconstruction of their evolution through medium-high redshift observations.

Unfortunately, because of current hardware limitations, the small mass and spatial scales of dwarf elliptical (dE) galaxies cannot be resolved in full cosmological and hydrodynamical simulations. On the modelling side, to predict the observed properties of dE galaxies it is therefore necessary to resort to semi-analytic models (Guo et al. 2011; Weinmann et al. 2011) or to perform a full hydrodynamical treatment on a limited volume with realistic initial conditions taken from cosmological simulations (Schroyen et al. 2013; Cloet-Osselaer et al. 2014). Each of the two approaches has its drawbacks. The former has to employ ad-hoc recipes for many of the physical processes involving baryonic physics. The latter necessarily neglects large-scale components (e.g., the intracluster medium or the dark matter halo of a massive cluster) which are known to affect the evolution of galaxies.

A complementary, "archaeological", approach is to study in detail the dwarf galaxy population in nearby clusters: the effects of their evolution and their interaction will be imprinted on their structural properties and on their kinematics and stellar populations.

The first question which has been tackled is that of the physical origin of dE in nearby clusters. Despite evidence of similarities in the observed properties (Chilingarian 2009) and scaling relations (Graham & Guzmán 2003) between dwarf and massive ellipticals, there is growing evidence that a significant fraction of the dE galaxies can be explained by a late-type galaxy population which has been recently accreted by cluster and has undergone environment-driven transformation in its morphological and stellar population properties (Conselice et al. 2001; Smith et al. 2012a, see also Chapter 3). Differences in the kinematic scaling relations (Toloba et al. 2012) and the higher mass-to-light (M/L) of dEs compared to that of giant ellipticals (Ryś et al. 2014) give further support to the notion that the two classes of galaxies do not share a common formation scenario.

Galaxy clusters can influence the morphology and stellar populations of the galaxies in different ways. The tidal effects experienced by a late-type galaxy as it interacts with the cluster potential and with other cluster galaxies in high-speed encounters ("harassment", Moore et al. 1998) can cause mass-loss and heating in the disc component, such that after a few orbits the galaxy closely resembles a non-rotating, round dwarf.

Ram-pressure stripping (RPS, Gunn & Gott 1972) and strangulation (Larson et al. 1980) refer to the action of the hot gas halo on the galaxies' gaseous components. Since gas is the primary source of fuel for star formation (SF), its removal will leave significant traces in the stellar population of the transformed galaxy. RPS refers to the removal of all the gas from the galaxy, resulting in a rapid SF quenching. Strangulation instead is the removal the cold gas halo surrounding the galaxy, so that inflow is stopped but SF

formation can proceed until all the gas in the disc is exhausted.

Simulations have shown that tidal and gas removal processes in clusters have a different dependence on the orbital properties of the galaxy inside the cluster and on the local density. The amount of harassment experienced by a galaxy depends strongly on the galaxy orbit (Smith et al. 2015): galaxies which do not plunge deep in the cluster core, where the galaxy density is higher and the potential is stronger, retain largely unaffected morphologies and experience very little mass loss. RPS instead has been shown to be effective also in low local density conditions (Cen et al. 2014), such as groups or the outskirts of galaxy clusters ($\gtrsim 2$ virial radii).

Which of the processes described above actually regulates the evolution of dEs in clusters is still a matter of debate. The internal kinematics of many dE galaxies in the Virgo cluster show remarkable similarities with those of disc galaxies (Toloba et al. 2011), providing support for the gas removal scenario via RPS or strangulation. Detailed dynamical models based on 3D kinematics (Ryś et al. 2014) of Virgo dEs have shown however that their rotation curves are not compatible with those of late-type galaxies, and that tidal harassment may play a role in determining their observed properties.

Spatially resolved kinematics, which can be used to construct accurate dynamical models, and high resolution kinematics, which are necessary to probe the low dynamical masses of dE galaxies, are however available only for nearby clusters like Virgo (Toloba et al. 2014) and Fornax (de Rijcke et al. 2001). These studies however, span a limited range both in redshift and in cluster density. Tentative efforts to derive cluster-centric trends are still faced with the degeneracies with galaxy orbit, which is a key parameter in the harassment scenario: a galaxy which is now in the outskirts may have already passed through the cluster core, and may therefore already have experienced substantial transformation. The way to overcome these limitations is to create statistically significant samples of dE galaxy properties across different environments, in order to partially remove the dependence on the orbital parameters. A first step in this direction was taken by (Penny et al. 2015), who investigated the internal kinematics of dE galaxies across different environments.

In this chapter, we improve on this work by analysing high- and medium-resolution X-Shooters spectroscopy of dE galaxies in the Centaurus Cluster, which is characterized by a lower galaxy density and velocity dispersion with respect to the Virgo and Perseus clusters.

In this work, we also study a sample of two compact elliptical (cE) galaxies in the Centaurus Cluster. Compact elliptical galaxies are characterised by a low luminosity, comparable to that of dwarf galaxies, but and a higher surface brightness, which makes them easier to detect with respect to classical dEs. cE galaxies have been studied in several works (Price et al. 2009; Chilingarian et al. 2009; Chilingarian & Zolotukhin 2015) which all showed that cEs present on average high velocity dispersions and metal-

rich ($\sim$ solar) stellar populations. This has been interpreted as evidence for a formation scenario characterized by tidal stripping of a more massive progenitor. Tidal streams have in fact been directly observed in group cEs (Huxor et al. 2011). We analysed the internal kinematics and the stellar population properties of the two cE galaxies to verify if their observed properties are compatible with the tidal stripping scenario.

The cluster itself and the sample selection are described in the two following subsections. In Sections 2.2 and 2.3 we describe the observations and the data reduction process. The analysis of the stellar kinematics and the internal velocity dispersions are presented in Sections 2.4 and 2.5. In Section 2.6 we describe our analysis of the stellar populations of the dE and cE galaxies. We summarize our results in Section 2.8.

We assume throughout the chapter a distance modulus for the Centaurus Cluster equal to $m - M = 33.28$ mag, derived by Mieske et al. (2005b) using the surface brightness fluctuation (SBF, Tonry & Schneider 1988) method. This corresponds to a distance $d = 45.3$ Mpc and a spatial scale of 220 pc arcsec^{-1}. We assume a Planck 2013 (Planck Collaboration et al. 2014) cosmology model, with $H_0 = 67.8$ km s^{-1} Mpc^{-1} and $\Omega_{\rm m} = 0.307$. Astronomical object nomenclature follows as much as possible the IAU recommendations[1], and all designation correspond to searchable objects in the NASA Extragalactic Database (NED).

2.1.1 The Abell 3526 Cluster

The Centaurus (Abell 3526) Cluster is a low-mass cluster (Girardi et al. 1998) visible from the southern hemisphere. The global kinematics of the Centaurus Cluster show marked differences with respect to other clusters (e.g., Perseus, see Chapter 3). Galaxies in the Centaurus Cluster possess a marked bimodal velocity distribution (Lucey et al. 1986; Stein et al. 1997, see Figure 2.1) given by the main cluster body at $V \simeq 3000$ km s^{-1} (commonly denoted as Cen30) and a second component at $V \simeq 4500$ km s^{-1} (Cen45). The two components possess very different velocity dispersions, with $\sigma_{\rm P} \simeq 500$–$930$ km s^{-1} (depending on the study) for Cen30 and $\sigma_{\rm P} \simeq 130$–$260$ km s^{-1} for Cen45. The two kinematic components present on average a distinct spatial distribution and distinct morphological and photometric properties. These differences have led Stein et al. (1997) to conclude that the Cen45 component is in fact not a proper cluster but a loose structure, more similar to a poor group, which is lying approximately at the same distance of the main cluster body (Cen30) or very close in projection. These analyses, in general, show that the Centaurus Cluster is a not yet a relaxed system, and its recent accretion history involves interaction with significant substructure.

Another peculiarity of the Centaurus Cluster is that a fraction of the dwarf galaxy population, in velocity space, is strongly clustered around the main galaxy NGC 4696 (Stein et al. 1997) and does not seem to follow the general cluster potential, as is typical

[1] `http://cdsweb.u-strasbg.fr/Dic/how.html`

for other clusters (Held & Mould 1994; Conselice et al. 2001). The clustering properties of the dE population in Abell 3526 are therefore intermediate between those of a true cluster and those of loose groups (Ferguson & Binggeli 1994). A comprehensive photometric study of the dwarf and compact galaxies in Centaurus was performed by Misgeld et al. (2009), who find a continuos distribution of photometric properties from dwarf to giant galaxies, and therefore argue for a common formation scenario of the two classes.

These peculiarities of the cluster must be taken into account when the properties of dwarf galaxies are related to the environment in which they reside.

2.1.2 Sample selection

The target dE and cE galaxies in this study were selected from the Centaurus Cluster Catalogue (Jerjen & Dressler 1997, hereafter CCC) and from Chiboucas & Mateo (2007, hereafter CM07). Confirmed cluster membership, by CCC, CM07 or Stein et al. (1997), was required for all targets. Basic photometric data were taken from the most recent literature reference: where available, we used V band data from Misgeld et al. (2009, hereafter MHM09), otherwise from CM07 SEXTRACTOR V band data were used. Since CCC 1 has incorrect profile fitting in CM07, profile data was taken from the CCC, which however has only B band data. The difference in structural parameters is assumed to be not significant but we do note that, being a nucleated dwarf, a mild gradient in stellar population is expected. CCC 228 has no corresponding object in the CM07 or MHM09 databases: its structural parameters were taken from CCC B band photometry, while its total magnitude was derived from the CCC B_T magnitude assuming a B extinction $A_B = 0.48$ (see CM07, section 3.7) and an optical colour $B-V = 0.8$, which is a typical value for dwarf galaxies in Centaurus (CM07) and corresponds to the $B-V$ value given by theoretical models for a $\sim$ 8–9 Gyr, [Fe/H] ~ -1 SSP (Maraston 1998). The galaxy projected ellipticities ϵ are all taken from the CM07 database.

The final sample contains eight nucleated dE galaxies (dE,N), one non-nucleated dE galaxy and two cE galaxies. Basic photometric properties of the sample galaxies are listed in Table 2.1. All galaxies were selected to be passive, with no evident sign of interaction or ongoing star formation.

The velocities of the sample galaxies with respect to the cluster velocity distribution is shown in Figure 2.1: all the selected galaxies appear to belong to the main body of the cluster (Cen30). The spatial distribution of galaxies in the cluster is shown in Figure 2.2, which displays the location of all galaxies from the CCC and CM07 catalogues with published radial velocities: the selected dwarf galaxy sample (blue circle) encompasses a wider range of local galaxy densities with respect to the compact elliptical sample (yellow triangles), which is instead concentrated near the cluster core.

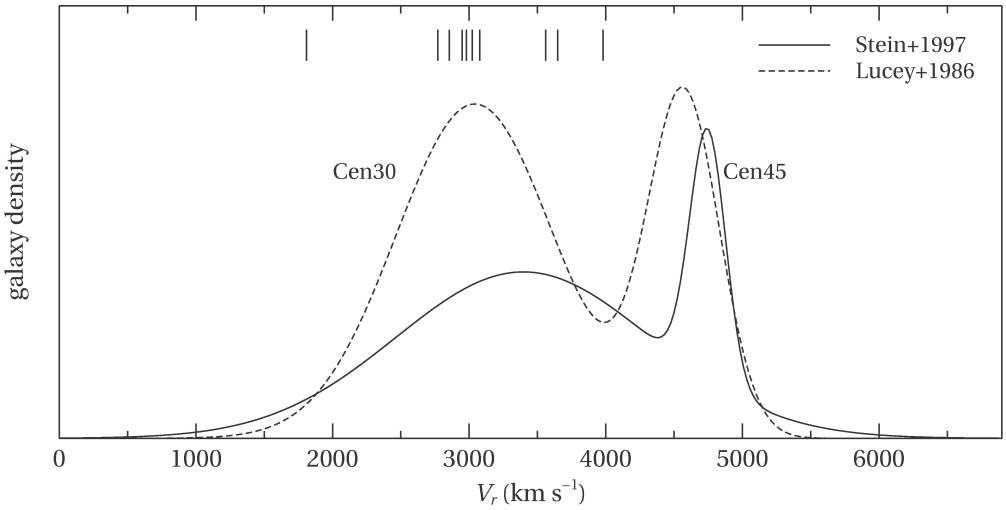

Figure 2.1: Velocity distribution of Centaurus Cluster galaxies. Vertical lines at the top of the plot mark the velocity of the dE and cE galaxies in the X-Shooter sample. The solid and dashed lines represent the double Gaussian fits obtained by, respectively, Stein et al. (1997) and Lucey et al. (1986) to the overall galaxy velocity distribution. The left and right peak of the distribution represent the Cen30 and Cen45 components, described in Section 2.1.

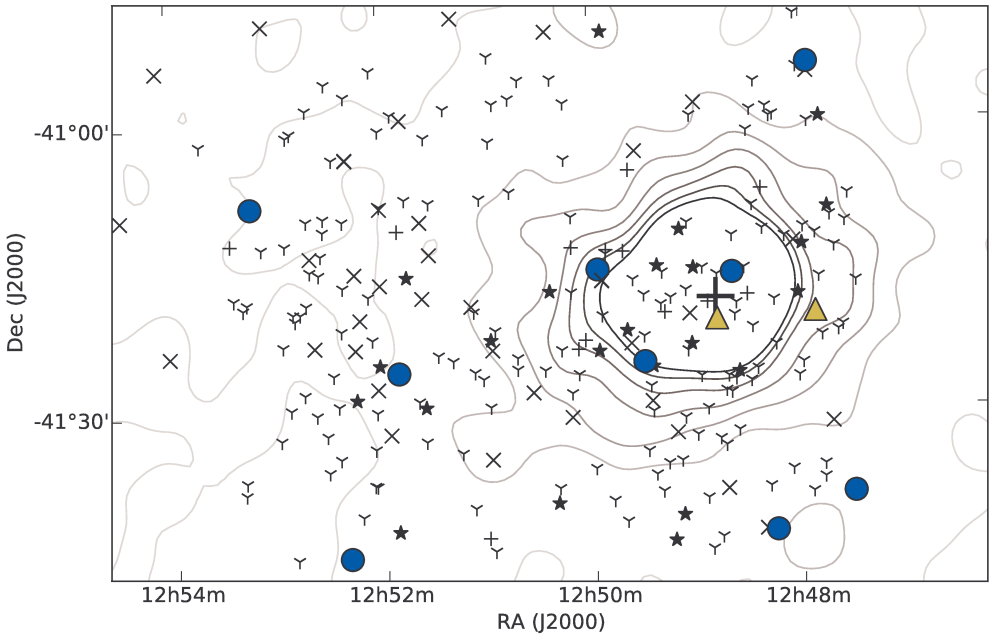

Figure 2.2: Sky map of the Centaurus Cluster (A3526), showing all galaxies with published radial velocity. Elliptical, spiral and dwarf galaxies are marked, respectively, by 'plus', 'x' and star symbols. 'Y' symbols represent galaxies with unknown morphological classification. Galaxies observed for the current study are marked by blue circles (dwarfs) and yellow triangles (compact ellipticals). X-Ray emission as measured by ROSAT (Allen & Fabian 1994) is shown by the contours, and the central 'plus' sign represents the brightest cluster galaxy, NGC 4696.

Table 2.1: Basic data for galaxies in the sample.

Object	R.A. (J2000)	Decl. (J2000)	Morph. type	m_V	$R_{V,\mathrm{eff}}$ (arcsec)	$\mu_{V,\mathrm{eff}}$ (mag arcsec^{-2})	n	ϵ	Ref. (a)	HRV (CM06)	HRV (SJF97)
CCC 1	12:47:30.3	-41:39:01	dE,N	16.23 ± 0.04	7.74	22.81		0.41	2,3	3743 ± 73	3527 ± 59
CCC 38	12:48:15.4	-41:42:59	dE,N	16.97 ± 0.05	5.58	22.33	1.00	0.25	1	3855 ± 83	3925 ± 45
CCC 61	12:48:39.7	-41:16:05	dE,N	16.23 ± 0.01	7.19	23.12	1.15	0.12	2	2659 ± 95	2910 ± 67
CCC 97	12:49:30.2	-41:25:16	dE,N	17.63 ± 0.05	3.07	22.10	1.00	0.05	1	2827 ± 61	2818 ± 30
CCC 125	12:49:56.4	-41:15:37	dE,N	16.17 ± 0.01	7.77	23.09	1.08	0.00	2		2880 ± 35
CCC 208	12:51:51.3	-41:25:58	dE,N	16.41 ± 0.05	8.77	21.77	0.86	0.38	1	3560 ± 60	3624 ± 22
CCC 228	12:52:21.0	-41:45:07	dE,N	16.81 ± 0.3	8.95	24.1			3		3212 ± 62
CCC 260	12:53:14.2	-41:08:29	dE,N	16.45 ± 0.05	8.07	22.49	0.82	0.36	1	2845 ± 114	2766 ± 43
[CM2007] 374	12:47:52.2	-41:20:14	cE	18.05 ± 0.05	2.20	21.33	1.00	0.14	1	2828 ± 88	
[CM2007] 435	12:47:55.8	-40:54:16	dE	17.33 ± 0.05	4.14	22.42	1.00	0.29	1	1817 ± 74	
[CM2007] 1214	12:48:48.6	-41:20:53	cE	17.71 ± 0.05	1.27	20.95	1.27	0.11	2	3053 ± 40	

(a) 1: Chiboucas & Mateo (2007); 2: Misgeld et al. (2009); 3: Jerjen & Dressler (1997)

2.2 Observations

Spectroscopic data were obtained using the X-Shooter (Vernet et al. 2011) spectrograph, mounted at the Cassegrain focus of the European Southern Observatory (ESO) Very Large Telescope (VLT) UT2 "Kueyen" telescope. X-Shooter allows the simultaneous acquisition of target spectra in three different wavelength ranges, corresponding to different "arms" of the spectrograph: the near-infrared (NIR), visible (VIS) and UV–blue region (UVB). Each arm is an independent cross dispersed echelle spectrograph completed with its own shutter and/or slit mask. For each arm the spectral format is fixed, and the observer can only choose the most suitable slit (and hence the spectral resolution) for a given observation.

Despite the limited slit length (11 arcsec) which does not allow a detailed spatially resolved investigation of the galaxy properties, the X-Shooter instrument is the ideal choice to study the internal kinematics and the stellar population properties of dwarf galaxies, because it allows the simultaneous acquisition of spectra of sufficiently high resolution (FWHM $\sim$ 30 $\mathrm{km\,s^{-1}}$) and spectra of sufficient signal-to-noise (S/N) ratio. The former is necessary to resolve the low velocity dispersion typical of dwarf galaxies ($\sigma \sim 30$ $\mathrm{km\,s^{-1}}$), while the latter is essential to derive reliable ages and metallicity estimates for the stellar populations.

The target galaxies were observed in two observing runs: the first one in March 2010 during ESO periods 84 and 85 and the second in April 2014 during ESO period 92 (throughout the chapter, we will refer to R1 and R2 to denote observations and data coming, respectively, from the first and second run of observations). During R1, the spectrograph slit was aligned with the galaxy position angle. During R2, because of failures of the atmospheric dispersion correctors of X-Shooter, the slit was aligned at the parallactic angle. Observation dates, together with program IDs and exposure times for each object are listed in Table 2.2. To perform a coherent data analysis on the whole dataset, observing and data reduction parameters were kept consistent between the two runs. Table 2.3 list the slit setup of the X-Shooter spectrograph for the two runs of observations, as well as the wavelength interval and resolution for each spectrograph arm. For the UVB arm, the 1.6 arcsec slit was chosen to achieve a good S/N in the 350–550 nm range which, being rich in hydrogen and metal (mainly iron and and magnesium) absorption lines, is the primary interval in which to perform detailed stellar population analyses, which require higher S/N ratios. In the VIS arm we chose the 0.7 arcsec slit to achieve a higher spectral resolution (sacrificing S/N) to perform accurate measurements of the galaxy stellar kinematics. The decrease in S/N ratio is mitigated by the presence of the strong Hα and Ca II lines, which can effectively be used to measure reliable internal velocity dispersions. In the NIR arm, a wide slit ($1\farcs5$) was again used in P84 and P85 to maximize S/N ratio, while in P92 the K-band blocking filter was used to reduce scattered light in the J and H band. All galaxies were observed in SLIT mode using an

offset-sky strategy with object-sky-object pattern. Exposure times in Table 2.2 refer to the object spectra; the exposure times for the offset sky frames are the same as the ones of a single science exposure. The timing was optimized for the optical bands. For CCC 260, because of night time constraints, only one science exposure was acquired.

During the observations, together with science spectra and calibration frames (biases and flats), the spectra of several standard stars were acquired to perform flux calibration and telluric absorption removal. The spectrum of HD 111486 was also acquired in both runs to serve as velocity standard star in the following data analysis. Table 2.4 lists all the standard stars acquired during the observations, together with their spectral class as listed on the SIMBAD[2] database.

2.3 Data reduction

Data reduction was performed using ESO-VLT instrument pipelines[3] for the X-Shooter instrument. Data acquired during R1 and R2 were reduced, respectively, using pipeline versions 1.3.7 and 2.0.0. The main science reduction was performed through the `xsh_scired_slit_offset` recipe, which includes standard steps in the reduction of echelle spectroscopy: bias and flatfield correction, wavelength calibration, order tracing and merging and flux calibration.

The spatial resolution of the final 2D rectified spectra is $0\farcs16$ pixel^{-1} for the UVB and VIS arms, and $0\farcs21$ pixel^{-1} for the NIR. One-dimensional spectra in the UVB were obtained from 2D frames using a custom implementation of the optimal extraction algorithm by Horne (1986), and the separate spectra corresponding to each exposure were co-added to obtain the final spectrum for each object. In the VIS band the final 1D and 2D spectra from the pipeline contain prominent residuals from the subtraction of the sky emission. As an example, Figure 2.3 shows the spectrum of CCC-208 (red line) in the Ca II triplet (CaT) wavelength region: the residual O_2 emission generates serious contamination for the λ8498 and the λ8542 absorption features, and the λ8662 line is completely obscured by OH emission. To extract 1D spectra in the VIS we therefore adopted a different strategy, based on the sky subtraction code SKYCORR[4] (Noll et al. 2014): we used the final 2D spectra from the pipeline to compute the variance and spatial profile maps (see Horne 1986) which were used to extract separately the 1D spectrum from the object frames (without sky subtraction) and the offset sky frames. These 1D spectra were then processed with SKYCORR with standard parameters for X-Shooter (see Noll et al. 2014, and the software manual) to obtain the final galaxy spectra. The final result (for CCC-208, as an example) is shown in Figure 2.3 (black line): the

[2] `http://simbad.u-strasbg.fr`

[3] `http://www.eso.org/sci/software/pipelines/`

[4] `http://www.eso.org/sci/software/pipelines/skytools/skycorr`

Table 2.2: Observation log

ESO Prog. ID	Obs. date	Object	Exp. time (s)
084.B-1083(A)	2010-03-22	CCC 1	2×1350
	2010-03-24	CCC 125	2×1250
		[CM2007] 1214	2×1500
085.B-0279(A)	2010-04-18	CCC 61	2×1500
		[CM2007] 374	2×1500
		[CM2007] 435	2×1800
092.B-0897(A)	2014-03-30	CCC 208	2×1500
		CCC 38	2×1500
		CCC 97	2×1800
		CCC 228	2×1800
		CCC 260	1×1500

Table 2.3: X-Shooter spectral (slit) setup

Spectrograph arm	$\lambda\lambda$ (µm)	Slit	Nominal resolution
ESO P84 & P85 (Run 1)			
UVB	0.33−0.56	1.″6	3300
VIS	0.56−1.02	0.″7	11000
NIR	1.02−2.40	1.″5	3300
ESO P92 (Run 2)			
UVB	0.30−0.56	1.″6	3300
VIS	0 .56−1.02	0.″7	11000
NIR	1.02−2.40	0.″9 JH	5300

Table 2.4: List of standard stars acquired during observations

Name	Type	Spectral class
Run 1		
HD 111486	Velocity	K0II
GD 71	Spectrophotometric	DA1.5 (WD)
GD 153	Spectrophotometric	DA1.2 (WD)
Hip 035621	Telluric	B2V
Hip 057996	Telluric	B7V
Hip 060099	Telluric	B8V
Run 2		
HD 111486	Velocity	K0II
Hip 045754	Telluric	B8V
Hip 054185	Telluric	B9.5V
Hip 060517	Telluric	B9V

sky emission residuals are almost completely eliminated, and clean Ca II absorption features are recovered. Residual cosmic rays are ignored by the analysis software (see Section 2.4.1) and were therefore not manually removed from the 1D spectra.

The optimal extraction algorithm co-adds all the spectra corresponding to the pixels along the slit and weights each spectrum using the spatial light profile along the slit and the pixel variances. Despite the weighting scheme of the algorithm, the choice of the radius up to which the co-adding has to be performed is important both because it allows the removal of unwanted noise resulting from the inclusion of pixels too far away from the galaxy centre and because it is determined by the type of problem under study. For the current study, in order to use the available formulas to compute the galaxy dynamical mass (see Section 2.5.2) and to be consistent with the available literature on the dynamics of early-type galaxies (ETGs) (Cappellari et al. 2006; Ryś et al. 2014), we are mostly interested in the galaxy properties inside the effective radius R_e, i.e. the radius enclosing one half of the total galaxy luminosity. All galaxies, except for the two cEs and CCC-97, have effective radii which extend beyond or up to the edges of the spectrograph slit. For these galaxies, we extracted the 1D spectrum from all pixels in the aperture. To have a consistent analysis for all galaxies in the sample, we extracted the spectra of the cE galaxies and that of CCC-97 from the aperture inside R_e.

One of the cE galaxies (CM07-374) was found to have a nearby interloper (< 2 arcsec), which according to the spectrum is an F type star. The star is unresolved in DSS images but is clearly resolved by the VLT both in the acquisition images and in the 2D spectrum. To remove the contribution of the interloper, we fitted a Gaussian function to its spatial profile, and cut from the 2D spectrum frames all pixels below 3σ from the stellar centre. This procedure effectively removes most of the light from the star, while preserving a consistent fraction of the light from the galaxy: on the side where the interloper lies, the spectrum is cut at ≈ 0.8 arcsec from the photometric centre, which is approximately the seeing FWHM for the night of the observation, but smaller than the galaxy effective radius (2.2 arcsec).

The final UVB spectra for all the sample galaxies are shown in Figure 2.4, while the VIS spectra are shown in Figure 2.5. The VIS spectra are shown, for clarity, only in the H α and CaT wavelength regions.

2.4 Stellar kinematics

We analysed the final spectra of the galaxies in the Centaurus sample using the full-spectrum fitting package ULySS[5] (Koleva et al. 2009b). ULySS is a user-friendly IDL package that allows the simultaneous determination of the parameters of the line-of-sight velocity distribution (LOSVD), as described in this section, as well as the parameters of

[5] http://ulyss.univ-lyon1.fr/

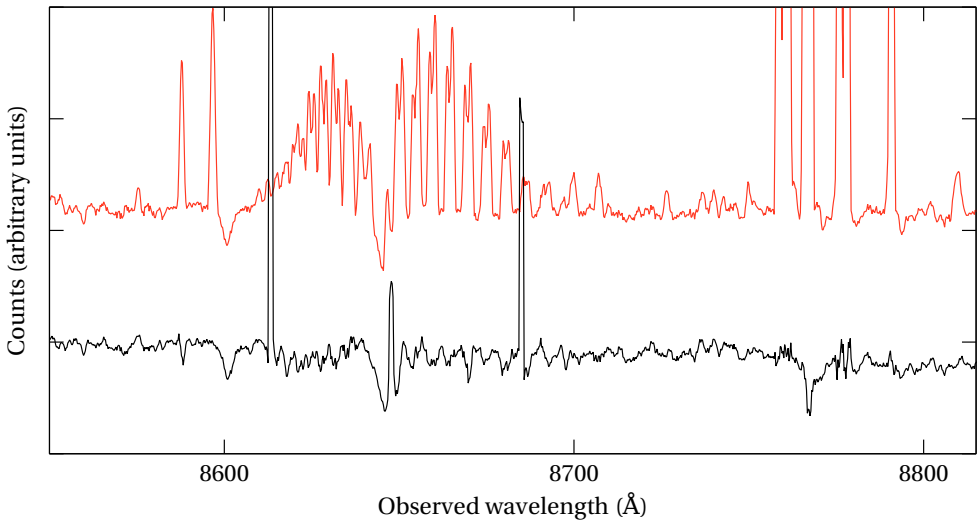

Figure 2.3: Observed spectrum of CCC-208 in the Ca II triplet region. Red line: Final 1D spectrum from the ESO X-Shooter pipeline. Black line: Final spectrum processed with SKYCORR. For clarity, both spectra were smoothed with a 5–px (1.25 Å) boxcar filter.

the stellar population of a given spectrum, discussed in Section 2.6.1.

2.4.1 The analysis method: full spectrum fitting

Early methods to derive stellar velocity dispersions in galaxies derived the spectrum LOSVD using quotient (Sargent et al. 1977) or cross-correlation (Tonry & Davis 1979) methods in Fourier space. These techniques, however, usually work under the restrictive assumption of Gaussian broadening, and are particularly prone to the effects of template mismatch. Although efforts have been made to overcome these limitations (Bender 1990), direct fitting in pixel space (Rix & White 1992) has become in the last decades the *de facto* standard to derive stellar (and gas) kinematics in galaxies. The ULySS software package uses this approach to fit an observed spectrum against a model (details of the algorithm are given below). The code itself is modelled after PPXF (Cappellari & Emsellem 2004, hereafter CE04), but is has been explicitly adapted to derive atmospheric parameters for stars (Wu et al. 2011) and compute star formation and metal enrichment history of galaxies (Koleva et al. 2008b). In addition, ULySS provides facilities to define custom components and to run Monte Carlo simulations to derive reliable error estimates on the parameters and possible degeneracies in the solution. The package, together with a comprehensive set of tutorials, is freely available on the web.

The model spectrum is constructed as a linear combination of k non-linear components, optionally convolved with an LOSVD. The model is also optionally multiplied by a

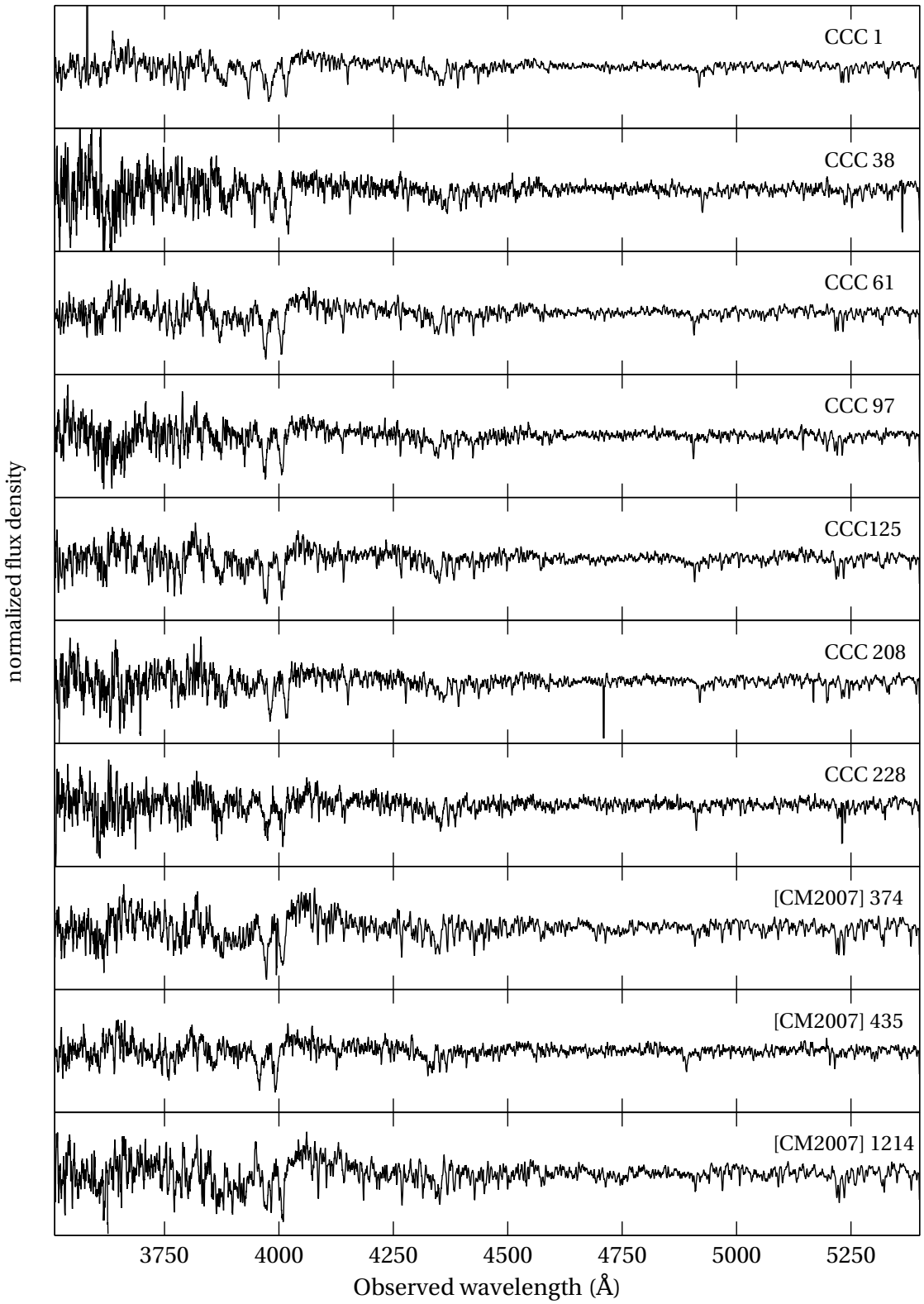

Figure 2.4: UVB spectra for the sample galaxies. The spectra are smoothed with a 5 px boxcar filter and are normalized using a 5^{th} degree polynomial, in order to aid visualization.

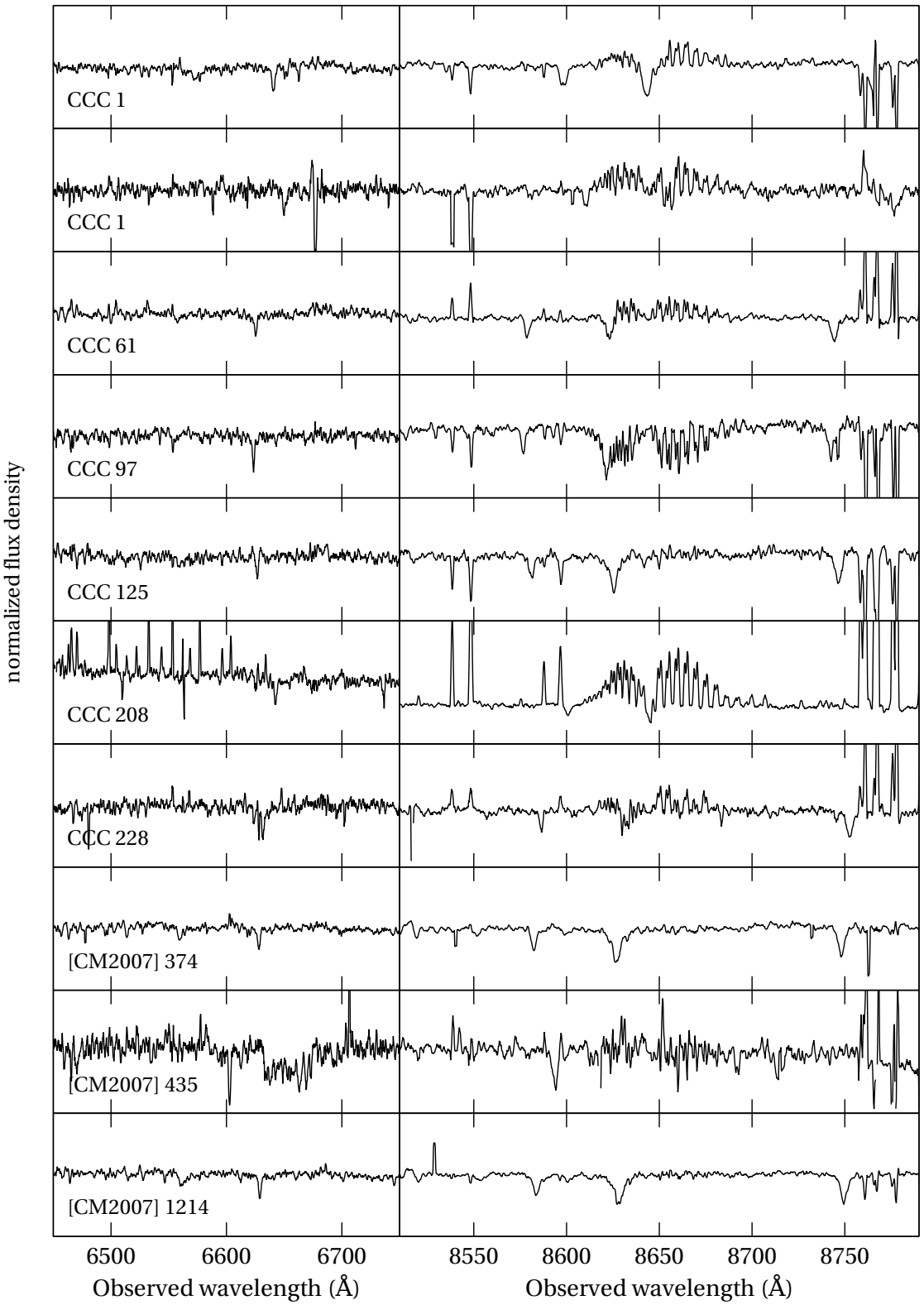

Figure 2.5: VIS spectra for the sample galaxies. The left and right column for each row (i.e., each galaxy) show, respectively, the H α and CaT region of the spectrum. As in Figure 2.4, the spectra are smoothed with a 5 px boxcar filter and normalized.

$n^{\rm th}$ degree polynomial $P_n(\lambda)$ and summed with another polynomial $Q_m(\lambda)$. The general formula for the flux of a model spectrum $F_{\rm mod}$ is:

$$F_{\rm mod}(\lambda) = P_n(\lambda) \times \left({\rm LOSVD}(\theta_{\rm L}) \otimes \sum_{i=1}^{k} W_i \, {\rm CMP}(\theta_{\rm C}) \right) + Q_m(\lambda) \ , \qquad (2.1)$$

where $\otimes$ denotes convolution, W_i is the weight of each component, and $\theta_{\rm L}$ and $\theta_{\rm C}$ are the parameters (in general non-linear) of the LOSVD and components, respectively. ULySS follows the common approach (van der Marel & Franx 1993, CE04) of parametrizing the LOSVD as a Gauss-Hermite expansion: $\theta_{\rm L} = (V, \sigma, h_3, h_4)$, where V, σ, h_3, h_4 represent, respectively, the shift, dispersion, skewness and kurtosis of the velocity distribution. In the following analysis, we only focus on the kinematic parameters V and σ, because the medium-low *S/N* ratio of the dwarf galaxies in our sample does not allow the accurate determination of significant deviations from a Gaussian LOSVD.

The choice of components parameters $\theta_{\rm C}$ depends instead on the type of component under consideration: for the analysis of star formation histories, for example, typical parameters are the age and metallicity (and optionally α-element abundance ratio) of the stellar population.

The multiplicative polynomial $P(\lambda)$ can be used effectively to absorb the effects of imprecise flux calibration and galactic extinction, while the additive polynomial $Q(\lambda)$ is useful in a limited set of circumstances (e.g. improper background subtraction) and was not further considered in our analysis, also because it is degenerate with the depth of the absorption lines, and may bias the results of the fitting.

The best fitting model parameters $(\theta_{\rm L}, \theta_{\rm C})$ are then derived by minimizing the χ^2 given by

$$\chi^2 = \sum_{i=1}^{N} \left(\frac{F_{{\rm obs},i} - F_{{\rm mod},i}}{\Delta F_{{\rm obs},i}} \right)^2 \ , \qquad (2.2)$$

where $F_{\rm obs}$ is the observed galaxy spectrum, $\Delta F_{{\rm obs},i}$ is the error on $F_{{\rm obs},i}$ and the sum is intended over all good pixels. Both the galaxy and model spectrum are rebinned, prior to the fitting process, to a common scale linear in $\ln \lambda$, so that a Doppler wavelength red- or blue-shift corresponds to a linear shift which is constant along the spectrum. The minimization itself is performed using the IDL implementation (MPFIT, Markwardt 2009) of the Levenberg-Marquardt method (LM) (Moré 1978).

ULySS optionally performs a cleaning of the input spectrum, to remove residual cosmic ray features or incorrectly subtracted sky lines. The basic algorithm is a based on an iterative k–sigma clipping rejection, where the the sigma is computed as the standard deviation of the residuals after the first model fit. The rejection scheme itself is more sophisticated, and is optimized to avoid the rejection of pronounced emission lines but to correctly remove extended sky features. We refer the interested reader to

the online documentation of the ULY_FIT routine. The /CLEAN option was always used in the fitting procedures employed to derive galaxy kinematics.

The LM algorithm requires as input a guess for each parameter. The guess values for the galaxy radial velocity V was determined using the IRAF task fxcor, which performs a cross-correlation of the observed spectrum with a template. The radial velocity values obtained through the cross-correlation analysis were added to the peculiar velocity (see Section 2.6.1 for its derivation) to obtain the final radial velocities V, which are listed in Table 2.6. We did not correct for the heliocentric velocity of the earth, because the accurate derivation of the galaxy velocity is not the primary focus of the current study. Furthermore, since the V parameter was left free to vary during the fitting procedures, only a reasonable guess is required for the following analysis. The obtained galaxy redshifts are consistent with the literature values: compared to the CM07 catalogue, the median offset is 20 $\mathrm{km\,s^{-1}}$ and the mean absolute deviation is 105 $\mathrm{km\,s^{-1}}$ (the maximum deviation is 208 $\mathrm{km\,s^{-1}}$ for CCC 1). Compared to the Stein et al. (1997) catalogue, the median offset is 8 $\mathrm{km\,s^{-1}}$ and the mean absolute deviation is 55 $\mathrm{km\,s^{-1}}$ (the maximum deviation is 150 $\mathrm{km\,s^{-1}}$ for CCC 228).

We used different templates to construct the model spectrum F_{mod} for the dynamical and stellar population analyses of the Centaurus dE and cE galaxies: galaxy kinematics were derived by fitting the VIS arm spectroscopy with stellar templates acquired with the same instrument and spectral setup of the galaxy observations. The template set, together with the results and the description of the simulation to derive the uncertainties are described in the next Section.

Stellar populations were instead derived using high resolution SSP models applied to UVB band spectra. The detailed data analysis procedure for the stellar populations, together with the Lick index analysis, is described in Section 2.6.

To derive the internal velocity dispersions of the sample galaxies, we performed a fit of the VIS galaxy spectra with a set of 7 G and K template stars downloaded from the ESO Phase 3 archive[6] (pipeline-reduced products). In order to avoid the need to correct the templates or the observed galaxies for the instrumental broadening, all star templates were required to be obtained by X-Shooter with the same spectral setup (i.e. the same slit). All downloaded spectra were acquired under ESO programs 189.B-0925 (P.I. Trager) for the realization of the X-Shooter Spectral Library[7] (Chen et al. 2014, XSL). The template set used in the fitting is listed in Table 2.5, together with rough estimates of their atmospheric parameters obtained by running ULySS TGM procedures on the VIS spectra using the Elodie 3.2 library. The precise value of the parameters is not crucial, as long as spectral types representative of typical dwarf galaxy stellar populations are selected, but we note that the difference with respect to the most recent

[6] http://archive.eso.org/wdb/wdb/adp/phase3_spectral/form
[7] http://xsl.u-strasbg.fr/

values found in the SIMBAD database[8] (from Prugniel et al. 2011) are within 10% for $T_{\rm eff}$, 25% for $\log g$ and 33% for [Fe/H].

2.4.2 Analysis of reliability

Given the importance of establishing realistic errors on the internal velocity dispersions of low-mass galaxies, we performed an extensive set of ULySS runs on simulated galaxy spectra with different noise levels, following the procedures outlined in Cody et al. (2009, hereafter Co09) and Toloba et al. (2011).

Simulations

A first set of simulations was performed using the velocity standard KIII star HD 111486. The star VIS spectrum was broadened, using the ULySS `uly_spect_losvdconvol` routine, with different input LOSVDs corresponding to $\sigma_{\rm in}$ = 8, 10, 20 and up to 70 $\mathrm{km\,s^{-1}}$ in steps of 10 $\mathrm{km\,s^{-1}}$. Random noise was added corresponding to 15 values of S/N linearly spaced in $\log S/N$ between 1 and 50 $\mathrm{px^{-1}}$. The input S/N values were computed according to

$$sn_i = sn_*^{i/(n-1)} \qquad i = 0, \ldots, n-1 \ , \tag{2.3}$$

with $n = 14$ and $sn_* = 50$. This spacing was chosen to obtain a finer sampling in the typical (i.e. low, ~ 10) S/N range of the Centaurus Cluster targets, and to study the performance of the analysis software on very low S/N spectra. Artificial noise generation was performed directly by the ULySS routine, via the `NSIMUL` and `SNR` keywords, which specify the number of simulations and the desired output S/N, according to the following scheme: from the input spectrum F the mean value of the flux is computed, and the mean error, for a desired output S/N sn_i is derived as

$$\bar{\delta} = \frac{\bar{F}}{sn_i} \cdot k_\nu \ , \tag{2.4}$$

where k_ν is a factor which traces the change of number of degrees of freedom. The number of degrees of freedom ν changes, for example, when the input spectrum is broadened to a given LOSVD, which causes adjacent pixels to become correlated. The mean error $\bar{\delta}$ is then multiplied by a normally distributed random array with $\mu = 0$ and $\sigma = 1$, and the resulting array is added by ULySS to the original spectrum.

For each set of input parameters value (S/N, $\sigma_{\rm in}$) we ran ULySS on 500 mock spectra, using the original star spectrum as template, and we derived the distributions of measured velocity shift and dispersion values. We did not perform specific simulations to derive the behaviour of the output parameters as a function of input V, both because the

[8] `http://simbad.u-strasbg.fr/simbad/`

Table 2.5: XSL stellar templates.

Star	$T_{\rm eff}$ (K)	[Fe/H]	$\log g$
HD 007595	4314	-0.43	1.6
HD 035179	4928	-0.41	2.2
HD 054828	4930	-0.50	2.5
HD 098468	4415	-0.30	1.6
HD 100906	4995	-0.33	2.2
HD 134063	4916	-0.42	2.5
HD 171367	4393	-0.47	1.8

primary goal in this analysis is the determination of the galaxy σ (redshifts are assumed known) and because, since the h_3 and h_4 parameters are not considered in the following, the velocity shift is not expected to correlate with any other LOSVD or component parameter. The simulations were repeated twice restricting the wavelength interval where the fitting is performed to the Hα ($\lambda\lambda$ = 6200–6800 Å) and CaT ($\lambda\lambda$ = 8300–8800 Å) regions.

An example of the typical output parameter distributions from the simulations is shown in Figure 2.6. The orange histograms represent the distributions of the measured values of $\sigma_{\rm m}$, binned in 2 km s^{-1} intervals, at a given input $\sigma_{\rm in}$ value (20 km s^{-1}for the upper panels, 50 km s^{-1} for the lower panels). Gaussian fits to each distributions are overlaid as solid black lines. The three panel columns refer to different input *S/N* ratios: $\approx$ 1, 7 and 16 px^{-1} which correspond to i = 0, 7 and 10 in equation 2.3 and were selected to highlight the accuracy of the LOSVD fitting algorithm at very low, low and medium *S/N* values. As expected, increasing the *S/N* of the input spectrum reduces the scatter in the distribution of the measured values. A second trend that can be evinced from the figure is that the scatter increases as a function of $\sigma_{\rm in}$. The first panel in each row shows the distribution for very noisy spectra ($S/N = 1$): in both sets of simulations the second histogram bin is the one with the largest number count. The excess of outputs with $\sigma_{\rm m}$ between 2 and 4 km s^{-1} is the result of failed fits: typically, a fit fails when the minimization algorithm is unable to find a minimum in the allowed parameter space. When this happens, the minimum found by the procedure has one of the parameters which settles on one of the limits of its "available" range. This solution cannot be considered reliable, because the true minimum lies outside of the explored parameter space, and was therefore discarded from the simulation results. For a fit to be rejected, we checked that one of the two following conditions was met:

1. the output σ value is equal to the *minimum* measured output σ of all the simulation set. Note that this criterion always removes at least *one* fit from all the simulation sets, but being one fit over 500 the final results of this analysis are not affected.

2. the output formal errors on σ is equal to 0. This is a consequence of the fact that

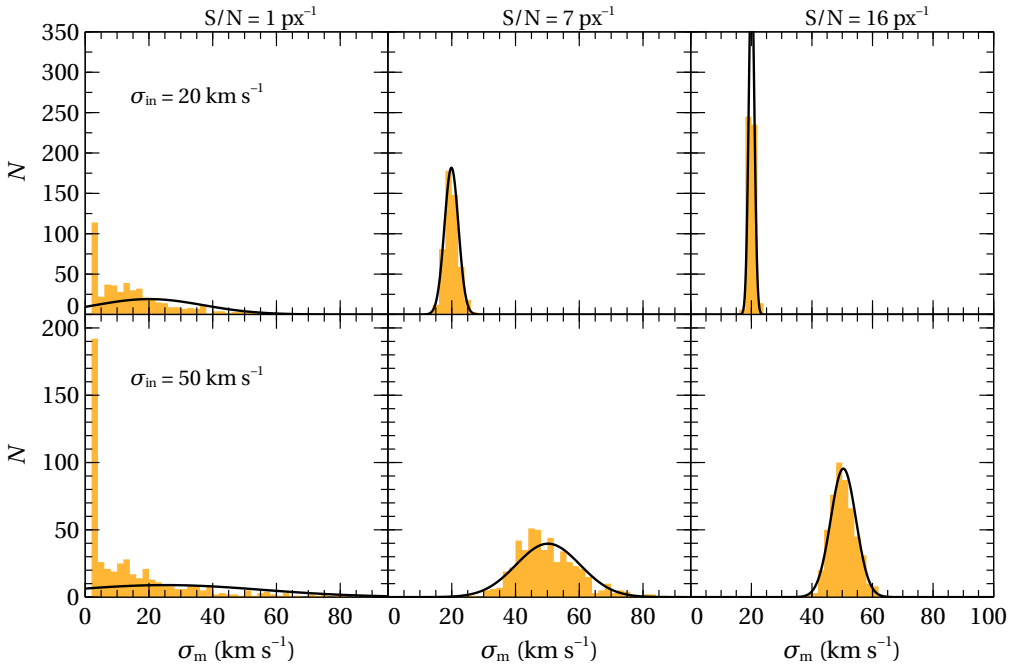

Figure 2.6: Output distributions of the measured σ_m value (orange histograms) from the ULySS simulation sets. The best fitting Gaussian function describing the distributions are shown as solid black lines. Parameters for the Gaussian functions were determined after the cleaning procedure. The upper row of the plot shows the distributions obtained for $\sigma_{in} = 20$ km s^{-1}, while the bottom row shows the results for $\sigma_{in} = 50$ km s^{-1}. Each column represents a different input S/N ratio: $S/N = 1$ for the first column, $S/N = 7$ for the second and $S/N = 16$ for the third.

the minimum in which the algorithm has settled is on the "border" of parameter space. MPFIT is therefore unable to compute the gradient of the χ^2 on which the output formal errors depend.

These criteria were applied only on the output σ parameter and not on the velocity shift parameter V because, since σ has the obvious theoretical $\sigma = 0$ lower bound, the LM method is more prone to "hit" the boundaries of σ than those of V, which has looser bounds. *A posteriori*, we found that indeed only a selection on the output σ values can be effective in removing failed fits.

The limits on V and σ are automatically set by ULySS: ± 2000 km s^{-1} for V and $[0.3v_{\rm sc}, 1000]$ km s^{-1} for σ, where $v_{\rm sc}$ is the pixel scale in km s^{-1}; the lower limit for σ is therefore ≈ 8 km s^{-1} for the UVB spectra (equal to the lower $\sigma_{\rm input}$) and ≈ 3 km s^{-1} for the VIS. We expect the number of failed fits in a simulation set to be dependent both on the input *S/N* ratio and on the dispersion (in km s^{-1} px^{-1}) of the input spectrum.

For each simulation set we computed the fraction of successful fits compared to the total number of simulated spectra, and after the removal of all failed fits we derived the sample mean and standard deviation, together with their uncertainties, of the distribution of the output parameters. The results are shown, as a function of input *S/N* ratio, in Figure 2.7 for stellar template simulations in the VIS arm.

The first, second and third panel columns show the simulation sets for the star HD 111486 using, respectively, the whole VIS wavelength range, the CaT region and the H α region in the fitting process. The line colour and style correspond to different values of $\sigma_{\rm in}$.

The top row of Figure 2.7 shows the fraction of successful fits after the removal of failed fits described above. The fraction, as expected, approaches 1 as the *S/N* of the spectra increases. Reducing the wavelength range over which the fitting is performed, the fraction of successful fits decreases, as can be seen in the second and third columns. In particular, for spectra with low *S/N* ratio restricting the fits to the CaT regions can cause more than 50% of them to fail. To ensure that a correct fit is performed, the input spectra should have $S/N \gtrsim 4$ when the fitting is performed over the whole wavelength range and $\gtrsim 10$ when only limited wavelength ranges are considered. The trend of rejected fraction with *S/N* depends only weakly on the input LOSVD σ (the three lines are similar in every panel), because the mid-high resolution in the VIS arm sets a lower boundary for σ which is well below the smallest $\sigma_{\rm in}$.

The second and third row in Figure 2.7 show the mean $\bar{V}$ and the standard deviation s_V for the measured V parameter (the velocity shift). As the *S/N* of the simulated spectra increases, the average shift approaches 0 (the input value) and the standard deviation of the measurements decreases. The simulation sets restricted to limited wavelength regions show significant deviations for *S/N* values smaller than $\simeq 10$, hence, as in the previous paragraph, this value should be considered a lower limit when fitting is per-

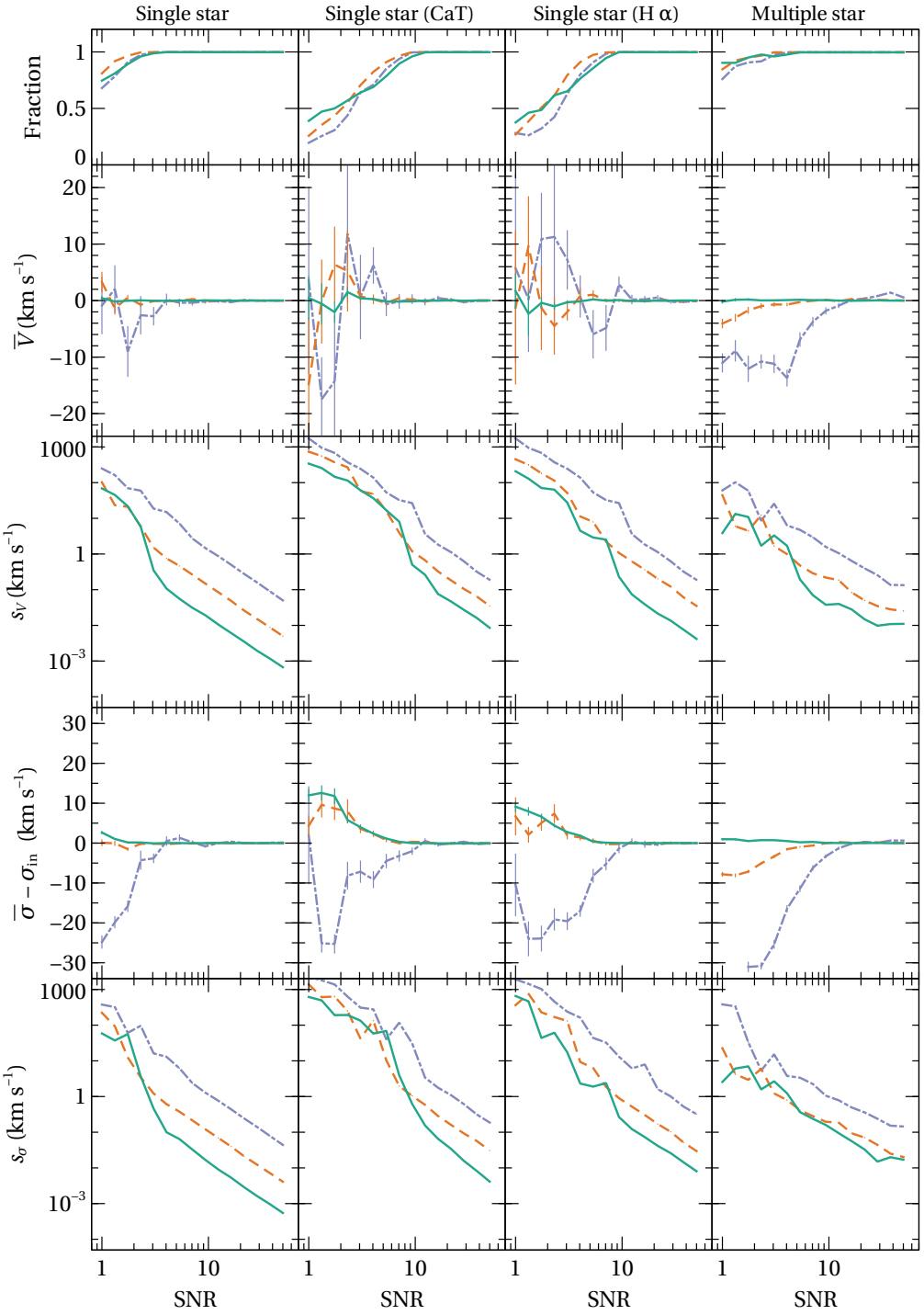

Figure 2.7: Results of the ULySS fitting to simulated VIS arm galaxy spectra, as a function of S/N ratio. From top to bottom, the panel rows show the fraction of "good" fits, the mean and standard deviation of the velocity shift and the mean and standard deviation of the measured velocity dispersion. The panel columns refer to different template sets and wavelength ranges, as discussed in the text. The green solid, orange dashed and purple dot-dashed lines represent, respectively, $\sigma_{\rm in} = 8$, 20 and 50 km s^{-1}.

formed only in a small wavelength region. A peculiar feature in the second row of the Figure is that the simulation sets with $\sigma_{\rm in} = 8$ km s^{-1} have a very low bias also for very low *S/N* spectra, where even the fraction of rejected fits is substantial. In the third row in the plot, the y axis (s_V) is shown in logarithmic scale because the standard deviation of the simulation measurements cover a very large range (~ 5 orders of magnitude). All the lines in the first three panels of the third row have relatively high scatter in the *S/N* range where the fraction of rejected fits is substantial. When the good fit fraction approaches 1, the scatter drops and roughly follows a power-law as a function of *S/N*, with slope which is ≈ -2 for the full wavelength range fits and slightly steeper ($\lesssim -2$) when limited wavelength ranges are used. A general trend that can be evinced from the first three columns is that increasing the input σ value the scatter of the V measurements increases because, since the absorption lines are broader, the definition of the exact centre of the spectral features is more uncertain.

The last two rows in Figure 2.7 display the mean (minus the input σ) and standard deviation of the measured LOSVD parameter $\sigma_{\rm m}$. The combination of low *S/N* ratio and high input velocity dispersion (purple dot-dashed lines) generates, in all panels, a negative bias in the average output σ values. This is likely due to the erroneous fitting by the algorithm, of the noise which is filling the absorption lines. For low $\sigma_{\rm in}$ values (and low *S/N*), we confirm the positive bias already found by Co09. The bias in the output $\sigma_{\rm m}$ values is very important: if one is interested only in the galaxy internal kinematics, parametrized by a simple Gaussian function with $h_3 = h_4 = 0$, it may be accounted for by carrying an additional uncertainty throughout the following analysis, but if one is interested in deriving the other LOSVD Gauss-Hermite parameters or other component parameters ($\theta_{\rm C}$), great care must be taken to account for possible degeneracies. For example, it has been shown that the SSP metallicity of a stellar population is degenerate with the σ of the measured LOSVD (Koleva et al. 2008a), so a significant bias in $\sigma_{\rm m}$ may affect the determination of the chemical enrichment properties of the stellar population. The standard deviation s_σ span almost 5 orders of magnitude from $S/N = 1$ to $S/N = 50$, and follows the same general trends as the standard deviations for V, with very similar high-*S/N* power-law slopes. At a given *S/N* and $\sigma_{\rm in}$ value, reducing the wavelength range used for the fits raises the output s_σ by approximately an order of magnitude. As in Co09, we also find that the scatter of the $\sigma_{\rm m}$ distribution increases with increasing $\sigma_{\rm in}$.

The whole set of simulations was also run using the set of seven template star spectra that were used to derive the internal kinematics of the galaxy sample. To account for the possible effects of template mismatch, we performed, for every $(S/N, \sigma_{\rm in})$ parameter pair, six subsets of 50 simulations. For each subset, we created the model spectrum by first selecting a random combination of the stellar spectra, with the allowed number of spectra going from 3 to 7. Each input spectrum was then normalized to a common flux

level by dividing it by its median value, and the selected combination of spectra was co-added using random proportions. Broadening and random noise was then added to the spectrum using the same procedure employed for the single star models. ULySS was then run on the simulated galaxy spectrum using the seven stellar templates and the same settings that were used for the observed galaxy spectra.

The results for the multiple stellar template simulations are shown in the fourth column of Figure 2.7. The general trends are similar to those of the single star simulations, but some differences are found. The first is that, using several template stars, at low S/N ratios the fraction of rejected fits decreases, because of the increase capacity of the code to find a suitable minimum in parameter space. The average shift $\bar{V}$ of the simulations $\bar{V}$ has a more regular behaviour, and a systematic shift is found at low S/N values for high $\sigma_{\rm in}$. The standard deviations of both the V and σ have in general a shallower profile (the slope is closer to ≈ -1.5), as a function of S/N, with respect to the single star simulations, in the sense that the dispersions are lower for low S/N, and higher at high S/N. We interpret this result as a higher efficiency of the algorithm at low S/N when multiple stars are used, and a lower efficiency of the algorithm (at high S/N) when there is not an exact correspondence between the "observed" spectrum and the template.

Estimation of the uncertainties on the velocity dispersion measurements

The distributions analysed in Figure 2.7, using the sample mean and standard deviation, represent the probability density of the measured *output* velocity dispersion $\sigma_{\rm m}$ at a fixed (and known) *input* velocity dispersion, or $P(\sigma_{\rm m}|\sigma_{\rm in})$. To derive estimates on the intrinsic galaxy LOSVD and its uncertainty, the inverse distribution is required, i.e. the probability density of the *input* (intrinsic) velocity dispersion given a σ value measured by the code, or $P(\sigma_{\rm in}|\sigma_{\rm m})$. Following Co09, the probability distributions $P(\sigma_{\rm m}|\sigma_{\rm in})$ were inverted using the following procedure: at each S/N value, the $\sigma_{\rm in}$ input grid was discretized into 1 $\mathrm{km\,s^{-1}}$ wide bins, from 0 $\mathrm{km\,s^{-1}}$ to 100 $\mathrm{km\,s^{-1}}$, and the $\bar{\sigma}$ and s_σ for each bin was determined by fitting, respectively, a linear and a quadratic relation to the results from the simulation sets for each of the eight $\sigma_{\rm in}$ values. Since s_σ is an increasing function of σ, the $2^{\rm nd}$ degree polynomial may generate negative values of s_σ for the lowest σ values of the grid. Values of s_σ were therefore enforced to be ≥ 2 $\mathrm{km\,s^{-1}}$, in order to be able to resolve the Gaussian distribution. At each grid point k, we determine the conditional probability $P(\sigma_{{\rm in},k}|\sigma_{\rm m})$ by applying

$$P(\sigma_{{\rm in},k}|\sigma_{\rm m}) = P(\sigma_{{\rm m},k}|\sigma_{\rm in}) \sum_{i=1}^{100} P(\sigma_{{\rm m},i}|\sigma_{\rm in}) \ . \tag{2.5}$$

The results of the inversion procedure are shown in Figure 2.8, which shows the

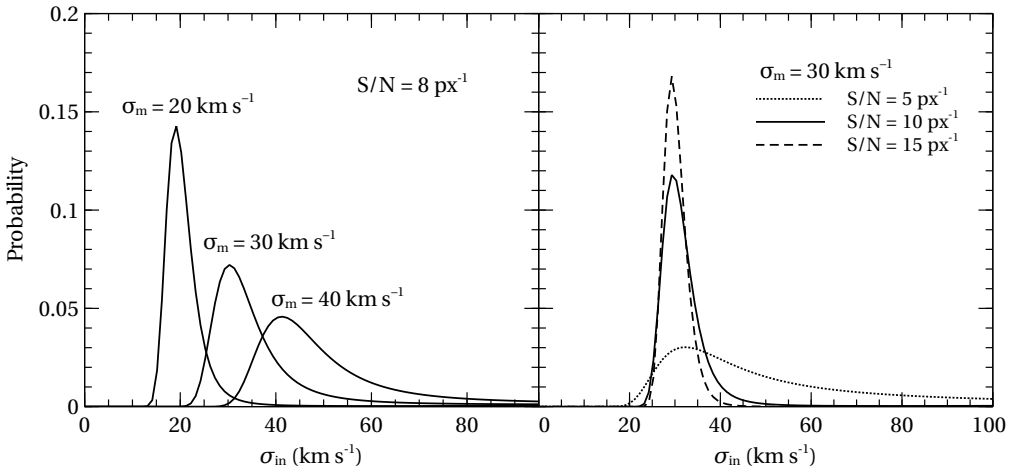

Figure 2.8: Probability distributions of the real velocity dispersion corresponding to a measured value of the LOSVD $\sigma_{\rm m}$. *Left panel*: Distributions are shown corresponding to different measured values of velocity dispersion (20, 30 and 40 $\mathrm{km\,s^{-1}}$). *Right panel*: Probability distributions for $\sigma_{\rm m} = 30$ $\mathrm{km\,s^{-1}}$ for different input signal–to–noise ratios: 5 (dotted line), 10 (solid) and 15 (dashed).

typical probability distributions of the real input velocity dispersion given a measured output value. The distributions are obtained using the simulation set with the seven template stars which were used to derive the galaxy internal kinematics. The left panel shows the result of the inversion for different values of $\sigma_{\rm m}$: 20, 30 and 40 $\mathrm{km\,s^{-1}}$ at fixed input $S/N = 8$ $\mathrm{px^{-1}}$, which corresponds roughly to the median S/N of the sample galaxies in the VIS band. While the distributions of $P(\sigma_{\rm m}|\sigma_{\rm in})$ are well represented by Gaussian functions (see Figure 2.6), the $P(\sigma_{\rm in}|\sigma_{\rm m})$ density functions are typically asymmetric: this is a result of the fact that simulations with higher intrinsic velocity dispersions have a larger scatter, therefore when a low $\sigma_{\rm m}$ is measured, it is not possible to rule out the possibility that $\sigma_{\rm in}$ is in fact higher. For higher values of $\sigma_{\rm m}$, this has also the effect of shifting the distributions so that the maxima of $P(\sigma_{\rm in}|\sigma_{\rm m})$ do not correspond exactly to the measured value of the velocity dispersion.

The right panel shows, for a measured velocity dispersion of 30 $\mathrm{km\,s^{-1}}$, how the distributions change as a fraction of S/N. Since a low input S/N broadens all the distributions $P(\sigma_{\rm m}|\sigma_{\rm in})$, the asymmetry and bias caused by high-$\sigma_{\rm in}$ distributions become more pronounced.

The effect of template mismatch in the stellar template fits was also investigated by re-running the simulations with two other template sets: a reduced 3 star set including only HD007595, HD098468 and HD171367, and an extended 19 star set with allowed $T_{\rm eff}$ extending to 6000 K, $\log g$ from 0 to 4 and [Fe/H] down to -1.5. Figure 2.9 shows the results obtained for a simulation with $\sigma_{\rm in} = 30$ $\mathrm{km\,s^{-1}}$ and S/N = 8. As more stars

are added to the template component (i.e. more stellar types) the precision in the σ determination *decreases*, because stars with the wrong parameters may be selected. For example, to fit the spectrum of a mixture of stars with low metallicity, at low S/N ratios the procedure might select a metal rich template with a high σ that renders absorption features more shallow because of the excessive broadening. This is also the cause of the additional bias that is measured when many stars with different atmospheric parameters are used to perform the spectrum fitting (see the dotted line in Figure 2.9). On the other hand, when the input parameter range is small, the precision increases, but the accuracy in the determination of galaxy LOSVD decreases, because a significant fraction of the galaxy light will come from stars with different characteristics with respect to the one used to construct the template.

The final 1-σ uncertainties on the galaxy velocity dispersion parameters were determined by integrating each distribution from the peak to ± 0.341 times the total area (Co09). The integration was performed for all input (S/N,$\sigma_{\rm in}$) parameters, and the uncertainty for the galaxy measured values was determined by linear interpolation. In order to derive accurate uncertainty estimates, it was necessary to establish a one-to-one correspondence between the input S/N of the simulations and the S/N of the observations. We used the DER_SNR code (Stoehr et al. 2008) which uses the median of the spectrum as the signal level, and the 3$^{\rm rd}$ order median absolute deviation as the noise estimate. The validity of the code was tested on the ULySS simulated spectra generated from the UVB and VIS arm data for HD111486: DER_SNR was run on a noise-added spectrum for each ULySS S/N input value (in steps of 1 px^{-1}). For the VIS arm spectra, we found full correspondence between the input S/N and the measured one up to $S/N \simeq 20\,{\rm px}^{-1}$. The correspondence is also verified for the UVB data up to $S/N \simeq 15\,{\rm px}^{-1}$, while after this value the estimate becomes slightly lower than the input S/N. We kept the S/N as mesured by DER_SNR, knowing that uncertainties can be slightly overestimated for high-S/N UVB data. The S/N measured by DER_SNR on the galaxy spectra is listed in the second column of Table 2.6.

2.5 Internal velocity dispersions of Centaurus dwarf and compact elliptical galaxies

The methods described in the previous section were employed to derive the estimates of the uncertainties in the LOSVD parameters. The internal velocity dispersion σ of the sample galaxies were derived by running ULySS on the VIS arm data, using the stars listed in Table 2.5 as templates. The `/CLEAN` option was always used, and the fitting was performed in the wavelength range from 6000 Å to 9800 Å, excluding the wavelength regions with prominent telluric absorption, i.e. $\lambda\lambda$ = 6855–6940 Å, 7165–7237 Å, 7580-7700 Åand 8125–8345 Å. The final results of the fitting are listed in Table 2.6. Figure 2.10

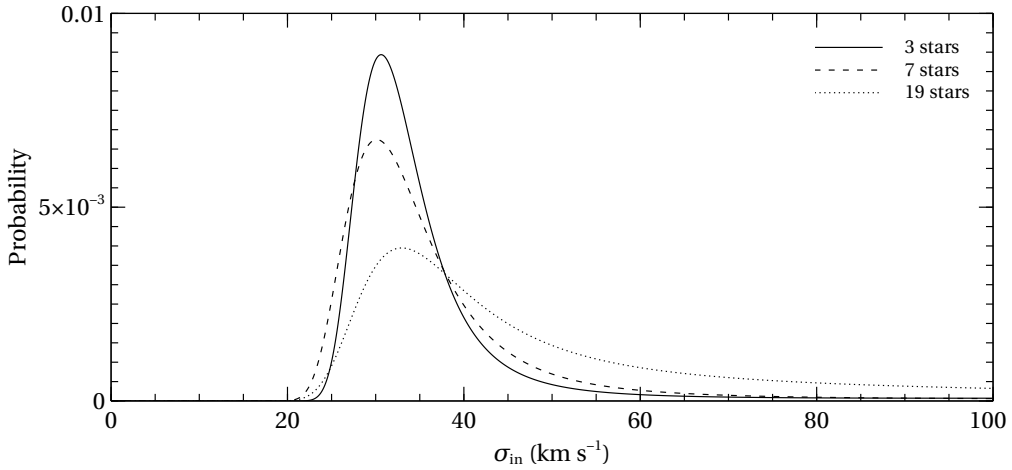

Figure 2.9: Probability distributions of the real input velocity dispersion for different template sets: 3 stars (solid line), 7 stars (dashed line, the same set used for the galaxy σ measurements), and 19 stars (dotted line). All distributions are shown for a simulation with $\sigma_{\rm in} = 30$ km s^{-1} and S/N = 8, performed in the VIS band.

shows the typical output of the ULySS fitting routines for three of the galaxies in the sample: the dwarf galaxies CCC 1 (moderate *S/N*) and CCC 38 (low *S/N*) and the compact elliptical [CM2007] 374. For clarity, the plot is only a "zoomed-in" on the CaT wavelength region ($\lambda\lambda$ = 8450–8700 Å), which contains the most prominent features in the VIS band, but we emphasize that the real spectrum used in the fitting contains almost 10 times as many pixels; the wide wavelength coverage of X-Shooter is therefore very important to avoid excessive uncertainties on the parameters, as discussed in the previous section. The graph shows, for each galaxy, the spectrum and the best fitting model in the upper panel and the residuals together with the formal errors in the lower panel. The effect of the ULySS internal cleaning procedure is shown by the rejected pixels, which are coloured in red. As can be seen from the fit for CCC-38, an efficient rejection algorithm is essential for very low *S/N* data, where prominent sky emission features remain after the data reduction steps.

The systematic offset of the peak of $P(\sigma_{\rm in}|\sigma_{\rm m})$ with respect to the measured velocity was considered only for galaxies where it exceeded 1 km s^{-1}, and is listed together with the other parameters in Table 2.6. The offset is only significant for four out of the ten galaxies in the sample. This bias describes an effect which is different from the usual statistical uncertainties and was not therefore added in quadrature to the uncertainty on the galaxy σ parameters. Since the offset values are in general small, we do not consider them further in the analysis, but we note that the velocity dispersion of the galaxies with low *S/N* VIS spectra (CCC 208, [CM2007] 435 and especially CCC 38) might be underestimated by an amount in any case $\lesssim 12\%$.

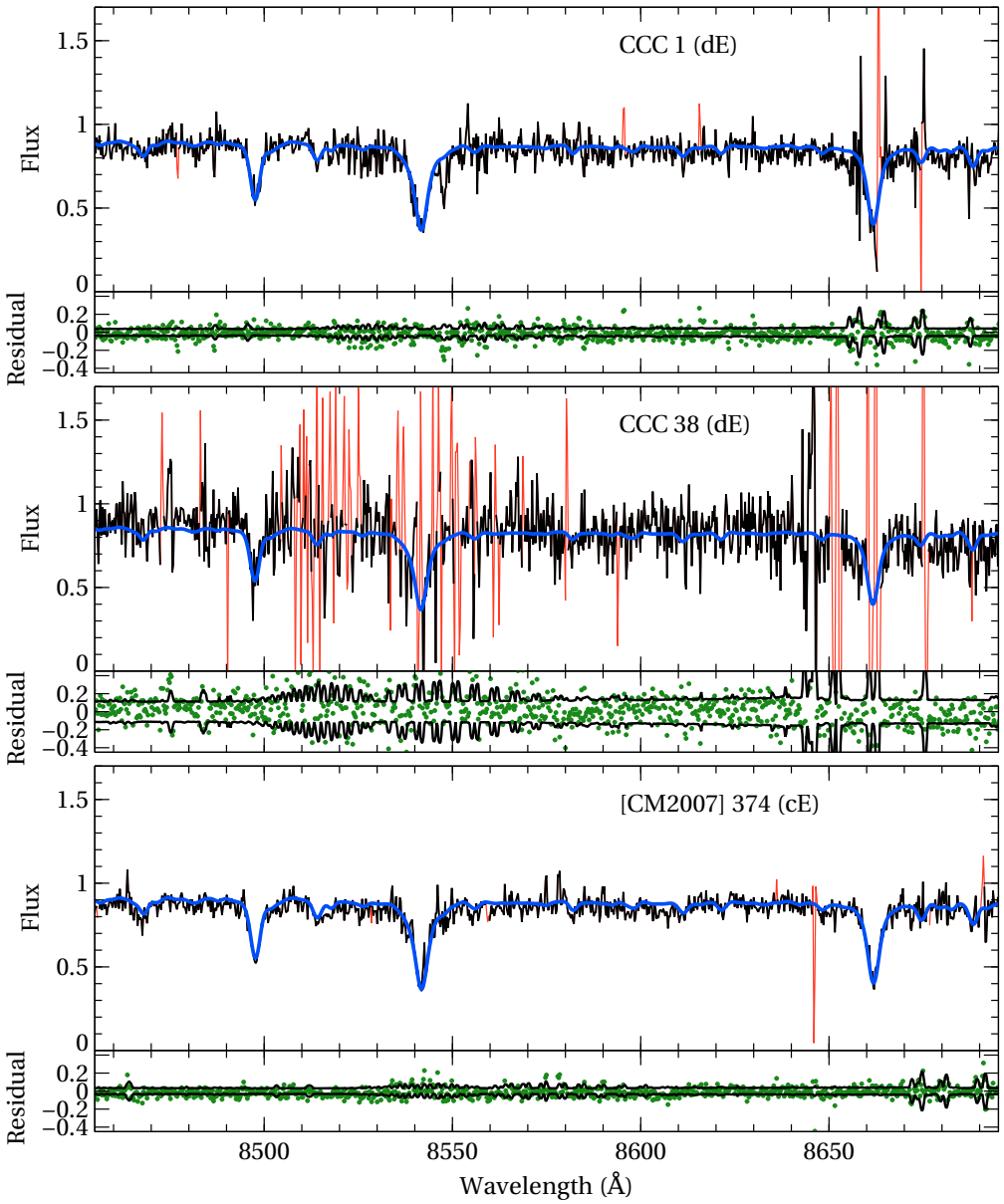

Figure 2.10: Sample ULySS kinematic fits for the sample galaxies, made using stellar templates from the XSL library, shown for clarity only in the CaT region. For each galaxy, the upper panel shows the spectrum flux (black line), the best fitting solution (blue line) and pixels rejected by the code (red lines). The bottom panel shows the residuals from the fit (green dots) and the input formal errors on each pixel (solid black line).

Table 2.6: Kinematic data for the Centaurus Cluster dE and cE galaxies.

Object	S/N (px^{-1})	V ($\mathrm{km\,s}^{-1}$)	σ ($\mathrm{km\,s}^{-1}$)	Systematic σ offset ($\mathrm{km\,s}^{-1}$)
Dwarf elliptical galaxies				
CCC 1	10	3535 ± 45	34 ± 7	
CCC 38	5	3964 ± 59	33 ± 19	4
CCC 61	12	2830 ± 25	41 ± 7	
CCC 97	8	2754 ± 29	31 ± 11	1
CCC 125	9	2923 ± 62	33 ± 10	
CCC 208	8	3632 ± 59	35 ± 14	2
CCC 228	6	3062 ± 46	23 ± 12	
[CM2007] 435	5	1785 ± 38	27 ± 16	2
Compact elliptical galaxies				
[CM2007] 374	16	2954 ± 16	35 ± 3	
[CM2007] 1214	17	2999 ± 13	37 ± 3	

As discussed in Section 2.3, the limited slit length and the final S/N ratios do not allow the determination of a spatially resolved profile of the velocity dispersions of the sample galaxies. We therefore assume the value derived using our optimal extraction algorithm (i.e., essentially, the central value of σ) as the best approximation to the internal velocity dispersion inside R_e, σ_e. Nevertheless, the values listed in Table 2.6 are the first reliable estimates, obtained with high resolution spectroscopy, of the internal velocity dispersions for dwarf elliptical galaxies in the Centaurus Cluster, and represent an important contribution in the compilation of dwarf galaxy kinematics across different environmental conditions.

2.5.1 The Faber–Jackson relation of dE galaxies in Centaurus

The derived values the internal velocity dispersion for our sample galaxies were used to investigate the faint-end Faber–Jackson (FJ Faber & Jackson 1976) relation for the Centaurus Cluster early-type galaxy population. Since dE and cE galaxies have different evolutionary histories, which translate in different occupied locations in the FP (see Chapter 1), we analysed them separately. In particular, since the sample of cE galaxies is limited to two objects, we derived th FJ relation only for the dE galaxies, while the cE were compared to other samples of compact stellar systems in a more qualitative way.

In order to compare our results with the ones obtained for dwarf galaxies in other cluster environments, we gathered from the literature the following datasets.

- Internal kinematics for Virgo Cluster dwarf galaxies were taken from the studies of Geha et al. (2003), Toloba et al. (2011) and Penny et al. (2015), all of which performed through medium-high resolution spectroscopy, which is feasible thanks to the relative "proximity" of the Virgo Cluster to the LG.

- Dwarf galaxies in the Coma Cluster analysed by Kourkchi et al. (2012, hereafter K12). SDSS r magnitudes were converted to V magnitudes using the relations by Lupton et al. (2005)[9], assuming a mean $g{-}r$ colour equal to 0.7 (Smith et al. 2009) and a distance modulus for Coma $m - M = 35.17$, obtained from our adopted cosmology for $z_{\rm CMB} = 0.024$. An additional sample of Coma dwarf galaxies not in common with K12 was taken from of Smith et al. (2009).

- Perseus Cluster dwarf galaxies by Penny et al. (2014, 2015), analysed through high resolution Keck-ESI spectroscopy. R-band magnitudes are converted to V-band magnitudes assuming $V-R = 0.45$.

The distribution of the cluster dE galaxies in the $\log\sigma$–M_V plane is shown in Figure 2.11, where filled circles represent the Centaurus dE galaxies. From the comparison with the other cluster environment samples, our dE galaxies are found to populate the faint end of the FJ relation ($M_V \gtrsim -17$). We computed an estimate of the slope of the FJ relation by fitting the $\log\sigma$–M_V distribution with a orthogonal distance regression algorithm (Boggs et al. 1989). We find

$$L_V \propto \sigma^{2.0\pm1.2}, \tag{2.6}$$

where L_V is the galaxy luminosity in the V band. The large uncertainty on the slope is due to the combined effect of the large uncertainties on the individual σ measurements and of the limited magnitude range covered by our observations ($-17 \lesssim M_V \lesssim -15$). The slope of the dE FJ relation is less steep than the classical value (≈ 4) for giant elliptical galaxies (Faber & Jackson 1976; Focardi & Malavasi 2012). The relation found for the Centaurus Cluster is consistent with the FJ obtained by K12 for Coma dwarfs: $L \propto \sigma^{2.34\pm0.19}$.

The relation between luminosity and internal velocity dispersion for the compact galaxies in our sample is shown in Figure 2.12, compared to a sample of Coma cE galaxies (Price et al. 2009) and a sample of cE galaxies selected from the VO (Chilingarian et al. 2009). The current cE sample is too limited to derive a quantitative estimate of the FJ relation, but the plot does show that a correlation is present between the luminosity and the velocity dispersion, and that the Centaurus compact galaxies, have a internal σ which is lower with respect to cE from other samples at the same magnitude.

2.5.2 Dynamical masses

Our high-resolution spectroscopy can be used to gain clues on the amount of dark matter content in the Centaurus dE and cE galaxies. We computed their stellar and dynamical masses using photometric and spectroscopic available data.

[9] `http://www.sdss.org/dr12/algorithms/sdssUBVRITransform/`

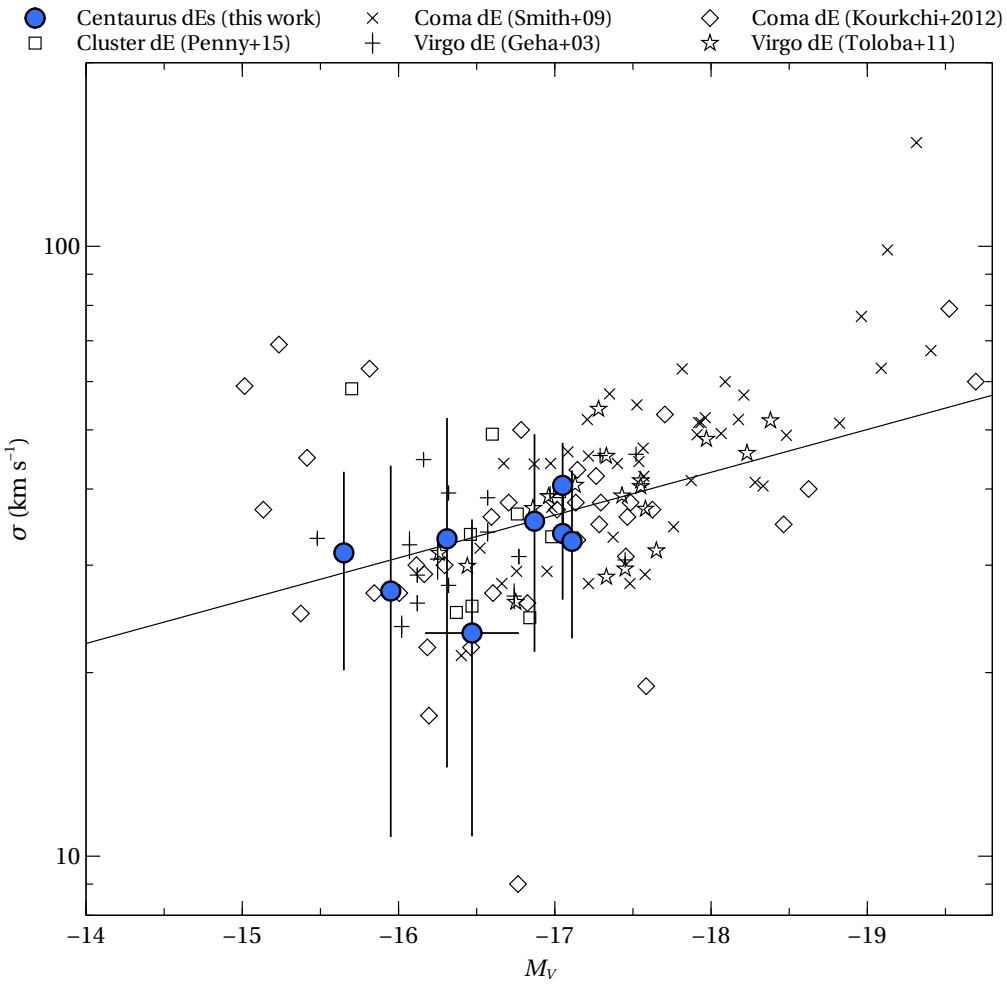

Figure 2.11: Faber-Jackson relation for the sample of Abell 3526 dwarf elliptical galaxies, shown as filled blue circles. Comparison samples of dE galaxies are from the Virgo Cluster (star and plus symbols), the Coma Cluster (cross and diamond symbols) and the Perseus Cluster (square symbols). The solid line represents a linear fit to the distribution of Centaurus dE galaxies.

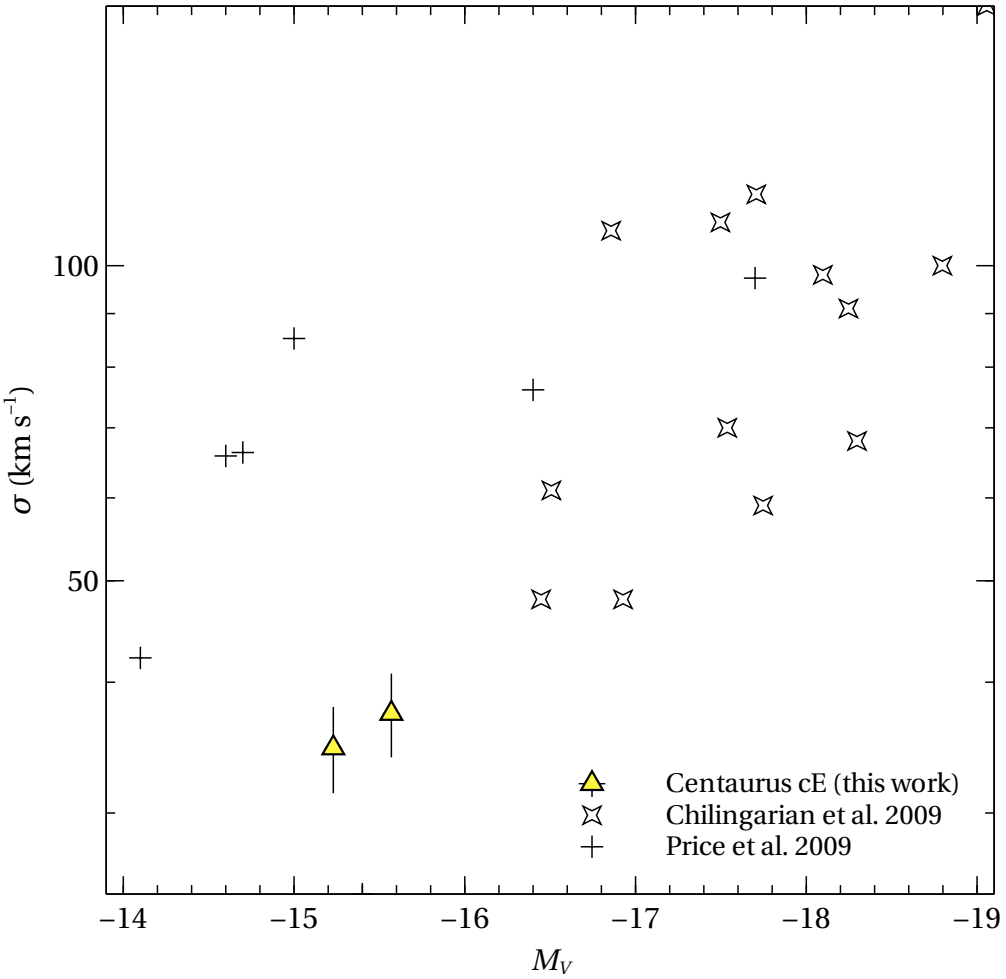

Figure 2.12: Faber-Jackson relation for the sample of Abell 3526 compact elliptical galaxies (yellow triangles).

The galaxy stellar masses were derived using the relations by Bell et al. (2003), which are based on the galaxy optical colours. We used the $B-V$ optical colour to derive the $M_\star/L_V$ ratio, using the relation

$$\log(M_\star/L_V) = -0.628 + (B-V) \times 1.305 \ . \tag{2.7}$$

The $B-V$ colours were derived using B magnitudes from Jerjen & Dressler (1997) and V magnitudes from Chiboucas & Mateo (2007) and Misgeld et al. (2009). For the objects in the CM07 catalogue, which have no corresponding match in the CCC, we assumed B–$V = 0.8$ for dwarf galaxies (see Section 2.1.2) and B–$V = 1$ for the compact ellipticals, taken from a reference 12 Gyr SSP with [Fe/H] = 0. We then derived the total stellar mass from the V-band M/L ratio by assuming a solar absolute V magnitude of 4.80[10].

To derive the dynamical masses of the dwarf and compact elliptical galaxies in our sample, we used the formula (Cappellari et al. 2006; Courteau et al. 2014)

$$M_{\rm dyn} = c\frac{\sigma_{\rm e}^2 R_{\rm e}}{G} \ , \tag{2.8}$$

where $\sigma_{\rm e}$ is the velocity dispersion inside the effectivewhich is derived applying the virial theorem to pressure supported systems. σ In order to use Equation 2.8 to estimate the galaxy mass, it is necessary to confirm that the sytem under study does not exhibit significant rotation. We analysed the rotation profile of the sample of Centaurus dE and cE galaxies within the limited slit length of X-Shooter. The velocity profile of the galaxy was obtained in both the UVB and in the VIS bands, to check for possible systematic effects.

With respect to the data analysis procedures described in Section 2.3, we changed only the spectrum extraction step: instead of performing an optimal extraction on the whole 2D spectra, we coadded the spectra corresponding to different regions of the spatial profile. The size of the regions were selected, to ensure a final S/N ratio for each coadded spectrum of at least 9 px^{-1} in the UVB and at least 5 px^{-1} in the VIS. The rest of the data analysis in the VIS band follows the procedures outlined above, while the analysis of the UVB data is described in the next section.

The final results are shown in Figures 2.13 and 2.14 for the dE and cE galaxies respectively. We find, in general, a good agreement between the "rotation curves" derived using the UVB and VIS arm data. Significant discrepancies are evident only for CCC 38 and in some of the outer bins in the VIS band, for example in [CM2007] 1214 and CCC 208. For CCC 38, we considered the UVB rotation profile more reliable, as the VIS band data has very low S/N, and might be affected by residual sky emission.

The majority of the galaxies in the X-Shooter sample do not exhibit prominent ro-

[10] `http://mips.as.arizona.edu/~cnaw/sun.html`

tation in the central kpc. For these galaxies Equation 2.8 provides a reasonable approximation for the dynamical mass. A notable exception seems to be [CM2007] 435, which has a difference in velocity between the positive and negative major axis of $\gtrsim 20$ km s^{-1} at a radius $R \simeq 0.5$ kpc. Since this value is comparable with the derived central velocity dispersion of the galaxy (27 km s^{-1}), a degree of rotational support for this galaxy cannot be excluded, but cannot be estimated at the present time due to the lack of both extended spectroscopic data and deep photometry. We therefore assumed that (2.8) holds also for [CM2007] 435.

The factor c which appears in equation 2.8 depends in general on the adopted dynamical and structural model of the galaxy under study (Bertin et al. 2002; Forbes et al. 2011). We adopt, following Forbes et al. (2014) and Penny et al. (2015), a c value equal to 6.5, which corresponds to an early type galaxy model following a Sérsic profile with $n \sim 2$. The final values of stellar mass $M_\star$ and dynamical mass $M_{\rm dyn}$ are listed in Table 2.7.

Figure 2.15 shows the derived mass values as a function of V band magnitudes. The figure shows that $M_\star$ (left panel) is in general smaller than the dynamical mass and that the difference is larger for low luminosity galaxies.

The direct relation betwen the stellar and dynamical mass is shown in Figures 2.16 and 2.17. Together with the mass estimates for the Centaurus dE and cE galaxies we show the $M_\star$ and $M_{\rm dyn}$ values for other samples in the literature. Data for dE galaxies were taken, as previously, from the samples of Geha et al. (2003), Toloba et al. (2011) and Penny et al. (2015). We complement the dE sample with galaxies from Chilingarian (2009), where the values of $R_{\rm e}$, σ and $M_\star$ were taken from the compilation by Norris et al. (2014). From the work of Norris et al. (2014) we also took stellar masses and dynamical parameters for compact stellar system (UCDs and cEs) and for LG dSph galaxies. We refer to the paper by Norris et al. for a complete list of the references and a description of the data gathering process.

Figure 2.16 shows the general trends for the low mass end of the galaxy sequence. At the lower stellar mass values ($\sim 10^{6\text{–}7}$ M$_\odot$) the compact UCD and the diffuse dwarf spheroidals occupy different loci in the $M_\star$–$M_{\rm dyn}$ plane: the dSph population has a much higher dynamical mass with respect to its stellar content, which is commonly interpreted as evidence of its higher dark matter content. At higher mass values ($\sim 10^{9\text{–}10}$ M$_\odot$) the dwarf and compact elliptical galaxy sequences also appear to be separated, albeit by a smaller gap, in the sense that more compact systems have a dynamical mass estimate which is more consistent with their measured stellar mass. A zoom in this mass range (Figure 2.17) shows that indeed the dynamical mass of dwarf galaxies in the literature is systematically higher than the inferred stellar mass. The dE galaxies in the Centaurus Cluster, however, lie closer, with respect to other dwarf galaxy samples, to the one-to-one relation between $M_\star$ and $M_{\rm dyn}$. We emphasize that almost all the dwarf galaxy

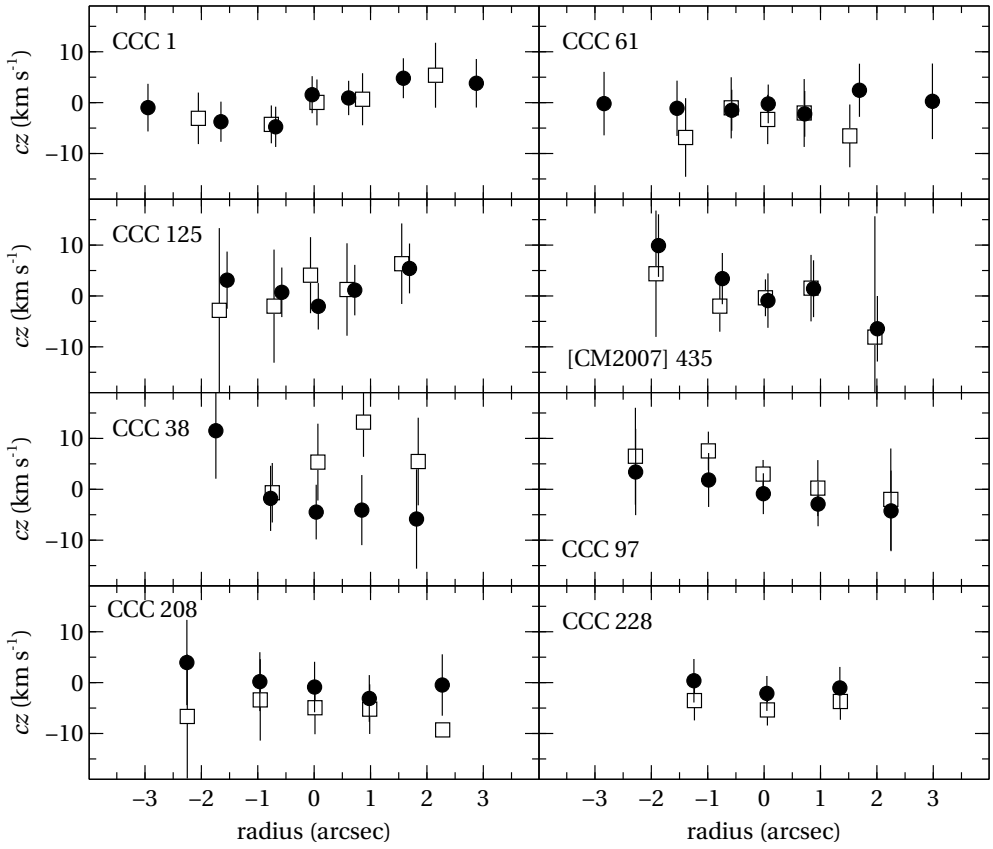

Figure 2.13: Velocity profiles along the slit for the sample dwarf elliptical galaxies. Filled circles and empty squares represent measurements from the UVB and VIS respectively.

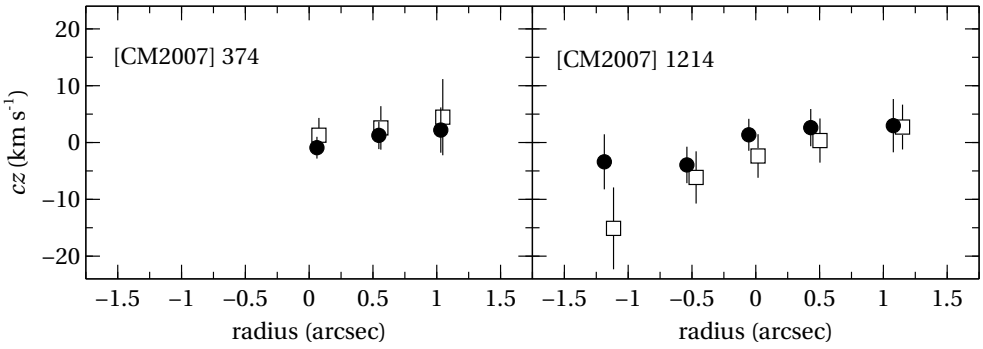

Figure 2.14: Rotation profiles for the two compact elliptical galaxies in the sample. Filled circles and empty squares represent measurements from the UVB and VIS respectively.

Table 2.7: Stellar and dynamical masses of the Centaurus Cluster dE and cE galaxies.

Object	$M_{\rm dyn}$ ($10^9 M_\odot$)	$M_\star$ ($10^9 M_\odot$)
Dwarf elliptical galaxies		
CCC 1	2.00 ± 0.75	2.10
CCC 38	2.10 ± 2.41	1.38
CCC 61	3.93 ± 1.36	3.37
CCC 97	1.31 ± 0.91	0.63
CCC 125	2.78 ± 1.71	1.79
CCC 208	2.46 ± 1.87	1.71
CCC 228	1.16 ± 1.24	0.84
[CM2007] 435	1.27 ± 1.57	0.67
Compact elliptical galaxies		
[CM2007] 374	0.88 ± 0.16	0.35
[CM2007] 1214	0.59 ± 0.11	0.58

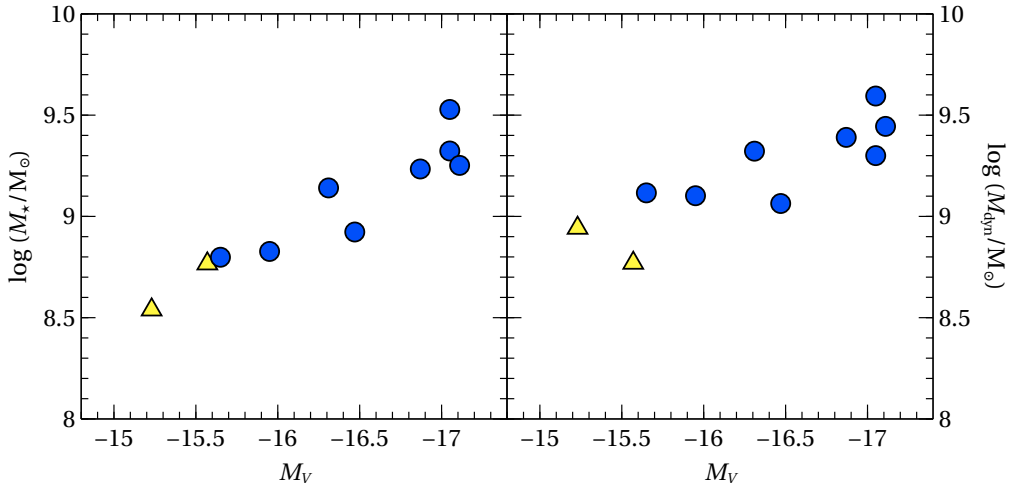

Figure 2.15: Stellar (*left panel*) and dynamical (*right panel*) masses of the sample dE (blue circles) and cE (yellow triangles) galaxies, shown as a function of V-band absolute magnitude.

data refer to objects in cluster environments (i.e., the Virgo or Perseus cluster); the only exception are data from (Penny et al. 2015), which also contain masses for nine dE galaxies in a group environment. For this reason, we have highlighted the data from Penny et al. with a grey fill in Figure 2.17.

2.6 Analysis of the stellar populations

The stellar population content of the sample galaxies was derived from X-Shooter UVB spectroscopic data using both full spectrum fitting, performed with ULySS and absorption indices in the Lick/IDS system. As described in Section 2.2, the UVB spectrograph was set up with the 1.″6 slit, in order to achieve a higher S/N ratio suitable for the study of the chemical and star formation properties of the galaxies. The main goal of our stellar population analysis is the derivation of the luminosity-weighted age and metallicity (in terms of [Fe/H] ratio) of the dE and cE galaxies in our sample.

2.6.1 Full-spectrum fitting analysis

To derive the stellar population chemical properties and SFH, we employ single stellar population (SSP) models as templates in the ULySS fitting routines. The SSP model spectra are a function of the age $t_{\rm SSP}$ and of the metallicity ([Fe/H]) of the stellar population: the model spectrum $F_{\rm mod}$ in equation 2.1 has therefore two component parameters $\theta_{\rm C}$ in addition to the LOSVD parameters $\theta_{\rm L}$.

The single stellar populations (SSPs) were produced using population synthesis programs: Pegase.HR (Le Borgne et al. 2004) together with the ELODIE 3.2 (Prugniel & Soubiran 2001; Wu et al. 2011) stellar library. The resolution of the library is 0.55 Å FWHM with wavelength coverage $\lambda\lambda = 3900$–6800 Å. All of the models were computed using Salpeter IMF in the mass range of 0.1 to 120 $\mathrm{M}_{\odot}$. Pegase.HR models use Padova isochrones (Bertelli et al. 1994), extended to thermally-pulsing regime of the asymptotic giant brand and post-asymptotic giant branch phases. The SSPs range is from -2.3 to 0.6 dex in metallicity and from 0.001 to 20 Gyr. Although in the extremes of the parameters space and at other wavelength ranges the models have large uncertainties, in the regions where our galaxies are situated the models have been proven to give reliable results (Koleva et al. 2008b).

To derive the correct parameters from spectrum fitting, it is necessary to take into account the line broadening introduced by the spectrograph. For the UVB arm, we account for this effect by deriving the line-spread-function (LSF, analogue of point-spread function in images), and applying the results to the model spectra before the fitting. To derive the UVB LSF we analysed the spectrum of the velocity template star HD111486 which was acquired during both observing runs. We employed the TGM component of ULySS together with the ELODIE 3.2 interpolator (Prugniel & Soubiran

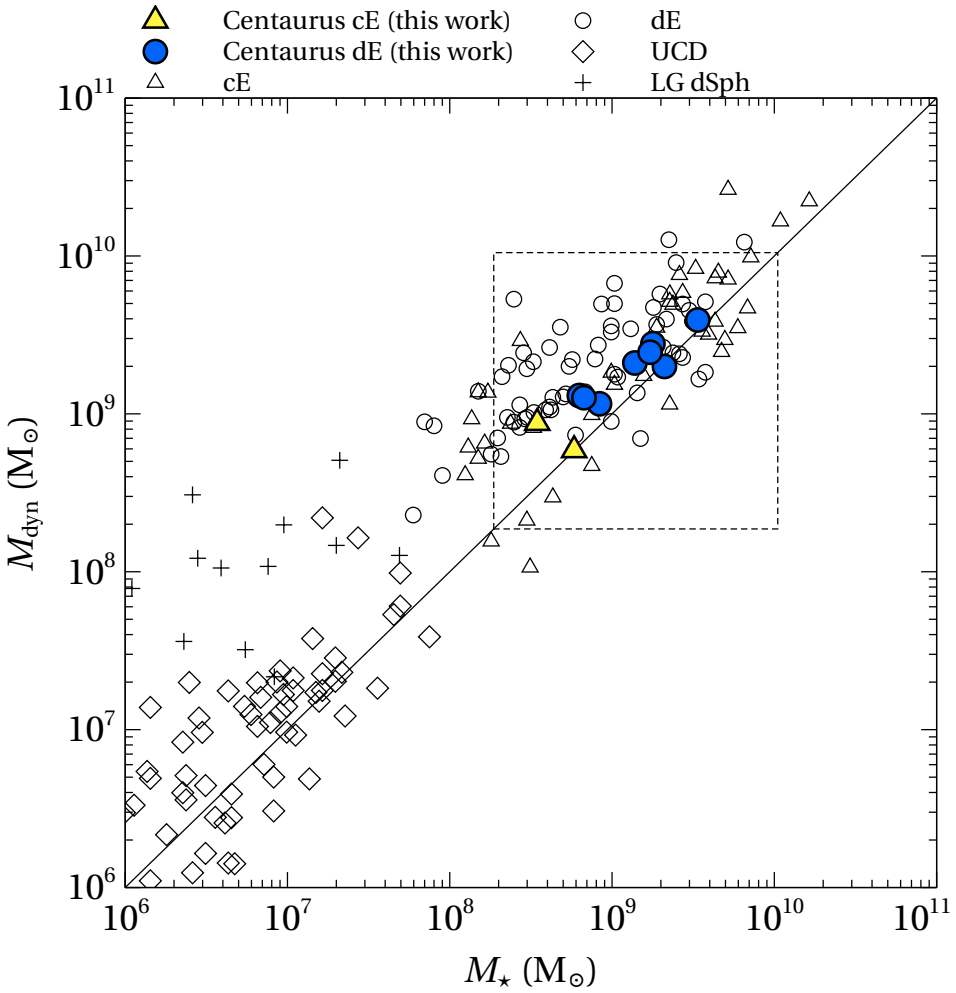

Figure 2.16: Comparison of dynamical mass and stellar mass estimates for low luminosity stellar systems. dE (blue circles) and cE (yellow triangles) in the Centaurus Cluster sample are shown together with dE (empty circles) dE (empty triangles), UCD (empty diamonds) and LG dSph ("plus" symbols) galaxies from other samples compiled from the literature (see text for the references).

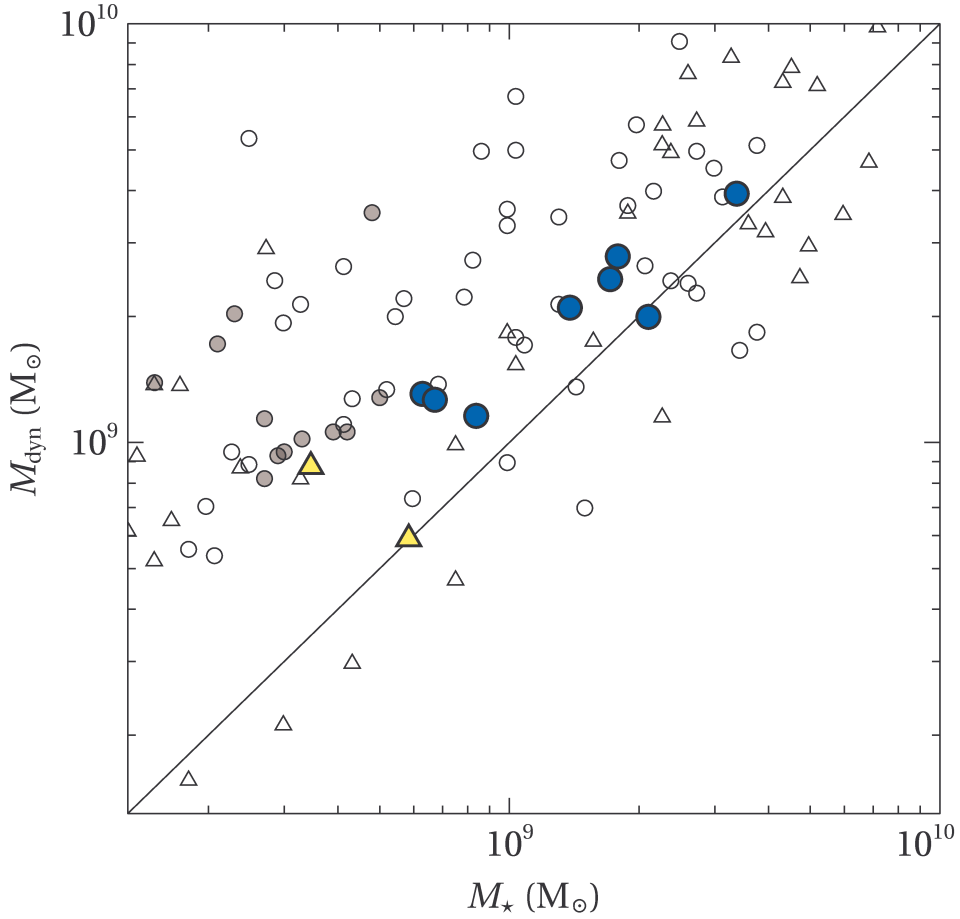

Figure 2.17: Same as Figure 2.16, but showing the zoom in the $\sim 10^8$–10^9 M$_\odot$ range of masses (dashed rectangle). Grey shaded circles represent the dEs in the sample of Penny et al. (2015).

2001; Wu et al. 2011) to determine the best fitting $T_{\rm eff}$, $\log g$ and [Fe/H], which are listed in Table 2.8 for both observing runs (R1 and R2). The parameter uncertainties are the estimated formal errors of the LM algorithm, and are excessively small because they were derived without an input error spectrum, which results in an equal weighing for all pixels.

Despite the small uncertainties, the atmospheric parameters for the star are mostly consistent, and differences between the two runs are, except for the VIS arm metallicity, at most $\sim 10\%$. Since the UVB arm has a much larger wavelength overlap with the ELODIE library, we use the UVB atmospheric parameters to create the model spectrum for the LSF derivation.

We then determined the UVB LSF by creating a spectral model of HD111486 using the ELODIE interpolator with the following parameters: $T_{\rm eff} = 4500\,{\rm K}$, $\log g = 2.0\,{\rm cm/s^2}$ and [Fe/H] $= -0.4$. Interpolating the model grid to the best matching atmospheric parameters, we minimized the effect of possible degeneracies, like the one between velocity dispersion and metallicity (Koleva et al. 2008a). We investigate the change of the LSF across the wavelength range by fitting 200 Å wide bins, overlapped by 100 Å. The result is shown in Figure 2.18, where the LSF for R1 and R2 are represented by purple squares and orange diamonds. Since the LSF is expected to be a smooth function of wavelength, a third degree polynomial was fitted the LSF, and is shown by the lines in the figure. The R1 data presents two data points where ULySS was unable to determine correctly the spectral broadening: these are marked in the plot by arrows, and were not used in the polynomial fitting.

In the upper panel of the figure the variation of velocity shift is shown as a function of wavelength. For both runs the $\bar{V}$ shift increases with the wavelength, with the difference between the two ends of the spectrum being larger ($\approx 20\,{\rm km\,s^{-1}}$) for the data taken during R1. A dependence of velocity shift on wavelength is not expected for spectroscopic data, and is likely an artefact of imperfect wavelength calibration by the ESO X-Shooter pipeline. A similar issue was encountered, but with an opposite dependence, by Chen et al. (2014) for stellar spectra acquired for the XSL program. The offset between the two curves is caused by the heliocentric velocity difference between the two runs.

The lower panel of Figure 2.18 shows the variation of the line broadening as a function of wavelength. In this case a shift is not expected between by the two runs, but is present because of the different seeing conditions under which the observations were made. In particular, the seeing FWHM during the first run was $\simeq 0.5\,{\rm arcsec}$, about one third of the slit width, while during the R2 acquisition it was $\simeq 2.0\,{\rm arcsec}$ and hence larger than the UVB spectrograph slit. To derive accurate stellar population parameters it is necessary that the spectral broadening is determined under the same conditions as the galaxy spectra. Since the resolution of the science observations is dominated by the slit width, we employed the LSF derived using the R2 spectrum of HD111486.

Table 2.8: Stellar atmospheric parameters for HD111486.

Spectrograph arm	$T_{\rm eff}$ (K)	$\log g$ (cm/s^2)	[Fe/H] (dex)
UVB(R1)	4499.5 ± 2.3	2.120 ± 0.006	-0.3888 ± 0.0027
VIS(R1)	4467.7 ± 3.6	2.068 ± 0.013	-0.3323 ± 0.0050
UVB(R2)	4474.3 ± 2.5	2.124 ± 0.007	-0.4097 ± 0.0029
VIS(R2)	4434.0 ± 3.6	1.860 ± 0.012	-0.4418 ± 0.0052

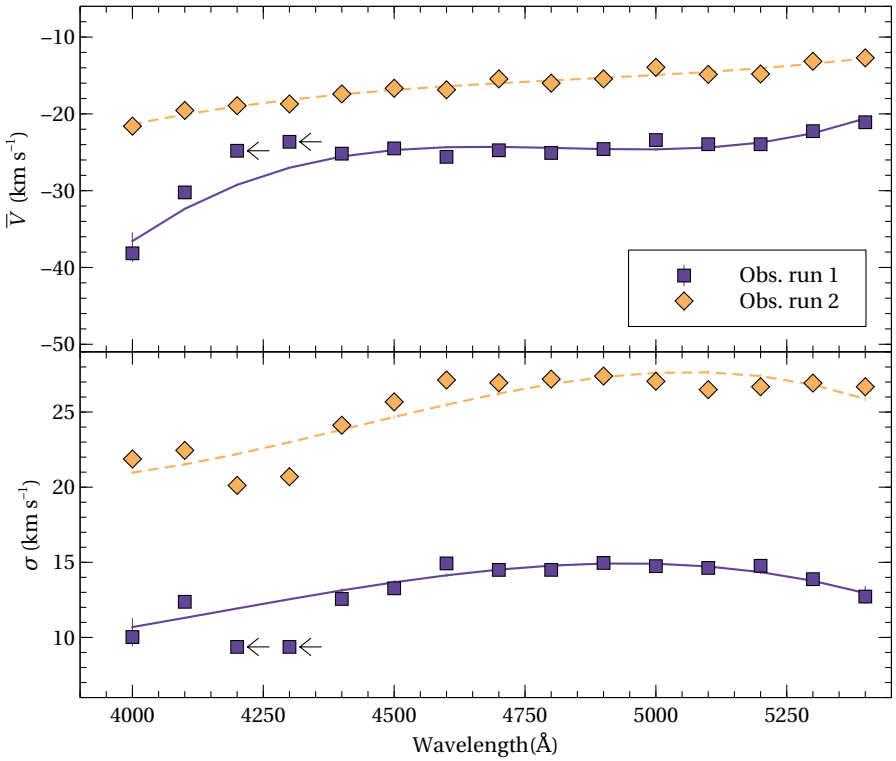

Figure 2.18: Velocity shift (upper panel) and line-spread (bottom panel) functions for the X-Shooter UVB arm. Dark purple squares and orange diamonds represent measurements from observing run 1 and 2, respectively. The solid and dashed lines are polynomial fits to the R1 and R2 data points. The data marked by the arrows were not considered in the polynomial fit.

We finally inserted the derived instrumental LSF into the Pegase.HR/ELODIE models and we analysed UVB arm spectra using the `ULY_SSP` routines. To perform the fit, the input σ parameter was kept fixed to the dispersion value derived in Section 2.5. The $t_{\rm SSP}$ and [Fe/H] parameter were left free, and the default ULySS values ($t_{\rm SSP} = 8\,$Gyr; [Fe/H] = -0.4) were given to the algorithm as guesses for the parameters. We employed in the fitting the internal ULySS interpolator, so that the output of the SSP analysis is the best matching solution, instead of the set of weighs of each SSP in the model grid. Sample ULySS SSP fits to the UVB galaxy spectra are shown in Figure 2.19.

2.6.2 Error analysis using simulated SSP spectra

To derive realistic uncertainties on the stellar population parameters we performed a set of simulations, following the basic procedures outlined in Section 2.4.2. Instead of stellar templates, we used the Pegase.HR/ELODIE SSP models to create the simulated galaxy spectra. Before adding the randomly generated noise, each model spectrum was convolved with the X-Shooter UVB LSF and was rebinned linearly in $\ln\lambda$ to the velocity scale of the UVB data ($30\,{\rm km\,s^{-1}}$). The SSP simulations were run with input values from the four-parameter space composed by σ, S/N $t_{\rm SSP}$, and [Fe/H]. The S/N and $\sigma_{\rm in}$ parameter grids are the same as in Section 2.4.2. The addition stellar population parameter input values are the following:

- $t_{\rm SSP} = 1,\ 2.5,\ 5,\ 7.5,\ 10,\ 12.5$ and 15 Gyr;
- [Fe/H] $= -1.5,\ -1.25,\ -1.0,\ -0.75,\ -0.5,\ -0.25,\ 0$ and 0.25.

For each (S/N, $\sigma_{\rm in}$, $t_{\rm SSP}$, [Fe/H]) combination 300 simulated spectra were generated and fitted with a default Pegase.HR/ELODIE component convolved with the UVB LSF. In contrast to the fitting procedure on the observed galaxy spectra, we left the σ parameter of the LOSVD free to vary in the fitting of the simulated spectra. While this choice possibly introduces an additional source of error, it generates conservative estimates of the uncertainties of the stellar population parameters.

The output parameters measured by ULySS are the velocity shift V and dispersion σ and the two parameters of the stellar populations. Visualizing the sample statistics of the four output parameters as a function of the four input parameters is a complex task. Since the V and σ behaviour as a function of S/N has already been discussed in Section 2.4.2, we focused our analysis on the stellar population parameters by analysing the output of the simulations with $\sigma_{\rm in} = 30\,{\rm km\,s^{-1}}$, which is approximately the average velocity dispersion of the dwarf galaxies in our sample (Table 2.6). The general results are largely unchanged if the output from other velocity dispersions are analysed, except for $\sigma_{\rm in} \leq 10\,{\rm km\,s^{-1}}$: since these dispersions are very close (or below) the lower σ limit set by the code (the UVB pixel velocity scale is $\approx 30\,{\rm km\,s^{-1}}$), a very large fraction of

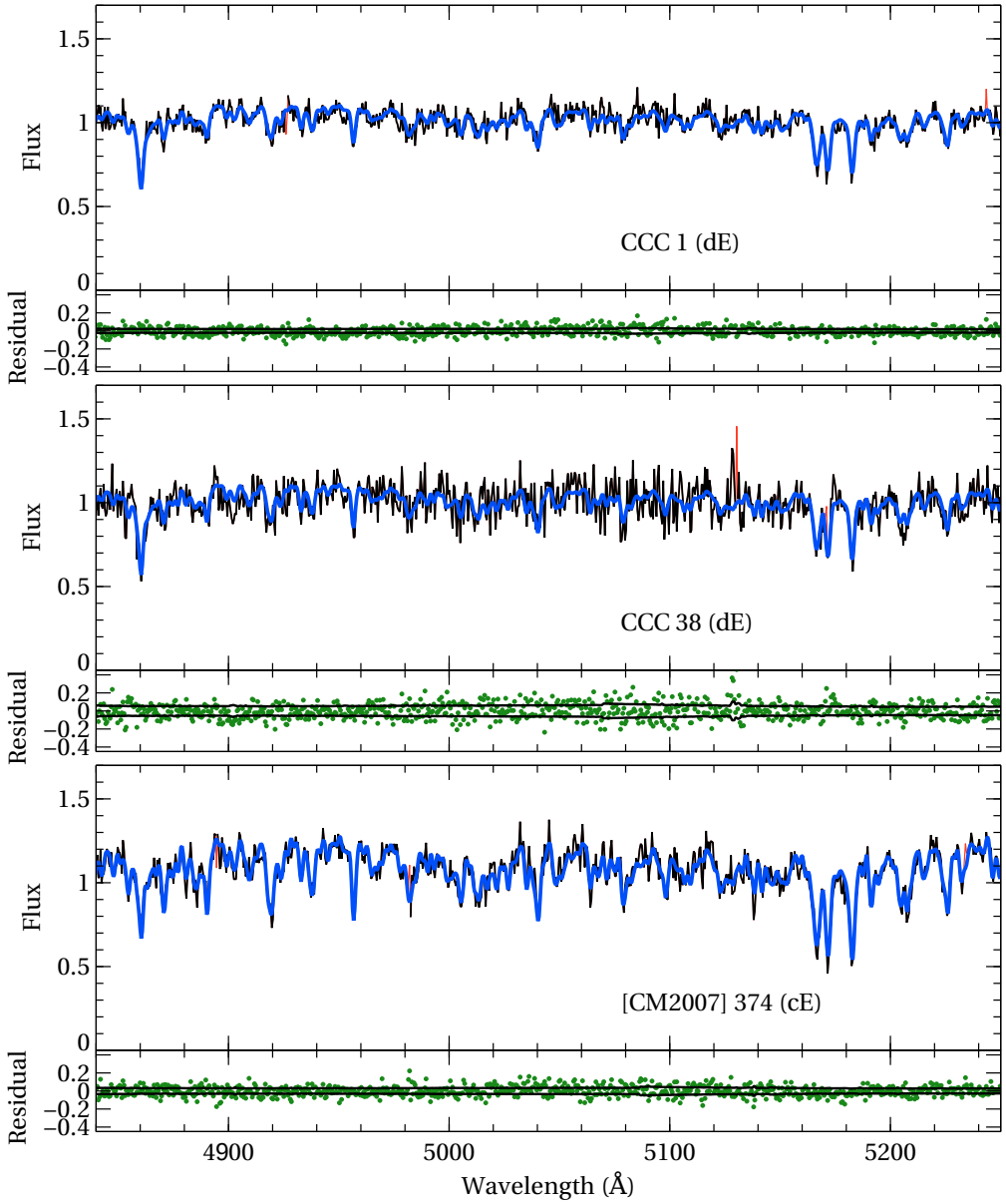

Figure 2.19: Sample ULySS SSP fits for Centaurus cE and dE galaxies, made using stellar population models from Pegase.HR/ELODIE 3.2. The galaxies shown in the three panels, as well as the lines and symbols, are the same as in Figure 2.10. Prominent features in the wavelength range selected are H β at 4861 Å and the magnesium triplet at 5160–5180 Å.

fits is rejected at low S/N ratios, biasing the results. Dispersion values above $20\,\mathrm{km\,s^{-1}}$, which are the ones of interest, are unaffected by this problem.

Since two new parameters were introduced in the fitting, we implemented additional checks for failed fits in the simulation analysis. A fit was labelled as failed if it satisfied the criteria listed in Section 2.4.2 or if one of the following two output conditions was met:

1. the error on age was equal to 0 or the output age value was equal to the maximum allowed by the models ($\simeq 20\,\mathrm{Gyr}$);

2. the error on metallicity was equal to 0.

For each input parameter set, now composed of S/N, t_{SSP} and [Fe/H], we computed the mean and standard deviation of the parameters [Fe/H] and $\log t_{\mathrm{SSP}}$ from the output distributions obtained after the rejection described above. The SSP age is measured in terms of the logarithm because, since the input model grid is linearly spaced in $\ln t_{\mathrm{SSP}}$, the output distributions are approximately Gaussian only if the log is considered instead of the absolute value.

The output distribution of the average and standard deviation are shown in Figures 2.20 and 2.21. In the first figure the columns correspond to three different input values of SSP age, while in the second they correspond to different input metallicities. The line colour and style have the opposite dependence, in the sense that they correspond to different input metallicities in Figure 2.20 and to different ages in Figure 2.21. From the top rows of both plots, which show the fraction of successful fits as a function of input S/N, we derived trends which are very similar to those observed in Figure 2.7: S/N values $\gtrsim$ 8–10 $\mathrm{px^{-1}}$ are required to obtain reliable results.

The trends observed at low S/N values both in the second row (average age minus the input value) and in the fourth row (average metallicity minus the input value) are actually artefacts of the LM algorithm: when the S/N is very low the code cannot efficiently explore the allowed parameter space and gives an output which is very close to the input guess value. This is clear, e.g., from the second row of panels in Figure 2.21: the average value of age ($\overline{\log t_{\mathrm{SSP}}}$) is greater than the input value for the SSP with input age equal to 2.5 Gyr (solid green line), and negative for the 12.5 Gyr (purple dot-dashed line). This is because, for low input S/N, the average output will be closer to the guess value, which is 8 Gyr, giving a negative offset for $t_{\mathrm{SSP,in}} = 12.5\,\mathrm{Gyr}$ and a positive one for $t_{\mathrm{SSP,in}} = 2.5\,\mathrm{Gyr}$. The curves for $t_{\mathrm{SSP,in}} = 7.5\,\mathrm{Gyr}$, as expected, are closer to 0 since the input age is almost the same as the guess value. A similar behaviour is seen for the metallicity in the third row of Figure 2.20.

Trends with input stellar population parameters can be seen in the panels showing the standard deviations of the output distributions (third and fifth rows in both figures). The precision of the age determination increases with decreasing age of the input SSP:

this is a known result, due to the fact that the spectra of galaxies with recent or ongoing star formation show more rapid variations than spectra of galaxies with an old and passively evolving stellar population. The scatter in the measured metallicity increases with decreasing metallicity and with decreasing input SSP age (see, for example, the first panel in the fifth row of both figures).

As in Section 2.4.2, we derived the uncertainties on each stellar population parameter by interpolating the means and standard deviations of the output distributions on a fine grid and inverting the probability densities according to equation 2.5. The final uncertainties are obtained by linearly interpolating the uncertainties for each input combination at the parameter values measured by ULySS on the galaxy spectra.

2.6.3 Lick index analysis

The full spectrum fitting technique is very powerful to derive single stellar population parameters, such as the global age and metallicity, because it effectively uses all the available information in the galaxy spectrum. However, since all the absorption features are used simultaneously in the fitting process, information on individual element abundance is lost. To keep track of the detailed enrichment properties of the Centaurus Cluster galaxies, we derived absorption indices in the Lick/IDS system from the UVB spectra. We restricted our measurements to a subset of the whole Lick system, focused on the absorption features of hydrogen, iron and the α-elements C, Ca and Mg. Additionally, we derived from our measured values the two metallicity-sensitive combinations (Thomas et al. 2003, hereafter TMB03) $\langle\mathrm{Fe}\rangle$ and $[\mathrm{MgFe}]'$:

$$\begin{aligned} \langle\mathrm{Fe}\rangle &= \mathrm{Fe5270} + \mathrm{Fe5335} \\ [\mathrm{MgFe}]' &= \sqrt{\mathrm{Mg}b(0.72 \times \mathrm{Fe5270} + 0.28 \times \mathrm{Fe5335})}\ , \end{aligned} \tag{2.9}$$

The index definitions follow Cardiel et al. (1998), and the actual measurement on the galaxy spectra was performed using the INDEXF software package (Cardiel 2010). The Lick system of absorption indices are usually taken at a resolution of ≈ 8 Å (Worthey & Ottaviani 1997). When the spectral resolution is different one must either convolve the spectrum to match the IDS resolution or apply suitable corrections derived observing Lick standard stars. Since no such observations were made during the observing run, we employed the former procedure: all galaxy spectra were convolved with a Gaussian function with an appropriate FWHM (variable with wavelength) to match the IDS spectral resolution.

Uncertainties on the output value of each index was derived using the INDEXF Monte Carlo routines: the indices are measured on a set of simulated spectra with added random noise, corresponding to different S/N ratios and the standard deviation is computed and

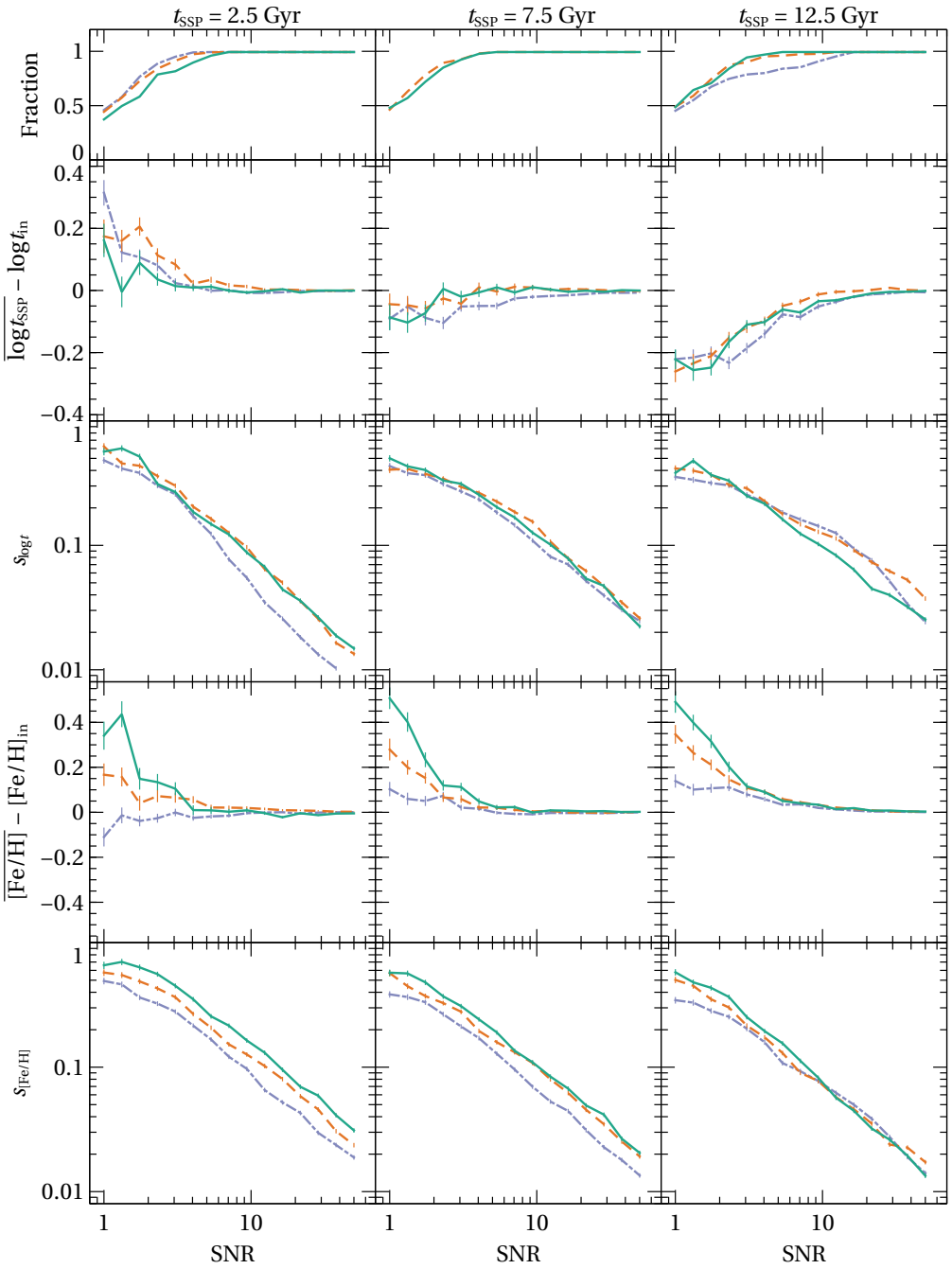

Figure 2.20: Results of the ULySS SSP fitting to simulated galaxy spectra, as a function of *S/N* ratio. From top to bottom, the panel rows show the fraction of "good" fits, the mean and standard deviation of $\log t_{SSP}$ and the mean and standard deviation of [Fe/H]. The panel columns correspond to different input ages of the stellar populations, respectively 2.5, 7.5 and 12.5 Gyr. The green solid, orange dashed and purple dot-dashed lines represent the different metallicities of the input SSP, respectively [Fe/H] = -1, -0.5 and 0.

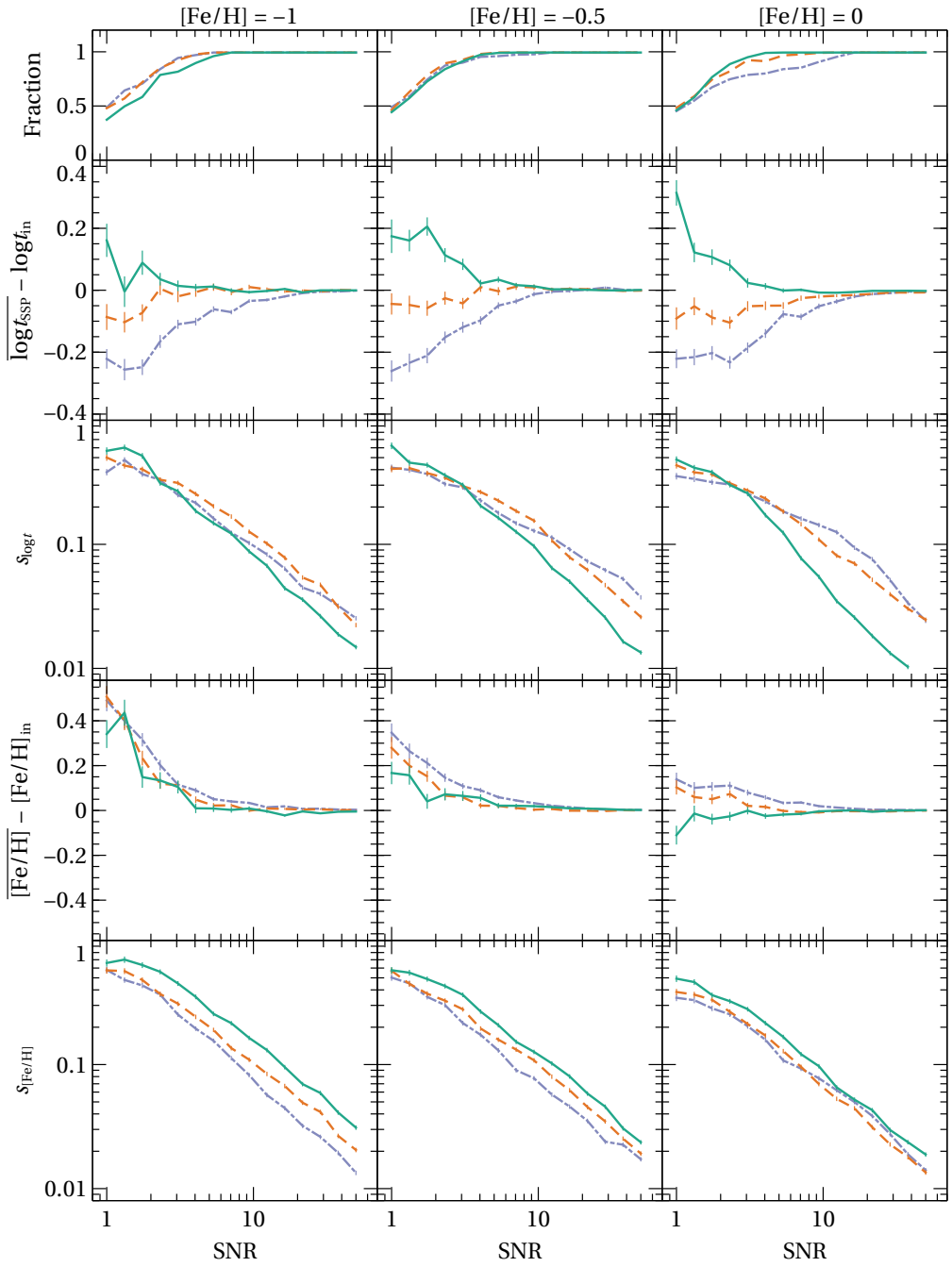

Figure 2.21: Same as figure 2.20, except that colums now represent different input metallicities: -1, -0.5 and 0 respectively for the first, second, and third column. The lines represent different input values of SSP age: 2.5 Gyr (green solid), 7.5 Gyr (orange dashed) and 12.5 Gyr (purple dot-dashed).

used as the estimated uncertainties.

2.7 Results of the stellar population analysis

2.7.1 Ages and metallicities of Centaurus dE and cE galaxies

The final values of the age and [Fe/H] parameter for the Centaurus dE and cE galaxies are presented in Table 2.9, together with the UVB S/N as measured by DER_SNR. Figures 2.22 and 2.23 show the result of our stellar population analysis for the dwarf and compact elliptical galaxies, respectively. The final ages and metallicity values are shown as a function of V band magnitudes.

Our results are compared to the stellar population analysis of the Coma Cluster dE galaxies by (Smith et al. 2009). The SSP ages we found (Figure 2.22, upper panel) for the Centaurus dE fall in the range spanned by other samples, with no obvious trend, and are consistent with an intermediate age passive population. A trend is more clear in the luminosity-metallicity relation (Figure 2.22, lower panel), where we recovered the usual dependency of [Fe/H] increasing with luminosity. Remarkably, with the exception of CCC 1, the Centaurus dwarf galaxies seem to follow a tighter sequence with respect to other samples. With the limited sample available, however, it is not possible to draw any quantitative conclusion on this issue.

None of the dE galaxies in the sample possesses a high ($\sim$ solar) metallicity. Higher metallicity dwarf galaxies were found in both the Coma Cluster (Poggianti et al. 2001) and the Perseus Cluster (Penny & Conselice 2008). This result could be either a bias caused by the limited magnitude range probed by the galaxies in the sample, or a true deficiency of metal-rich galaxies in the Centaurus Cluster. In the latter case, the paucity of metal-rich dwarfs could be directly linked with the fact that the Centaurus Cluster is a less massive and less evolved cluster, with respect to Coma and Perseus.

The comparison of the properties of the Centaurus Cluster compact ellipticals to the other samples shows some notable differences: we find an average stellar population of the cE galaxies which is younger and on average more metal rich than similar systems in other environments.

2.7.2 Line-strength indices

The full set of Lick indices for the sample galaxies is listed in Table 2.10.

igure 2.24 shows the index-index diagrams for the sample galaxies compared to the set of index measurement on Perseus Cluster dwarf galaxies (from Penny & Conselice 2008) is shown for reference in the plot. The upper panel shows the $\langle$Fe$\rangle$$-Mgb$ diagram, where both axes represent metallicity sensitive indices, which however mark the presence of elements with a different origin: the iron enrichment in a galaxy is mainly caused by

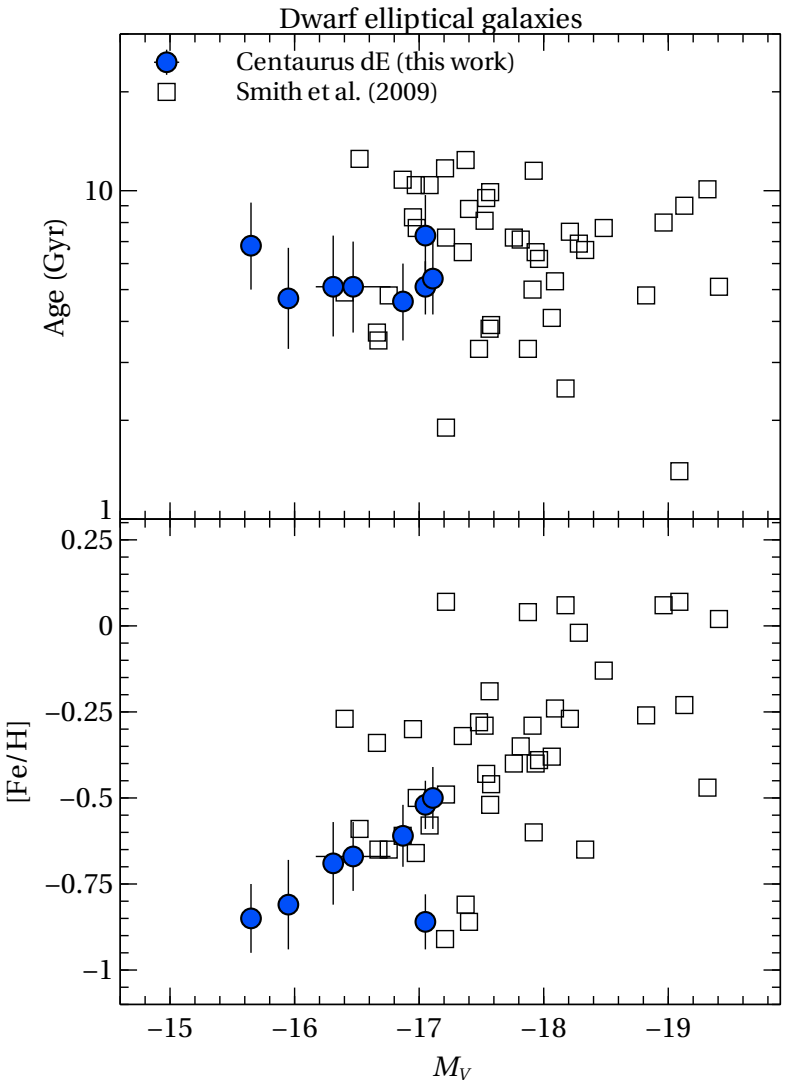

Figure 2.22: Age (*upper panel*) and metallicity (*lower panel*) as a function of V magnitude for the sample dwarf galaxies (blue filled circles). Empty squares represent dwarf galaxies in the Coma Cluster (Smith et al. 2009).

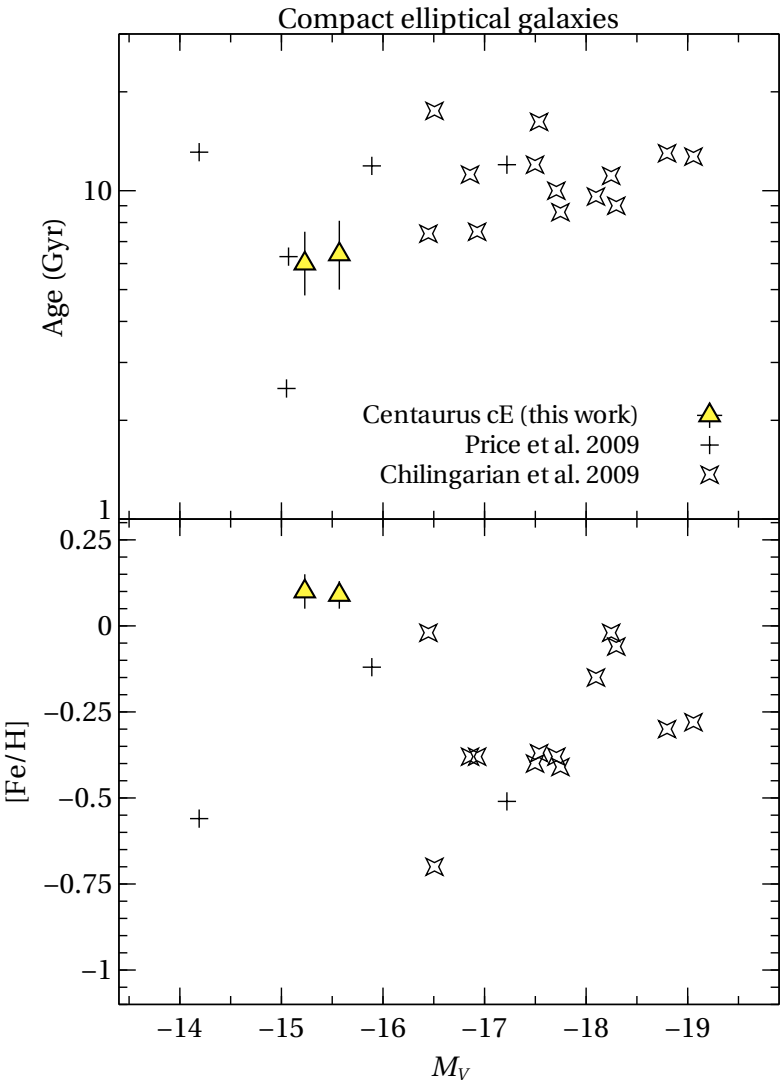

Figure 2.23: Same as Figure 2.22, for the sample Centaurus compact elliptical galaxies (yellow triangles). Crosses and 4-pointed stars represent cE galaxies from the studies of Price et al. (2009) and Chilingarian et al. (2009)

Table 2.9: Stellar population parameters for the Centaurus Cluster dE and cE galaxies.

Object	UVB S/N (px^{-1})	Age (Gyr)	[Fe/H]
Dwarf elliptical galaxies			
CCC 1	18	$7.3^{+2.4}_{-1.8}$	-0.86 ± 0.08
CCC 38	15	$5.1^{+2.2}_{-1.5}$	-0.69 ± 0.12
CCC 61	12	$5.1^{+1.0}_{-0.9}$	-0.52 ± 0.07
CCC 97	10	$6.8^{+2.4}_{-1.8}$	-0.85 ± 0.10
CCC 125	10	$5.4^{+1.6}_{-1.2}$	-0.50 ± 0.09
CCC 208	12	$4.6^{+1.4}_{-1.1}$	-0.61 ± 0.09
CCC 228	13	$5.1^{+1.9}_{-1.4}$	-0.67 ± 0.10
[CM2007] 435	10	$4.7^{+2.0}_{-1.4}$	-0.81 ± 0.13
Compact elliptical galaxies			
[CM2007] 374	13	$6.0^{+1.5}_{-1.2}$	0.10 ± 0.05
[CM2007] 1214	13	$6.4^{+1.7}_{-1.4}$	0.09 ± 0.04

the explosion of supernovae Type Ia, while the α-elements (Mg being one of these) are produced in the final stages of the evolution of very massive stars, which end their lives as Type II supernovae. Since the two processes (Type Ia and Type II supernova explosions) have very different timescales, the relative contribution of iron and α-elements (expressed in terms of the [α/Fe] ratio) can be effectively used to derive information on the formation timescale of the bulk of stars in a galaxy (Matteucci & Greggio 1986; Thomas et al. 2005). To this aim, in Figure 2.24 we overlay the TMB03 model grids, shown as a function of [Z/H] and [α/Fe], for a reference 11 Gyr age SSP. The two sets of galaxies (cEs and dEs) are found to be separated in the diagram because of their different global metallicities. The dE galaxies are relatively spread out over all possible [α/Fe] values, which means that at least some of them are compatible with short star formation timescales. The cE galaxies are instead located at the high metallicity-low [α/Fe] corner of the plot. Their evolutionary history appears therefore consistent with a more prolonged star formation.

The lower panel in Figure 2.24 shows the H β–$\langle$Fe$\rangle$ diagram for the sample galaxies. The two indices are sensitive to different properties of the stellar population: the Balmer index, measured on absorption features which are prominent in young stars, is sensitive to the age of the stellar population, while the iron index $\langle$Fe$\rangle$ is sensitive to the overall metallicity, as discussed above. The TMB03 model grids are shown in the plot for a reference [α/Fe] = 0 SSP. The metallicity ranges occupied by both the dE and cE galaxies are consistent with the values derived above using full spectrum fitting (see Table 2.9). The H β values for the sample galaxies rule out recent episodes of star formation, in agreement with our ULySS analysis. In fact, from the SSP model grids shown in the H β–$\langle$Fe$\rangle$ diagram the ages of the sample galaxies would appear older than the ones inferred using spectral fitting. This apparent discrepancy might be caused by unaccounted for residual H β emission, due to ongoing star formation, but is more likely

Table 2.10: Lick indices for the Centaurus dE and cE galaxies. The first row for each galaxy lists the index value and the second row the corresponding uncertainty.

Galaxy	HδA	HδF	CN1	CN2	Ca4227	G4300	HγA	HγF	Fe4383	Ca4455	Fe4531	C4668
CCC 1	0.48	0.97	-0.04	-0.04	-0.07	3.00	-2.08	0.30	2.30	0.31	0.76	2.28
	0.22	0.15	0.01	0.01	0.14	0.19	0.27	0.18	0.38	0.17	0.37	0.66
CCC 38	0.48	0.94	-0.02	-0.00	0.38	3.04	-1.83	0.59	2.47	0.97	2.47	2.06
	0.23	0.15	0.01	0.01	0.12	0.21	0.22	0.17	0.39	0.19	0.34	0.51
CCC 61	1.17	1.24	-0.06	-0.06	0.50	2.91	-2.31	-0.17	2.40	-0.11	1.93	2.92
	0.21	0.15	0.01	0.01	0.12	0.23	0.24	0.14	0.41	0.17	0.29	0.50
CCC 97	1.23	1.18	-0.03	-0.04	0.77	3.01	-2.63	-0.35	2.57	0.36	1.85	2.66
	0.21	0.14	0.01	0.01	0.11	0.21	0.24	0.14	0.41	0.18	0.34	0.51
CCC 125	0.67	1.06	-0.06	-0.05	-0.10	3.70	-2.50	0.09	2.16	-0.51	2.46	2.34
	0.22	0.16	0.01	0.01	0.13	0.20	0.24	0.16	0.31	0.15	0.28	0.58
CCC 208	0.65	1.60	-0.05	-0.05	0.49	3.52	-2.25	0.29	1.40	-0.51	1.45	3.83
	0.25	0.15	0.01	0.01	0.13	0.22	0.24	0.18	0.37	0.22	0.29	0.49
CCC 228	0.13	1.65	-0.07	-0.06	-0.05	2.23	-1.79	0.39	0.60	-0.24	1.60	4.52
	0.21	0.13	0.01	0.01	0.15	0.21	0.24	0.13	0.39	0.18	0.26	0.48
[CM2007] 425	2.16	2.14	-0.06	-0.04	-0.26	3.06	-1.12	0.24	1.04	-0.70	1.97	1.86
	0.21	0.14	0.01	0.01	0.16	0.22	0.21	0.16	0.37	0.21	0.27	0.43
[CM2007] 374	-1.24	0.47	0.06	0.09	0.82	4.88	-5.90	-1.73	3.57	-0.14	2.61	7.52
	0.22	0.16	0.01	0.01	0.14	0.19	0.21	0.16	0.31	0.18	0.34	0.39
[CM2007] 1214	-2.40	0.03	0.09	0.12	1.07	4.36	-5.15	-1.23	3.11	0.10	3.85	7.57
	0.21	0.16	0.01	0.01	0.15	0.21	0.23	0.16	0.38	0.21	0.37	0.42

Galaxy	Hβ	Fe5015	Mg1	Mg2	Mgb5177	Fe5270	Fe5335	Fe5406	$\langle$Fe$\rangle$	[MgFe]	[MgFe]$'$
CCC 1	1.71	2.33	0.01	0.11	2.18	1.55	1.62	0.71	1.59	1.86	1.85
	0.24	0.46	0.00	0.01	0.21	0.26	0.25	0.24	0.18	8.28	0.15
CCC 38	1.87	2.17	0.01	0.11	1.52	1.74	1.15	0.44	1.45	1.48	1.55
	0.18	0.44	0.00	0.00	0.19	0.22	0.25	0.26	0.17	6.42	0.13
CCC 61	2.35	3.10	0.01	0.12	2.95	1.60	1.40	0.86	1.50	2.11	2.14
	0.22	0.49	0.01	0.01	0.19	0.27	0.28	0.21	0.19	8.11	0.16
CCC 97	1.60	2.77	0.02	0.14	2.16	1.04	1.34	0.99	1.19	1.60	1.56
	0.18	0.55	0.00	0.01	0.25	0.23	0.26	0.23	0.17	5.52	0.15
CCC 125	1.72	2.69	0.00	0.15	2.61	1.88	1.49	1.68	1.68	2.09	2.15
	0.22	0.45	0.00	0.01	0.18	0.26	0.29	0.17	0.19	9.09	0.14
CCC 208	2.53	2.34	0.04	0.12	2.04	2.40	1.68	1.14	2.04	2.04	2.12
	0.19	0.51	0.00	0.01	0.24	0.22	0.34	0.21	0.20	10.14	0.16
CCC 228	1.89	0.58	0.02	0.15	3.03	1.77	1.57	1.84	1.67	2.25	2.28
	0.19	0.42	0.00	0.01	0.23	0.27	0.34	0.22	0.21	8.75	0.17
[CM2007] 425	2.19	2.75	0.00	0.07	1.37	1.36	1.23	0.61	1.29	1.33	1.35
	0.18	0.46	0.00	0.00	0.23	0.19	0.26	0.29	0.16	5.31	0.14
[CM2007] 374	1.61	3.75	0.10	0.26	4.12	3.10	2.75	1.39	2.92	3.47	3.52
	0.22	0.44	0.00	0.01	0.20	0.22	0.33	0.25	0.20	25.56	0.14
[CM2007] 1214	1.40	5.50	0.10	0.27	4.09	3.21	3.10	1.88	3.16	3.59	3.61
	0.22	0.40	0.00	0.00	0.15	0.24	0.30	0.19	0.19	29.46	0.13

an effect of the different input models used as the reference SSPs.

2.8 Summary and conclusions

In this chapter we have presented the first study of the internal kinematics and stellar populations for a sample of dwarf galaxies in the Centaurus Cluster. We exploited the capabilities of the X-Shooter spectrograph at the ESO VLT to obtain simultaneously high-resolution spectroscopy in the VIS band to study the stellar kinematics of the sample galaxies and high-S/N spectroscopy in the UVB for a characterization of their stellar populations.

The stellar kinematics was analysed using the ULySS full-spectrum fitting code in the wavelength range from 6000 Å to 9800 Å, using stellar templates from the XSL library. We correctly recovered the internal velocity dispersion for all the sample galaxies, and determined the first estimate of the slope of the FJ relation for the dE galaxies in the Centaurus Cluster. The logarithmic slope we found is consistent with dE galaxy samples from other clusters, but not with the classical FJ relation for elliptical galaxies. After verifying the absence of significant rotation for the galaxies, we derived an estimate of the dynamical mass. By comparison with the stellar masses derived from optical colours, we found dE M/L ratios which are systematically lower with respect to other samples from higher density environments. This result is at odds with the findings by (Penny et al. 2015), which instead find higher M/L ratios for low density environments. To derive accurate trends as a function of local density, however bigger samples and more homogeneous data analysis procedures are needed.

With our stellar population analysis we have recovered low metallicities and intermediate ages for all the sample dE galaxies. While Centaurus dEs generally follow the magnitude-metallicity relation of other cluster dEs, we do not find evidence for a more metal-rich ([Fe/H]$\gtrsim 0.03$) dwarf galaxy population, which was found in other clusters (Poggianti et al. 2001; Penny & Conselice 2008). A larger sample of galaxies is needed to verify if this is a true deficiency of the A3526 Cluster or if is a bias caused by the limited magnitude range probed by the current sample.

The two cE galaxies in the sample have lower velocity dispersions with respect to other cE samples from the literature, but still higher than the predicted relation for dwarf galaxies at the same magnitude. The kinematics, together with the high metallicity found in the stellar population analysis, support the scenario of formation from a more massive progenitor which has been tidally stripped of most of its mass.

In the next future, we plan to complement this work in the following aspects:

- Analyse imaging data from the ESO VLT Survey Telecope [11] to perform accurate photometry on the sample galaxies. A more detailed photometric modelling,

[11] https://www.eso.org/sci/facilities/paranal/telescopes/vst.html

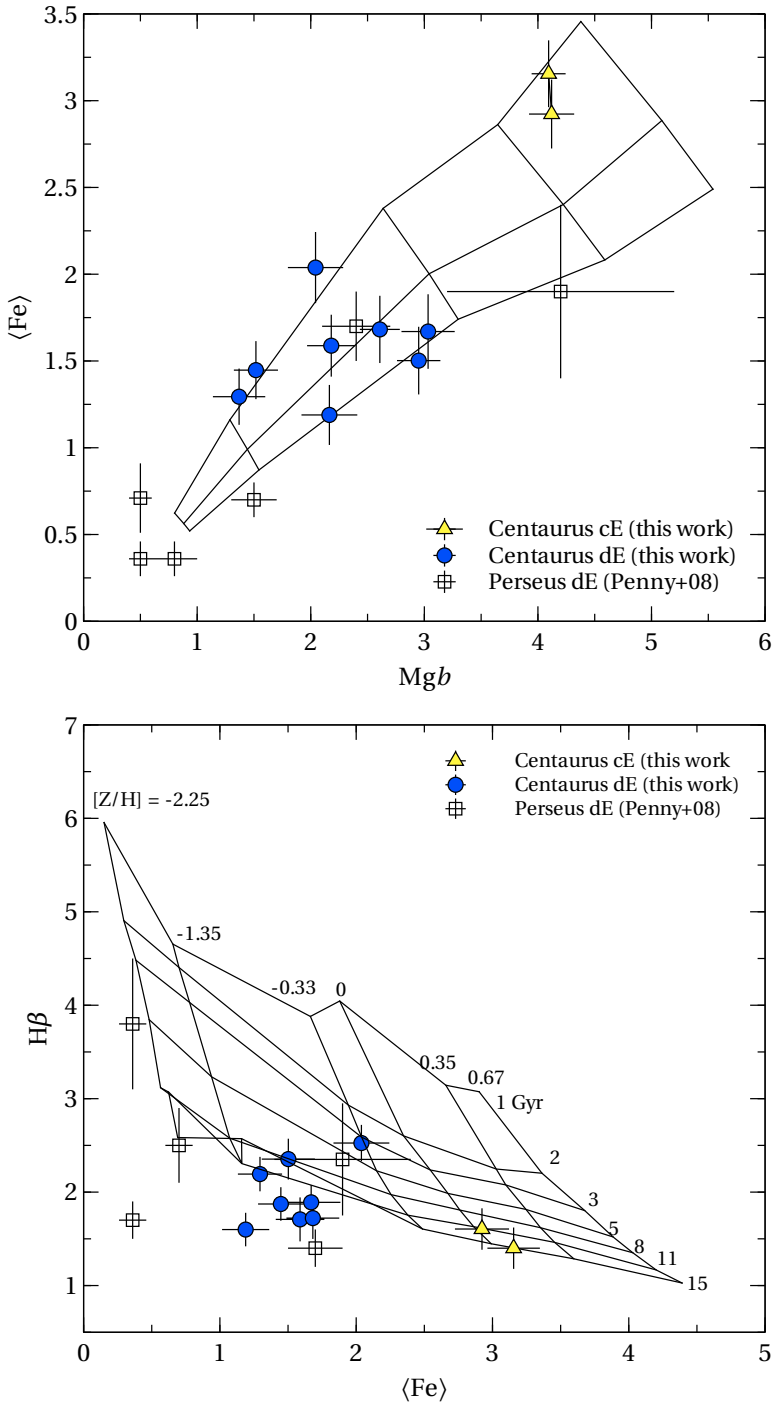

Figure 2.24: *Upper panel*: $\langle \mathrm{Fe} \rangle - \mathrm{Mg}b$ Lick index-index diagram for the Centaurus sample of galaxies. *Lower panel*: $\langle \mathrm{Fe} \rangle$ index-index diagram. Blue circles and yellow triangles represent respectively dE and cE galxies from the current sample. Empty squares represent Perseus Cluster dwarfs (from Penny & Conselice 2008. Model grids are from the TMB03 SSP models.).

combined with multi-wavelength data obtained from the Virtual Observatory web services, will allow us to derive more accurate estimates of the stellar mass of the galaxies.

- Analyse the near-infrared band data from X-Shooter. A significant fraction of the light in the NIR band comes from low-mass stars (van Dokkum & Conroy 2010). By analysing the NIR spectra, we hope to derive constraints on the initial mass function of the dwarf elliptical galaxies.

- Prepare and submit proposals to major observatories in the Southern hemisphere to obtain long-slit and integral-field unit (IFU) spectroscopy of the sample galaxies. Spatially resolved kinematics will allow us to perform the dynamical modelling required to study global motions and derive accurate mass-to-light ratios.

Chapter 3

Low-luminosity elliptical galaxies in the Perseus Cluster

Abstract

We present a photometric and spectroscopic study of low-luminosity early-type galaxies in the Perseus Cluster with the aim of increasing the number of spectroscopically confirmed members of the cluster and of characterizing the stellar populations of galaxies in the magnitude range that represents a transition from the giant to dwarf regime. Fibre spectroscopy was obtained at the William Herschel Telescope, and analysed using cross-correlation techniques. We provide new membership for 16 low luminosity ($M_r \gtrsim -19$) elliptical galaxies. By complementing our own spectroscopy with radial velocity data assembled from the literature and additional spectra from the Sloan Digital Sky Survey Data Release 12, we constructed an updated catalogue of Perseus Cluster members, which we use to compute updated values of the cluster velocity dispersion and the cluster mass and to verify the absence of significant substructure. Using full spectrum fitting, we derived consistent estimates of the luminosity-wighted ages and metallicities for the galaxies in our sample and for the Sloan Digital Sky Survey spectroscopic targets, and computed the first estimate of the mass-metallicity relation for the early type galaxy population of the Perseus Cluster. An extensive set of absorption indices in the Lick system was consistently measured on our own and Sloan spectra, and is made available to the community for future studies on the stellar populations in low-redshift clusters.

3.1 Introduction

Low redshift clusters maintain a crucial role in shaping our understanding of galaxy evolution, because it is only in nearby environments that we can observe and study in detail the least luminous and massive (i.e., dwarf: $M_B \gtrsim -18$, Boselli et al. 2008) galaxies. Studies of the luminosity function of galaxies across all environments consistently find negative logarithmic slopes ($\lesssim -1$) for the faint-end power-law (Tully et al. 2002; Popesso et al. 2005), which means that faint galaxies represent the most numerous type of galaxies in the Universe. Any cosmological model aspiring to successfully describe the history of the Universe must therefore correctly reproduce the observed properties of low-mass galaxies. However, because of their shallow gravitational potential, low-mass galaxies are the most susceptible to the environmental processes described in Chapter 1, e.g., ram-pressure stripping (Gunn & Gott 1972), harassment (Moore et al. 1998) or strangulation (Larson et al. 1980), which makes the formulation of a coherent picture for their evolution a daunting task. The problem is aggravated by the fact that faint galaxies also have low surface brightnesses, making the observational efforts often as strenuous as the modelling ones.

Dwarf elliptical (dE) galaxies represent one of the most common faint galaxy types in clusters and, as the name suggests, are associated to the giant elliptical galaxy population because of their spheroidal appearance. Evidence for a link between the two galaxy populations have been presented, for example, by Graham & Guzmán (2003) and Ferrarese et al. (2006) who pointed out the continuity in some of the scaling relations of early-type galaxies (ETGs), e.g. the relation between Sérsic index n and magnitude. However, a common formation scenario for the two classes of objects has been questioned by analysing both the structural properties (Lisker et al. 2006) and the internal kinematics (Geha et al. 2003; Toloba et al. 2012) of Virgo Cluster galaxies. Stellar populations of dE also show remarkable difference with respect to giant elliptical galaxies: dEs have on average lower metallicities and younger ages with respect to high-mass ETGs (Geha et al. 2003; Koleva et al. 2009a).

Differences in the global properties of dE galaxies with respect to giant ellipticals have been found both in the distribution of the cluster kinematics and the galaxy stellar populations. Conselice et al. (2001) showed that faint galaxies in the Virgo Cluster possess a higher velocity dispersion with respect to bright galaxies. This was interpreted as evidence for a late accretion of the dE galaxy population on the cluster. The detailed study performed by Smith et al. (2009) on dE galaxies in Coma showed that on average the galaxy age decreases with increasing radius, while such a trend is not seen for massive galaxies, strengthening the hypothesis of environmentally-driven processes acting on a (possibly late-type) galaxy population which is still in the process of being accreted by the massive cluster structure.

The interaction of galaxies with the cluster environment is probably not just ex-

plained by a single process. For example, studies of internal dynamics of dEs in the Virgo Cluster (Ryś et al. 2014) suggest that these galaxies are likely accreted late-types that have been transformed by tidal interactions, while stellar population gradients in cluster (and group) dEs found by Koleva et al. (2009a) are compatible with the strangulation scenario. The presence of significant samples of rotating dE galaxies (Toloba et al. 2011, 2015) have also provided support for the ram pressure stripping scenario. However, spatially resolved internal kinematics and stellar population properties of dE galaxies are available only for limited samples in nearby groups and clusters, with Virgo being the obvious main target because of its proximity (Toloba et al. 2014).

A complementary approach is to perform statistical studies on fibre spectroscopy of larger samples: Smith et al. (2012a) determined the properties of the stellar populations in Coma dwarfs to derive the age variation with respect to cluster-centric distance. The resulting gradients appear consistent with gas removal via efficient strangulation. However, also these studies are limited in the number of clusters wich have been targeted, and statistical spectroscopic studies on large dwarf galaxy samples are restricted only to a handful of clusters, among which are Abell 496 (Chilingarian et al. 2008) and Coma.

In this chapter, we perform and in-depth study of properties of the global low-luminosity galaxy population of the Perseus Cluster (Abell 426), which is one of the richest and more massive nearby clusters (Girardi et al. 1998) and has a more relaxed dynamical state and evolved assembly history with respect to Virgo.

Despite the dust extinction due to the cluster proximity (in projection) to the plane of the Milky Way ($b \approx -13$ deg), A426 has been extensively studied in the optical bands. The first extensive studies on the dwarf population in the Perseus Cluster core were performed by Conselice et al. (2003) and Penny & Conselice (2008). Using both photometry and spectroscopy the authors provided the first estimates of the stellar population properties of the dwarf galaxies in Perseus, uncovering the wide distributions both in ages and metallicities which had been observed in other clusters (e.g., Coma, Poggianti et al. 2001) The different observed properties imply either different formation scenarios or different degrees of environmental influence on the evolution of the dE galaxies.

These studies were followed-up by Hubble Space Telescope Advanced Camera for Surveys and Wide-Field Planetary Camera 2 imaging of the core of the cluster. Penny et al. (2009) and de Rijcke et al. (2009), analysing the dE and dwarf spheroidal (dSph) population, found no significant dependence on the local environment of some of the observed properties (e.g., mass-to-light ratios, scaling relations, etc.), compared to what is measured for galaxies in the Local Group and in other clusters. The authors also found remarkably regular morphologies in the cluster, at odds with the predictions of the harassment scenario which predicts the presence of remnant disc-like features (de Rijcke et al. 2003; Mastropietro et al. 2005), although the exact outcome of harassment

depends on the parameters of the galaxy orbit inside the cluster (Smith et al. 2015). The authors also argued that fraction of the dE galaxies near the core must possess significant amounts of dark matter (DM) to withstand the disruptive effects of the cluster potential. However, the later study by Penny et al. (2015), based on high resolution spectroscopy, inferred higher mass-to-light (M/L) ratios for dwarf galaxies in lower density environments. The detailed interplay between the cluster environment and the constituents of dwarf galaxies (stars, DM, and gas) is therefore still unclear. A complete mapping of the observed properties of dwarf galaxies is therefore of primary importance to place further constraints on their evolutionary histories.

In this chapter we address the issue of the origin of the faint galaxy population in the Perseus Cluster. We analyse fibre spectroscopy to determine new cluster members in the cluster and utilize the results, together with literature data and spectral data from the Sloan Digital Sky Survey (SDSS) to derive the cluster kinematics and global trends in the stellar populations of the cluster galaxies. In Section 3.2 we present the reduction and analysis of spectroscopic data from the William Herschel Telescope (WHT), In Section 3.3 we combine the results with literature and archival data to create a new database of cluster radial velocities, which we use to study the global cluster kinematics. In Section 3.4 we present the results of the analysis of the galaxy stellar populations. In Section 3.5 we summarize and present our conclusions.

I assume throughout the chapter a Planck 2013 cosmological parameter set (Planck Collaboration et al. 2014), with Hubble constant $H_0 = 67.8\,\mathrm{km\,s^{-1}Mpc^{-1}}$ and matter density parameter $\Omega_\mathrm{m} = 0.307$. We adopt the cluster recession velocity measured in Section 3.3 ($z_\mathrm{cl} = 0.0177$) which corresponds to a distance modulus of $m - M = 34.5$, a distance of 77.9 Mpc and a angular scale equal to $22.7\,\mathrm{kpc\,arcmin^{-1}}$.

3.2 Spectroscopy

3.2.1 Sample selection

A total of 73 early-type galaxies was selected for the spectroscopic follow up within a 1 deg circle centred around a point in the sky roughly 4 arcmin west of the centre of the Abell 426 (A426) Cluster: RA(2000) = $3^\mathrm{h}19^\mathrm{m}24^\mathrm{s}$, Dec. (2000) = $41°30'42''$. A mosaic of SDSS r-band frames of the sky region is shown in Figure 3.1, together with the targets selected for observations. Following the criteria and scientific aim outlined above, these comprise 39 dwarf early type galaxies and 34 faint galaxies (mainly ellipticals) from the catalogue of Brunzendorf & Meusinger (1999, hereafter BM99). Of the dE galaxies, 31 are from the catalogue of Conselice et al. (2003, hereafter CGW03) and 8 from the Hubble ACS catalogue of Penny et al. (2009, hereafter P09). From each catalogue only galaxies without published radial velocity were selected, in order to increase the spectroscopic sample of confirmed cluster members. Table 3.1 lists the names and coordinates for all

target galaxies. The additional column $V_{\rm lit}$ contains radial velocity estimates from the literature which were published or released *after* the observations were carried out (see Section 3.3.1), with the corresponding reference in Column "Ref".

3.2.2 Observations and data reduction

The targets were observed, during the nights of 2007 November $4^{\rm th}$ and $5^{\rm th}$, with the wide-field multifibre AF2/WYFFOS spectrograph, mounted at the prime focus of the 4.2-m William Herschel Telescope. The selected grating was R300B, a ruled grating blazed at 4000 Å with 300 lines mm^{-1}. This results in an approximate dispersion of 1.6 Å pixel^{-1} in the 3900–8600 Å wavelength range, at a resolution of ~ 9 Å. The choice of grating is optimized for the current investigation: a low resolution which allowed for an increased S/N ratio and wavelength range, thereby increasing our capabilities in terms of redshift and stellar population parameter determination.

A different fibre configuration was used during each of the two nights of observation, and twelve 1800-s exposures were acquired for each configuration, together with bias frames, sky and dome flat fields, and He and Ne arc frames for calibration. A sample science exposure from the first night of observations is shown in Figure 3.2. Air masses ranged from 1 to 1.65 during the first night and from 1 to 1.9 during the second night. To remove the contribution from the sky background and to compute fibre throughput, offset sky pointings were taken during each night of observation, and dedicated sky fibres were allocated within each science exposure. Custom configurations were also observed during each night to acquire the spectra of standard stars. These included velocity and spectrophotometric standards, to be employed for radial velocity measurements and to correct galaxy spectra for the response curve of the instrument, respectively. The full set of standard stars is listed in Table 3.2, together with stellar spectral type from the SIMBAD database.

Data reduction was performed within the IRAF environment, using the CCDPROC task to take care of image cosmetics and the DOFIBERS task for the extraction and calibration of individual galaxy spectra. Each step of the data reduction procedure was performed separately for each night of observation.

After all raw data frames were trimmed to remove overscan, the master bias (obtained by averaging) was subtracted from each frame. He and Ne lamp frames were combined to create one "master" lamp for calibration. We created combined lamps from the frames acquired both at the beginning and at the end of the night, to check for possible systematic shifts during one observing run. All science frames were cleaned of cosmic rays using the IRAF COSMICRAYS task. The master flat frame was created by averaging the dome flats.

We then ran the DOFIBERS task using separately as input each science frame for spectrum extraction, dome flats for fibre trace determination, the sky flat to compute

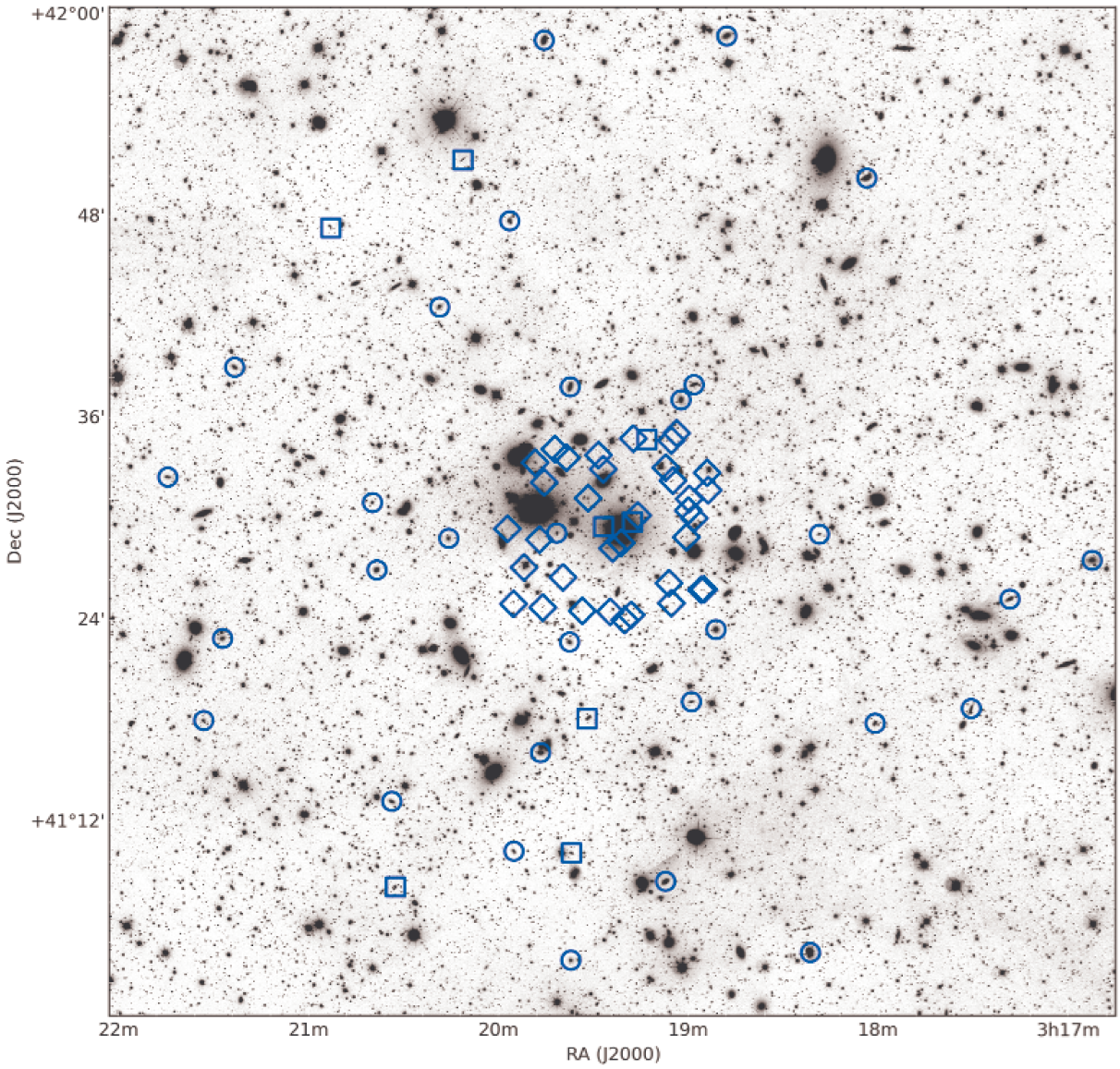

Figure 3.1: Sky map of Abell 426. Blue symbols mark objects selected for spectroscopic observations. Circles, squares and diamonds represent, respectively, confirmed cluster members, non-member background objects and galaxies with unknown membership, according to our following analysis. The optical background is the SDSS r-band image downloaded from the SDSS mosaic web service (`http://dr12.sdss3.org/mosaics`).

Table 3.1: Basic position and radial velocity data for Perseus Cluster galaxies observed with AF2/WYFFOS. The last column lists the external reference for galaxies with available radial velocity.

Obs. Date	Target	RA (J2000)	DEC (J2000)	$V_{\rm lit.}$ (km s^{-1})	Ref.[a]
2007-11-04	P09 1a16	$03^{\rm h}19^{\rm m}57\overset{\rm s}{.}40$	$+41°29'31\overset{''}{.}8$	···	
	P09 1a18	$03^{\rm h}19^{\rm m}52\overset{\rm s}{.}10$	$+41°27'14\overset{''}{.}3$	···	
	P09 3a8	$03^{\rm h}19^{\rm m}26\overset{\rm s}{.}70$	$+41°29'39\overset{''}{.}9$	···	
	[BM99] 125	$03^{\rm h}16^{\rm m}51\overset{\rm s}{.}35$	$+41°27'33\overset{''}{.}8$	···	
	[BM99] 139	$03^{\rm h}17^{\rm m}17\overset{\rm s}{.}60$	$+41°25'17\overset{''}{.}2$	6246 ± 3	S
	[BM99] 146	$03^{\rm h}17^{\rm m}30\overset{\rm s}{.}09$	$+41°18'47\overset{''}{.}7$	···	
	[BM99] 167	$03^{\rm h}18^{\rm m}00\overset{\rm s}{.}60$	$+41°17'56\overset{''}{.}7$	4209 ± 4	S
	[BM99] 170	$03^{\rm h}18^{\rm m}02\overset{\rm s}{.}55$	$+41°50'22\overset{''}{.}3$	···	
	[BM99] 178	$03^{\rm h}18^{\rm m}18\overset{\rm s}{.}09$	$+41°29'11\overset{''}{.}7$	···	
	[BM99] 208	$03^{\rm h}18^{\rm m}47\overset{\rm s}{.}26$	$+41°58'50\overset{''}{.}8$	5244 ± 3	S
	[BM99] 210	$03^{\rm h}18^{\rm m}51\overset{\rm s}{.}06$	$+41°23'32\overset{''}{.}7$	6185 ± 5	S
	[BM99] 215	$03^{\rm h}18^{\rm m}57\overset{\rm s}{.}92$	$+41°38'06\overset{''}{.}6$	4089 ± 3	S
	[BM99] 227	$03^{\rm h}19^{\rm m}07\overset{\rm s}{.}13$	$+41°08'34\overset{''}{.}1$	7899 ± 3	S
	[BM99] 252	$03^{\rm h}19^{\rm m}36\overset{\rm s}{.}93$	$+41°10'15\overset{''}{.}7$	···	
	[BM99] 253	$03^{\rm h}19^{\rm m}37\overset{\rm s}{.}09$	$+41°03'53\overset{''}{.}1$	···	
	[BM99] 255	$03^{\rm h}19^{\rm m}37\overset{\rm s}{.}43$	$+41°37'58\overset{''}{.}8$	8585 ± 2	S
	[BM99] 267	$03^{\rm h}19^{\rm m}45\overset{\rm s}{.}85$	$+41°58'35\overset{''}{.}8$	4805 ± 2	S
	[BM99] 282	$03^{\rm h}19^{\rm m}55\overset{\rm s}{.}15$	$+41°10'21\overset{''}{.}6$	4902 ± 4	S
	[BM99] 287	$03^{\rm h}19^{\rm m}56\overset{\rm s}{.}81$	$+41°47'51\overset{''}{.}0$	···	
	[BM99] 305	$03^{\rm h}20^{\rm m}11\overset{\rm s}{.}85$	$+41°51'28\overset{''}{.}5$	···	
	[BM99] 317	$03^{\rm h}20^{\rm m}19\overset{\rm s}{.}11$	$+41°42'42\overset{''}{.}9$	···	
	[BM99] 331	$03^{\rm h}20^{\rm m}32\overset{\rm s}{.}67$	$+41°08'13\overset{''}{.}7$	···	
	[BM99] 338	$03^{\rm h}20^{\rm m}38\overset{\rm s}{.}87$	$+41°27'04\overset{''}{.}3$	···	
	[BM99] 340	$03^{\rm h}20^{\rm m}40\overset{\rm s}{.}34$	$+41°31'04\overset{''}{.}6$	···	
	[BM99] 355	$03^{\rm h}20^{\rm m}53\overset{\rm s}{.}94$	$+41°47'24\overset{''}{.}2$	···	
	[BM99] 389	$03^{\rm h}21^{\rm m}24\overset{\rm s}{.}47$	$+41°39'05\overset{''}{.}1$	···	
	[BM99] 392	$03^{\rm h}21^{\rm m}27\overset{\rm s}{.}81$	$+41°22'57\overset{''}{.}2$	···	
	[BM99] 410	$03^{\rm h}21^{\rm m}45\overset{\rm s}{.}55$	$+41°32'31\overset{''}{.}6$	···	
	[CGW2003] 1	$03^{\rm h}18^{\rm m}53\overset{\rm s}{.}50$	$+41°31'50\overset{''}{.}1$	···	
	[CGW2003] 3	$03^{\rm h}18^{\rm m}54\overset{\rm s}{.}90$	$+41°25'55\overset{''}{.}3$	···	
	[CGW2003] 9	$03^{\rm h}18^{\rm m}59\overset{\rm s}{.}80$	$+41°30'37\overset{''}{.}1$	···	
	[CGW2003] 10	$03^{\rm h}19^{\rm m}00\overset{\rm s}{.}40$	$+41°29'02\overset{''}{.}4$	5845 ± 47	P
	[CGW2003] 11	$03^{\rm h}19^{\rm m}03\overset{\rm s}{.}50$	$+41°35'13\overset{''}{.}6$	···	
	[CGW2003] 13	$03^{\rm h}19^{\rm m}04\overset{\rm s}{.}70$	$+41°32'24\overset{''}{.}6$	···	
	[CGW2003] 14	$03^{\rm h}19^{\rm m}05\overset{\rm s}{.}20$	$+41°25'07\overset{''}{.}0$	···	
	[CGW2003] 26	$03^{\rm h}19^{\rm m}17\overset{\rm s}{.}30$	$+41°34'54\overset{''}{.}5$	···	

[a] 'P': Penny & Conselice (2008); 'S': SDSS DR12

Table 3.1: (*continued*) Basic position and radial velocity data for Perseus Cluster galaxies observed with AF2/WYFFOS.

Obs. Date	Target	RA (J2000)	DEC (J2000)	$V_{\rm lit.}$ (km s^{-1})	Ref.
	[CGW2003] 27	$03^{\rm h}19^{\rm m}17\overset{\rm s}{.}60$	$+41°29'57\overset{''}{.}7$	125580 ± 51	P
	[CGW2003] 28	$03^{\rm h}19^{\rm m}18\overset{\rm s}{.}00$	$+41°24'25\overset{''}{.}3$	···	
	[CGW2003] 31	$03^{\rm h}19^{\rm m}21\overset{\rm s}{.}20$	$+41°28'42\overset{''}{.}5$	8662 ± 14	P
	[CGW2003] 35	$03^{\rm h}19^{\rm m}24\overset{\rm s}{.}70$	$+41°24'36\overset{''}{.}3$	···	
	[CGW2003] 37	$03^{\rm h}19^{\rm m}26\overset{\rm s}{.}90$	$+41°33'05\overset{''}{.}1$	70960 ± 23	P
	[CGW2003] 40	$03^{\rm h}19^{\rm m}31\overset{\rm s}{.}70$	$+41°31'21\overset{''}{.}3$	···	
	[CGW2003] 41	$03^{\rm h}19^{\rm m}33\overset{\rm s}{.}50$	$+41°24'39\overset{''}{.}4$	···	
	[CGW2003] 43	$03^{\rm h}19^{\rm m}38\overset{\rm s}{.}60$	$+41°33'46\overset{''}{.}1$	···	
	[CGW2003] 45	$03^{\rm h}19^{\rm m}41\overset{\rm s}{.}70$	$+41°29'17\overset{''}{.}0$	3120 ± 27	P
	[CGW2003] 49	$03^{\rm h}19^{\rm m}46\overset{\rm s}{.}10$	$+41°24'51\overset{''}{.}2$	8457 ± 38	P
	[CGW2003] 50	$03^{\rm h}19^{\rm m}55\overset{\rm s}{.}40$	$+41°25'04\overset{''}{.}4$	···	
	[CGW2003] 54	$03^{\rm h}19^{\rm m}48\overset{\rm s}{.}60$	$+41°33'28\overset{''}{.}6$	3363 ± 38	P
2007-11-05	P09 1a12	$03^{\rm h}19^{\rm m}47\overset{\rm s}{.}20$	$+41°28'53\overset{''}{.}9$	···	
	P09 3a11	$03^{\rm h}19^{\rm m}23\overset{\rm s}{.}90$	$+41°28'23\overset{''}{.}0$	···	
	P09 4a11	$03^{\rm h}18^{\rm m}57\overset{\rm s}{.}90$	$+41°30'09\overset{''}{.}8$	···	
	P09 5a6	$03^{\rm h}19^{\rm m}28\overset{\rm s}{.}40$	$+41°33'55\overset{''}{.}8$	···	
	P09 6a1	$03^{\rm h}19^{\rm m}07\overset{\rm s}{.}00$	$+41°33'10\overset{''}{.}7$	···	
	[BM99] 183	$03^{\rm h}18^{\rm m}21\overset{\rm s}{.}35$	$+41°04'19\overset{''}{.}2$	···	
	[BM99] 218	$03^{\rm h}18^{\rm m}58\overset{\rm s}{.}89$	$+41°19'15\overset{''}{.}2$	···	
	[BM99] 219	$03^{\rm h}19^{\rm m}02\overset{\rm s}{.}09$	$+41°37'12\overset{''}{.}3$	5549 ± 4	S
	[BM99] 249	$03^{\rm h}19^{\rm m}31\overset{\rm s}{.}96$	$+41°18'15\overset{''}{.}1$	···	
	[BM99] 256	$03^{\rm h}19^{\rm m}37\overset{\rm s}{.}57$	$+41°22'48\overset{''}{.}4$	5505 ± 5	S
	[BM99] 268	$03^{\rm h}19^{\rm m}46\overset{\rm s}{.}75$	$+41°16'13\overset{''}{.}4$	4576 ± 3	S
	[BM99] 315	$03^{\rm h}20^{\rm m}16\overset{\rm s}{.}04$	$+41°28'57\overset{''}{.}8$	···	
	[BM99] 333	$03^{\rm h}20^{\rm m}33\overset{\rm s}{.}87$	$+41°13'18\overset{''}{.}6$	6819 ± 5	S
	[BM99] 399	$03^{\rm h}21^{\rm m}33\overset{\rm s}{.}63$	$+41°18'03\overset{''}{.}9$	···	
	[CGW2003] 2	$03^{\rm h}18^{\rm m}53\overset{\rm s}{.}80$	$+41°32'52\overset{''}{.}3$	···	
	[CGW2003] 4	$03^{\rm h}18^{\rm m}55\overset{\rm s}{.}70$	$+41°25'54\overset{''}{.}4$	···	
	[CGW2003] 7	$03^{\rm h}18^{\rm m}59\overset{\rm s}{.}50$	$+41°31'18\overset{''}{.}9$	···	
	[CGW2003] 15	$03^{\rm h}19^{\rm m}05\overset{\rm s}{.}20$	$+41°34'48\overset{''}{.}1$	···	
	[CGW2003] 16	$03^{\rm h}19^{\rm m}06\overset{\rm s}{.}00$	$+41°26'18\overset{''}{.}7$	6577 ± 45	P
	[CGW2003] 22	$03^{\rm h}19^{\rm m}13\overset{\rm s}{.}00$	$+41°34'51\overset{''}{.}8$	···	
	[CGW2003] 25	$03^{\rm h}19^{\rm m}15\overset{\rm s}{.}90$	$+41°30'20\overset{''}{.}3$	70320 ± 59	P
	[CGW2003] 30	$03^{\rm h}19^{\rm m}20\overset{\rm s}{.}10$	$+41°24'06\overset{''}{.}6$	···	
	[CGW2003] 44	$03^{\rm h}19^{\rm m}39\overset{\rm s}{.}70$	$+41°26'39\overset{''}{.}1$	···	
	[CGW2003] 46	$03^{\rm h}19^{\rm m}42\overset{\rm s}{.}30$	$+41°34'16\overset{''}{.}6$	···	
	[CGW2003] 48	$03^{\rm h}19^{\rm m}45\overset{\rm s}{.}70$	$+41°32'18\overset{''}{.}0$	···	

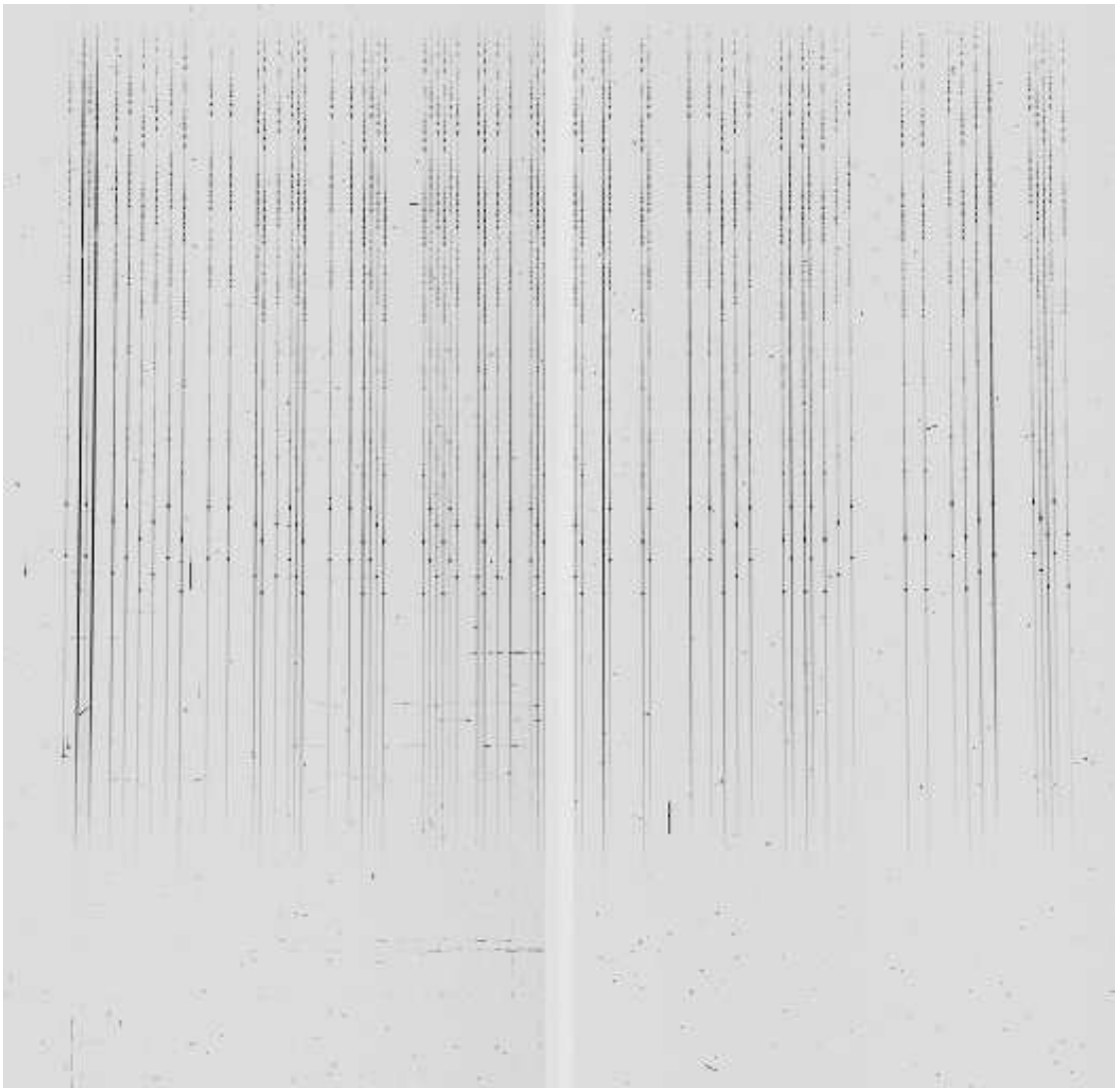

Figure 3.2: Raw AF2/WYFFOS 1800-s science exposure from the first night of observation. The spectral direction is aligned with the vertical axis, with blue wavelengths at the bottom and red wavelengths at the top. Dotted patterns at the top of each trace correspond to sky emission lines in the red part of the spectrum ($\lambda > 6000$ Å).

Table 3.2: Spectrophotometric and velocity standard stars. Spectral types are from the SIMBAD database.

ID	Spectral type	α (J2000)	δ (J2000)	Type [a]
BD+28 4211	0p	$21^h51^m11^s$	$+28°51'50''$	S
Hiltner 600	B1	$06^h45^m13^s$	$+02°08'16''$	S
G24-9	DC	$20^h13^m56^s$	$+06°42'55''$	S
HR 2600	K2III	$06^h59^m02^s$	$+38°03'08''$	V
HR 6349	F9V	$17^h05^m17^s$	$+00°42'09''$	V

[a] 'V': velocity; 'S': spectrophotometric

fibre throughput and master lamp frames for wavelength calibration. The aperture identification table was prepared using the observing logs and finding charts. The main steps in the DOFIBERS task are (details can be found in Valdes 1995):

Aperture identification: It is performed using a horizontal cut to the master flat image.

Aperture trace fitting: The trace for each aperture is fitted as a function of vertical position.

Scattered light removal: scattered light is determined by fitting a function to all the data *outside* the defined apertures.

Flat field removal: using the master dome flat. During this step, the spectra are also corrected for differences in fibre throughput using twilight sky flats.

Wavelength calibration: For fibre data it is usually necessary to manually identify emission lines in arc spectra only for one aperture, and the rest are automatically reidentified by the DOFIBERS task. WYFFOS data, however, present significant shifts from adjacent apertures, caused by the way fibres are grouped at the entrance of the spectrograph. The typical "sawtooth" pattern is visible in Figure 3.2: roughly in the middle of the image, on each trace, there are pairs of darker spots which mark the 5577 Å and 5889 Å sky emission lines. The emission lines are shifted by several tenths of pixels from one aperture to the next, and the same position is repeated only every three apertures. This causes the reidentification algorithm in DOFIBERS to fail for all fibres which do not share the dispersion relation with the reference one (ideally, for two thirds of the fibres, if all are used). For these aperture, reidentification had to be performed manually.

Aperture extraction: Science spectra are extracted, *without* sky subtraction (see below).

The DOFIBERS task can optionally be used to perform sky subtraction, by combining the sky spectra from the dedicated fibres and subtracting the combined sky from the science spectra. The results from this procedure were however found to be unsatisfactory, in the sense that the sky was often over subtracted. We then implemented sky subtraction using two different methods:

I. Sky subtraction from each science frame is performed using the combined sky from DOFIBERS but the sky spectrum is scaled and shifted in order to minimize the rms in two wavelength intervals (5500–6000 Å and 7000–8000 Å). This procedure, which we implemented in PYTHON, uses the IRAF SKYTWEAK task to derive the correct scale and shift factors.

II. Sky subtraction is performed using offset sky frames. An average sky level shift is initially found by computing the ratio of fluxes between the science and sky frames, using sky dedicated fibres in the science exposure. The offset sky spectra are then scaled according to this ratio and subtracted to the galaxy spectra acquired through the same fibre.

Both these methods were found to give more accurate results with respect to the internal DOFIBERS method. Method II, despite being theoretically more justified (unlike method I, it does not depend on empirical *a posteriori* corrections) was also found to be slightly affected by sky over-subtraction. In particular, the method is very sensitive to the determination of the sky scaling factor, which can be severely affected, for example, by cosmic rays. For the following analysis we therefore employed sky-subtracted spectra obtained through method I.

Relative flux calibration was achieved by deriving the instrumental response curve from spectrophotometric standard star spectra. The response function, which is given by the combined effects of telescope, fibre, spectrograph sensitivity and detector efficiency, change significantly between different fibres. We reduced the spectra for the three available stars (Hiltner 600, BD+28 4211 and G24-9) and created an average response function which was applied to the galaxy spectra, after correcting for the atmospheric extinction at the La Palma observing site (King 1985). Maximum relative errors between pairs of response functions are of the order of 2% in the wavelength region between 4000 and 8300 Å. We adopt this error as an estimate of the precision of flux calibration. The spectrum of velocity standard HR 2600 was reduced using identical procedures as the rest of the target galaxies.

The DOFIBERS task can optionally create as part of the output for each fibre an estimate of the sky spectrum and 1-σ error spectrum computed based on photon statistics. This output is produced only if the "internal" sky subtraction algorithm is enabled. Since an estimate of the variance spectrum is required by the analysis software, we performed a full DOFIBERS run, and assigned the output error spectra to the corresponding

galaxy spectra derived according to method described above.

Examples of the final galaxy reduced spectra are shown in Figure 3.3: the top panel shows an example of a typical "bright", relative to the current sample ($M_r \approx -19$), early type galaxy with medium/high *S/N* ratio; the middle panel shows instead a low-luminosity galaxy ($M_r \approx -17.5$) with a low *S/N* ratio; in the lower panel a late-type galaxy is shown (classified by BM99 as SB/SB0) with prominent emission lines in the Hα-[S II] wavelength region.

3.2.3 Data analysis

Radial velocities were measured by means of the cross correlation technique (Tonry & Davis 1979), using the RVSAO (Kurtz & Mink 1998) package. Briefly, the galaxy and template spectra ($g(\lambda)$ and $t(\lambda)$) are first rebinned linearly to $\ln\lambda$, and preprocessed to optimize the following Fourier analysis. Preprocessing typically involves continuum suppression, apodization, zero padding and Fourier filtering of both high (i.e., noise) and low (i.e.residual continuum variation) frequencies. The discrete Fourier transform of the galaxy and template spectra ($G(k)$ and $T(k)$) are computed and the cross-correlation $C(k)$ is derived as the product of the Fourier transform of the object spectrum with the conjugate of the transform of the template spectrum

$$C(k) = \frac{1}{N\sigma_g\sigma_t} G(k)T^*(k) \ , \tag{3.1}$$

where N is the number of bins (i.e., pixels) in the spectra and σ_g and σ_t are, respectively, the rms of the galaxy and template spectra. The galaxy redshift is finally determined by fitting the peak of the cross-correlation by a quadratic polynomial. The routine that performs the cross-correlation (XCSAO) also returns an estimate of the error δv on the derived radial velocity which is given by

$$\delta v = \frac{3w}{8(1+R_{\rm xc})} \ , \tag{3.2}$$

where w is the FWHM of the correlation peak and $R_{\rm xc}$ is the ratio of the height of the peak and $\sqrt{2}$ times the average peak height of a "remainder function" a (see Tonry & Davis 1979, section III.c.i.). The function a is introduced to account for the possible mismatch between the galaxy and template spectrum, and is defined as the difference between the measured correlation function and a perfect correlation of the template with a broadened version of itself. The value of $R_{\rm xc}$ is commonly used as a measure of the quality of the cross-correlation (see below) and is listed for reference in Table 3.3 together with the error on each redshift measurement.

The cross-correlation function was first computed using the observed spectrum of standard star HR 2600, in order to have results independent from instrumental broad-

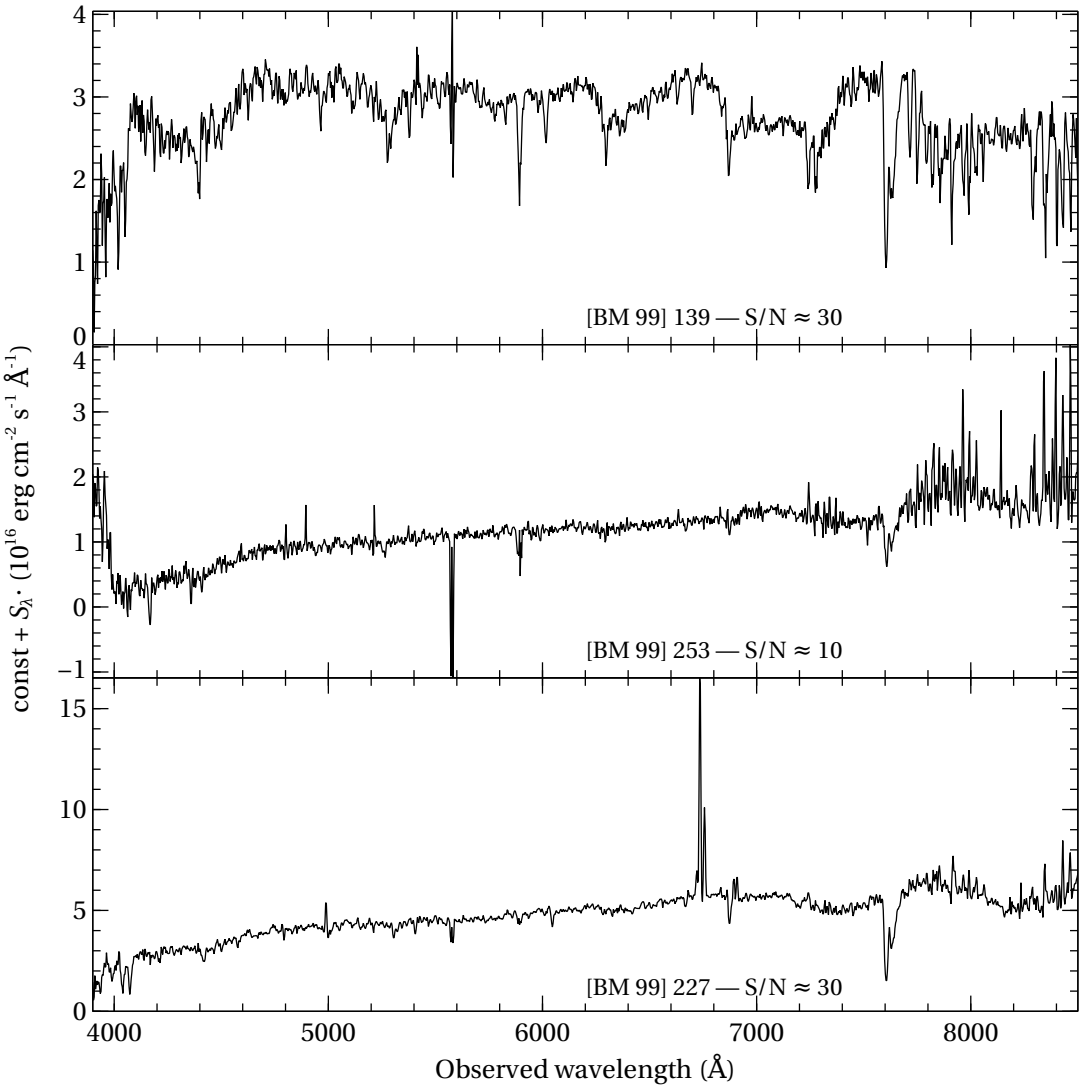

Figure 3.3: Example spectra for the AF2/WYFFOS galaxy sample, as a function of observed wavelength, after relative flux calibration. All galaxies in this figure were confirmed cluster members after our cross–correlation analysis.

ening. We then checked our results using a synthetic spectrum of the same spectral type of the template, taken from the BLUERED library (Bertone et al. 2008), which was appropriately convolved with the instrumental broadening function. Cross-correlation parameters were chosen to minimise the contributions from residuals of sky subtraction and telluric absorption. Residual cosmic rays and imperfectly subtracted sky lines were masked during the cross-correlation analysis using the interactive capabilities of XCSAO. Heliocentric radial velocities are listed in Table 3.3. The final values are derived by adding the template radial velocity, obtained by cross-correlating the template with the synthetic star spectrum, to the results of the cross-correlation. Final errors are the quadratic sum of the errors from the two separate cross-correlations (galaxy–template and template–synthetic spectrum). Following Kurtz & Mink (1998), only measurements with cross-correlation coefficient $R_{\rm xc} > 3$ were labelled as reliable. The cut in cross-correlation quality eliminates 35 galaxies from the sample, which were not further analysed and are not listed in Table 3.3.

Six of the galaxies show prominent emission lines. The redshift was derived in this case using the EMSAO task, again from the RVSAO package.

A summary of the results of the cross-correlation analysis, divided by catalogue, is reported in Table 3.4. The separation between cluster members and non-members is discussed in the next section.

3.3 Cluster kinematics and scaling relations

3.3.1 Additional samples from the literature

In order to identify cluster members in our spectroscopic sample study the global properties of the cluster galaxy population, we created an expanded catalogue of all galaxies with published redshifts in the area covered by BM99. The BM99 catalogue itself was updated with new redshift measurements from the NED[1] online database, raising total to 213 from the 164 known at the epoch of 1999. The sample was then augmented with spectroscopic data from the SDSS DR12[2] database, which contains spectra obtained with two special plates (1665 and 1666) devoted to the Perseus-Pisces region. These "special"[3] plates were actually observed in 2003, but were not included in the public database until DR8, which was distributed in January 2011. This is the reason why some of these galaxies were not excluded in the proposal preparation phase for the current investigation. The sample was then completed with radial velocities from Kent & Sargent (1983) not included in the other catalogues: these are mostly objects to the west of the cluster centre. SDSS *ugriz* photometry was derived for all galaxies

[1] http://ned.ipac.caltech.edu/

[2] http://sdss.org/

[3] http://classic.sdss.org/dr7/products/spectra/special.html

Table 3.3: Basic photometric data and measured radial velocities for Perseus Cluster galaxies observed with AF2/WYFFOS. Photometric data are given only for confirmed cluster members.

Target	$r_{\rm eff}$ (arcsec)	M_r	$g-r$	V_r (km s^{-1})	$R_{\rm xc}$	S/N	Cluster member
[BM99] 215	8.33	-19.34	0.80	4102 ± 29	14.3	32	Y
[BM99] 139	9.85	-19.38	0.76	6234 ± 30	13.2	28	Y
[BM99] 267	4.51	-20.45	0.82	4844 ± 31	13.8	51	Y
[BM99] 333	10.79	-18.35	0.75	6811 ± 29	13.3	21	Y
[BM99] 255	6.01	-20.19	0.78	8597 ± 31	13.0	59	Y
[BM99] 208	13.04	-19.74	0.73	5225 ± 33	11.4	22	Y
[BM99] 338	13.2	-18.76	0.72	4859 ± 34	11.1	21	Y
[BM99] 210	15.8	-19.09	0.75	6168 ± 33	11.1	26	Y
[BM99] 249	···	···	···	34741 ± 33	10.7		N
[BM99] 219	12.11	-19.28	0.79	5582 ± 37	10.1	25	Y
[BM99] 125	19.11	-19.51	0.63	5791 ± 36	9.5	20	Y
[BM99] 256	10.68	-19.05	0.72	5485 ± 35	9.5	23	Y
P09 3a8	···	···	···	40485 ± 43	8.3		N
[BM99] 392	10.02	-18.66	0.72	6921 ± 40	8.2	13	Y
[BM99] 268	7.94	-19.52	0.71	4569 ± 40	8.1	48	Y
[BM99] 282	7.94	-18.31	0.71	4909 ± 43	7.8	33	Y
[BM99] 331	···	···	···	27094 ± 43	7.5		N
[BM99] 389	15.7	-18.21	0.79	5597 ± 42	7.4	11	Y
[BM99] 170	27.1	-19.49	0.69	7200 ± 46	7.1	16	Y
[CGW2003] 22	···	···	···	40470 ± 42	6.9		N
[BM99] 167	9.66	-18.81	0.71	4161 ± 46	6.8	20	Y
[BM99] 315	12.17	-18.58	0.74	4194 ± 49	6.8	12	Y
[BM99] 340	3.99	-18.06	0.71	4458 ± 44	6.8	15	Y
[BM99] 287	10.19	-18.62	0.47	7557 ± 54	4.9	18	Y
[BM99] 399	6.37	-18.24	0.77	4730 ± 62	4.8	10	Y
[BM99] 146	20.75	-18.39	0.64	7295 ± 66	4.5	14	Y
[BM99] 253	12.14	-17.79	0.68	4924 ± 60	4.5	13	Y
[CGW2003] 27	···	···	···	34589 ± 107	3.7		N
[BM99] 317	14.11	-17.89	0.75	5883 ± 79	3.6	31	Y
[BM99] 410	15.35	-18.32	0.7	5272 ± 83	3.5	9	Y
[CGW2003] 45	···	-16.79	0.53	3136 ± 93	3.4	11	Y
[BM99] 218	11.41	-17.71	0.62	4933 ± 69	3.3	13	Y
[BM99] 178	8.15	-17.38	0.17	7633 ± 130	EL	16	Y
[BM99] 227	13.53	-19.79	0.52	7893 ± 1	EL	35	Y
[BM99] 183	···	···	···	7319 ± 28	EL	31	Y
[BM99] 355	···	···	···	12109 ± 22	EL		N
[BM99] 305	···	···	···	12200 ± 32	EL		N
[BM99] 252	···	···	···	20409 ± 66	EL		N

Table 3.4: Summary of cross-correlation analysis performed with XCSAO on the reduced AF2/WYFFOS spectra.

Catalogue	Cluster Members	Background Galaxies	Unsuccessful x-correlation	Total
BM99	29	5	0	34
CCGW03	1	2	28	31
Penny et al. (2009)	0	1	7	8
Total	30	8	35	**73**

by cross–matching the coordinates of galaxies in the radial velocity database with the SDSS photometry tables.

We did not restrict the Sloan photometric data to objects with clean photomety[4], as doing so would have significantly reduced the number of galaxies in the sample. However, in order to avoid biased results because of incorrect photometry, we created a second database containing galaxies with clean photometry from the SDSS to double check all conclusions based on the photometric data of the galaxies. We used Sloan `modelMag` values, corrected for extinction using the corresponding `extinction` column, as the equivalent of the total magnitudes for each band. The effective radius $r_{\rm eff}$ for each galaxy was also taken from the SDSS database by discriminating the best fitting model to the surface brightness profile, using the `lnLDeV_r` and `lnLExp_r` database fields: the `deVRad_r` value was adopted as effective radius for best-fitting de Vaucouleurs profiles, and `expRad_r` for exponential profiles.

Some galaxies in the BM99 catalogue do not have a photometric counterpart in the Sloan database. The photometric pipeline fails because these objects are located near the very centre of the cluster, were crowding and intra-cluster light hampers a correct estimation of the optical background. For the most luminous galaxies in this region, we downloaded B_T^0 and V_T^0 magnitudes (de Vaucouleurs et al. 1991) from the NED database, which were converted to the SDSS system using the relations by Lupton et al. (2005)[5]. The remaining galaxies without reliable optical photometry or colour information, i.e. galaxies with only B band magnitude from BM99, were kept for the analysis of the global cluster kinematics, but were eventually discarded for the study of the galaxies' stellar population. Objects in common between the two catalogues (BM99 and SDSS) were counted only once, and their radial velocity data was taken from the SDSS.

Known dwarf elliptical members were added from the PC08 catalogue and from Penny et al. (2014). We derived Sloan g and r magnitudes from B and R magnitudes using the relations by Lupton et al. (2005). Approximate effective radii were converted from the published scale radii r_0 and Sérsic n values by applying the formula (Graham

[4] `http://www.sdss.org/dr12/tutorials/flags/`
[5] `http://www.sdss.org/dr12/algorithms/sdssUBVRITransform/`

& Driver 2005) $r_e = r_0 b^n$, where b is a constant which depends on n. It is usually approximated by $b(n) = 1.9992n - 0.3271$ (Ciotti & Bertin 1999).

3.3.2 Cluster membership

To identify real members of the A426 Cluster a first selection was made in redshift space, using radial velocities from all available catalogues.The velocity distribution histogram is shown in Figure 3.4, with vertical lines at the top of the figure marking galaxies observed with the WHT. A background structure is known to occupy the same region of sky of the Perseus Cluster at $cz \sim 14000$ km s^{-1} (Huchra et al. 1999). This structure is however well separated, in redshift space, from the cluster (the grey histogram), and choosing $cz = 11000$ km s^{-1} as the upper limit for A426 ensures that no galaxies from the background structure are included in the analysis. We also set $cz = 2000$ km s^{-1} as the lower limit for the radial velocity.

The velocity cut reduces the sample of WYFFOS galaxies to 30 members. The SDSS sample is restricted to 205 galaxies, of which 105 are in common with the sample from BM99. Thirteen galaxies in the WYFFOS sample have a corresponding spectrum in the SDSS database, while no new spectroscopic datum is found in the updated BM99 catalogue which is not already present in the Sloan data. Considering also the galaxy in common with the PC08 sample, WYFFOS data provide new membership for sixteen galaxies. The galaxies with previous redshift determination were used for a consistency check on our derived velocities: all measurements are compatible with the corresponding objects in the SDSS, and the median offset ($V_{\rm WYFFOS} - V_{\rm SDSS}$) is -7 km s^{-1} with an average dispersion of 17 km s^{-1}.

We refined the selection of cluster members by considering distribution of galaxies in a "phase-space" defined by the $(V_r, D_{\rm cc})$ coordinates, where V_r is the measured radial velocity and $D_{\rm cc}$ is the projected distance to the cluster centre, coincident with the position of the brightest cluster galaxy (BCG) NGC 1275 ($\alpha_{\rm J2000}$ = 3:19:48.1, $\delta_{\rm J2000}$ = +41:30:42). The choice of NGC 1275 as the physical centre of the Perseus Cluster is justified by the proximity of the centre of the X-Ray emission, determined from the ROSAT images by fitting a Gaussian function to the cluster peak ($\alpha_{\rm J2000}$ = 3:19:48.0, $\delta_{\rm J2000}$ = +41:30:38). The phase-space diagram is shown in Figure 3.5, with yellow filled circles marking galaxies observed at the WHT. Dashed lines in the figure show the escape velocity at each radius derived from the dynamical models of KS83. The group of high velocity galaxies at $D_{\rm cc} > 0.7$ deg, delimited in Figure 3.5 by the dotted rectangle in the upper right corner, appears separated from the main body of the cluster, and comparison with the dynamical models indicates that most galaxies in the group are probably not bound to the cluster. These galaxies were therefore excluded from the Perseus Cluster sample, and not analysed further. Figure 3.5 shows the spatial distribution of the excluded galaxies with respect to the rest of the cluster. Except for

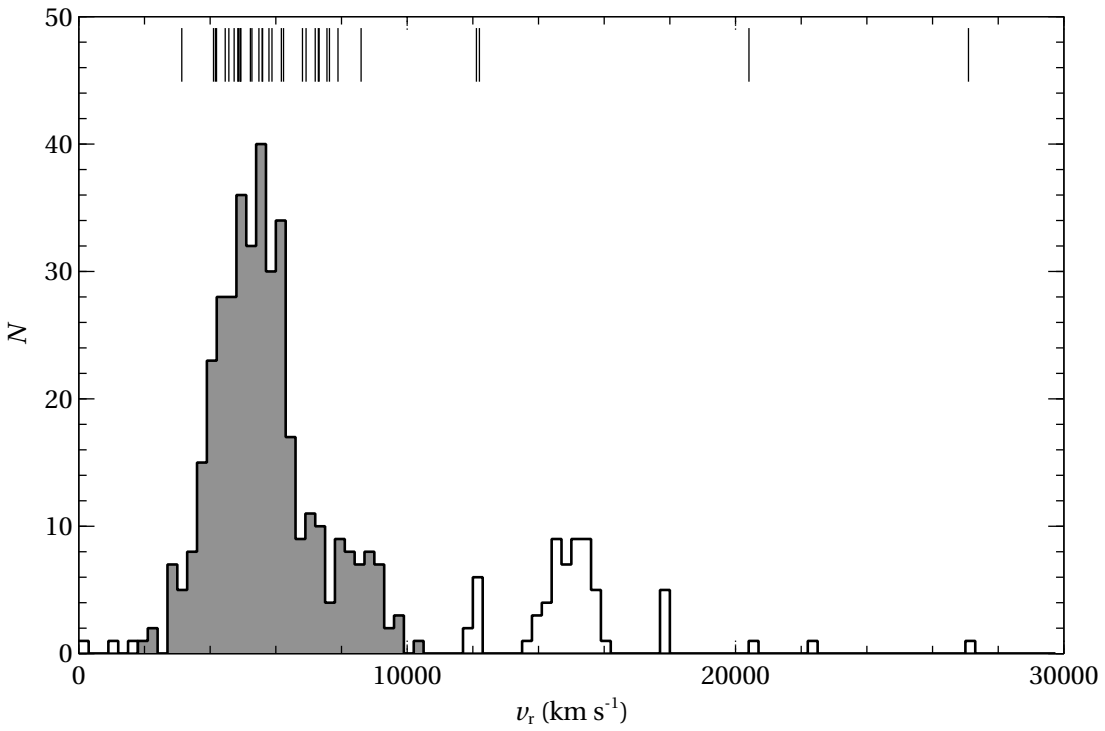

Figure 3.4: Velocity histogram for the BM99 catalogue sky area. The grey shaded area represents the selected A426 Cluster members. Vertical lines at the top of the graph mark the radial velocities of galaxies observed with AF2/WYFFOS with measurable redshift.

the clear deficiency of galaxies in the east direction, the excluded galaxies appear not to belong to a single structure.

The final Perseus Cluster spectroscopic database used in the following analysis is composed of 354 galaxies, of which 19 have unreliable or incomplete photometry. The restricted sample with *clean* SDSS photometry contains 169 galaxies. Figure 3.7 shows the spatial distribution of the combined sample of galaxies in the Perseus Cluster.

3.3.3 Cluster mass

The updated sample of galaxies with radial velocity was used to estimate the cluster virial mass, which was derived by Girardi et al. (1998, hereafter G98) using a sample with less than one third of the presently available redshifts. To compute cluster dynamical parameters we adopted the same procedure employed by G98, who exploited the virial theorem applied to projected global properties of the cluster.

The basic assumptions of the method are:

1. galaxies are in equilibrium within the cluster gravitational potential, i.e. the virial theorem applies;

2. the system has spherical symmetry;

3. the galaxy number distribution traces the mass distribution.

The virial mass $M_{\rm V}$ of the system can be derived as

$$M_{\rm V} = \frac{3\pi}{2}\frac{\sigma_{\rm P}^2 R_{\rm PV}}{G}, \tag{3.3}$$

where $\sigma_{\rm P}$ and $R_{\rm PV}$ represent, respectively, the projected velocity dispersion and the projected virial radius of the cluster. The velocity dispersion of the cluster $\sigma_{\rm P}$ was computed according to the prescriptions by Beers et al. (1990, hereafter, BFG90), using biweight estimator $S_{\rm BI}$ (BFG90, eq. 9) to derive the "scale" parameter and jackknife resampling for the confidence intervals $IS_{J_{BI}}$. The projected virial radius is defined as

$$R_{\rm PV} = \frac{N(N-1)}{\sum_{i>j} R_{ij}^{-1}}\ , \tag{3.4}$$

where N corresponds to the number of galaxies considered and R_{ij} is the projected distance between galaxies i and j. Equation 3.4 is valid if the "aperture" inside which galaxies are considered extends at least to the true virial radius $R_{\rm vir} = 2.44$ Mpc h^{-1}, which we computed according to equations 9–11 in G98. Our estimate is higher than to the value in G98 because of the higher value of the projected velocity dispersion $\sigma_{\rm P}$. The radial velocity sample for the Perseus Cluster galaxies contains galaxies up to

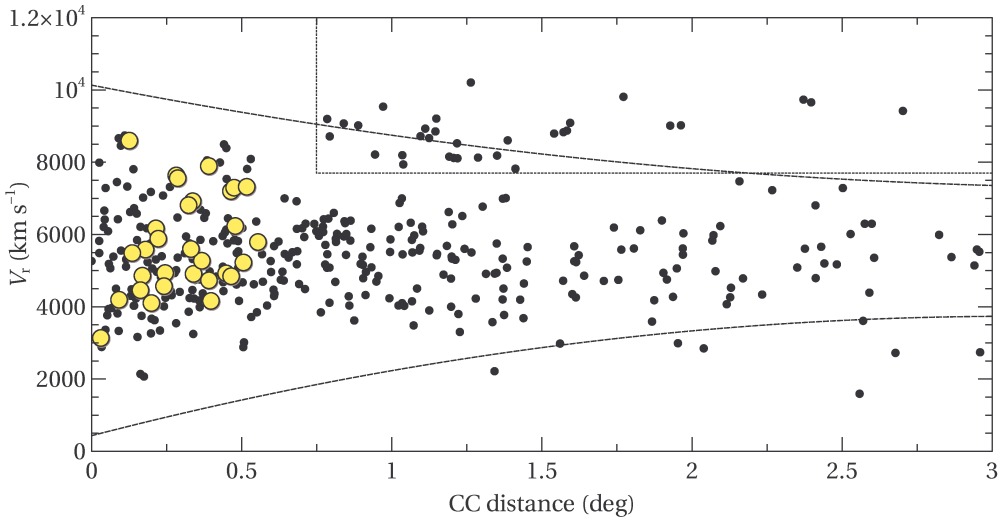

Figure 3.5: Redshift as a function of projected cluster-centric distance for galaxies in the Perseus Cluster. Yellow filled circles are member galaxies from the WYFFOS sample. Black dots represent all galaxies with radial velocities from the BM99, PC08, KS83 and SDSS catalogues. Dashed lines represent the escape velocity for the dynamical models of Kent & Sargent (1983).

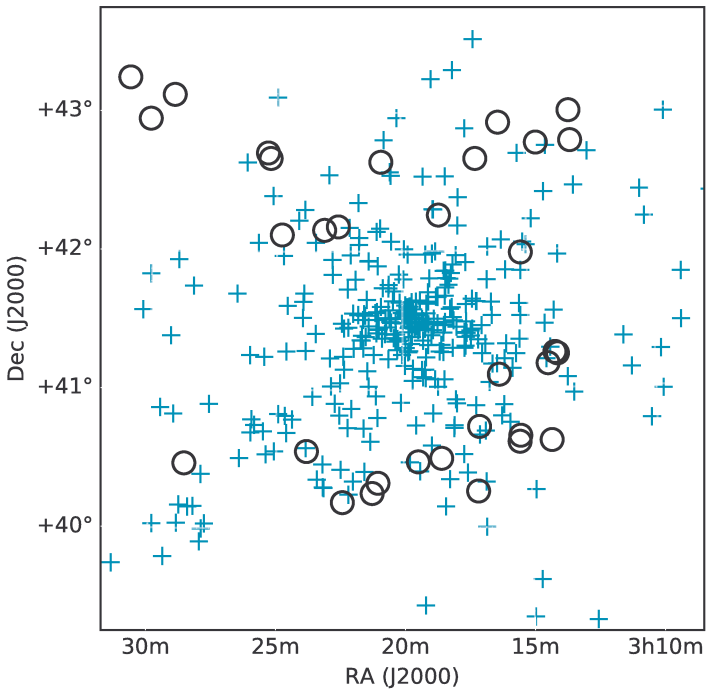

Figure 3.6: Spatial distribution of galaxies with $V_r > 7500\,\mathrm{km\,s^{-1}}$ and $D_{\mathrm{cc}} > 0.7$ deg.

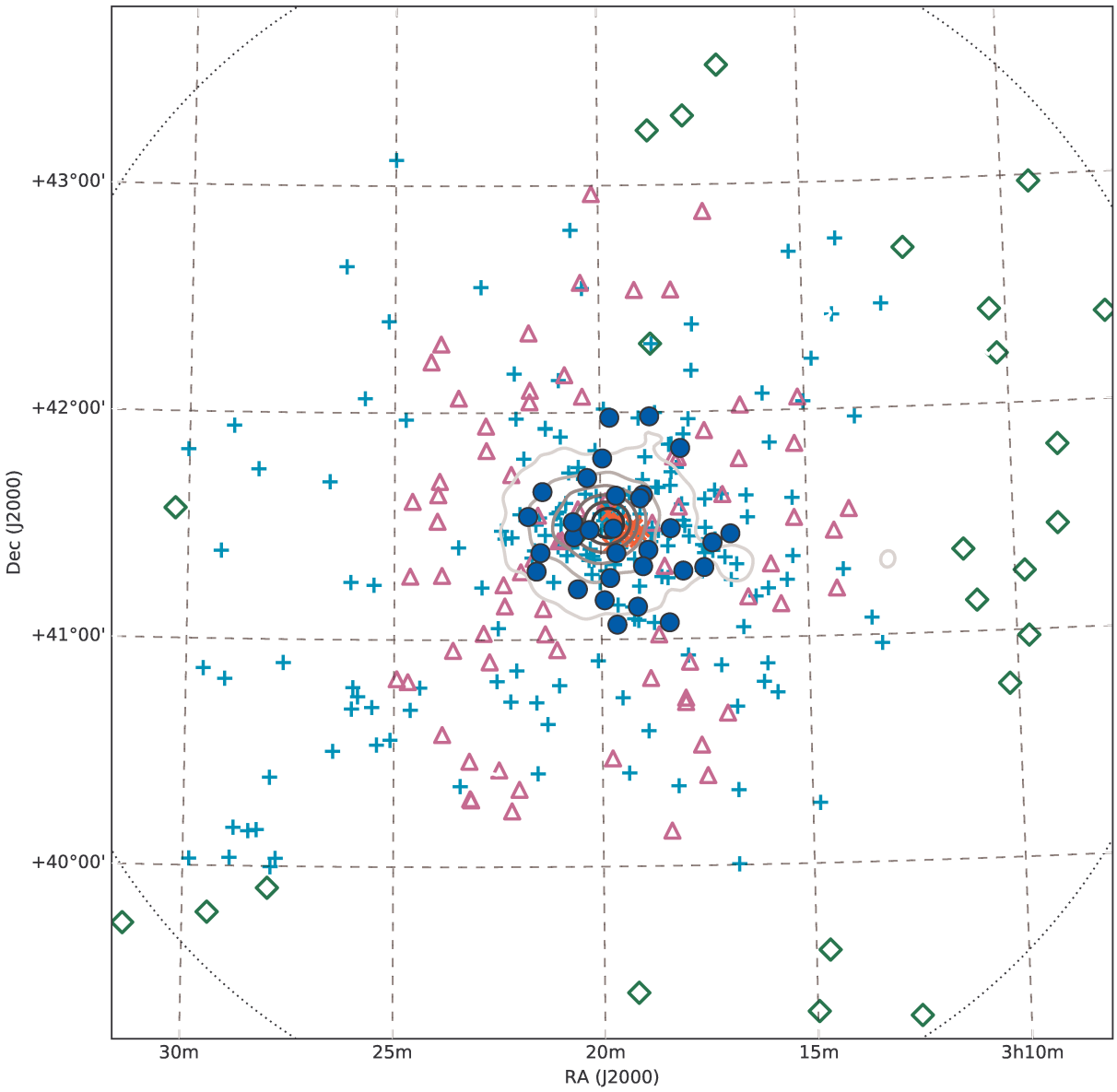

Figure 3.7: Spatial distribution of Abell 426 galaxies with published or newly derived radial velocity. Filled circles represent galaxies observed in this work, while cyan 'plus', red 'x' markers, green diamonds and magenta empty triangles represent, respectively, galaxies from BM99, PC08, KS83 and SDSS catalogues. Grey-scale contours show asinh-scaled X-Ray flux from *ROSAT* All-Sky Survey data. The dotted circle represents the virial radius $R_{\rm vir}$ (see Section 3.3.3).

Table 3.5: Dynamical properties of the Perseus Cluster of galaxies.

	N	$\sigma_{\rm P}$ $({\rm km\,s^{-1}})$	$R_{\rm PV}$ $(h^{-1}$ Mpc)	M_V $(h^{-1}10^{14}$ M$_\odot)$
Girardi et al. (1998)	113	1026^{+106}_{-64}	1.35 ± 0.15	$15.60^{+3.65}_{-2.61}$
This work	347	1218 ± 103	1.083 ± 0.003	17.62 ± 4.0

$R_{\rm max} = 2.73$ Mpc h^{-1} (as in G98), so we apply equation Equation 3.4 to compute the projected virial radius. To derive the cluster virial mass we considered only galaxies inside the true virial radius $R_{\rm vir}$, and derived the cluster virial mass $M_{\rm V}$ according to Equation 3.3. The actual calculation was performed iteratively, because the value of $\sigma_{\rm P}$ affects our estimate of $R_{\rm vir}$, while $R_{\rm vir}$ determines the region inside which $\sigma_{\rm P}$ is computed. Starting by the values of $\sigma_{\rm P}$ and $R_{\rm vir}$ derived from the whole sample of galaxies, the procedure reached convergence after only two iterations. This is expected because of the small number of galaxies at large cluster-centric radii: the total number of galaxies changes by a few units (in fact, only 7 galaxies are excluded at the end of the iteration) and the estimate of $\sigma_{\rm P}$ is therefore practically not affected.

The results of the dynamical analysis are reported, together with the original results by G98, in Table 3.5. Since the galaxy positions are assumed error-free, the error on $R_{\rm PV}$ obtained using Equation 3.4 was derived using jackknife resampling. The lower value of $R_{\rm PV}$, with respect to G98, is caused by the increased sampling of the galaxy population in the centre of the cluster, which increases the denominator in Equation 3.4. Despite the lower $R_{\rm PV}$, the mass estimate $M_{\rm V}$ is higher than the value derived by G98, because of the increased $\sigma_{\rm P}$ which was obtained using a three times more numerous sample of galaxies.

The estimate $M_{\rm V}$ of the virial mass is derived under the assumption that all the mass in the cluster is contained within the virial radius, but this is not a realistic assumption for observed galaxy clusters, where the region of matter gravitationally bound to the cluster may extend up to $\sim 5\ R_{\rm vir}$. In order to account for the mass outside $R_{\rm vir}$, a corrected virial mass estimate $M_{\rm CV}$ has to be computed according to equation (8) in G98, where a "surface" correction term C is added to the mass given by Equation 3.3. The value of C depends on the cluster velocity dispersion profile $\sigma(R)$, which is related to the anisotropy profile $\beta(r)$ by the Jeans equation (Binney & Tremaine 1987). The anisotropy parameter β is related to the orbit distribution inside a cluster, and is defined as $\beta = 1 - \sigma_\theta^2/\sigma_r^2$, where σ_θ and σ_r represent the velocity dispersion along the polar coordinates r and θ. We adopt instead the median value of the correction obtained by G98 for clusters with decreasing velocity dispersion profile (type A clusters, in G98 terminology). According to G98, the median value of C for type A clusters is 39%, while the A426 value is closer to 42%: adopting the median value the corrected virial mass

estimate for the Perseus Cluster of galaxies is $M_{\rm CV} = (10.75 \pm 3.6) \times 10^{14}\ h^{-1}\ {\rm M}_{\odot}$.

The validity of the $M_{\rm CV}$ estimate given above was checked by plotting the velocity dispersion profile $\sigma(R)$, given by the projected velocity dispersion computed using *all* galaxies inside R: the result is shown in the left panel of Figure 3.8. We confirm, using our updated radial velocity catalogue, that the Perseus Cluster has a decreasing dispersion profile, as was found by Fadda et al. (1996), and that the adopted C correction is justified. A decreasing $\sigma(R)$ profile is expected when the anisotropy parameter increases with radius, i.e. galaxies have more isotropic orbits near the centre while in the outer parts the orbits are mostly radial (Merritt 1987). The dispersion profile is therefore in agreement with a dynamical state in which a mainly relaxed cluster is surrounded by infalling galaxies which have recently become bound to the main body of the cluster.

In the right panel of Figure 3.8 the velocity dispersion is shown as a function of SDSS r–band absolute magnitude. Despite the low statistics in the faintest magnitude bin, there is a clear trend of increasing velocity dispersion with decreasing galaxy luminosity, which we interpret as evidence that dwarf and LLE galaxies in the Perseus Cluster are not part of the primordial galaxy population, but have instead only recently been accreted and have yet to reach equilibrium with the bulk of the galaxies in the cluster (Conselice et al. 2001; Penny & Conselice 2008).

Test for substructure

To check that the velocity dispersion estimates do not depend on peculiar features in the cluster, such as substructure or merging between different subclusters, we performed on the full spectroscopic sample the Dressler & Shectman (1988, hereafter DS88) test. The DS88 test for cluster substructure gives an estimate of how much the local kinematics differ from the global kinematics. For each galaxy in the sample, the quantity

$$\delta_i^2 = \left(\frac{N_{\rm nn}+1}{\sigma^2}\right)\left[(\bar{V}^i_{\rm local} - \bar{V})^2 + (\sigma^i_{\rm local} - \sigma)^2\right] \tag{3.5}$$

is computed. $N_{\rm nn}$ is the number of nearest neighbours considered in computing the local kinematics, and is usually set to 10 galaxies. $\bar{V}^i_{\rm local}$ and $\sigma^i_{\rm local}$ are the local average velocity and velocity dispersion computed for the $N_{\rm nn}+1$ galaxies (galaxy i plus its $N_{\rm nn}$ neighbours), while $\bar{V}$ and σ correspond to the global cluster average velocity and velocity dispersion (computed according to Beers et al. 1990). The global statistic $\Delta = \sum_i \delta_i$ was computed: in case of negligible substructure, the value of Δ should approach the number of galaxies N in the cluster. For the spectroscopic sample of Perseus Cluster galaxies we obtained $\Delta/N = 1.27$. The same calculation was repeated on 5000 simulated clusters, obtained by randomly shuffling the velocities between the galaxies. This step of the DS88 test is carried out to estimate the likelihood of the observed distribution having been generated by chance.

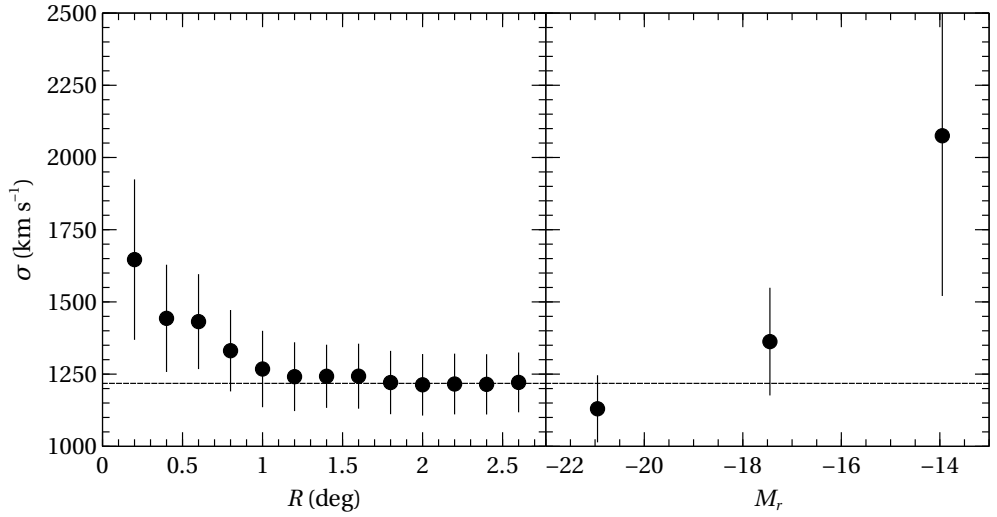

Figure 3.8: *Left panel*: Velocity dispersion profile $\sigma(R)$. *Right panel*: velocity dispersion as a function of absolute SDSS r magnitude. The dashed horizontal line marks the global $\sigma_{\rm P}$ value of the cluster.

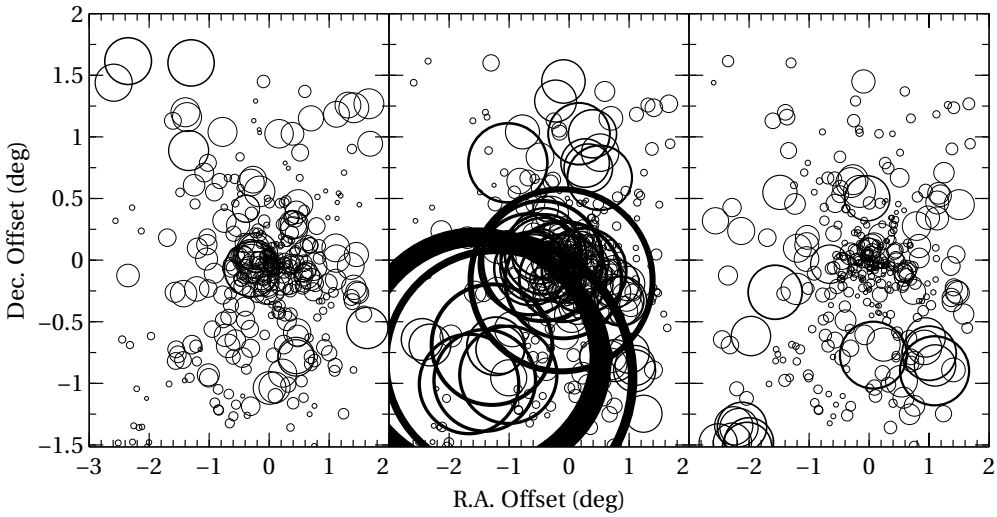

Figure 3.9: Bubble plots for the Dressler & Shectman (1988) test. *Left panel*: Observed velocity distribution. The size of each circle is proportional to e^{δ}. *Middle panel*: Velocity distribution for the simulated sample with the biggest Δ value. *Right panel:* velocity distribution for the simulated sample with Δ value closest to the median of the set of simulations.

Figure 3.9 shows the typical DS88 "bubble plot", where the size and thickness of each solid circle is proportional to e^{δ_i}, and gives therefore a measure of the deviation of the local kinematics from the global kinematics: the observed distribution (in the left panel) is more similar to the distribution for the median Δ value (right panel) with respect to the distribution with maximum deviations (middle panel). The fraction of simulations showing a higher δ value than the observed one is 0.03. We therefore conclude that there is no significant evidence for substructure in the Perseus Cluster, and that the mass estimate derived in the preceding section is not affected by an artificially high velocity dispersion caused by interacting large-scale structures.

3.3.4 Morphological classification

Together with photometric and radial velocity data, the analysis of the distribution of galaxy properties should take into account information on their morphological type. The only catalogue with explicit morphological classification is BM99, while there is no information on morphology in the SDSS database, since galaxies in the Perseus-Pisces region were not included in the Galaxy Zoo citizen science project. We therefore implemented a simple classification scheme for the galaxies in the SDSS spectroscopic catalogue based on colour and surface profile information, to divide the complete sample in two coarse morphological type bins: "early"-type and "late"-type galaxies. The $g-r$ colour was used to separate red and blue galaxies and the `fracDeV_r` parameter was employed to separate galaxies exhibiting exponential or de Vaucouleurs $r^{1/4}$ profiles: `fracDeV_r` is equal to the fraction of the de Vaucouleurs profile in a composite model fit (in the SDSS r-band) to the surface brightness profile of the source, where the assumed model is the sum of an exponential and an $r^{1/4}$ profile. In principle, both the colour of a galaxy and its surface brightness profile are directly related with its morphological type, in the sense that early-type galaxies have redder colours and radial profiles following the de Vaucouleurs law.

This correspondence was checked for the Perseus Cluster galaxies using the sample in common between the BM99 catalogue and the SDSS database. The result is shown in Figure 3.10, where the position of the galaxies is given by `fracDeV_r` on the abscissa and by the $g-r$ colour on the ordinate. Both photometric properties were taken from the SDSS database. The symbols and colours of the markers denote the morphological classification of the galaxies by BM99. The upper panel and the right panel show the histogram of the `fracDeV_r` and colour distributions for the sample. Figure 3.10 shows clearly that, assuming a perfect classification by BM99, it is not possible to clearly separate early-type from late-type galaxies based on colour or surface brightness profile information: the distributions of both $g-r$ and `fracDeV_r` are nearly identical for E/S0 and for S/SB galaxies. There are, however, differences between the two distributions: the colour histogram (right panel) shows that for $g-r \gtrsim 0.65$ the majority of galaxies

Table 3.6: Correspondence table between the adopted morphological criteria for the SDSS galaxies and the classification by BM09.

Morphology (BM99)	"Early" bin	"Late" bin	Total
Complete sample			
E/S0	84	20	104
S/SB	62	40	102
Irregular	1	5	6
Unknown	3	3	6
"Clean" sample			
E/S0	33	9	42
S/SB	26	23	49
Irregular	1	1	2
Unknown	0	1	1

is of the E/S0 type, while S/SB make up the bulk of the $g-r \lesssim 0.65$ distribution. The main contribution to the `fracDeV_r` distribution is due to late type galaxies up to `fracDeV_r`~ 0.6. We therefore adopted the following classification criterion for galaxies in the SDSS database: we labelled as early-type all galaxies with `fracDeV_r` (the fraction of de Vaucouleurs profile in the composite model fit) greater than 0.6, *and* with $g-r$ between 0.65 and 0.95. The remaining set of galaxies, which also contains anomalously red objects, was labelled as late. The applied cuts in colour and `fracDeV_r` are overlaid as dashed lines in Figure 3.10.

The difficulty to separate early from late type galaxies in the `fracDeV_r`–g–r diagram is not caused by incorrect photometry by the SDSS pipeline: Figure 3.11 shows the distribution of galaxies in the same photometric space using only the "clean" dataset. The main trends between different galaxy populations are the same as those for the complete dataset. The results of our choice of cuts for the separation of A426 galaxies are therefore largely independent of the quality of the photometry.

Table 3.6 lists the results of the applied colour and surface brightness profile cuts to the complete and clean samples of Perseus galaxies: despite the high degree of contamination, the proportion of E and S0 galaxies in the "early"-type bin is higher with respect to that of the S and SB galaxies.

Galaxies from the BM99 catalogue with no corresponding match in the SDSS catalogue were flagged as early-type if their morphological type was listed as being E or S0. Galaxies from PC08 were flagged as early dwarfs.

3.3.5 Scaling relations

The final color–magnitude diagram (CMD) and $R_{\rm e}$–magnitude relation for the spectroscopic sample of Perseus Cluster galaxies are shown in Figure 3.12. The two scaling

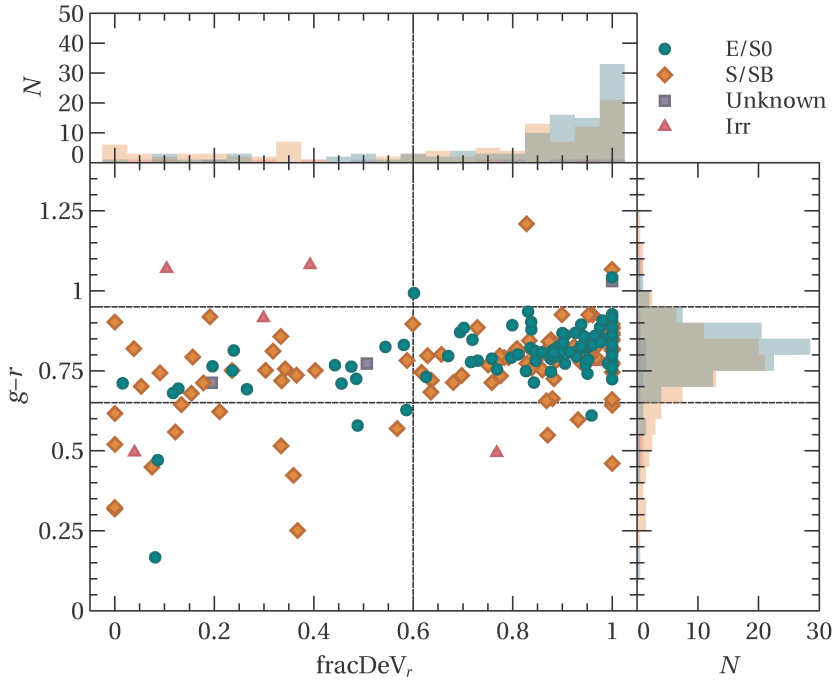

Figure 3.10: Colour-`fracDeV_r` diagram for the complete sample of galaxies in common between the BM99 and SDSS catalogues. Colour and shape of the symbols denote the classification by BM99. The histograms on the upper and right panel show the `fracDeV_r` and colour distributions for the different types of galaxies. Vertical and horizontal dashed lines represent the adopted `fracDeV_r` and colour cuts used to classify the galaxies in the SDSS database.

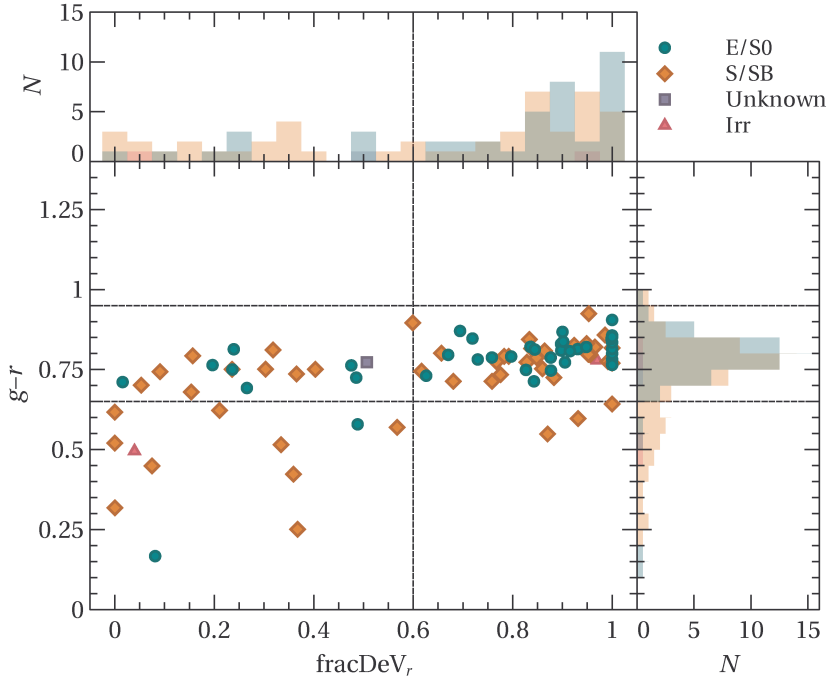

Figure 3.11: Same as Figure 3.10, showing only galaxies from the restricted sample with "clean" SDSS photometry.

relations are shown in the left column for early-type bright (black dots) and dwarf (grey triangles) galaxies. In the left column we show the same relations for late-type. Yellow filled circles represent LLE galaxies observed with the WHT and are shown, for reference, also in the right panel column of the plot without colour fill. The morphological separation follows the procedure described in the preceding section.

The overlap between the distributions of early-type and late-type galaxies in the CMD (upper panel row) is expected based on the way in which the two samples were constructed. Also the difference between the two R_e-magnitude distributions shown in the lower panels is a consequence on the cut we applied on the shape of the surface brightness profile, favouring diffuse objects in the late-type class and concentrated objects in the early-type class.

It is interesting to note that the distribution of sample LLEs selected for observations with the WHT is similar to the distribution of late-type galaxies, while it is offset from the relation between R_e and magnitude of bright ETGs. The two classes of objects may therefore not share the same evolutionary history.

A more detailed investigation of the morphologies of early-type galaxies in Perseus is currently planned and will be conducted in the near future making use of the available SDSS imaging data.

3.4 Stellar populations

Using the combined spectral database of AF2/WYFFOS and SDSS galaxies, we performed a detailed study of the stellar populations of early type galaxies in the Perseus Cluster. The spectra of all SDSS cluster members were downloaded from the SDSS bulk spectrum query web page (`http://dr12.sdss3.org/bulkSpectra`). A *spectroscopic* early type galaxy sample was created by visual inspection of the individual spectra and removing all galaxies with clear emission line features. The final SDSS spectroscopic sample subjected to the analysis of the galaxy stellar population is composed of 165 objects, of which 13 are in common with the WYFFOS galaxy sample.

The main goal of our analysis was the determination of the main SSP-equivalent stellar population parameters: as in Chapter 2, the derivation of the age and metallicity of sample galaxies was performed using two different methods: Lick indices and full spectrum fitting with ULySS.

3.4.1 Lick indices

Line strength indices were computed using the INDEXF program (Cardiel 2010). Together with each index measurement, INDEXF computes the uncertainty on the measurement and an estimate of the signal–to–noise (S/N) ratio per Å, provided the error spectrum

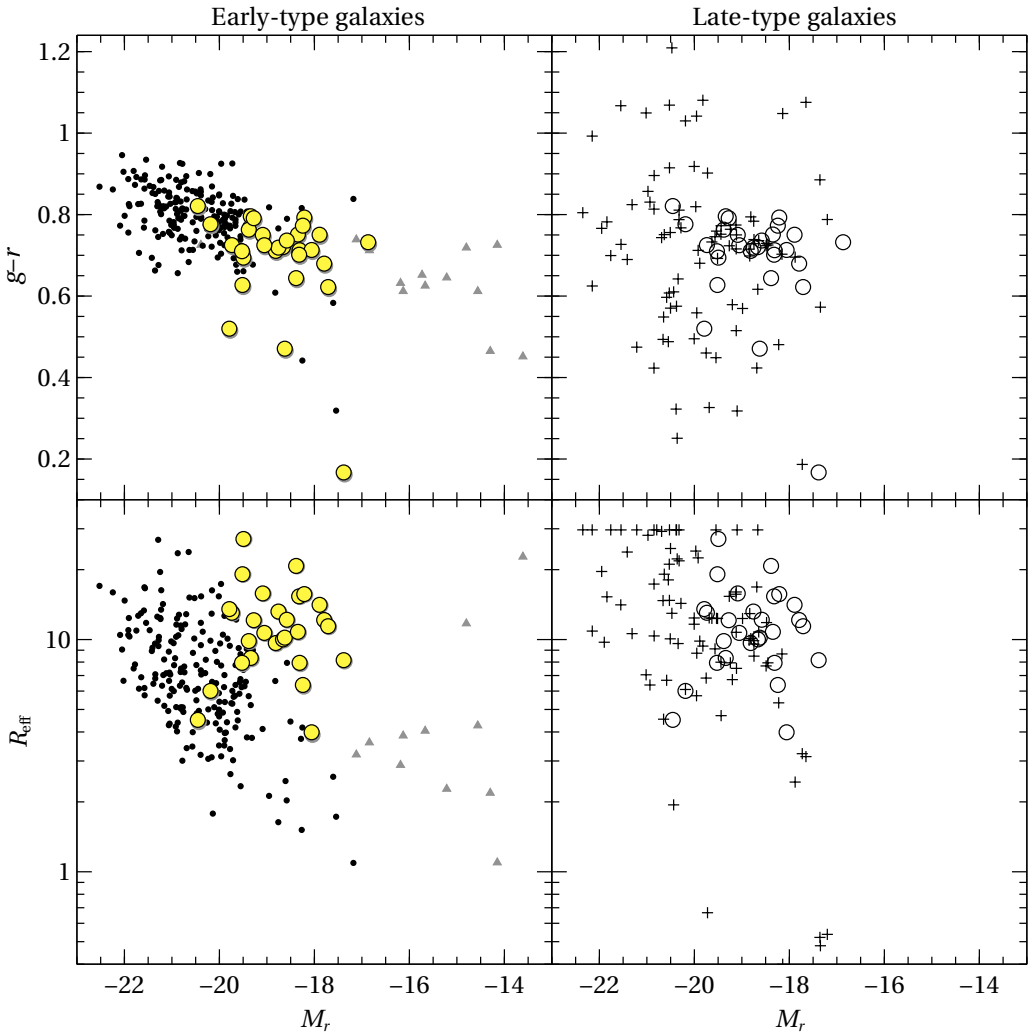

Figure 3.12: Colour–magnitude relation (*upper panels*) and R_e–magnitude relation (*lower panels*) for the Perseus confirmed cluster members. The left column shows the two scaling relations for early-type galaxies (black dots) and dE galaxies from PC08 (grey triangles). The right column shows the scaling relations for late-type galaxies. Yellow filled circles represent early-type galaxies observed with the WHT. They are shown for reference without colour fill also in the right panel column.

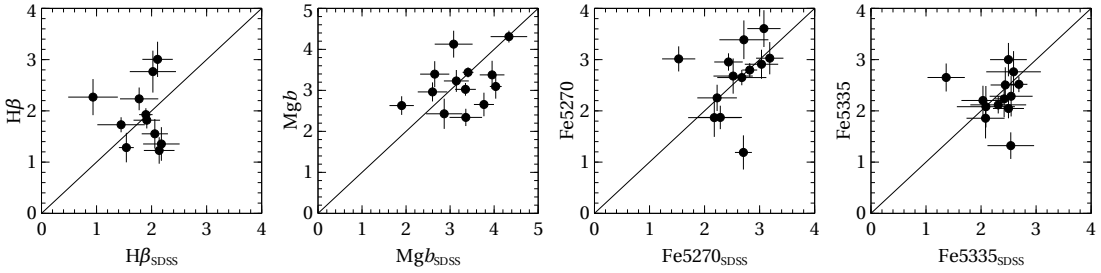

Figure 3.13: Comparison of Lick indices measurements for galaxies in common with the SDSS spectroscopic survey. The solid line in each panel represents a one-to-one relation.

is available. To obtain reliable results, we restrict our analysis only to galaxies with an average S/N greater than 20 Å^{-1} (see Table 3.3) over the range covered by the indices.

The Lick/IDS system of indices is defined for spectra taken at a FWHM $\sim$ 8 Å (Worthey & Ottaviani 1997). We did not correct WYFFOS spectra for instrumental broadening because the resolution is approximately the same across the whole wavelength range (FWHM $\sim$ 8.8 Å). Sloan spectra were instead corrected for instrumental broadening, since the SDSS spectrograph has a higher resolution ($R \sim 2000$, FWHM $\sim$ 3 Å at 6000 Å). The actual broadening was obtained by convolving a Gaussian function with variable σ at every pixel of the spectrum. The σ_λ at each wavelength λ is given by the quadratic difference between the Lick/IDS instrumental σ, as given in the Appendix of Worthey & Ottaviani 1997, and the SDSS instrumental σ, derived assuming a constant resolution $R = 2000$ across the whole wavelength range.

A consistency check was made by comparing the index measurements on AF2/WYFFOS spectra with the corresponding values obtained from the SDSS spectra for the 13 galaxies in common between the two samples. The plot is shown for the set of indices composed by Hβ, Mgb, Fe5270 and Fe5335, on which the following analysis was based. The result is shown in Figure 3.13: there is good agreement between the two sets of measurements, especially for the iron indices Fe5270 and Fe5335.

The full set of measured indices is listed in Table 3.9. The set of indices measured on the SDSS galaxies will be made available to the community when this work is published, and the complete database will be added to the CDS archives[6].

Figure 3.14 shows the $\langle\mathrm{Fe}\rangle - \mathrm{Mg}b$ and $\mathrm{H}\beta - \langle\mathrm{Fe}\rangle$ diagrams for the sample of A426 galaxies, compared with index measurements for dwarf galaxies in the same cluster (PC08) and superimposed on model grids from Thomas et al. (2003). In the $\langle\mathrm{Fe}\rangle - \mathrm{Mg}b$ diagram, the model grid is shown for a 11 Gyr SSP, while an $[\alpha/\mathrm{Fe}] = 0$ SSP is used as the reference model in the $\mathrm{H}\beta - \langle\mathrm{Fe}\rangle$ diagram. The $\langle\mathrm{Fe}\rangle - \mathrm{Mg}b$ diagram (left panel) is a commonly used diagnostic to infer the $[\alpha/\mathrm{Fe}]$ ratio of the sample galaxies. The

[6] `http://cdsweb.u-strasbg.fr/`

majority of early type galaxies in our spectroscopic sample appears consistent with solar or slightly super-solar values. The H $\beta-\langle$Fe$\rangle$ diagram (left panel) uses instead a Balmer index and the average iron index to break the age-metallicity degeneracy. The majority of early-type galaxies in the Perseus Cluster has spectral absorption features which are consistent with intermediate to old and metal poor stellar populations.

3.4.2 Full spectrum fitting

We performed full spectrum fitting on the high S/N spectra with the ULySS sofware package (Koleva et al. 2009b). The details of the method are given in Section 2.4.1; we outline in the following only important details and the steps in which the analysis differs from the one presented in the previous chapter. We fitted the galaxy spectra with SSP models from Le Borgne et al. (2004), which are based on the ELODIE 3.1 (Prugniel & Soubiran 2001; Prugniel et al. 2007) stellar library. To account for the broadening introduced by the spectrograph optics, we derived the LSF of the WYFFOS spectrograph using the observed spectrum of HR6349: we first determined the atmospheric parameters ($T_{\rm eff}$, $\log g$ and [Fe/H]) of the star using the ELODIE 3.1 model library and the ULySS "TGM" routines. We then used these parameters to extract a high-resolution spectrum of the star from the model library, and compared the two using the dedicated ULySS routines to derive the LSF. For the SDSS data, we utilized the LSF which is provided together with the ULySS package. The two LSFs were then smoothed across the wavelength range and applied to the SSP model components used in the fit.

The uncertainties on the stellar population parameters were computed through Monte Carlo simulations according to the procedure outlined in Section 2.4.2. All SSP simulation were re-run in order to account for the wider parameter range spanned by the Perseus Cluster galaxies (with respect to that of the dwarfs analysed in the previous chapter) and for the different instrumental resolution and dispersion of the WYFFOS and SDSS spectra. The parameter grid over which we ran the simulations is given in Table 3.7. For every parameter combination 300 simulations were run at both the SDSS and WYFFOS resolution. The final uncertainties were derived by inversion and interpolation as described in Section 2.4.2. The complete database ages and metallicities of the SDSS galaxies will also be made available to the community with the publication of the present work.

The final values of ages and metallicities is listed in Table 3.8. We used the spectra of the galaxies in common between the SDSS and WHT samples to performed a consistency check on the derived values of age and metallicity. The result, shown in Figure 3.15, is that we find good agreement between the two sets of measurements for both the SSP-equivalent ages and metallicities. This result serves also as an independent check on the validity of our data reduction procedure.

The distribution of metallicities is shown in Figure 3.16 as a function of the SDSS r

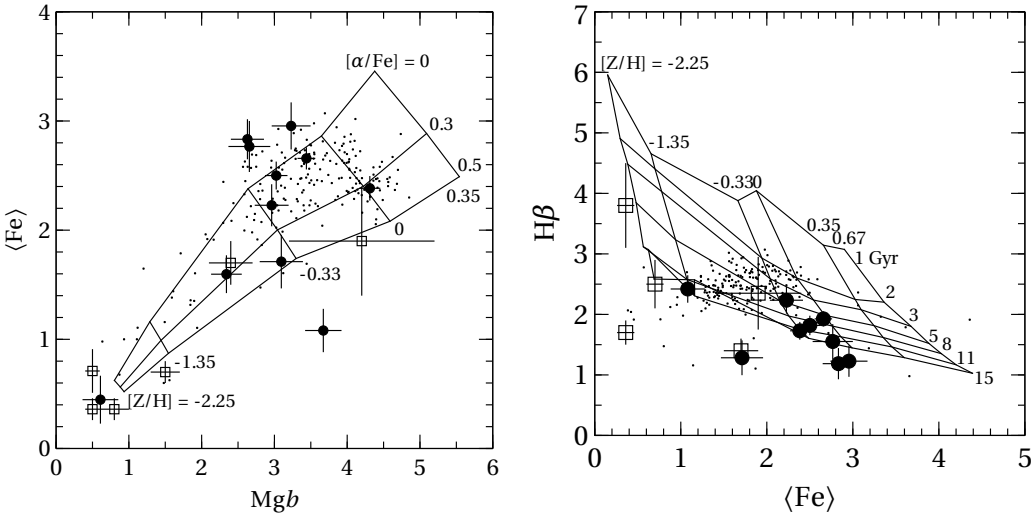

Figure 3.14: Lick index-index diagrams for the A426 sample of galaxies, shown as black filled circles. Dwarf galaxies from Penny & Conselice (2008) are shown as empty squares, while black dots represent early type galaxies from the SDSS spectroscopic sample.

Table 3.7: Parameter grid for the SSP simulations.

Parameter	Values
[Fe/H]	-1.75, -1.5, -1.25, -1, -0.75, -0.5, -0.25, 0, 0.25
$t_{\rm SSP}$ (Gyr)	1, 2.5, 5, 7.5, 10, 12.5, 15, 19.5
$\sigma_{\rm in}$ (km s^{-1})	25, 50, 100, 150, 200, 250, 300
S/N	5, 10, 15, 20, 25, 30, 35, 40, 45, 50, 55, 60

Table 3.8: M/L ratio, stellar masses, and SSP-equivalent ages and metallicities for the sample of low-luminosity early type galaxies in the Perseus Cluster observed with AF2/WYFFOS.

[BM99]ID	$\log(M_\star/L)_r$	$\log(M_\star/\mathrm{M}_\odot)$	Age (Gyr)	[Fe/H] (dex)
125	0.232 ± 0.011	9.89 ±0.02	4.95 ±0.97	-0.21 ± 0.061
139	0.381 ± 0.008	9.99 ±0.01	5.13 ±0.63	0.054 ± 0.033
146	0.25 ± 0.016	9.46 ±0.02	1.69 ±0.22	-0.404 ± 0.173
167	0.324 ± 0.01	9.71 ±0.01	10.59±2.21	-0.453 ± 0.07
170	0.306 ± 0.009	9.96 ±0.01	2.55 ±0.21	-0.225 ± 0.11
178	-0.273± 0.017	8.54 ±0.02	18.11±1.16	-1.776 ± 0.042
208	0.339 ± 0.008	10.09±0.01	5.51 ±0.84	-0.133 ± 0.054
210	0.367 ± 0.01	9.86 ±0.02	3.56 ±0.61	-0.004 ± 0.038
215	0.417 ± 0.008	10.01±0.01	5.19 ±0.52	-0.217 ± 0.04
218	0.227 ± 0.017	9.17 ±0.03	4.78 ±2.17	-0.743 ± 0.164
219	0.412 ± 0.011	9.98 ±0.02	7.78 ±1.09	-0.225 ± 0.058
227	0.114 ± 0.006	9.89 ±0.01	3.46 ±0.38	-0.469 ± 0.017
253	0.29 ± 0.018	9.26 ±0.03	5.33 ±1.76	-0.534 ± 0.159
255	0.396 ± 0.006	10.33±0.01	7.35 ±0.64	0.011 ± 0.017
256	0.339 ± 0.011	9.82 ±0.02	8.17 ±1.2	-0.205 ± 0.057
267	0.445 ± 0.005	10.48±0.01	12.17±0.77	-0.009 ± 0.023
268	0.323 ± 0.007	9.99 ±0.01	7.37 ±0.62	-0.226 ± 0.031
282	0.326 ± 0.011	9.51 ±0.02	11.02±1.81	-0.527 ± 0.046
287	0.06 ± 0.01	9.37 ±0.02	1.08 ±0.09	-0.164 ± 0.103
315	0.352 ± 0.02	9.64 ±0.03	8.28 ±3.41	-0.513 ± 0.124
333	0.368 ± 0.013	9.56 ±0.02	4.96 ±0.92	-0.101 ± 0.051
338	0.333 ± 0.013	9.69 ±0.02	8.29 ±1.19	-0.139 ± 0.06
340	0.326 ± 0.015	9.41 ±0.02	4.87 ±1.42	-0.2 ± 0.073
389	0.414 ± 0.016	9.55 ±0.02	2.85 ±0.58	0.561 ± 0.04
392	0.334 ± 0.015	9.65 ±0.02	5.15 ±1.34	0.014 ± 0.07
399	0.392 ± 0.016	9.54 ±0.02	20.0 ±0.0	-0.4 ± 0.031

Table 3.9: Lick/IDS indices for the AF2/WYFFOS sample of galaxies. The first and second data rows for each galaxy correspond, respectively, to the index value and the 1–σ errors.

ID	Ca4227	G4300	HγA	HγF	Fe4383	Ca4455	Fe4531	Hβ	Fe5015	Mgb	Fe5270	Fe5335	Fe5406	$\langle Fe \rangle$	[MgFe]$'$
139	0.91	4.91	-4.52	-0.22	5.10	0.69	2.43	1.23	3.96	3.23	2.91	3.00	1.53	2.95	3.08
	0.29	0.48	0.53	0.31	0.60	0.32	0.44	0.26	0.52	0.27	0.28	0.33	0.24	0.22	0.17
210	0.55	5.62	-4.14	-0.23	6.28	1.36	3.99	1.55	5.34	2.66	3.03	2.51	1.31	2.77	2.77
	0.29	0.46	0.53	0.32	0.57	0.32	0.45	0.29	0.57	0.29	0.31	0.35	0.27	0.23	0.19
215	1.19	2.93	-4.19	-0.91	4.03	0.20	2.67	2.23	5.17	2.96	2.25	2.20	1.24	2.23	2.58
	0.23	0.43	0.44	0.27	0.52	0.27	0.39	0.22	0.48	0.23	0.26	0.29	0.21	0.19	0.15
227	0.08	2.97	-0.89	0.29	2.10	1.25	1.95	-1.77	2.63	2.34	1.87	1.32	0.38	1.60	2.01
	0.26	0.46	0.44	0.27	0.57	0.28	0.41	0.24	0.44	0.21	0.23	0.26	0.20	0.17	0.14
255	1.18	4.90	-4.75	-1.24	4.02	1.13	3.53	1.93	3.66	3.44	2.80	2.52	2.54	2.66	3.06
	0.13	0.22	0.25	0.15	0.29	0.14	0.21	0.13	0.26	0.12	0.13	0.15	0.14	0.10	0.08
267	1.56	5.26	-5.41	-1.61	3.98	1.56	2.43	1.73	4.11	4.31	2.65	2.12	1.56	2.38	3.28
	0.18	0.30	0.34	0.21	0.39	0.19	0.27	0.15	0.30	0.14	0.15	0.17	0.12	0.11	0.09
282	3.41	4.95	-2.73	1.28	-1.73	0.53	5.18	1.19	1.09	2.63	3.01	2.65	0.45	2.83	2.77
	0.19	0.41	0.44	0.25	0.61	0.30	0.37	0.26	0.50	0.23	0.24	0.27	0.22	0.18	0.15
317	0.26	7.09	-7.23	-2.53	3.88	-1.00	1.62	2.42	-0.29	3.67	1.28	0.88	2.21	1.08	2.07
	0.21	0.24	0.30	0.17	0.35	0.22	0.30	0.23	0.47	0.25	0.27	0.29	0.23	0.20	0.20
219	0.16	6.17	-5.57	-0.93	6.11	-0.36	3.03	1.28	2.53	3.09	1.19	2.23	1.70	1.71	2.14
	0.29	0.45	0.54	0.32	0.59	0.33	0.47	0.29	0.62	0.30	0.33	0.36	0.27	0.25	0.21
268	3.46	4.38	-3.31	0.35	0.68	0.78	3.91	1.82	2.51	3.02	2.95	2.05	1.23	2.50	2.86
	0.12	0.27	0.28	0.17	0.38	0.18	0.25	0.16	0.32	0.15	0.17	0.19	0.15	0.13	0.10
183	0.56	0.00	1.27	0.94	0.01	0.15	1.16	-1.56	-1.12	0.61	0.48	0.41	-0.12	0.45	0.53
	0.15	0.30	0.27	0.17	0.44	0.24	0.33	0.22	0.47	0.25	0.29	0.33	0.25	0.22	0.17

magnitude (left panel) and the stellar mass $M_\star$ (right panel) derived using the relations based on optical colours by Bell et al. (2003). We derived an analytical expression for the "mass–metallicity" relation for the early type galaxy population in the Perseus Cluster by performing a linear fit to the data points, using the ODRPACK orthogonal distance regression software (Boggs et al. 1989). The linear fits to the relations are

$$\begin{aligned} [\mathrm{Z/H}] &= (-0.118 \pm 0.012) M_r - (2.4 \pm 0.2) \\ [\mathrm{Z/H}] &= (0.34 \pm 0.26) \log(M_\star/\mathrm{M}_\odot) - (3.54 \pm 0.27) \ . \end{aligned} \tag{3.6}$$

We confirm the presence of a very tight correlation of the measured metallicity with the galaxy luminosity and stellar mass for the early-type galaxy population in the Perseus Cluster. In order assess the influence of the environment on the galaxy population, we will investigate in a forthcoming work the dependence of the stellar population parameters on the morphological type and on the position within the cluster, to check for the presence of the radial trends in the cluster dwarf population which characterise other nearby clusters (Smith et al. 2009).

3.5 Summary and conclusions

In this chapter, we analysed spectroscopic data from a large sample of LLE galaxies in the Perseus Cluster, to determine the origin of the dwarf galaxy population.

Combining our radial velocities with published and archived data, we analysed the velocity dispersion of the galaxy population as a function of galaxy magnitude. We confirmed the presence of higher velocity dispersion of the faint galaxies with respect to the luminous ones, in agreement with the findings by Penny & Conselice (2008). We used the three-fold increase in radial velocities of our updated database to compute a more precise estimate of the cluster velocity dispersion inside the virial radius of the cluster. The derived value of σ_P is slightly higher than previous estimates (G98) but agrees within the quoted uncertainties. We used the updated values of velocity dispersion and virial radius to compute an estimate of the optical mass of Abell 426, which is also found slightly higher than previous estimates (G98), but consistent within the errors. We verify the validity of our mass estimate by confirming the absence of significant substructure in the cluster.

By analysing the velocity dispersion profile as a function of magnitude, we confirm that the faint galaxy population possesses a higher velocity dispersion with respect to bright galaxies, supporting a scenario in which dE galaxies come from an external late-type galaxy population which has been accreted by the cluster only recently, and has yet to reach equilibrium with the cluster potential.

We performed full-spectrum fitting measurements on our spectra and on all SDSS spectra of early-type galaxies to derive estimates of the ages and metallicities of the

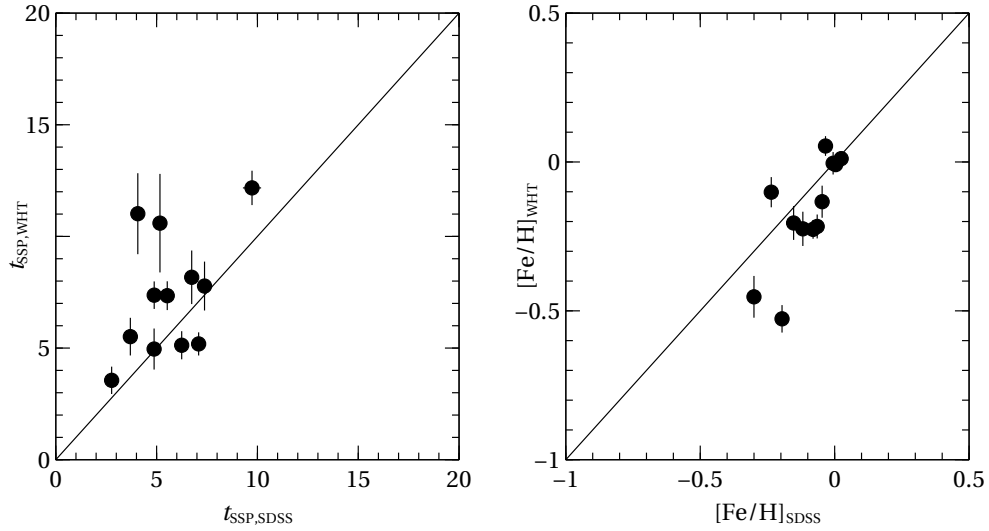

Figure 3.15: Comparison of SSP-equivalent ages (*left panel*) and metallicities (*right panel*), between ULySS measurements performed on SDSS spectra (x-axes) and WHT spectra (y-axes).

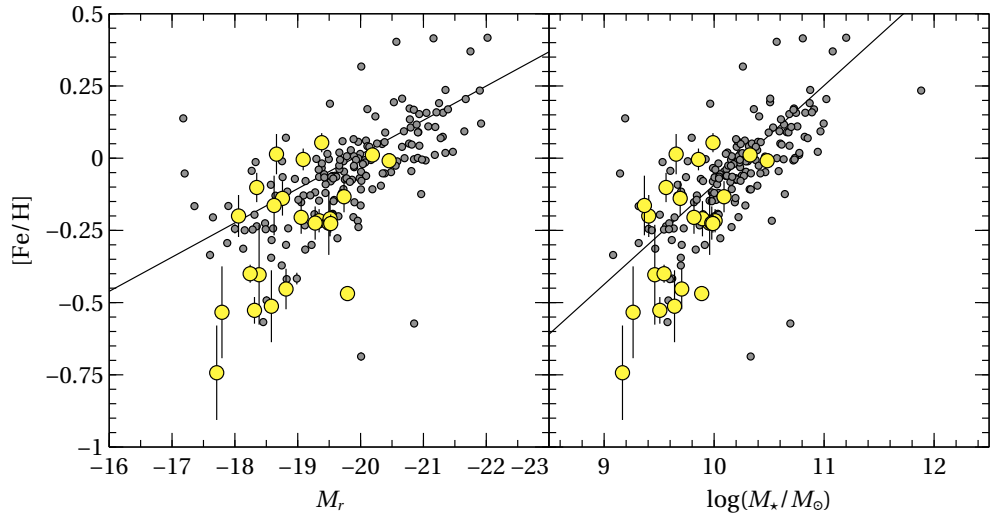

Figure 3.16: Metallicity scaling relations for Perseus early type galaxies. The [Fe/H] ratio is shown as a function of r-band magnitude (*left panel*) and log of the stellar mass (*right panel*). Yellow filled circles correspond to the low luminosity sample spectra from AF2/WYFFOS, while gray filled circles correspond to SDSS spectroscopic data.

galaxy stellar populations, which we used to derive the first estimate of the mass-metallicity relation of the Perseus Cluster. We also measured on all the spectra the line-strength index in the Lick system.

Future planned work will focus on a more detailed analysis of the SDSS photometry aimed at the derivation of correct structural parameters of faint galaxies. The primary goal will be to construct cleaner samples of dE galaxies, separated by morphology, in order to investigate the presence of radial trends in the stellar population. The analysis will also be used to investigate the different spatial and redshift distribution of the various dE classes (see, e.g., Lisker et al. 2007).

Chapter 4

Bulges of isolated disc galaxies

Abstract

We present photometry and long-slit spectroscopy for 12 S0 and spiral galaxies selected from the Catalogue of Isolated Galaxies. The structural parameters of the sample galaxies were derived from the Sloan Digital Sky Survey r-band images by performing a two-dimensional photometric decomposition of the surface brightness distribution. This was assumed to be the sum of the contribution of a Sérsic bulge, a Freeman disc, and a Ferrers bar characterized by elliptical and concentric isophotes with constant ellipticity and position angles. The rotation curves and velocity dispersion profiles of the stellar component were measured from the spectra obtained along the major axis of galaxies. The radial profiles of the Hβ, Mg and Fe line-strength indices were derived too. Correlations between the central values of Mg_2, $\langle\mathrm{Fe}\rangle$, H$\beta$ and velocity dispersion were found. The age, metallicity and [α/Fe] enhancement of the stellar population in the center and at the radius where bulge and disc give the same contribution to the total surface brightness were obtained using stellar population models with variable element abundance ratios. Two classes of bulges are identified: the intermediate-age bulges ($\sim$ 3 Gyr) with solar metallicity and old bulges ($\sim$ 15 Gyr) with a large spread in metallicity. Most of the sample bulges display super-solar [α/Fe] enhancement, no gradient in age and negative gradients of metallicity and [α/Fe] enhancement. These findings support a formation scenario via dissipative collapse where environmental effects are remarkably less important than in the assembly of bulges of galaxies in groups and clusters.

4.1 Introduction

Stellar populations are a powerful diagnostics to constrain the assembly history of galaxy bulges. In the current picture, dissipative collapse (e.g., Gilmore & Wyse 1998), merging and acquisition events (e.g., Cole et al. 2000), and secular evolution (e.g., Kormendy & Kennicutt 2004) are considered as possible processes driving the formation of bulges. According to theoretical models, these processes give rise to different properties of the stellar populations in galaxy centres and different trends of age, metallicity, and star-formation timescale as a function of the galactocentric distance.

For example, the metallicity gradients are a measurement of the amount and duration of gas dissipation and contain information concerning the importance of interactions and secular processes. Stars form at all galactocentric distances during the dissipative collapse of a protogalactic cloud and they remain on their orbits with little migration towards the centre. On the contrary, the gas dissipates inward and it is continuously enriched by the evolving stars. In this way, the stars formed in the central region of a galaxy are predicted to be more metal-rich than those born in its outskirts. Supernova-driven galactic winds (Arimoto & Yoshii 1987) start when the energy injected into the interstellar medium by supernovae matches the galaxy binding energy. These winds eliminate the gas suppressing the fuel needed for star formation. The outer regions develop the winds before the central ones, where the star formation and chemical enrichment continue for a longer time. Strong negative gradients are expected in dissipative collapse models as both star formation and galactic winds act in steepening any incipient gradient. In hierarchical formation models, the situation is somewhat contradictory. Some authors suggest that clustering and merging erase the metallicity gradient (e.g., Bekki & Shioya 1999), while others argue that the metallicity gradient is moderately affected by interactions since the violent relaxation preserves the position of the stars in the local potential (e.g., van Albada 1982). Such a dichotomy possibly depends on how the properties of the resulting galaxy are related to the gas-to-stellar mass ratio of the progenitors. If they are characterized by a large gas fraction, the resulting metallicity gradient is indeed steeper. The predictions for bulges slowly formed through dissipationless secular processes are even more contradictory. In this scenario the bulge is formed by the redistribution of the disc stars due to the instabilities triggered by bars, ovals, and spiral arms. The metallicity gradient could be either amplified since the resulting bulge has a smaller scalelength than the disc or erased as a consequence of disc heating (Moorthy & Holtzman 2006).

In the last decade, a major observational effort was performed to derive the stellar population properties in large number of bulges (e.g., Jablonka et al. 2007; Morelli et al. 2008, 2012; González Delgado et al. 2014; Seidel et al. 2015; Wilkinson et al. 2015) to be compared to those of elliptical galaxies (e.g., Sánchez-Blázquez et al. 2006; Annibali et al. 2007; Kuntschner et al. 2010; McDermid et al. 2015) and galaxy discs (Sánchez-Blázquez

et al. 2014; Morelli et al. 2015b).

Stellar populations of bulges show a complex variety of properties. Bulges ages are spread between 1 and 15 Gyr. Such a large difference seems to be driven by the morphological type of the host galaxy (Ganda et al. 2007). The timescale of the last major star-formation burst spans between 1 to 5 Gyr, as derived from the central values of α/Fe abundance ratio (Thomas & Davies 2006). In general, α/Fe is constant over the observed radial ranges and many bulges have a solar abundance ratio (Jablonka et al. 2007; Morelli et al. 2008, 2012). Independently of their structural properties and whether they reside in low or high surface-brightness discs, most bulges are characterised by a negative metallicity gradient, which is one of the tighter predictions made by theoretical models for the dissipative collapse (Gilmore & Wyse 1998; Pipino et al. 2010). On the other hand, the absence of stellar population gradients measured in some bulges is an clear indication that bulge stars were redistributed as a consequence of external and internal processes, like minor mergers and slow rearrangement of the disc material, respectively (Bekki & Shioya 1999; Kobayashi 2004).

In many cases the difficulty in determining the mechanism driving the assembly history of the bulge is probably due to the fact that the dissipative collapse, minor and major mergers, and secular evolution are all having an effect in reshaping the structure of disc galaxies. Furthermore, phenomena driven by the environment like gas stripping, harassment, and strangulation are likely to play a role in mixing up the properties of the stellar populations (La Barbera et al. 2014). However, to date the observational evidences on how the environment influences the stellar populations of bulges are sparse and the analysis of both the central values of age, metallicity, and star formation timescale (Denicoló et al. 2005; Reda et al. 2007) and their radial gradients (Katkov et al. 2015) does not lead to any firm conclusion. In addition, the comparison of the results obtained for galaxies in different environments is not straightforward. Part of the difficulty lies in addressing the relative importance of one-to-one interactions and the local galaxy density, and this reflects the lack of suitable control samples to which the properties of bulges of interacting and/or cluster galaxies can be compared. As a matter of fact, the samples of field galaxies studied so far include also galaxies in pairs and loose groups.

A way to make simpler the observational picture is studying the bulges of isolated galaxies, for which the interactions with the surrounding environment or with other galaxies are likely to be negligible. Therefore, it could be possible to use the stellar population diagnotics to disentangle between bulges formed from dissipative collapse and those assembled via secular evolution. To this aim, here we analyse the stellar populations of the bulges of a carefully selected sample of high surface-brightness isolated disc galaxies to be compared with the complementary samples of bulges in high surface-brightness cluster galaxies and giant low surface-brightness galaxies which we studied in in the past several years (Pizzella et al. 2008; Morelli et al. 2008, 2012, 2015a).

The chapter is organized as follows. The selection of the isolated galaxy sample is described in Section 4.2. Sections 4.3 and 4.4 describe the analysis of the photometric and spectroscopic data, respectively. In Section 4.5 we describe the analysis of the stellar populations of the sample bulges and in Section 4.6 we conclude and summarize our main results.

4.2 Galaxy sample

Late-type galaxies in the sample were selected from the Catalogue of Isolated galaxies (CIG, Karachentseva 1973), which comprises 1051 galaxies. The criterion adopted by the CIG catalogue is that no other galaxy with diameter d (with $1/4D < d < 4D$, where D is the diameter of the CIG galaxy) should lie within $20d$ of the selected galaxy. Assuming an average diameter ($D = 20$ kpc) and field velocity ($V = 150$ km s^{-1}), the selected CIG galaxy should not have passed close to a mass perturber in the last 3×10^9 years.

The CIG catalogue was mined to find galaxies following four requirements:

1. having declination $\delta < 50°$
2. covering the Hubble sequence from S0 to Sbc, in order to resolve the bulge
3. possesing a moderate inclination ($i < 70°$)
4. being inside a local volume of 100 Mpc

These constraints restrict the CIG to 22 galaxies, of which 6 were discarded because they lie outside the photometry footprint of the Sloan Digital Sky Survey (SDSS). Of the remaining 16 galaxies, 12 were observed in the follow-up spectroscopic observing run, and therefore constitute the main sample under study. Their basic properties are listed in Table 4.1. Figure 4.1 shows a colour-composite image for each galaxy, taken from the SDSS Finding Chart service.

4.3 Photometry

In order to derive meaningful parameters regarding the stellar population of bulges, it is necessary that the various galactic components (bulge, disc and possibly a bar) are clearly separated, i.e. that the regions where the light from each component component dominates over the others is clearly defined. Early approaches to "bulge-disc decomposition" (Kormendy 1977) involved fitting ellipses to galaxy isophotes, and deriving structural parameters by fitting the one-dimensional surface brightness profile. The 1D approach has the advantage that it is relatively insensitive to localized features in the

Table 4.1: Parameters of the sample galaxies. The columns show the following. Column (2): morphological classification from Lyon Extragalactic Database (LEDA); column (3): numerical morphological type from LEDA. The typical error on T is 1.0; column (4): apparent isophotal diameters measured at a surface-brightness level of $\mu_B = 25$ mag arcsec^{-2} from LEDA; column (5): total observed blue magnitude from LEDA; column (6): radial velocity with respect to the CMB reference frame from LEDA; column (7): distance obtained as $V_{\rm CMB}/H_0$ with $H_0 = 75$ km s^{-1} Mpc^{-1}; column (8): absolute total blue magnitude from B_T corrected for extinction as in LEDA and adopting D;

Galaxy	Type	T	$D_{25} \times d_{25}$ (arcmin)	$B_{\rm T}$ (mag)	$V_{\rm CMB}$ (km s^{-1})	D (Mpc)	$M_{B_{\rm T}}$ (mag)
(1)	(2)	(3)	(4)	(5)	(6)	(7)	(8)
CGCG 034-050	Sb	1.0	0.95×0.52	14.53	3808	50.7	-18.99
CGCG 088-060	S0a	0.0	0.83×0.67	15.21	4725	63.0	-18.79
CGCG 152-078	E/S0	-2.8	0.48×0.47	15.81	6227	83.0	-18.78
CGCG 206-038	S0a	-0.5	0.81×0.69	14.86	6103	81.3	-19.69
IC 2473	Sbc	3.5	1.07×0.74	14.72	8325	111.0	-20.50
NGC 2503	Sbc	4.0	0.95×0.79	14.80	5711	76.1	-19.61
NGC 2712	SBb	3.1	2.95×1.58	12.78	2001	26.7	-19.35
NGC 2955	SABb	3.2	1.50×0.82	13.58	7254	96.7	-21.34
UGC 4000	SABb	2.9	1.44×0.46	14.88	9491	126.5	-20.63
UGC 4341	S0a	-0.1	1.17×0.59	14.66	6081	81.1	-19.88
UGC 5026	S0	-2.0	0.91×0.62	14.30	4480	59.7	-19.57
UGC 5184	Sb	3.0	1.02×0.65	14.73	6806	90.7	-20.05

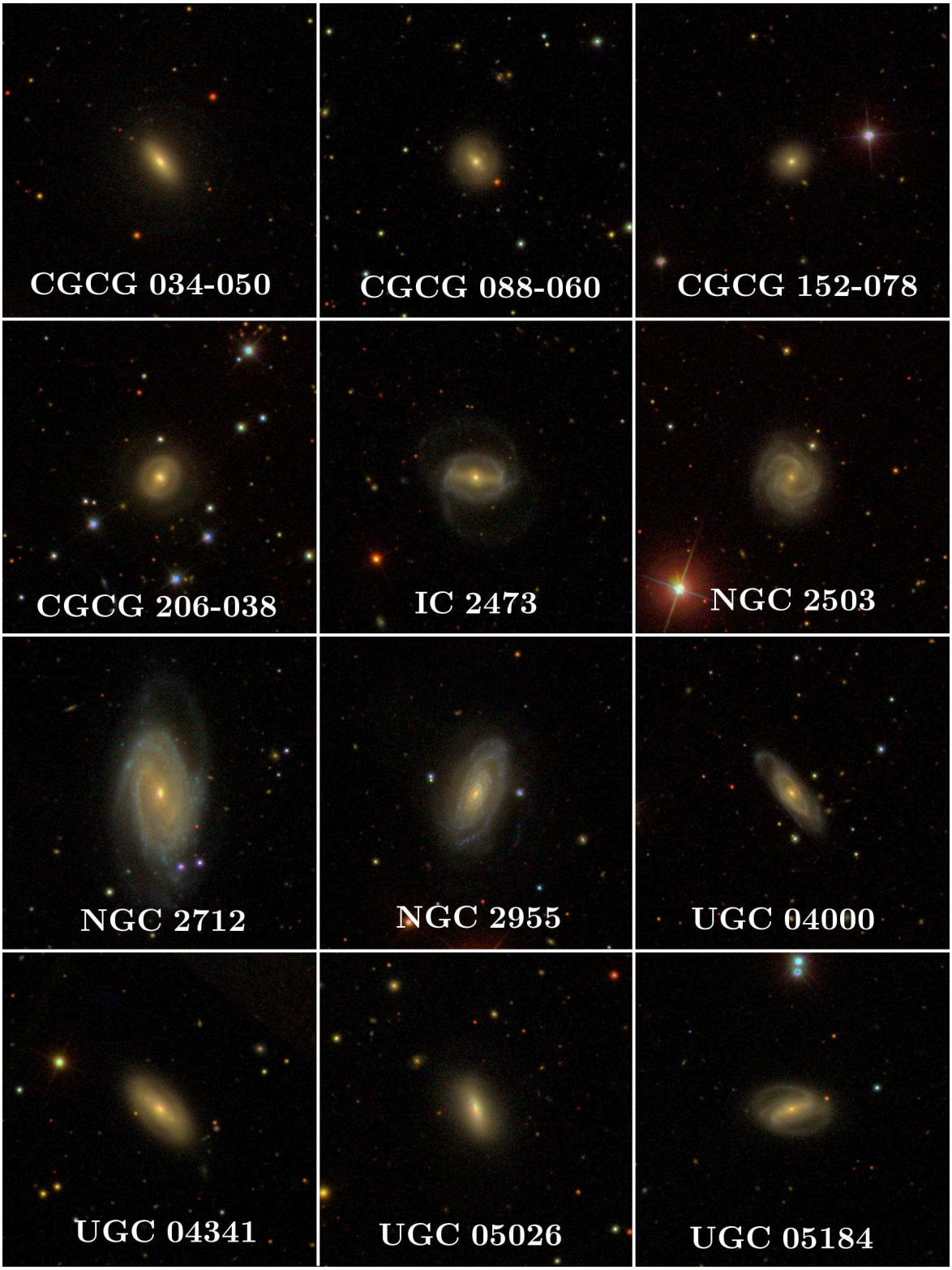

Figure 4.1: Color images of the isolated galaxies in the sample, taken from the SDSS Finding Chart service (`http://skyserver.sdss.org/dr12/en/tools/chart/chartinfo.aspx`). Each cutout is $\sim$ 4 arcmin on the side. North is up and East is left.

galaxy light distribution, because one is averaging over an entire elliptical annular region. It has, however, been shown (Byun & Freeman 1995) to provide non-unique decompositions, and it is unable to recover large scale peculiar features, such as isophote twists and ellipticity changes as a function of radius. Performing the decomposition in pixel space directly in two dimensions, it is instead possible to take advantage of these same features to break the degeneracies between the various combinations of parameters (Peng et al. 2002), and for this reason almost all recent work on the structural parameters of galaxies employs 2D algorithms. Example codes which perform 2D structural decomposition are GIM2D (Simard 1998), GASPHOT (Pignatelli et al. 2006) and GALFIT (Peng et al. 2002). Each code employs different algorithms and has its strengths and limitations (the interested reader should consult the appropriate reference) but we chose to employ the Galaxy Surface Photometry Two-Dimensional Decomposition code (GASP2D, Méndez-Abreu et al. 2008) because of its ease of use and because of the small requirement of input guess parameters (which can be very important in some minimization algorithms) by the user.

4.3.1 SDSS imaging data

Imaging data for the sample galaxies was obtained from the SDSS (York et al. 2000), by inserting galaxy names in the Data Release 12 (DR12) Bulk Imaging Search web service[1]. The primary and most updated reference for all SDSS-related data and algorithms is the DR12 website (`http://www.sdss.org/dr12`).To perform bulge-disc decompositions I employed images acquired through the i filter: light emitted in the red i band is a better tracer of the stellar mass in galaxies (which is dominated by old stars), and especially of their spheroidal component (Humason et al. 1956). An example i–band frame is shown in Figure 4.2.

SDSS images are FITS files composed of four extensions:

1. The 2048×1489 sky-subtracted image I, with pixel intensities given in nanomaggies. A maggy is the flux f of the source relative to the standard source f_0 (which defines the zeropoint of the magnitude scale). The standard source for each SDSS band is close to but not exactly the AB source (3631 Jy), meaning that a nanomaggy is approximately 3.631×10^{-6} Jy;

2. a 2048 px 1D calibration array c, to convert nanomaggies back to DN (data number) counts;

3. FITS binary table with data (a 256×192 array s, and two interpolation arrays for the x and y direction) to derive the sky image subtracted to the original calibrated frame;

[1] `http://dr12.sdss3.org/bulkFields`

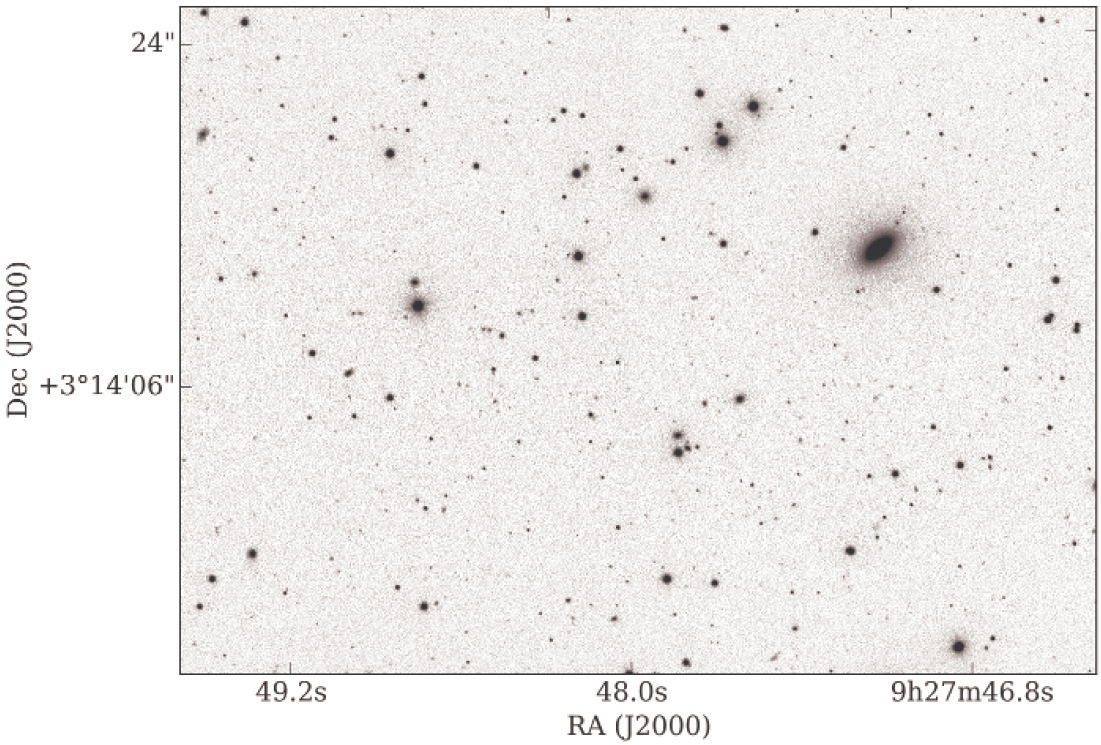

Figure 4.2: SDSS i–band image for CGCG 034-050.

4. table with astrometric and observing metadata.

In order to use correct Poissonian noise estimates and sky background in the calculation of the galaxies structural parameters, I converted the sky subtracted image back to DN by dividing the image I by the calibration image C obtained by replicating the c array along the 1489 rows. The sky image S was obtained by bilinear interpolation of the s image on the values defined by the x and y arrays in the third FITS extension. In this phase, I derived for each galaxy the magnitude and surface brightness μ zeropoints[2]:

$$\begin{aligned} \mathrm{ZP}_{\mathrm{mag}} &= 22.5 - 2.5 \log \bar{C} \ , \\ \mathrm{ZP}_{\mu} &= 22.5 - 2.5 \log \bar{C} + \log 0.396127 \ , \end{aligned} \tag{4.1}$$

where $\bar{C}$ is the mean of the calibration image C, and 0.396127 is the SDSS CCD pixel scale, in arcsec. The average value of the sky image ($\bar{S}$) was also saved for the following analysis. The images I/C image was rotated to align the y image axis with the North–South direction (using the `SPA` FITS header keyword) and a 601×601 px frame was cut around the galaxy centre.

4.3.2 Bulge–disc decomposition: the code

GASP2D is an IDL code that fits the two-dimensional surface brightness distribution of a galaxy with a photometric model using a the MPFIT implementation (Markwardt 2009) of the Levenberq-Marquardt algorithm for non-linear least-square minimization (Moré 1978).

The photometric model we adopted for the spiral galaxies in our sample is given by the sum of a bulge component, a disc component and an optional bar component. Every component is a function of the generalized elliptical isophote radius r_{cmp} (cmp = 'b' for the bulge, 'd' for the disc and 'bar' for the bar) defined as

$$\begin{aligned} r_{\mathrm{cmp}} = \Big[& (-(\xi - \xi_0) \sin \mathrm{PA}_{\mathrm{cmp}} + (\eta - \eta_0) \cos \mathrm{PA}_{\mathrm{cmp}})^{(2+c)} \\ & - ((\xi - \xi_0) \cos \mathrm{PA}_{\mathrm{cmp}} + (\eta - \eta_0) \sin \mathrm{PA}_{\mathrm{cmp}})^{(2+c)} / q_{\mathrm{cmp}}^{2+c} \Big]^{1/(2+c)} \ , \end{aligned} \tag{4.2}$$

where ξ and η correspond to the physical (i.e., pixel) coordinates, aligned with right ascension and declination, of the galaxy image on the plane of the sky, and (ξ_0, η_0) is the position of the galaxy centre. $\mathrm{PA}_{\mathrm{cmp}}$ is the ellipse position angle with respect to the north–south direction and q_{cmp} is the constant minor-to-major axis ratio of the ellipse (the ellipticity e_{cmp} is equal to $1 - q_{\mathrm{cmp}}$). The parameter c regulates the shape of the isophotes: $c = 0$ corresponds to a perfect ellipse while the the isophotes appear boxy and discy, respectively, for $c > 0$ and $c < 0$: in this sense, the c parameter serves the same

[2] `http://www.sdss.org/dr12/algorithms/magnitudes/`

purpose as the $\cos 4\theta$ Fourier coefficient commonly employed in isophote fitting. Perfect ellipses ($c = 0$) are hard-coded in GASP2D for the bulge and disc components, while the generalized form is used for bars, in order to account for the variety in possible shapes. The analytic expressions for the three components are:

Bulge: The bulge component is defined a Sérsic (1968) law, which is the most widely used parametrization for the surface brightness distribution in spheroids (Graham & Guzmán 2003):

$$I_{\rm b}(r_{\rm b}) = I_{\rm e} 10^{-b_n[(r_{\rm b}/r_{\rm e})^{1/n}-1]} \ , \tag{4.3}$$

where $r_{\rm e}$ is the effective radius (i.e., the radius inside which one half of the total light is emitted), $I_{\rm e}$ is the surface brightness at $r_{\rm e}$ and n is the shape parameter describing the curvature of the surface brightness profile. The value of b_n can be derived numerically (Ciotti & Bertin 1999; Graham & Driver 2005) and is approximated by the relation $b_n = 0.868n - 0.142$ (Caon et al. 1993).

Disc: The disc follows the Freeman (1970) exponential law:

$$I_{\rm d} = I_0 {\rm e}^{-r_{\rm d}/h} \ , \tag{4.4}$$

where h is the disc scale length (i.e., the length over which the surface brightness drops by a factor of e) and I_0 is the surface brightness at $r = 0$.

Bar: The bar follows the projected surface density of a three-dimensional Ferrers ellipsoid (Ferrers 1877)

$$I_{\rm bar} = I_{0,\rm bar} \left[1 - \left(\frac{r_{\rm bar}}{a_{\rm bar}} \right)^2 \right]^{(n_{\rm bar}+1/2)} \ , \tag{4.5}$$

Here $I_{0,\rm bar}$, $a_{\rm bar}$ and $n_{\rm bar}$ denote, the central surface brightness, length and shape parameter of the bar, respectively.

Other models, such as a point source (i.e., a PSF model) and King profiles are available in GASP2D, but were not employed in the current study. Apart from the ellipse shape parameter for the bulge and disc, all other parameters in the model are variable and can be fixed or used in the fitting through appropriate switches in the program input files: variable parameters include therefore the model centre coordinates (ξ_0 and η_0), which are assumed to be the same for all components, q and PA for every component, the $c_{\rm bar}$ shape parameter, and the full set of surface brightness profile parameters for every component ($I_{\rm e}$, $r_{\rm e}$, n, I_0, h and optionally $I_{0,\rm bar}$, $a_{\rm bar}$, and $n_{\rm bar}$). The choice on whether to keep a parameter fixed or not may depend on the type of analysis at hand: for example, in some complicated models, especially those with a bar, fixing some

parameters or placing tighter constraints on the allowed value ranges may help the fitting algorithm in avoiding spurious minima or unphysical models. Throughout our analysis the parameters which were left free to vary were ξ_0, η_0 and all geometrical and surface brightness parameters of the bulge and disc components. For the bar components, when needed, $\mathrm{PA_{bar}}$ and a_{bar} and $I_{0,\mathrm{bar}}$ were left as fit parameters while c and n_{bar} were kept fixed. Exceptions to the above settings will be noted in the appropriate section for each galaxy.

The intensity, in photon counts, of the galaxy model I_{m} is then given at each pixel (ξ, η) by the sum of all single components:

$$I_{\mathrm{m}}(\xi,\eta) = I_{\mathrm{b}}(\xi,\eta) + I_{\mathrm{d}}(\xi,\eta) \tag{4.6}$$

for models without a bar and

$$I_{\mathrm{m}}(\xi,\eta) = I_{\mathrm{b}}(\xi,\eta) + I_{\mathrm{d}}(\xi,\eta) + I_{\mathrm{bar}}(\xi,\eta) \tag{4.7}$$

for models with a bar. The model is then compared to observed galaxy image I_{g}, weighting each pixel with the variance of its total observed photon counts due to the contribution of both galaxy abd sky. The variance is computed assuming photon noise limitation by taking into account the detector readout noise (RON). The χ^2 evaluated by the minimization algorithm is therefore

$$\chi^2 = \sum_{\xi=1}^{N}\sum_{\eta=1}^{M} \frac{[I_{\mathrm{m}}(\xi,\eta) - I_{\mathrm{g}}(\xi,\eta)]^2}{I_{\mathrm{g}}(\xi,\eta) + I_{\mathrm{s}}(\xi,\eta) + \mathrm{RON}^2} \ , \tag{4.8}$$

where N and M are the width and height, in pixels, of the galaxy image. The presence of foreground stars or macroscopic CCD defects may be dealt with by providing an appropriate pixel mask to the code, and masked pixels were not be used in the fit. The χ^2 is determined using only pixels inside a maximum fitting radius which can be fixed by the user either directly or in a parametric form.

Seeing effects, which are critical to model correctly the central regions of galaxies, are taken into account by performing a convolution in Fourier space of the model image with a two-dimensional PSF given by a Moffat (1969) distribution:

$$f(r,\alpha,\beta) = \frac{\beta-1}{2\alpha\pi}\left[1+\left(\frac{r}{\alpha}\right)^2\right]^{-\beta} \ , \tag{4.9}$$

where α is related to the seeing FWHM, as:

$$\alpha = \frac{\mathrm{FWHM}}{2\sqrt{2^{1/\beta}-1}} \ ,$$

and β is a parameter of the distribution.

A key step in non-linear least-squares minimization algorithms is creating a set of initial guesses for the parameters used in the fitting. GASP2D with respect to other 2D decomposition codes, generates automatically a set of reasonable initial parameters by interacting with the IRAF task ELLIPSE. ELLIPSE can be run either manually by the user or directly by the IDL code, generating in the process the pixel mask using SEXTRACTOR (Bertin & Arnouts 1996). Since the sample of galaxies is not prohibitively large, the former option was chosen in order to maintain complete control over the creation of the pixel mask. The ELLIPSE task provides (ξ_0, η_0), I, PA, and ellipticity as a function of radius. The guess parameters for the disc component are determined using only the outer portion of ELLIPSE profiles, where the contribution from the bulge component is expected to be negligible: I_0 and h are found fitting the exponential law to the I profile, while PA and ellipticity guesses are simple averages. This guess disc profile is subtracted from the original profile and a Sérsic law is fitted to the residuals, to obtain I_e, n, and r_e. $\mathrm{PA_b}$ and q_b are obtained by interpolating the PA and ellipticity profiles at r_e. If the model comprises also a bar, guess parameters are taken at the maximum of the radial ellipticity profile.

GASP2D performs three fits of the model to the image, one after the other. Each fit is stopped when the χ^2 reaches minimum, i.e., when the relative change in χ^2 between successive iterations is below some fixed threshold (10^{-7}). At the end of each fit, the model image is constructed and subtracted from the observed image. Each pixel in the residual image with absolute value greater than a second fixed threshold is added to the pixel mask, and rejected in the next fits. The parameters of the fitting solution are used as guess parameters for the following fit, and after three such iterations the procedure stops and the output is generated. The output consists of a text file with the best-fitting parameters and the 2D image of the best-fitting model. GASP2D also performs an ELLIPSE run on the model image, to compare the intensity, PA, and ellipticity profiles with those of the observed galaxy. In the output graphics, zero points from Equation 4.1 are used to recover the surface brightness from the image pixel intensities:

$$\mu = -2.5 \log I + \mathrm{ZP}_\mu \ .$$

Uncertainties on the best-fitting parameters were derived through Monte-Carlo simulations: in principle, errors can be derived directly by the MPFIT implementation, which uses the pixel variances to compute formal estimates, but these are sensitive to the method chosen to compute the weights. Repeated runs on simulated galaxies, while more time consuming, give more realistic confidence intervals and can help in understanding if there are clear degeneracies between the parameters.

4.3.3 Bulge–disc decomposition: the procedure

Prior to running the GASP2D code on the SDSS image, we performed IRAF ELLIPSE fitting on the images to determine the initial pixel mask, the starting guess parameter for the 2D decomposition and estimates, and an estimate of the average sky counts and standard deviation. An example ELLIPSE run is shown in Figure 4.3 for galaxy CGCG 206-038. The starting point is the rotated and sky-subtracted i-band image (Figure 4.3, upper panel): at this stage, the PSF FWHM and β parameters were determined using the IRAF radial profile tool from the IMEXAMINE task on the point sources in the image (averaging the results), and an estimate of the sky rms was obtained by averaging the statistics of 5×5 px areas in several regions of the image far from the central galaxy. Before running ELLIPSE we masked out all the sources distinct from the main galaxy, such as foreground stars and background galaxies (Figure 4.3, lower left panel). On frames, such as the one in the figure, where the galaxies was close to the border, we also masked out every pixel not belonging to the original frame. Finally the task itself was run, and the elliptical isophotes were determined (Figure 4.3, lower right panel). Both the ELLIPSE and GASP2D fitting procedures were stopped at the radius $r_{\rm max}$ where the mean intensity drops below the sky rms value. A typical output from the ELLIPSE initial run can be seen in Figure 4.4. The vertical dashed lines represent $r_{\rm max}$, which is derived using the intensity profile (Figure 4.4, upper left quadrant). Beyond the maximum radius, the ELLIPSE task itself is unable to provide reasonable fits to the galaxy surface brightness, therefore no values of PA and ϵ are given. From the ellipse results, the guess parameters are derived as described in the previous section, and GASP2D is finally run on the images.

For each galaxy, a first GASP2D fitting was performed with a model (referred to as "basic") composed of a bulge and a disc component, and the output for each galaxy was inspected separately, to check the quality of the fits. While for some of the galaxies a basic model was found sufficient to fairly reproduce the overall light distribution and individual parameter profiles (see, e. g., CGCG 035-050 or UGC 4341 in Figure 4.6), for some galaxies there were large scale features which were not properly fitted by a basic model. As expected, these features are primarily associated with the presence of a bar. As an example we refer again to Figure 4.4, where the dotted line shows the ellipse fit to the basic model image. While the part of the image occupied by the bulge is roughly consistent between the model and the galaxy, a single disc cannot well reproduce the "bump" in the intensity profile at $r \sim 40$ px and the behaviour at large radii. The difference is even more pronounced for the ellipticity profile, while it is absent in the PA profile because the disc and the bar have roughly the same orientation with respect to the North–South direction.

For the galaxies showing clear hints of a bar component, we performed a first fit using a model composed of bulge, disc, and bar with all bar parameters (except $n_{\rm bar}$ and

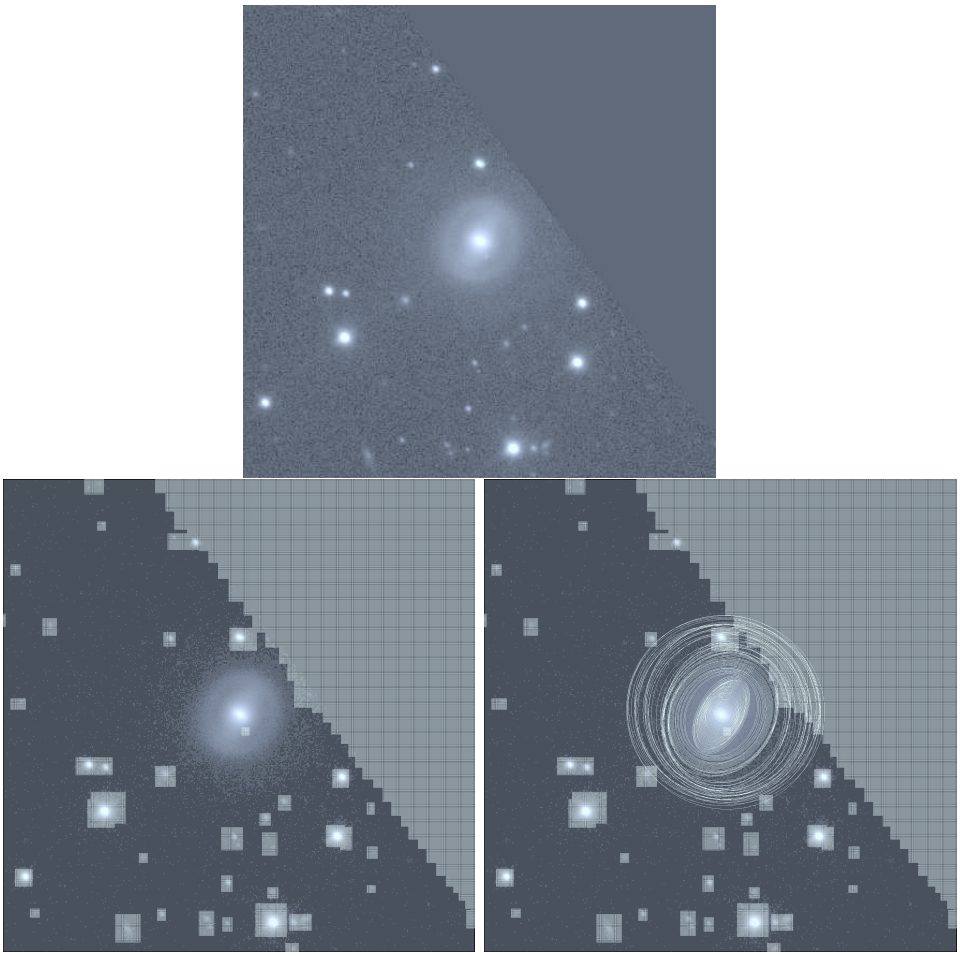

Figure 4.3: IRAF ELLIPSE fitting on the image of CGCG 206-038. *Top*: original sky-subtracted rotated image. *Bottom left*: pixel mask covering spurious sources and the pixels outside the image boundary. *Bottom right*: elliptical isophotes from the fit.

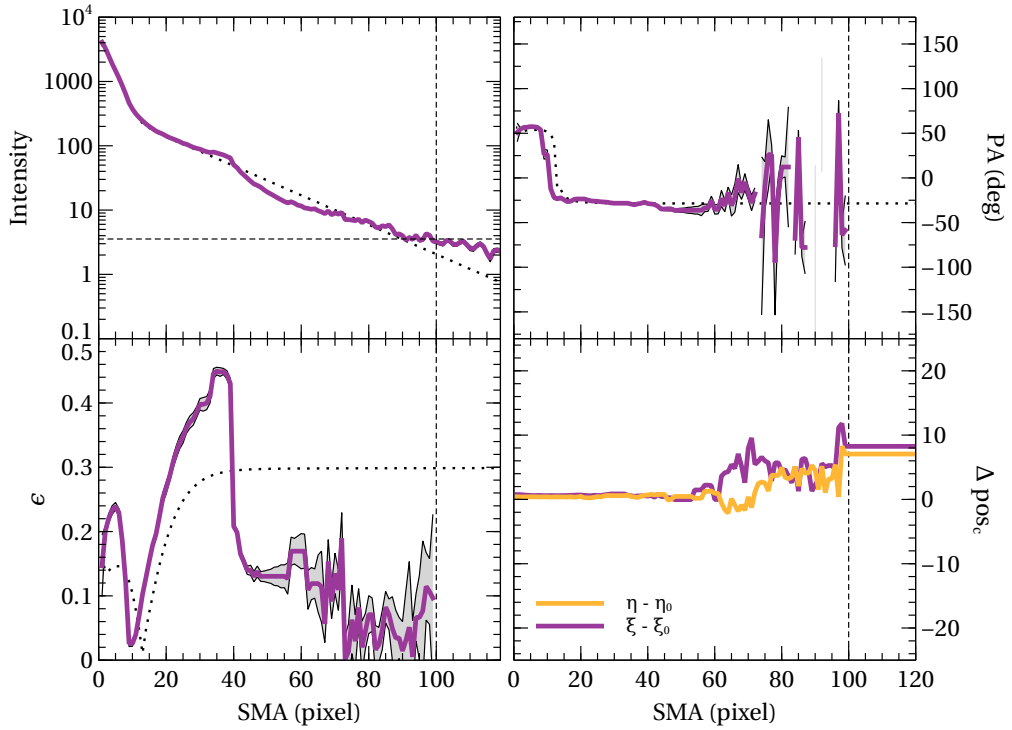

Figure 4.4: Results of IRAF ELLIPSE fitting for CGCG 206-038. Ordinates, from the top left quadrant in a clockwise direction, are pixel intensity, PA, ellipticity and difference in the centre coordinates (purple for x axis, orange for y axis). All quantities are plotted as a function of the ellipse semi-major axis (SMA).Grey shaded areas give 1-σ errors on the parameters. Vertical dashed lines mark the maximum fitting radius, while the horizontal dashed line in the intensity profile represents the background sky rms.

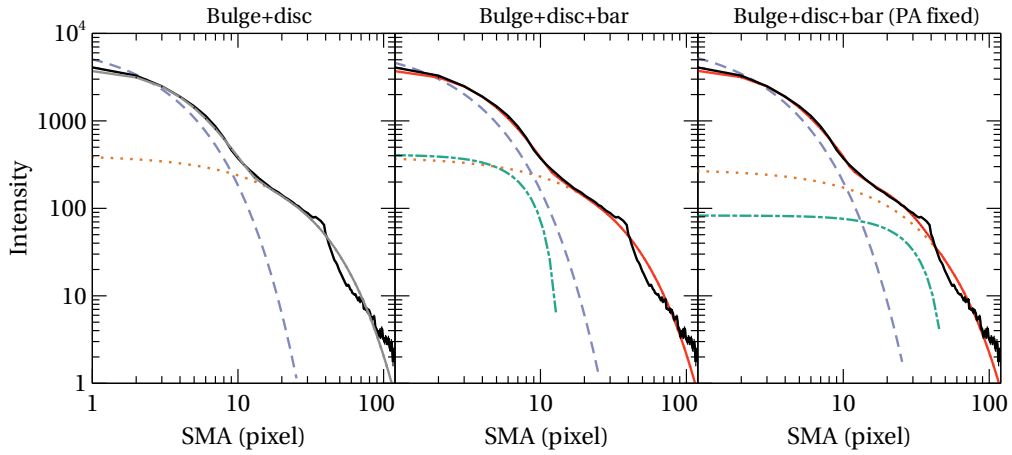

Figure 4.5: ELLIPSE intensity profiles of different models for galaxy CGCG 206-038. Bulge, disc, and bar are represented by the blue dashed, red dotted and green dot–dashed lines, respectively. The grey solid line is the composite model profile while the black solid line is the original galaxy profile.

$c_{\rm bar}$) left free to vary. When fitting this composite model, GASP2D was frequently found to produce small bars with dimensions comparable to those of the bulge component. An example is shown by the intensity profile for CGCG 206-038 in Figure 4.5, where we have scaled logarithmically also the abscissa to clarify the component trends in the central region: the left panel shows the basic model fit (bulge+disc), while in the middle panel a bar was added to the model. The bar component is smaller and less luminous than the bulge, and its contribution cannot accounts for the bump at ~ 40 px. When the "free" bar fitting did not produce accurate results, we performed multiple fits fixing or limiting certain bar parameters in order to get more reasonable results. The first test we performed in all cases, which incidentally proved to give correct results in the case of CGCG 206-038 (right panel in Figure 4.5), was to fix the bar position angle: the PA is easier to determine, with respect to the other component parameters, also by visual inspection. In some cases, however, multiple combinations of fixed/free parameters had to be tested before an acceptable fit was found. A galaxy-by-galaxy description of the fitting process is outlined hereafter, and final GASP2D plots are shown for all the sample galaxies in Figure 4.6. Tables 4.2, 4.3 and 4.4 list the full decomposition results for bulge, disc and bar, respectively.

CGCG 034-050: The overall shape and orientation are correctly fitted by GASP2D. The outer portion of the disc is slightly rounder with respect to the model, but more complicated models would not substantially change the fitting parameters in the central (i.e., bulge) part of the galaxy.

CGCG 088-060: The simple basic profile was not able to correctly reproduce the peaks in the ellipticity profile. The addition of a bar with free parameters (except for $n_{\rm bar}$ and c) generates a much better model which, apart from recovering most of the ellipticity changes, significantly reduces the residuals.

CGCG 152-078: The basic fit gives acceptable results. Errors in the ellipticity and PA profiles appear significant, but this is caused by the fact that the galaxy itself is almost perfectly round. In fact, both the 2D and the surface brightness profile residuals are quite small.

CGCG 206-038: As discussed in the previous section, a bar with fixed PA had to be added to the model to obtain a better fit. There are some relatively high residuals especially in the outer rim of the disc ($r \simeq 22$ arcsec), which are visible both in the 1D profile and in the 2D map as a yellow circle: a ring-like structure is visible also in the colour image and is not currently accounted for by the models. Since only the outer parts of the profile are affected by this feature, the model with fixed PA for the bar was kept as best-fitting solution.

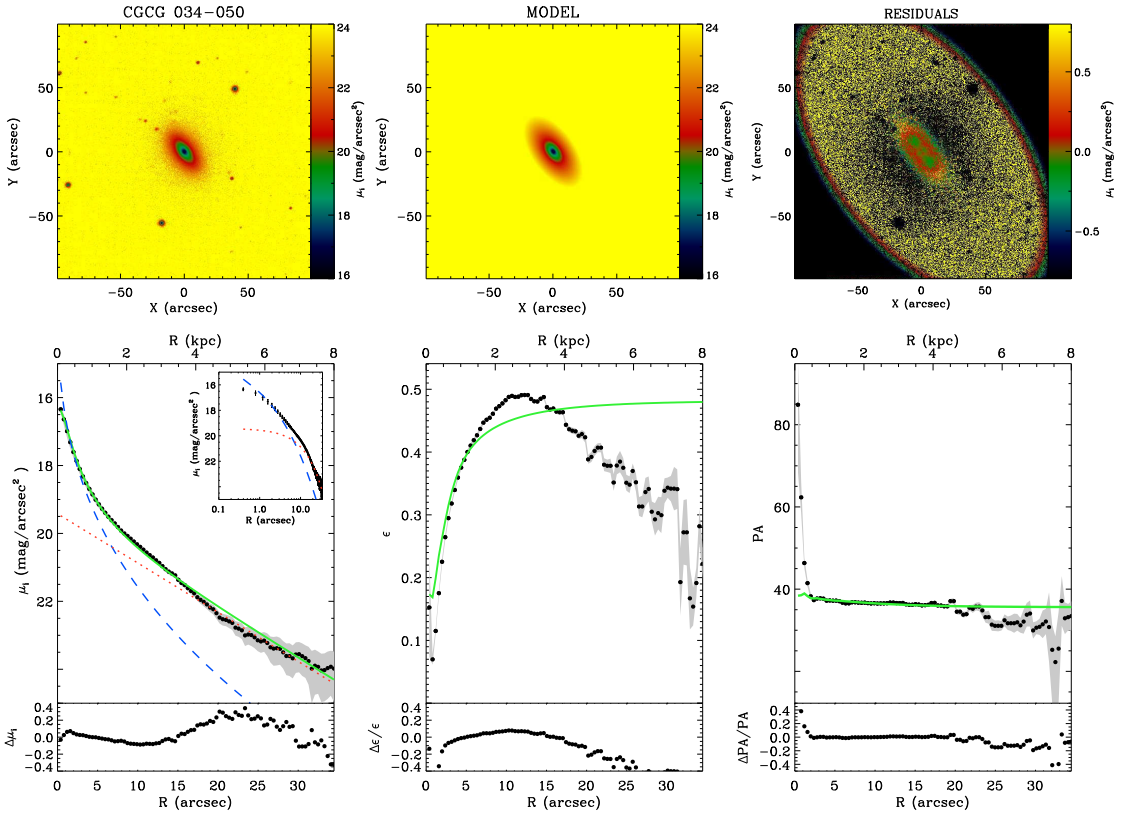

Figure 4.6: Two-dimensional photometric decomposition of the sample galaxies. Upper panels (from left to right): Map of the observed, modeled and residual (observed-modeled) surface-brightness distribution of the galaxy. The surface-brightness range of each image is indicated at the right of the panel. All images were rotated to have the galaxy major axis parallel to rows. In each panel the spatial coordinates with respect to the galaxy centre are given in arcsec. Lower panels (from left to right): Ellipse-averaged radial profile of surface-brightness, position angle, and ellipticity measured in the observed (dots with error-bars) and modeled image (solid line). The dashed and dotted lines represent the intrinsic surface-brightness contribution of the bulge and disc, respectively. The difference between the ellipse-averaged radial profiles extracted from the observed and modeled images is also shown.

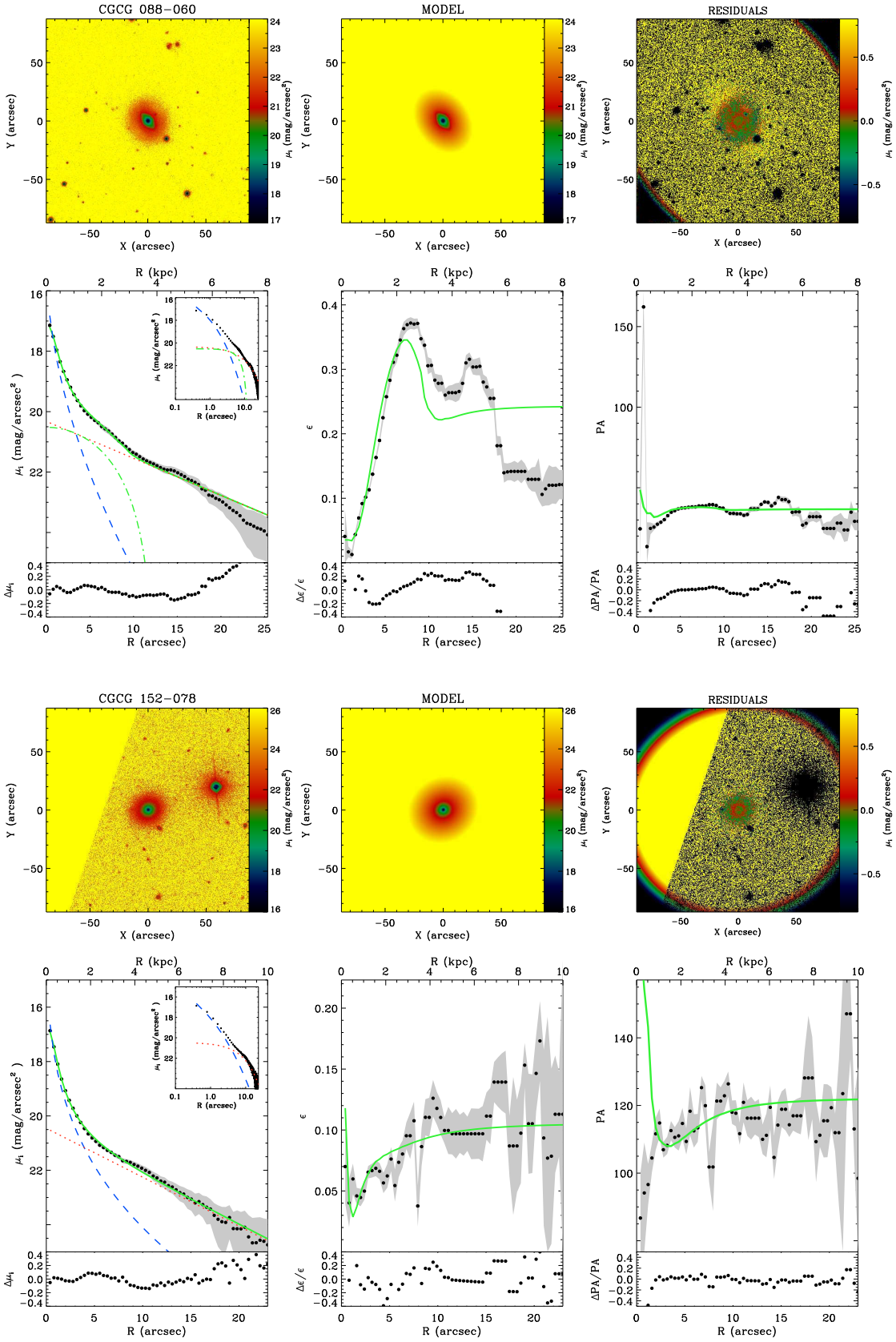

Figure 4.6: Continued.

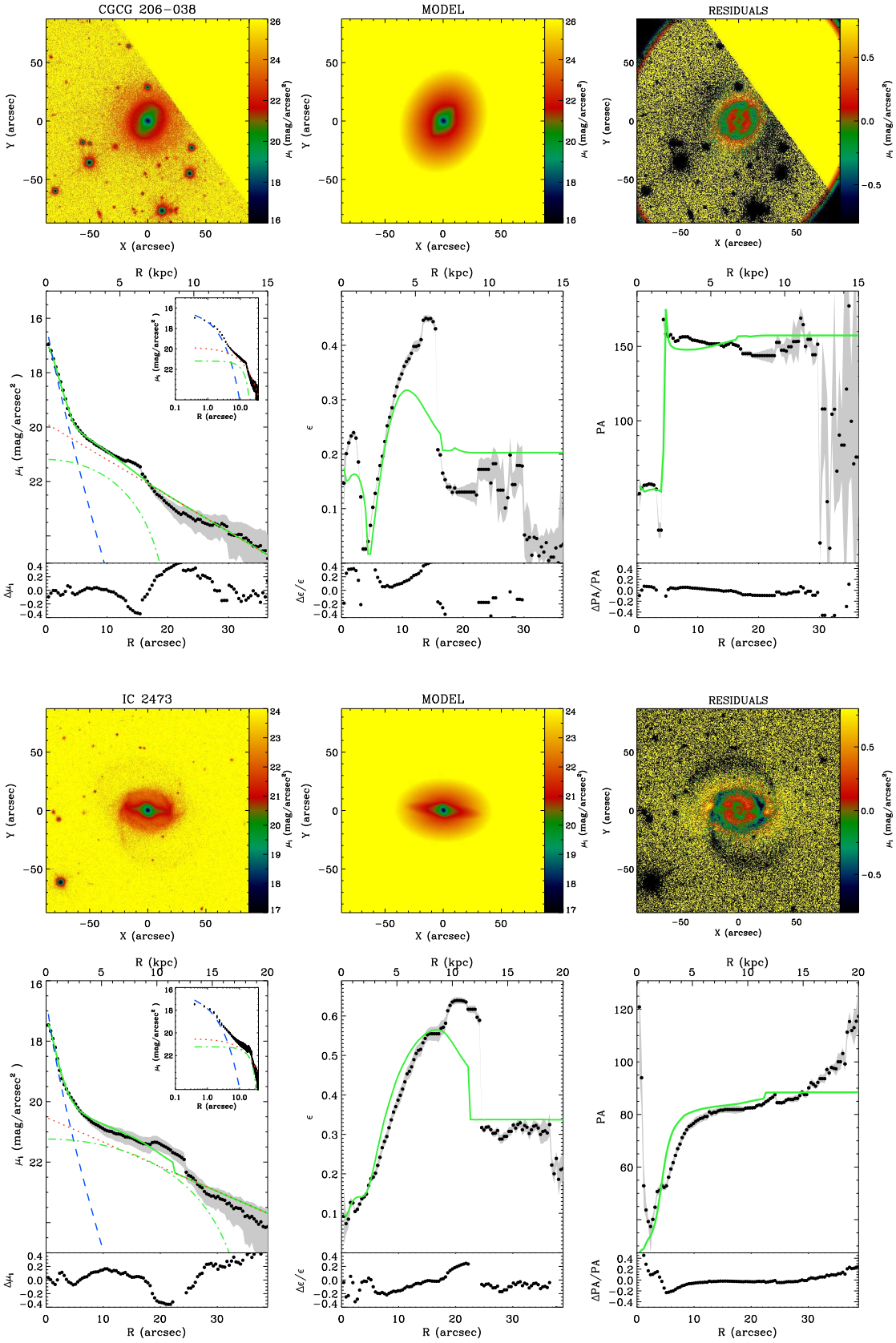

Figure 4.6: Continued.

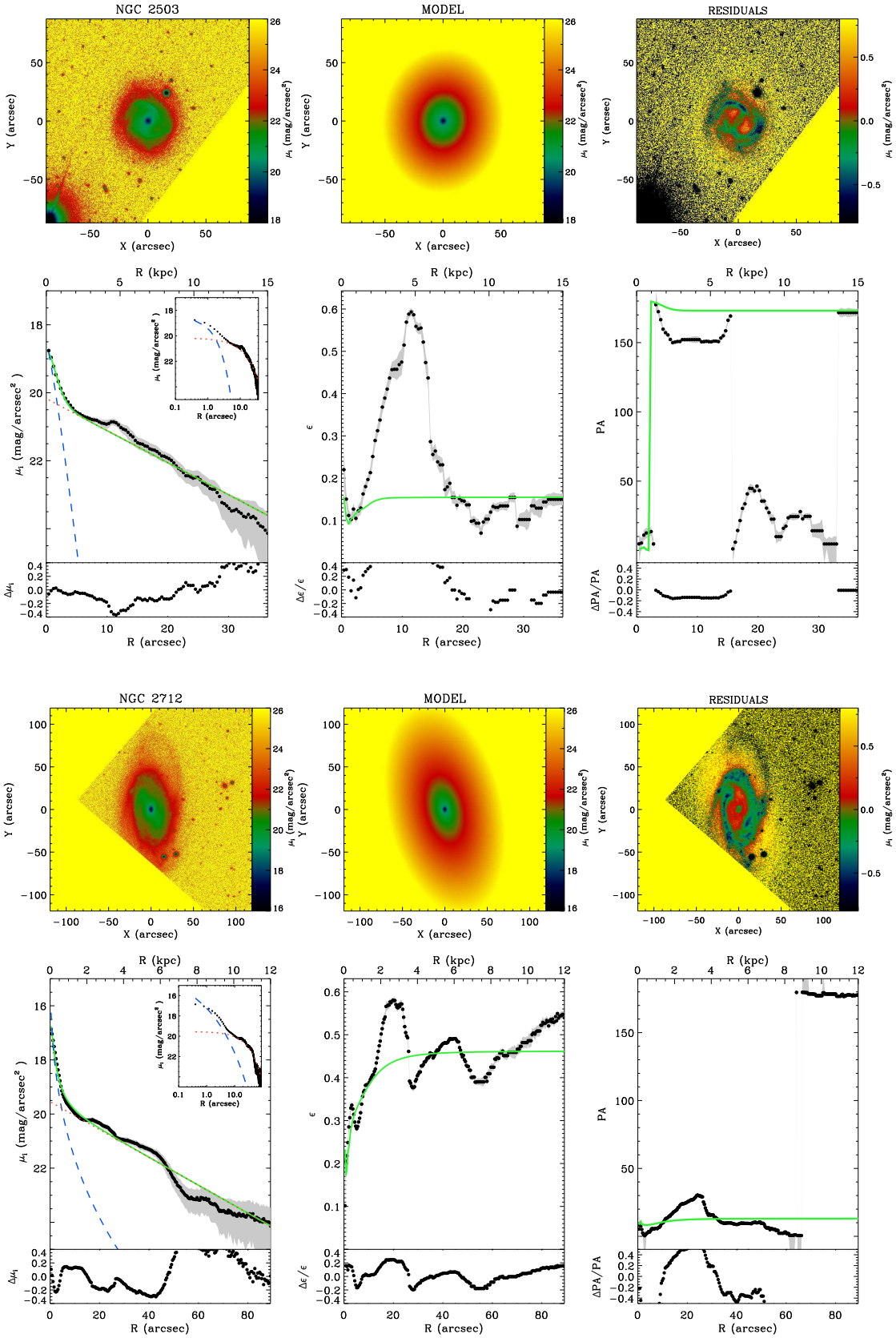

Figure 4.6: Continued.

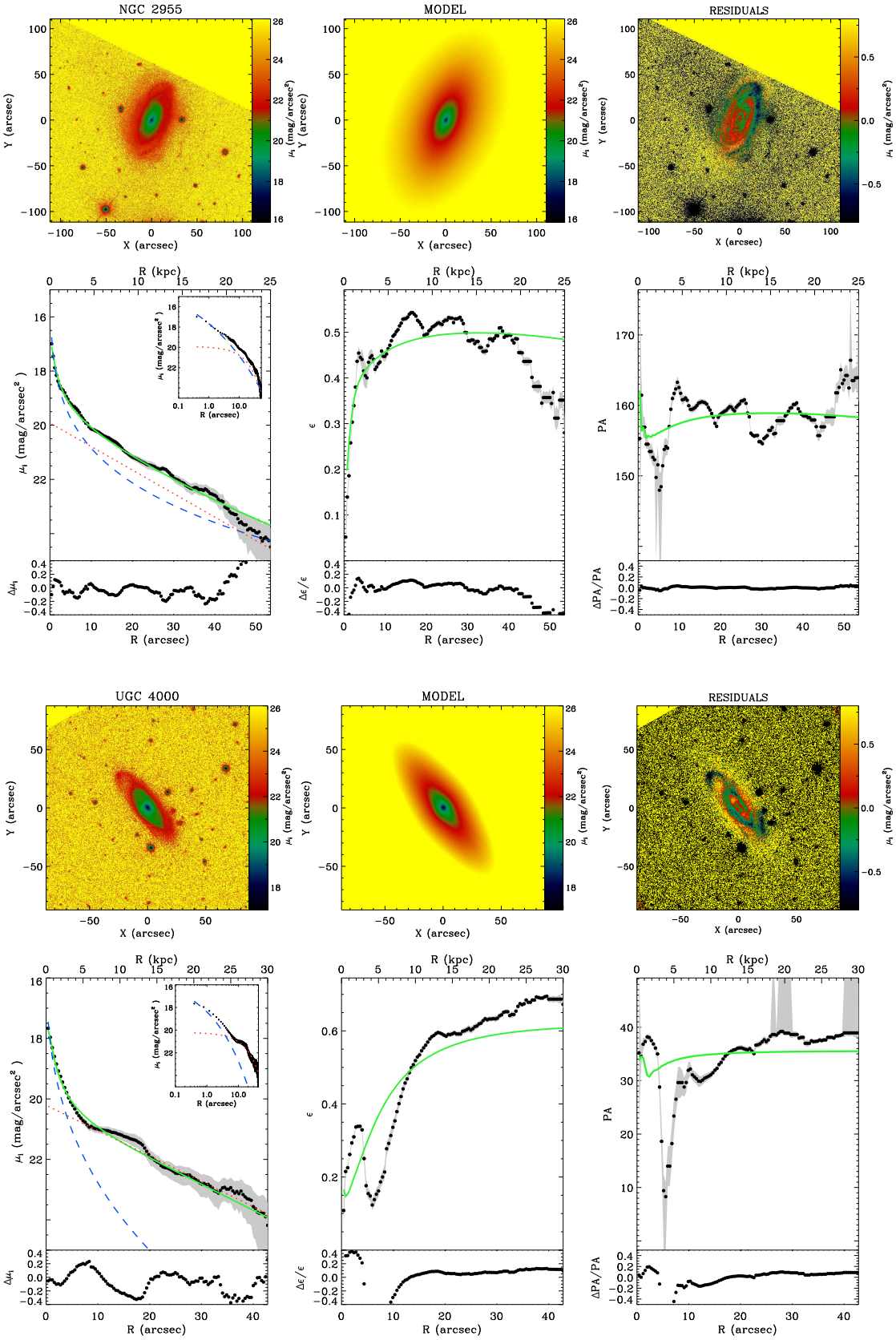

Figure 4.6: Continued.

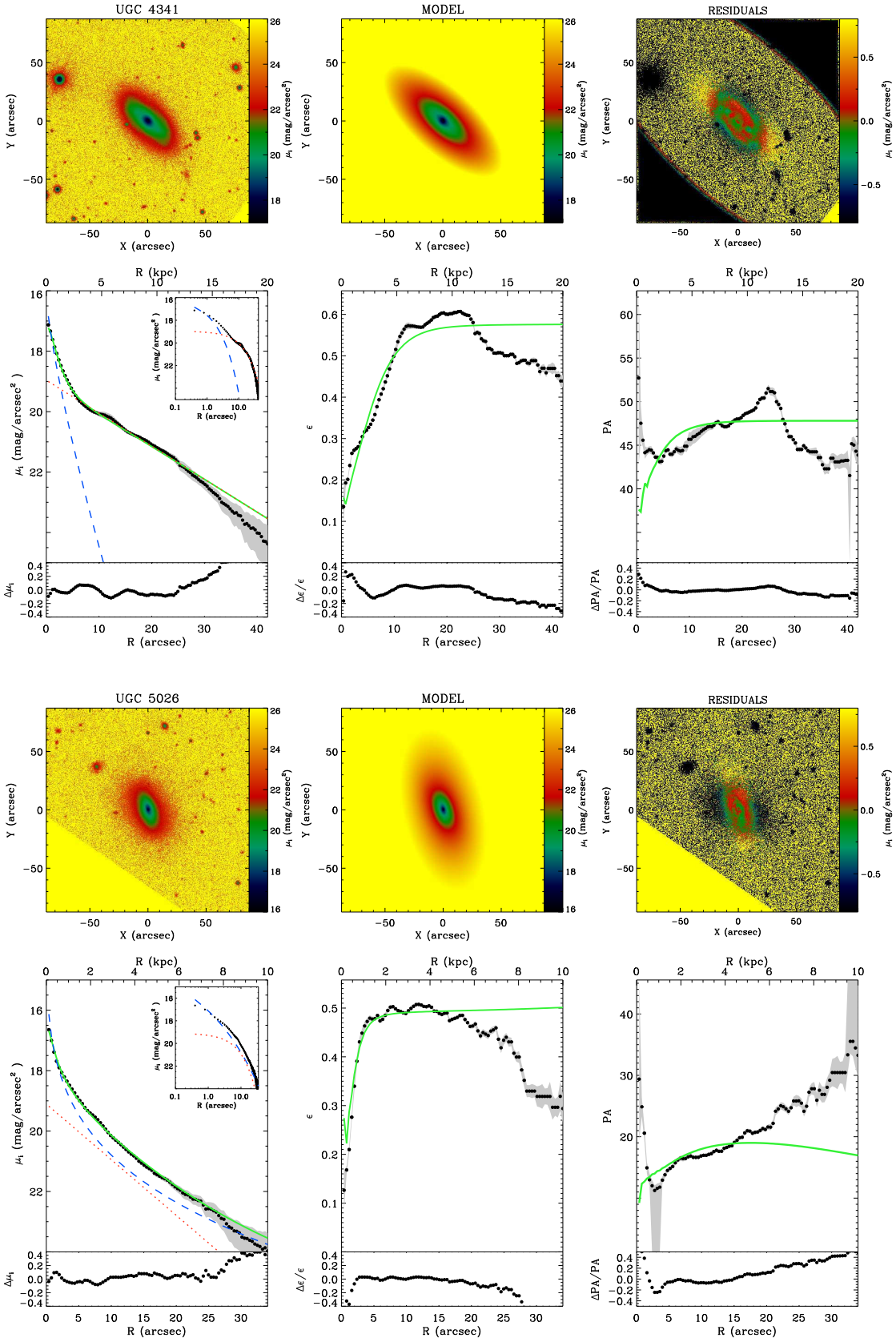

Figure 4.6: Continued.

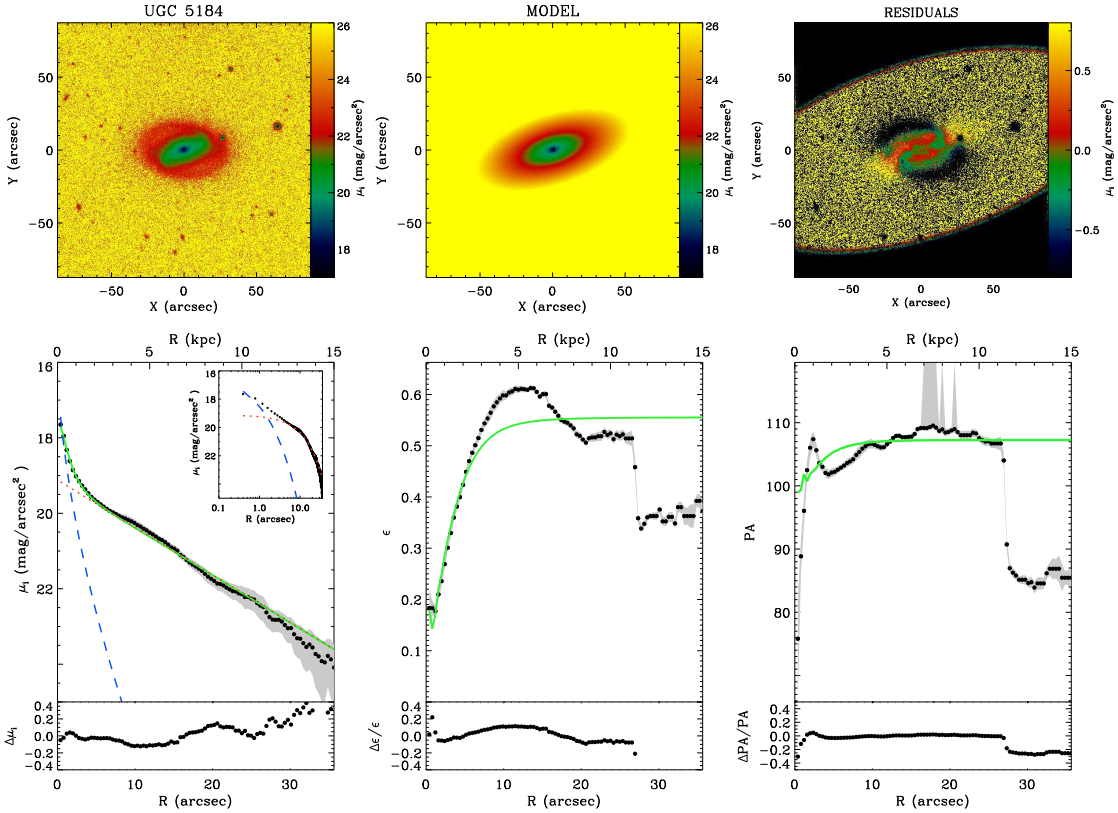

Figure 4.6: Continued.

IC 2473: This almost face on spiral galaxy shows prominent features such as a bar and spiral arms. The best-fitting model was found by simply adding the bar component to the bulge+disc model. Although the model image seems to show an excessive contribution from the bar, the residual image shows that this is not the case. Significant deviations from the model are visible only in the external part of the galaxy, where the spiral arms are located.

NGC 2503: NGC 2503 is classified as a barred galaxy, and indeed from the image mosaic it appears as if there is an elongated structure in the central parts. Also the 1D ellipticity profile shows a prominent peak at $r \simeq 10$ arcsec. However, the GASP2D minimization algorithm was unable to find a reasonable fit to the bar. Tests to model the ellipticity excess were performed with a "free" bar, a bar with fixed PA, q or both, and a bar with fixed parameters. All the tests proved to be unsuccessful, so the basic bulge+disc model was kept as the best-fitting solution. In fact, although the ellipticity profile of the model is significantly different from the derived one, the intensity profile and residual image do not display large discrepancies. We concluded that the size of the bulge should not be affected in this case by the bar parameters

NGC 2712: The fit was characterized by the same problems as NGC 2503. Despite showing a prominent bar, no reasonable fit was found and the final model contained only bulge and disc.

NGC 2955: The basic bulge+disc model provided a good fit to the data.

UGC 04000: The galaxy is classified as barred, but only the basic model gave a reasonable fit. The central bar, being highly inclined with respect to the line of sight, is not fitted correctly by more complicated models.

UGC 04341: The best-fitting solution was given by the basic model with bulge and disc.

UGC 05026: The basic model with bulge and disc was adopted as the best-fitting solution.

UGC 05184: No reasonable fit was obtained including a bar in the model. For this reason, the basic model was kept as the best solution.

4.3.4 Determination of $r_{\mathbf{bd}}$

The model parameters from the 2D decomposition were used to determine the radius $r_{\rm bd}$, defined as the radius where the bulge contribution to the integrated light starts to

Table 4.2: Bulge component parameters from GASP2D decompositions for the sample of isolated galaxies.

Galaxy	I_e (mag arcsec^{-2})	r_e (arcsec)	n	q_b	PA_b (degrees)	L_{bulge}/L_T
CGCG 034-050	18.38 ± 0.12	2.93 ± 0.10	2.57 ± 0.15	0.55 ± 0.09	37.54 ± 0.10	0.56
CGCG 088-060	18.70 ± 0.12	1.50 ± 0.10	1.85 ± 0.15	0.95 ± 0.09	1.46 ± 0.10	0.26
CGCG 152-078	19.09 ± 0.12	1.68 ± 0.10	3.48 ± 0.15	0.92 ± 0.09	102.64 ± 0.10	0.49
CGCG 206-038	18.44 ± 0.12	2.09 ± 0.10	1.27 ± 0.15	0.85 ± 0.09	54.94 ± 0.10	0.41
IC 2473	18.87 ± 0.12	1.98 ± 0.10	1.31 ± 0.15	0.81 ± 0.09	30.75 ± 0.10	0.18
NGC 2503	22.89 ± 0.12	8.84 ± 0.10	4.26 ± 0.15	0.54 ± 0.09	153.67 ± 0.10	0.11
NGC 2712	18.12 ± 0.06	2.22 ± 0.06	0.99 ± 0.10	0.66 ± 0.05	1.72 ± 0.05	0.09
NGC 2955	23.10 ± 0.12	26.60 ± 0.10	5.56 ± 0.10	0.72 ± 0.09	0.00 ± 0.10	0.59
UGC 4000	20.64 ± 0.12	4.12 ± 0.10	2.69 ± 0.10	0.83 ± 0.09	27.60 ± 0.10	0.33
UGC 4341	18.61 ± 0.12	2.06 ± 0.10	1.30 ± 0.10	0.73 ± 0.09	39.62 ± 0.10	0.18
UGC 5026	20.64 ± 0.12	9.49 ± 0.10	3.85 ± 0.10	0.48 ± 0.09	12.62 ± 0.10	0.69
UGC 5184	19.25 ± 0.12	1.53 ± 0.10	1.66 ± 0.10	0.71 ± 0.09	98.78 ± 0.10	0.10

Table 4.3: Disc component parameters from GASP2D decompositions for the sample of isolated galaxies.

Galaxy	I_0 (mag arcsec^{-2})	h (arcsec)	q_d	PA_d (degrees)	L_{disc}/L_T
CGCG 034-050	19.42 ± 0.11	7.48 ± 0.10	0.51 ± 0.10	35.39 ± 0.10	0.44
CGCG 088-060	20.32 ± 0.11	8.87 ± 0.10	0.76 ± 0.10	36.65 ± 0.10	0.65
CGCG 152-078	20.57 ± 0.11	6.32 ± 0.10	0.89 ± 0.10	122.65 ± 0.10	0.51
CGCG 206-038	20.88 ± 0.11	10.69 ± 0.10	0.29 ± 0.10	157.33 ± 0.10	0.18
IC 2473	20.52 ± 0.11	13.28 ± 0.10	0.66 ± 0.10	88.42 ± 0.10	0.69
NGC 2503	20.34 ± 0.11	11.98 ± 0.10	0.87 ± 0.10	2.20 ± 0.10	0.89
NGC 2712	19.35 ± 0.05	19.43 ± 0.06	0.55 ± 0.04	13.49 ± 0.06	0.91
NGC 2955	19.59 ± 0.11	12.47 ± 0.10	0.38 ± 0.10	154.95 ± 0.10	0.41
UGC 4000	20.21 ± 0.11	12.94 ± 0.10	0.34 ± 0.10	35.76 ± 0.10	0.67
UGC 4341	18.96 ± 0.11	9.95 ± 0.10	0.42 ± 0.10	47.81 ± 0.10	0.82
UGC 5026	19.22 ± 0.11	6.06 ± 0.10	0.50 ± 0.10	26.41 ± 0.10	0.30
UGC 5184	19.12 ± 0.11	8.63 ± 0.10	0.44 ± 0.10	107.24 ± 0.10	0.90

Table 4.4: Bar component parameters from GASP2D decompositions for the sample of isolated galaxies.

Galaxy	$I_{0,bar}$ (mag arcsec^{-2})	a_{bar} (arcsec)	n_{bar}	q_{bar}	PA_{bar} (degrees)	c	L_{bar}/L_T
CGCG 088-060	20.52 ± 0.14	12.59 ± 0.15	2	0.39 ± 0.10	39.30 ± 0.10	0.0001	0.08
CGCG 206-038	20.93 ± 0.14	26.36 ± 0.15	2	0.78 ± 0.10	143.76 ± 0.10	0.0001	0.41
IC 2473	21.24 ± 0.14	37.04 ± 0.15	2	0.21 ± 0.10	83.47 ± 0.10	0.0001	0.13

dominate over the light from the other components. Since the analysis of bulge dynamics and stellar populations was performed with long-slit spectroscopy, the $r_{\rm bd}$ value had to be determined along the slit direction, which was always chosen (see Section 4.4) to be aligned with the galaxy major axis. One cannot, however, simply take the intersection between the 1D profiles from ELLIPSE fitting, because the various components are in general not aligned one with the other. A simplification of the general case can be seen in Figure 4.7, where an hypothetical galaxy is composed of a bulge (inner ellipse) and a disc (outer ellipse) which has the major and minor axes aligned with the coordinate axes. The angle between the major axes of the two ellipses is θ. In this case, if the value of $r_{\rm bd}$ is computed directly from the 1D profiles, an angle $\theta = 0$ would be implicitly assumed, which would lead to an overestimation of the bulge contribution. To have a correct estimate of the value of $r_{\rm bd}$ it is necessary to take into account the full 2D information of the surface brightness distribution: first, a 2D image of every component was constructed using the best-fitting parameters from GASP2D; the various model components were then rotated with respect to one another according to the differences in position angles, and added together. The value of $r_{\rm bd}$ was finally computed by comparing the luminosity profiles of the various components along a 1-px wide slice aligned with the galaxy mayor axis (i.e., with the long-slit). The final one-dimensional profiles constructed in this way are shown for each galaxy in Figure 4.8, and the derived values of $r_{\rm bd}$ are listed in Table 4.8.

4.4 Spectroscopy

4.4.1 Observations and data reduction

Observations were carried out at the Observatorio del Roque de los Muchachos in La Palma (Canary Islands) on the nights from 20th to 23rd January 2012. Galaxy spectra were acquired at the 3.58-m diameter TNG telescope using the DOLORES[3] low resolution spectrograph, equipped with a 2048×2048 px E2V CCD (0.252 arcsec px^{-1} scale). The instrument was operated in long-slit spectroscopic mode employing the VHR-V grism (0.95 Å px^{-1} dispersion) and two different slit setups: the 0.7 arcsec slit was used for the acquisition of galaxy and Lick standard spectra; the 2 arcsec slit was used for spectrophotometric standards. The VHR-V covers the wavelength range from 4800 to 6700 Å, with resolutions $\simeq 2000$ and $\simeq 850$ for the $0\farcs7$ and 2 arcsec slits respectively.

A minimum of three spectra was acquired for each galaxy of the sample. Total exposure times and slit position angles are listed in Table 4.5. Together with the galaxy and standard star spectra, the following calibration frames were obtained at the telescope: biases, dome flats, sky flats, and Ar+Kr+Ne+Hg lamp arc spectra. Flats and reference

[3] http://www.tng.iac.es/instruments/lrs/

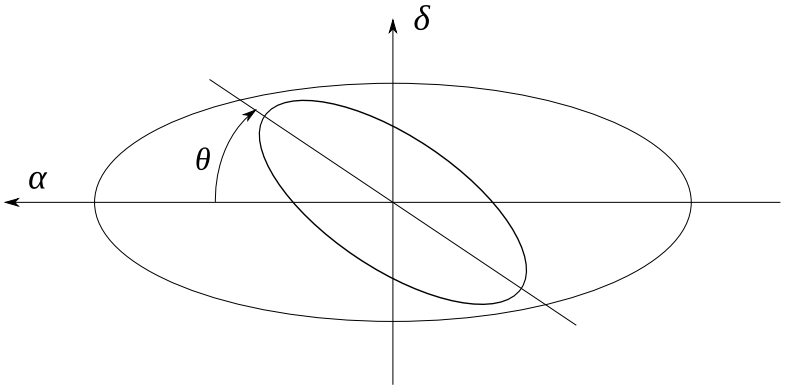

Figure 4.7: Schematic diagram of misaligned galaxy components on the plane of the sky. The inner and outer ellipses represent the bulge and disc components, respectively. For simplicity, the major and minor axes of the disc ellipse are aligned with the α and δ coordinates.

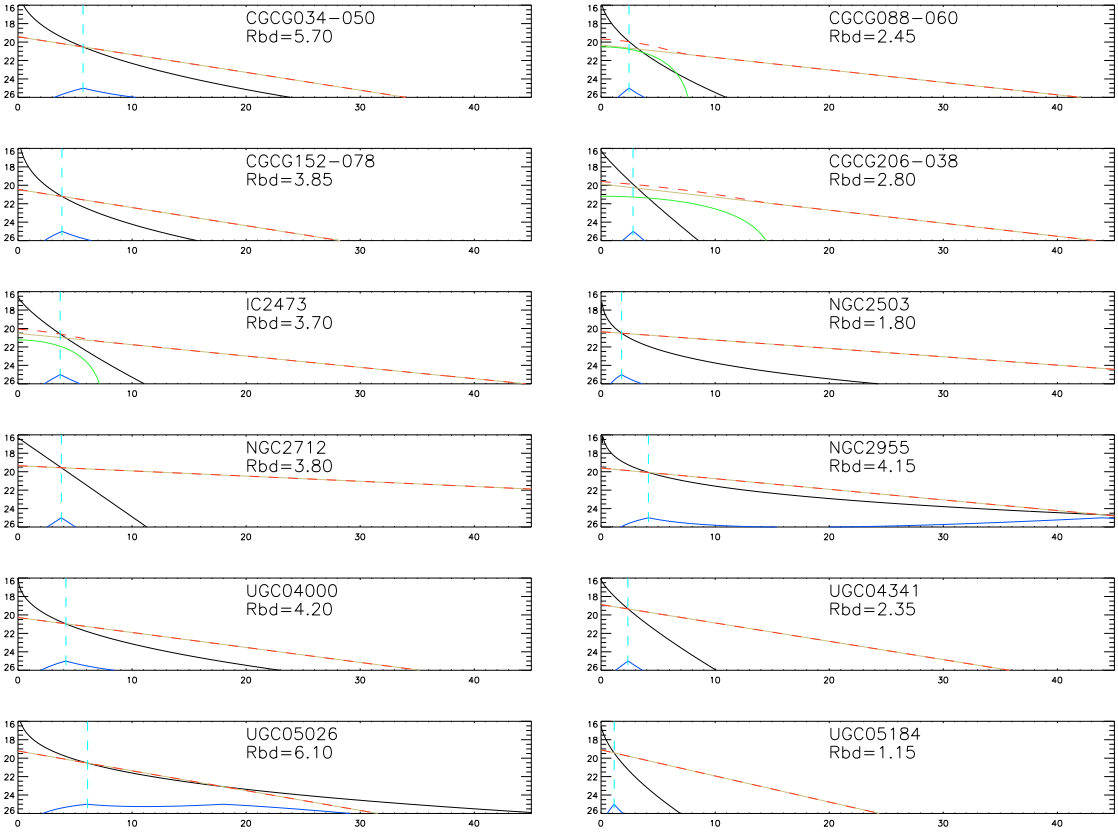

Figure 4.8: Final $r_{\rm bd}$ values for the sample of isolated galaxies. The bulge, disc, and bar components are shown by the solid black, dashed red and solid green lines, respectively. The khaki line is the composed surface brightness profile of the bar and disc components. The blue solid line is the absolute difference between the bulge profile and the integrated profile of the other components, scaled arbitrarily to occupy the lower part of the panels. The vertical dashed cyan line marks the minimum of the difference, and hence the position of $r_{\rm bd}$.

Table 4.5: Log of the spectroscopic observations of the sample of isolated spiral and S0 galaxies

Galaxy	Date	Exposure time (s)	PA (deg)
CGCG 034-050	2012-01-21	7200	37.1
CGCG 088-060	2012-01-23	9600	32.5
CGCG 152-078	2012-01-23	7200	-60.0
CGCG 206-038	2012-01-22	7200	-30.0
IC 2473	2012-01-21	7200	95.9
NGC 2503	2012-01-23	9600	4.5
NGC 2712	2012-01-20	7200	4.3
NGC 2955	2012-01-20	7200	159.4
UGC 4000	2012-01-20	9000	37.4
UGC 4341	2012-01-22	7200	45.3
UGC 5026	2012-01-22	7200	22.8
UGC 5184	2012-01-22	7200	84.8

arc spectra were obtained using both slits, except for the sky flat frame, which was only acquired with the 0.7 arcsec slit. We therefore created a separate reduction procedure for data frames acquired with the 2 arcsec slit, in which the division of the spectra by the skyflat level is substituted with a division by an image of constant unity value. The effect of this substitution does not significantly affect our final results, because the 2 arcsec slit was only used for the spectra of spectrophotometric standard stars, which have a very high S/N ratio. They are not sensibly affected by the sky illumination correction.

All the raw frames were inspected both visually and through the IRAF task `imstat` to check for macroscopic defects. The first one or two frames acquired in each night (which were always bias frames) were found to have a standard deviation around the mean value which is higher, by a factor $\gtrsim 100$, than the average standard deviation of all other biases, because the bottom lines of the CCD contain very high counts, and sometimes are even saturated. Despite the fact that this region of the image was eventually trimmed, we excluded these images from further analysis. In each night we were left with a minimum of 8 bias frames, which was enough to compute a reliable bias average. Saturated standard star spectra were discarded.

Data reduction

Data reduction was performed with the IRAF software package, following the standard procedure for long-slit observations. All reduction steps were repeated for all the images acquired in each night. After trimming the overscan region in all the raw images, the average of the bias frames was computed, together with two average dome flats (one for each slit).

Flatfield corrections were computed separately for each slit. The average bias was

subtracted from the dome flat, and the `response` task was used to create the normalized flatfield image. The task first fits a 20^{th} degree polinomial to each image row and divides the original image by the fit to generate an image with a flat profile along the dispersion direction. The resulting image is then normalized again by dividing it with a 9^{th} degree spline fit performed along each column. For the 0.7 arcsec slit spectra, the same operations were performed on the sky flat frames to obtain the sky illumination correction. The final flatfield was obtained by multiplying the sky and dome correction frames.

All object and arc lamp spectra were finally corrected, with the `ccdproc` task, using the average bias and the final flatfield for the corresponding slit.

Prior to wavelength calibration, cosmic rays were removed using the IRAF implementation of the L.A.COSMIC[4] (van Dokkum 2001) software package. L.A.COSMIC is based on Laplacian edge detection. It distinguishes cosmic rays from astronomical point or extended sources based on the sharpness of the edges of each feature, and it is iteratively applied to remove extended cosmic rays. The IRAF `lacos_spec` task is an *ad hoc* version for 2D spectroscopic data and operates after removing sky emission lines and object profiles. The removal is achieved by fitting 1D functions to each row and column of the 2D image. Because of the way light propagates inside the telescope and instrument optics, the sky lines appear curved in DOLORES long-slit spectra with an offset between edge and image centre that reaches ~ 10 px (i.e., greater than the line FWHM). To fit the "moving double peak" pattern that appears as one is scanning along the columns, the degree of the polynomial for the column fit had to be set to a quite high value. After extensive tests, a 16^{th} degree polynomial was found to be the best compromise between speed and reliability of the background estimation. L.A.COSMIC was not applied to arc spectra. The contrast between the line and background flux is indeed so high that the sharp edges of the emission lines are flagged as cosmic rays by the routine and are progressively "chewed away" in each successive iteration. With six iterations, practically all cosmic rays were correctly removed from the galaxy images. An example of the final result of cosmic ray rejection for CGCG 206-038 is displayed in Figure 4.9. Extended defects remained in some of the images (7 out of a total of 42), and were later removed prior to the image combination phase.

Wavelength calibration was achieved by fitting a 4^{th} degree Chebyshev polynomials to the wavelengths of the lines identified on the ArHe+HgKr lamp spectra using the line list available on the TNG website[5]. Looking at the wavelength calibrated spectra of stars, we noticed a shift of ~ 100 Å of the Hβ absorption line. The cause of the erroneous calibration was the misidentification in the online list of the line at $x \sim 200$ px as Kr II at 4857.2 Å. Since this is the only clear line in the ArHe+HgKr spectrum with $\lambda < 5000$

[4] `http://www.astro.yale.edu/dokkum/lacosmic/`
[5] `http://www.tng.iac.es/instruments/lrs/`

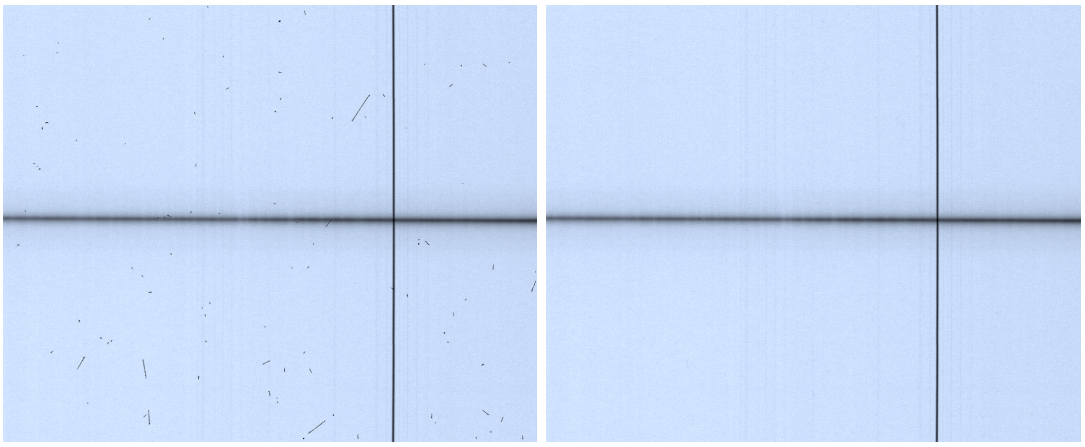

Figure 4.9: Two-dimensional spectrum of CGCG 206-038 before (left panel) and after (right panel) cosmic ray rejection.

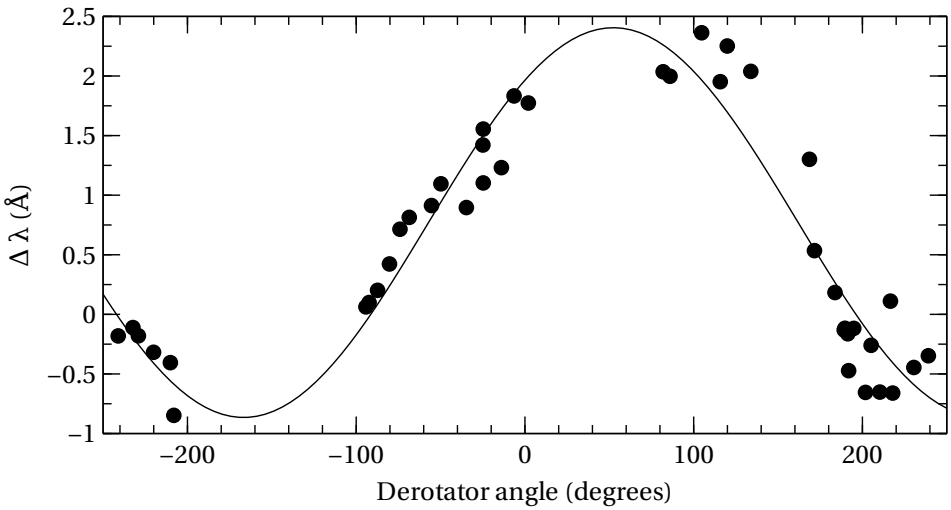

Figure 4.10: Average wavelength shift ($\Delta\lambda$) as a function of derotator angle θ. Each filled circle corresponds to a different wavelength-calibrated frame. The black line represents a least-squares cosine fit to the data. The best-fitting solution is $f(\theta) = 0.77 + 1.64\cos(-0.014\theta + 0.75)$ where θ is expressed in degrees.

Å, it is crucial for a reliable calibration of the Hβ - [O III] region. We corrected the wavelength by first re-fitting the line positions excluding the putative Kr line. Although practically all the wavelengths < 5300 Å were extrapolated, the fit was usually good (rms $\lesssim 0.1$ Å). The obtained solution was applied to the lamp spectrum and allowed the identification of the line as Hg I at 4916 Å. The repositioning of stellar Hβ lines at the correct wavelength confirmed the validity of our identification. The whole calibration procedure was rerun with the new wavelength value. The average rms of each fit was $\lesssim 0.06$ Å, and the overall accuracy of the calibration was tested by computing the offset between the measured wavelength of the sky emission lines and the theoretical values listed in Osterbrock et al. (1996). Several exposures showed a systematic shift (up to 2 Å) of all emission-line wavelengths. According to Marinoni et al. (2013) the wavelength shifts arise from telescope flexures in the DOLORES spectrograph. We checked for a possible systematic effect by measuring the position of a set of sky lines (5577, 5889, 5896, 6300, 6499 and 6554 Å) in all wavelength-calibrated frames and computing the average shift for each frame. We show the derived shifts as a function of derotator angle (FITS header keyword `ROT-POS`) in Figure 4.10, together with a cosine-function fit to the data. Since the trend with derotator angle is the same that is highlighted by Marinoni et al., with maxima and minima in the same positions, the cause of the wavelength shifts was identified with telescope flexures. After removing the average shift in the wavelength direction from each image, the offset rms of sky line positions was $\lesssim 0.3$ Å ($\simeq 2$ km s^{-1} at 5000 Å).

Sky subtraction was performed by fitting a 6^{th} degree polynomial to the spectrum background which was selected in two regions above and below the galaxy spectrum. The spectrum with the highest S/N of a spectrophotometric standard star was selected for each night and was extracted using standard IRAF routines. The sensitivity function was derived by comparison with the appropriate flux table, and applied to all the galaxy spectra obtained in the same night for flux calibration. The galaxy spatial profiles were obtained by summing the central 1000 columns, and the shift between different exposures of the same galaxy was found by computing the difference between the positions of the profile peak, which was determined by gaussian fitting. All the exposures of the same galaxy were shifted to match the profile of the first frame in the sequence.

Before averaging the shifted spectra, the residual defects were removed by hand by substituting a high flux value (in our case 999) to a rectangular region surrounding the cosmic ray. By applying an average sigma clipping in the combination procedure, all defects were eliminated because the underlying flux level is of the order of 10^{-17} erg cm^{-2} s^{-1} Å^{-1}. The spectra were averaged, instead of summed, to avoid the generation of artificial data by the IRAF `imcombine` routine. When the image are summed the `imcombine` task compensates for bad pixels by taking an average of the non-rejected pixels in all the other images. This artificial data is not generated when the images are

averaged, because bad pixels are simply rejected.

The header keywords of all the FITS files were changed in order to have the spatial axis centred on peak of the galaxy continuum, and the pixel increments in arcseconds. The use of the average instead of the sum in the combination phase avoided the need for a change in the exposure time keyword. The frames were finally trimmed in the spatial direction, by an amount specific to each galaxy, to include only the object spectrum and a small portion of the sky ($\sim$ 20 arcsec) to compute accurate S/N ratios in the data analysis phase.

4.4.2 Data analysis

The kinematics of the sample of galaxies were investigated by applying the pPXF (Cappellari & Emsellem 2004) and GANDALF (Sarzi et al. 2006) IDL codes to the calibrated spectra. pPXF is a penalized pixel fitting program that fits an observed spectrum with a linear combination of non-linear components. The basic algorithm and output, given in terms of the first four Gauss-Hermite coefficients (v, σ, h_3 and h_4), is the same as ULySS (see Section 2.4.1). But, unlike ULySS it is not tailored specifically to the study of simple stellar population parameters, and does not have an internal interpolator to derive the combination of parameters of the single best-fitting simple stellar population (SSP). The typical pPXF output is therefore given in terms of weights of each template component. Together with pPXF the GANDALF absorption and emission line fitting code was used in the analysis of the galaxy spectra. In particular the gas emission lines were modelled as Gaussian functions and were treated as additional spectral components in the fitting process. The IDL code is then able to solve simultaneously for the optimal combination of stellar templates and for the intensity and amplitude of the emission lines. GANDALF also provides the possibility to couple the kinematics and/or intensity of pairs or groups of emission lines, for example those produced by the same atomic species. The templates used in the fitting process were the MILES SSP models from Vazdekis et al. (2010).

The 2D galaxy spectra were first rebinned in the spatial direction to obtain a minimum $S/N \simeq 20$ per resolution element, in the external parts. The average noise rms was taken from the statistics of the sky background regions in the 2D reduced frames. The galaxy and template spectra were then rebinned to a common scale in $\ln \lambda$ corresponding to $\Delta v = 50\,\mathrm{km\,s^{-1}\,px^{-1}}$, and the SSP models from the MILES library were convolved with a Gaussian function to match the resolution of the VHR-V grism. The pixel scale was chosen in order to sample the grism FWHM with at least two pixels in the rebinned spectrum. For each galaxy, GANDALF was run on the spectra corresponding to each spatial position (after rebinning), using an additive 8^{th} degree polynomial (Q_m in Equation 2.1) to account for errors in flux calibration and continuum shape differences between the galaxy and templates. A typical output from a pPXF+GANDALF fit

is shown in Figure 4.11.

Figure 4.12 shows the stellar kinematics of all galaxies in the sample. We found a general good agreement between the velocity curves from the positive and negative semi-major axes, except for UGC 5026. Fixing the h_3 and h_4 parameters to 0, we were able to recover consistent kinematics also for this galaxy.

4.5 Stellar populations

4.5.1 Lick indices

The Mg, H β and Fe Lick indices (Worthey et al. 1994, see Section 2.6.3 for their definitions) were measured on the flux-calibrated spectra using custom IDLroutines. The $\langle$Fe$\rangle$ and [MgFe]$'$ index combinations were computed according to Equation 2.9. Prior to the measurement of the line-strength indices, the galaxy spectra were degraded to the FWHM = 8.4 Å Lick/IDS resolution (Worthey & Ottaviani 1997) through Gaussian convolution. Since atmospheric seeing was the dominant effect during observations, no focus correction was applied (Mehlert et al. 1998).

Errors on the line-strength indices were derived from photon statistics and CCD readout noise, and they were calibrated by means of Monte Carlo simulations. Fifty different simulations were run for each spectrum by adding Gaussian random noise, which was scaled to the standard deviation of the residuals given by subtracting the model fit to the observed spectrum. The standard deviation of the measurements was taken as the uncertainty on the line-strength index value.

Observed spectra were also corrected for contamination by H β emission lines. In gas rich galaxies, such as the ones in the sample, the filling of hydrogen absorption lines caused by nebular emission can artificially bias the determination of ages towards higher values (i.e., older stellar populations). The contamination was taken into account by measuring the hydrogen equivalent width on the observed spectrum after subtraction of the emission line flux from the GANDALF fits. Only H β emission lines detected with $S/N > 3$ were subtracted from the observed spectra.

The complete set of Lick indices measured on the sample galaxies as a function of radius is shown in Figure 4.13.

We measured central values of the Fe, H β, and Mg indices by computing the average of all points inside $0.3r_{\rm e}$, weighting each point for its S/N ratio. Table 4.6 lists the central values of the indices for the sample galaxies together with the central value of velocity dispersion σ, which was computed in the same way as the index values.

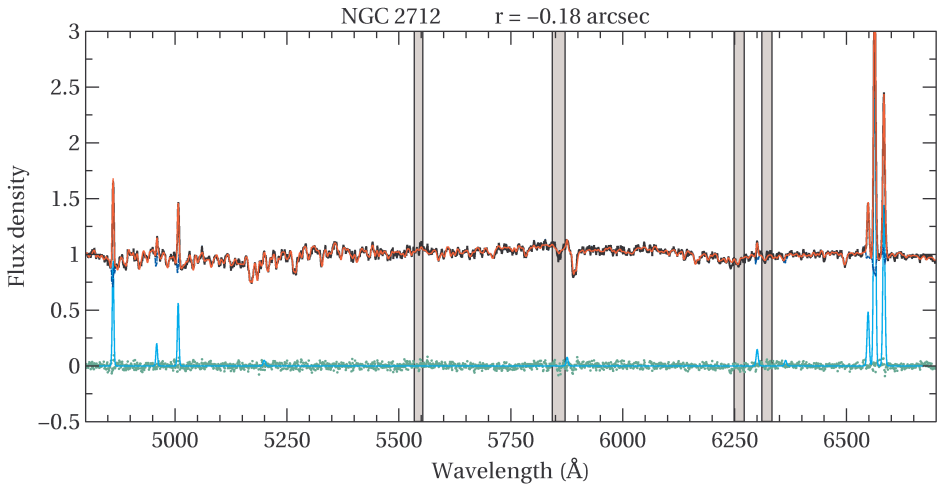

Figure 4.11: Example of the GANDALF+PPXF fit of the central spectrum of NGC 2712 ($r = -0.18$ arcsec). The observed spectrum is shown as a black solid line, while the emission line and stellar template models are given by the blue dashed and cyan solid lines, respectively. The total template (stars + emission lines) is the solid red line, and residuals from the model fit are shown at the bottom of the plot as green dots. Grey shaded areas mark sky emission regions which were excluded from the fit.

4.5.2 Central values of age, metallicity, and α/Fe enhancement

We derived the stellar population properties in the centre of the sample galaxies by comparing the measurements of the line-strength indices with the model predictions by Thomas et al. (2003) for the single stellar population as a function of age, metallicity, and α/Fe enhancement

The central values of Hβ, [MgFe]$'$, $\langle$Fe$\rangle$, and Mgb are plotted in Figure 4.14. The values of Hβ and [MgFe]$'$ are compared with the model predictions for two stellar populations with solar ([α/Fe] = 0 dex) and super-solar α/Fe enhancement ([α/Fe] = 0.5 dex), respectively. The age and metallicity of the stellar population in the Hβ-[MgFe]$'$ diagram are almost insensitive to the variations of the α/Fe enhancement. The values of $\langle$Fe$\rangle$ and Mgb are compared with the model predictions for two stellar populations with an intermediate (2 Gyr) and old age (6 Gyr), respectively. The metallicity and α/Fe enhancement of the stellar population in the $\langle$Fe$\rangle$–Mgb diagram are almost insensitive to the variations of the age. We calculated the age, metallicity, and α/Fe enhancement in the centre of the sample galaxies from the central values of line-strength indices given in Table 4.7 by following (Morelli et al. 2008). The derived values are representative of the properties of the stellar population of the sample bulges. The central values of age, metallicity, and α/Fe enhancement and their corresponding errors are listed in Table 4.7 and the histograms of their number distribution are shown in Figure 4.15.

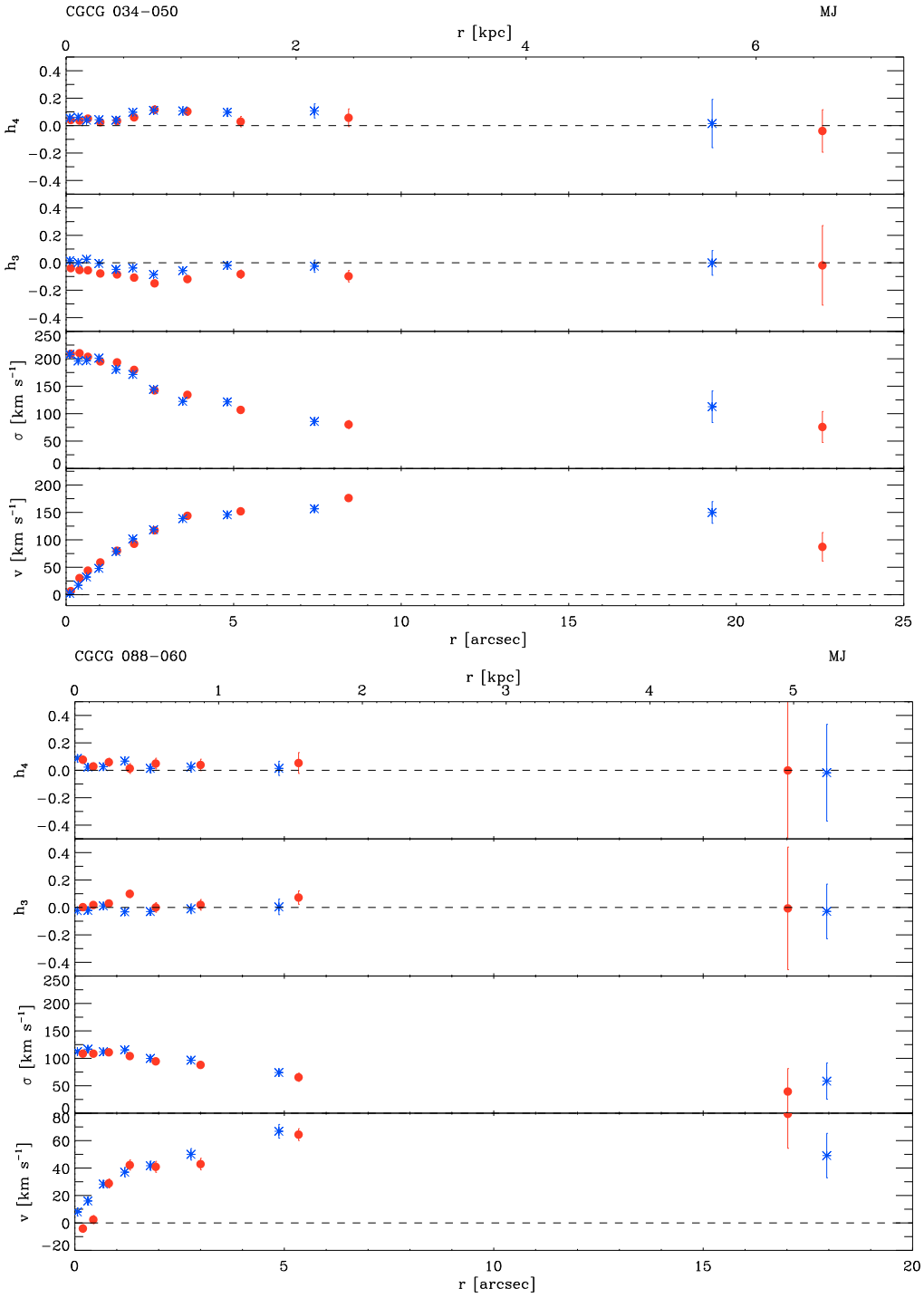

Figure 4.12: Stellar kinematics measured along the major axis of the galaxies. The curves are folded around the nucleus. Asterisks and dots refer to data measured along the approaching and residing sides of the galaxy, respectively. The radial profiles of the line-of-sight velocity (v) after the subtraction of the systemic velocity, the velocity dispersion (σ), the third- and fourth-order coefficients of the Gauss–Hermite decomposition of the LOSVD (h3 and h4) are shown (panels from top to bottom).

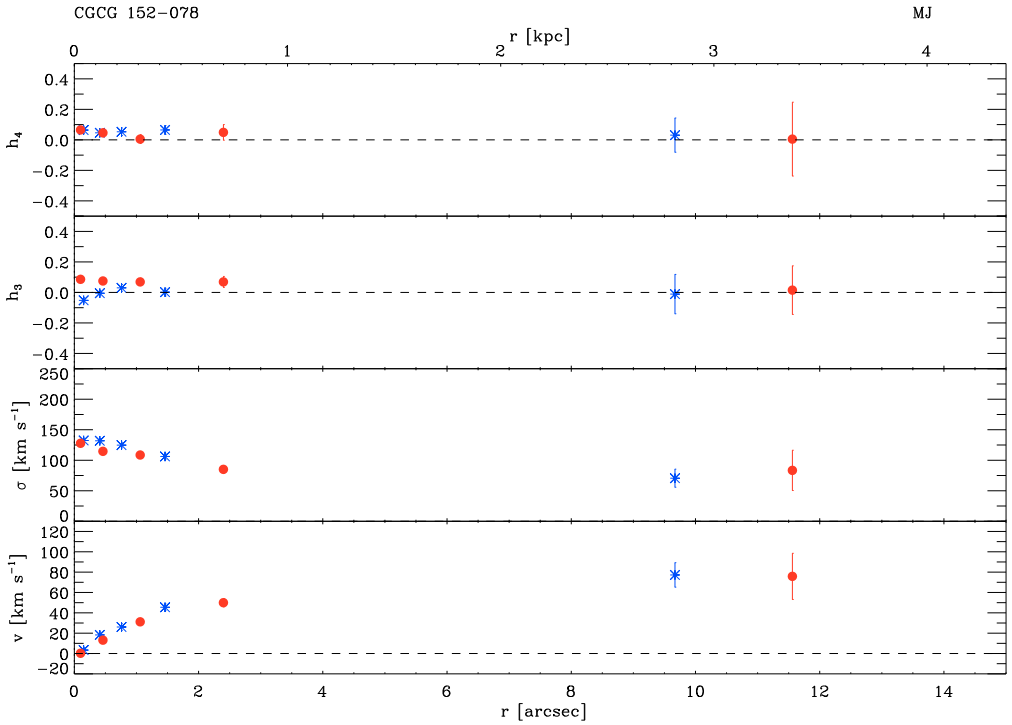

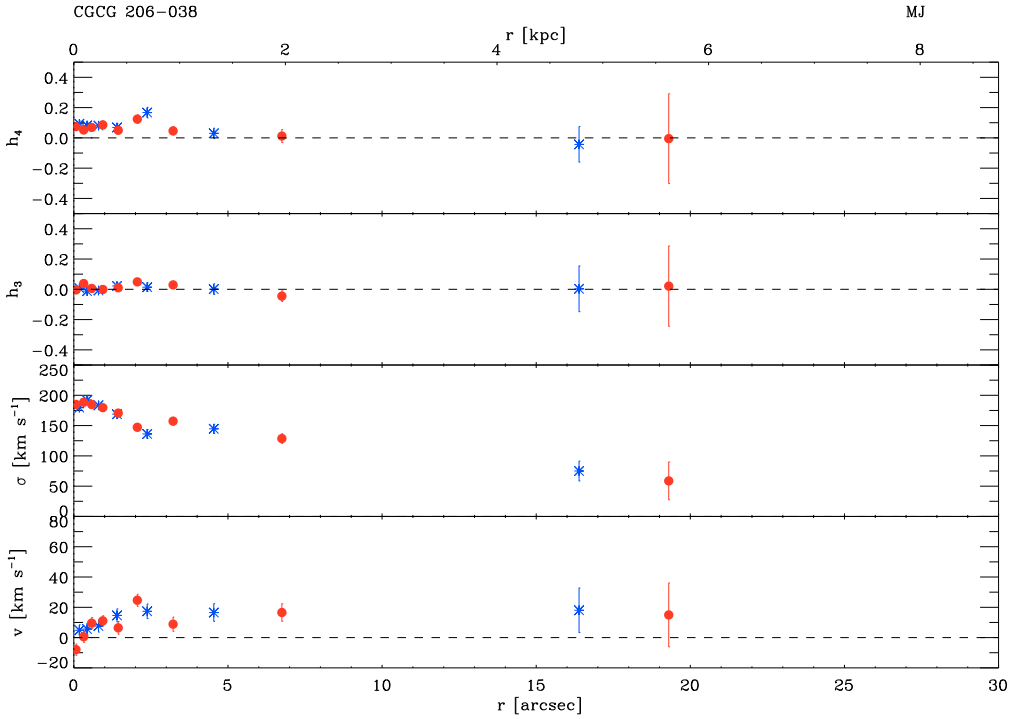

Figure 4.12: Continued.

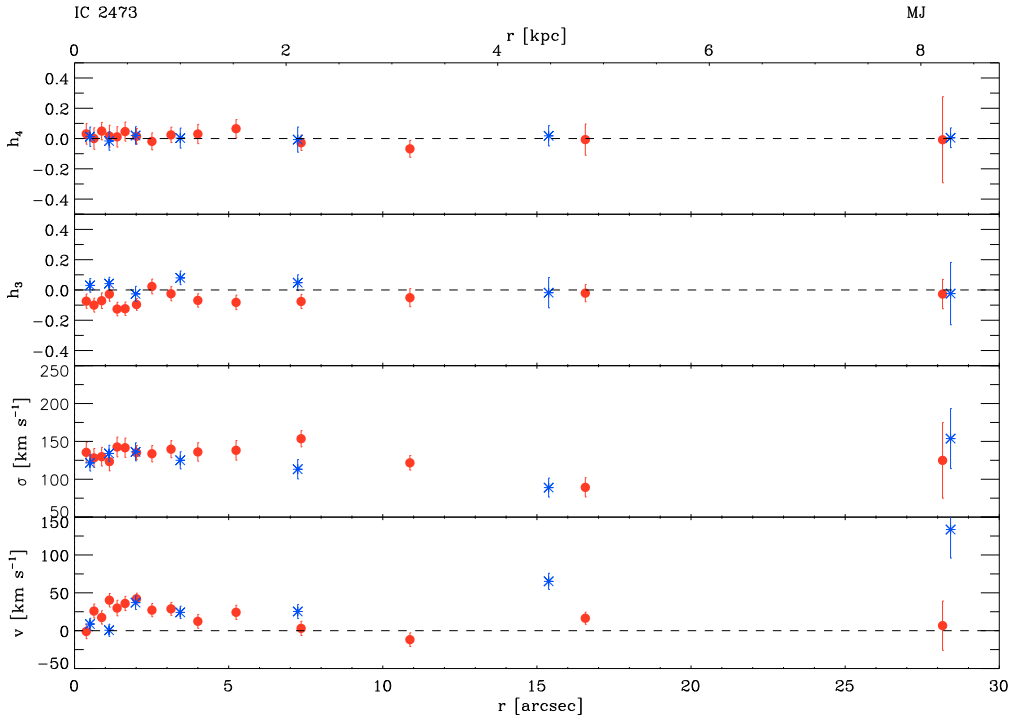

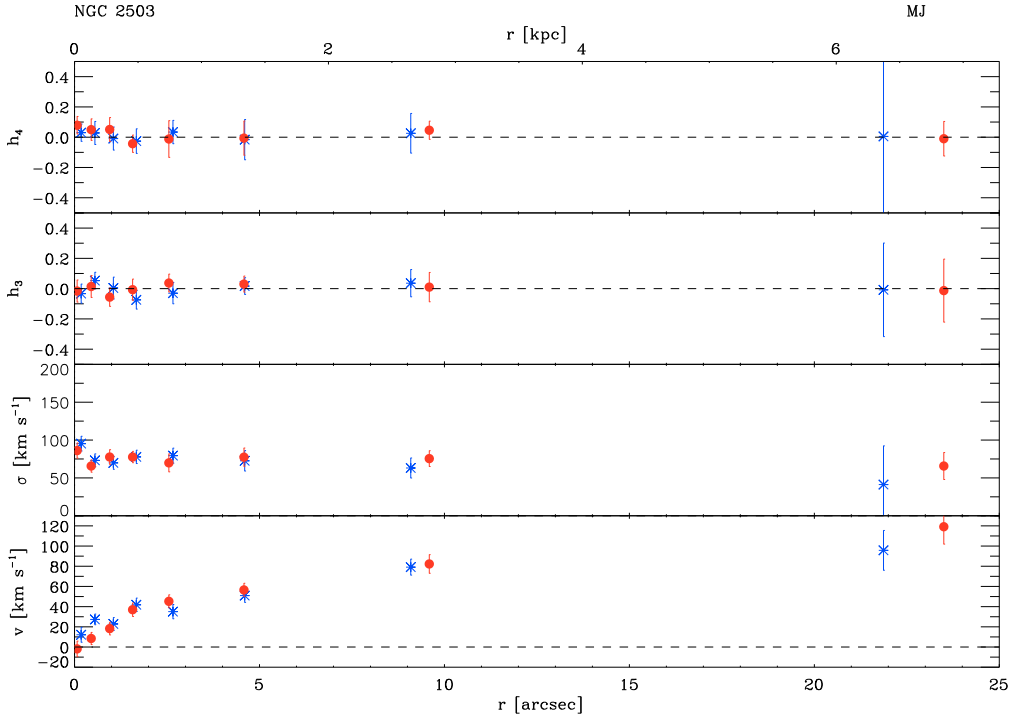

Figure 4.12: Continued.

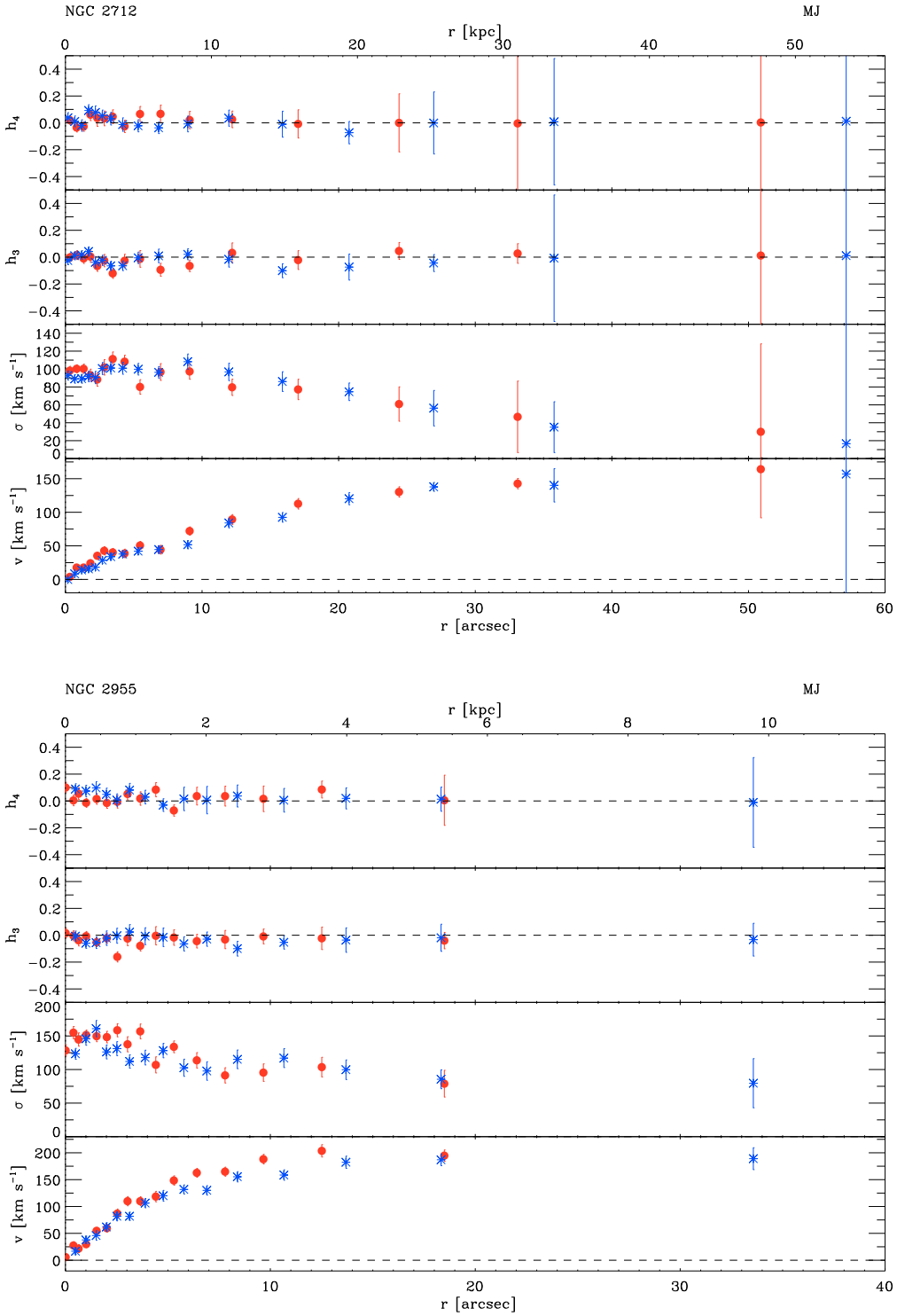

Figure 4.12: Continued.

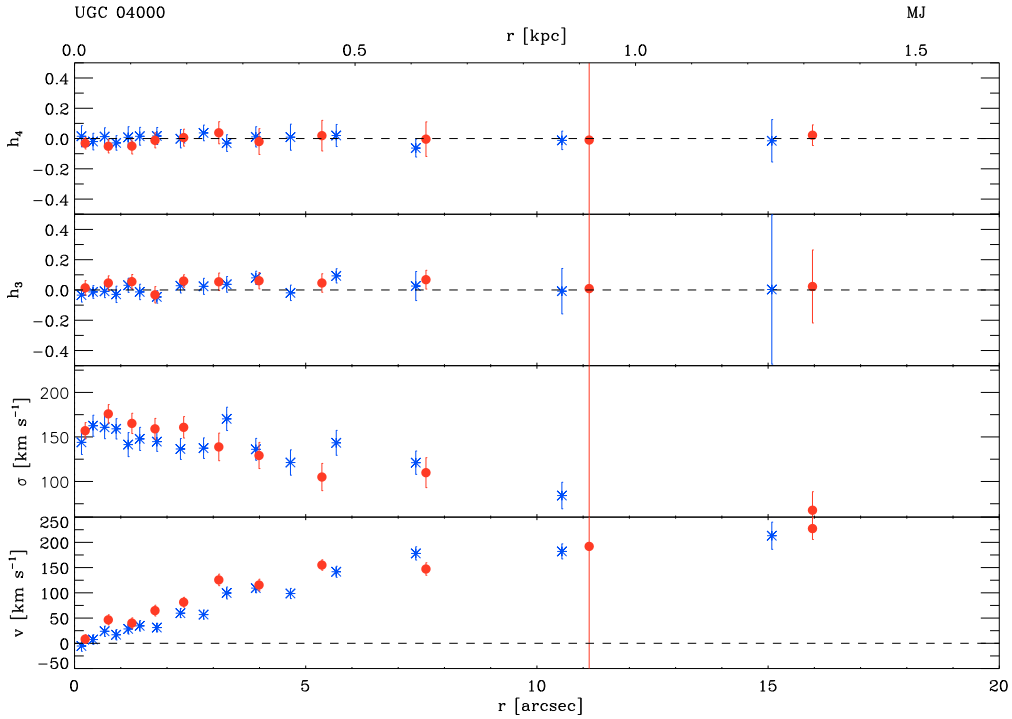

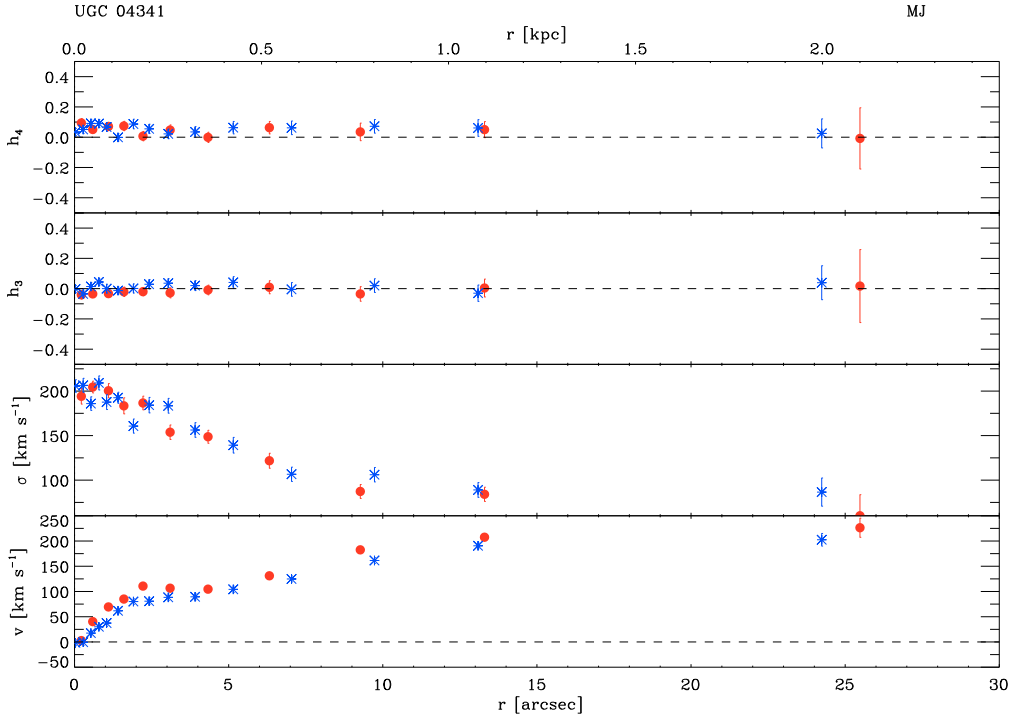

Figure 4.12: Continued.

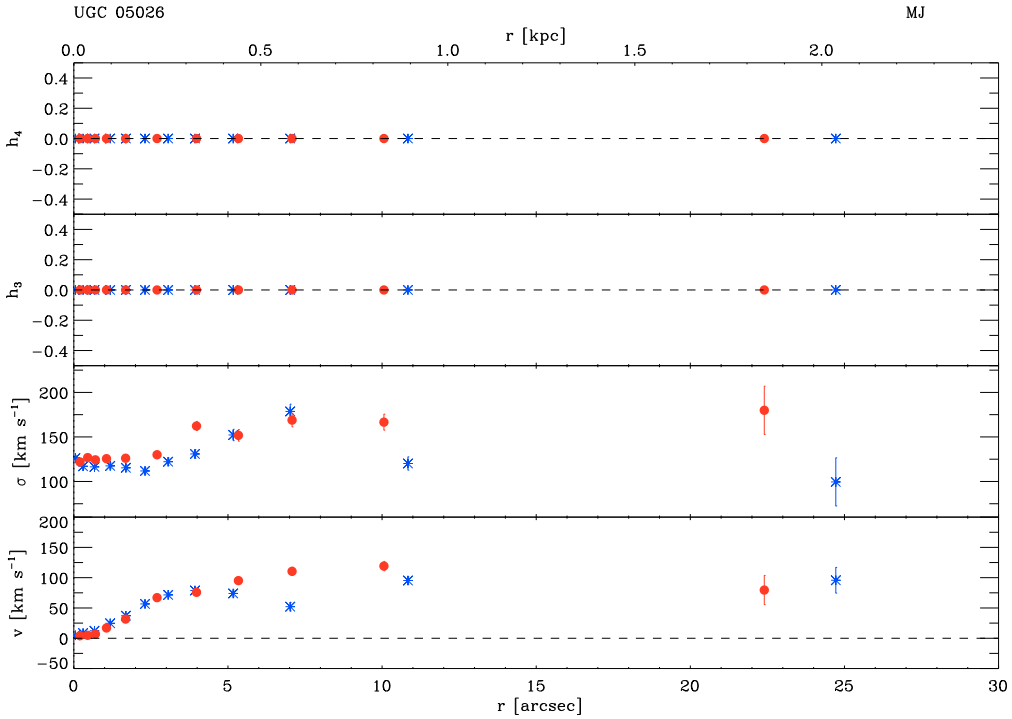

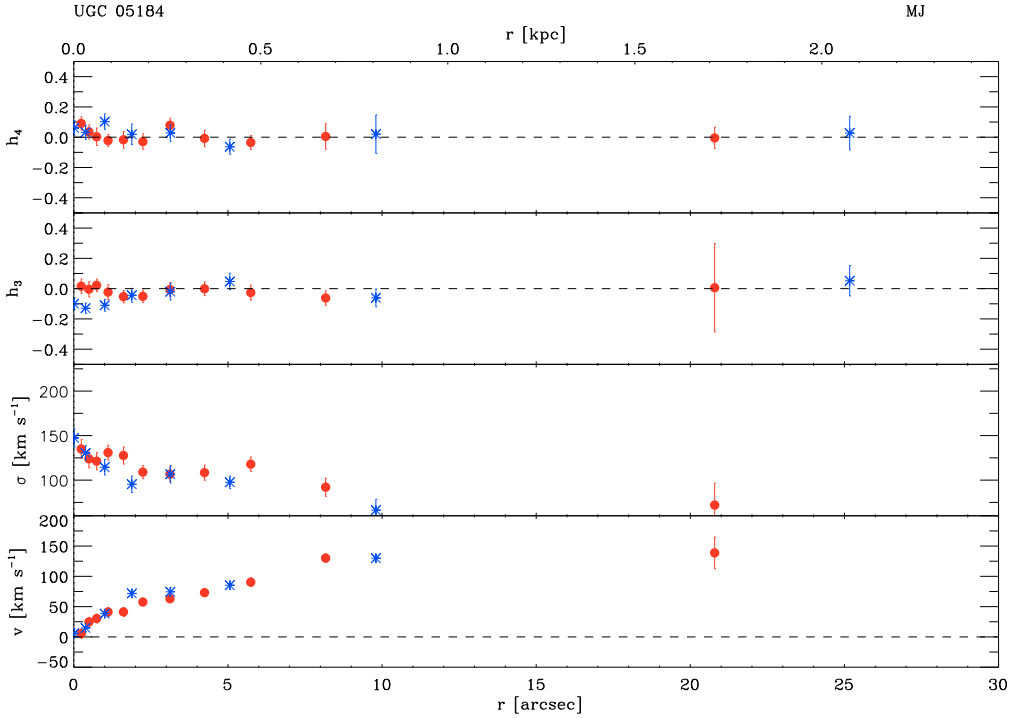

Figure 4.12: Continued.

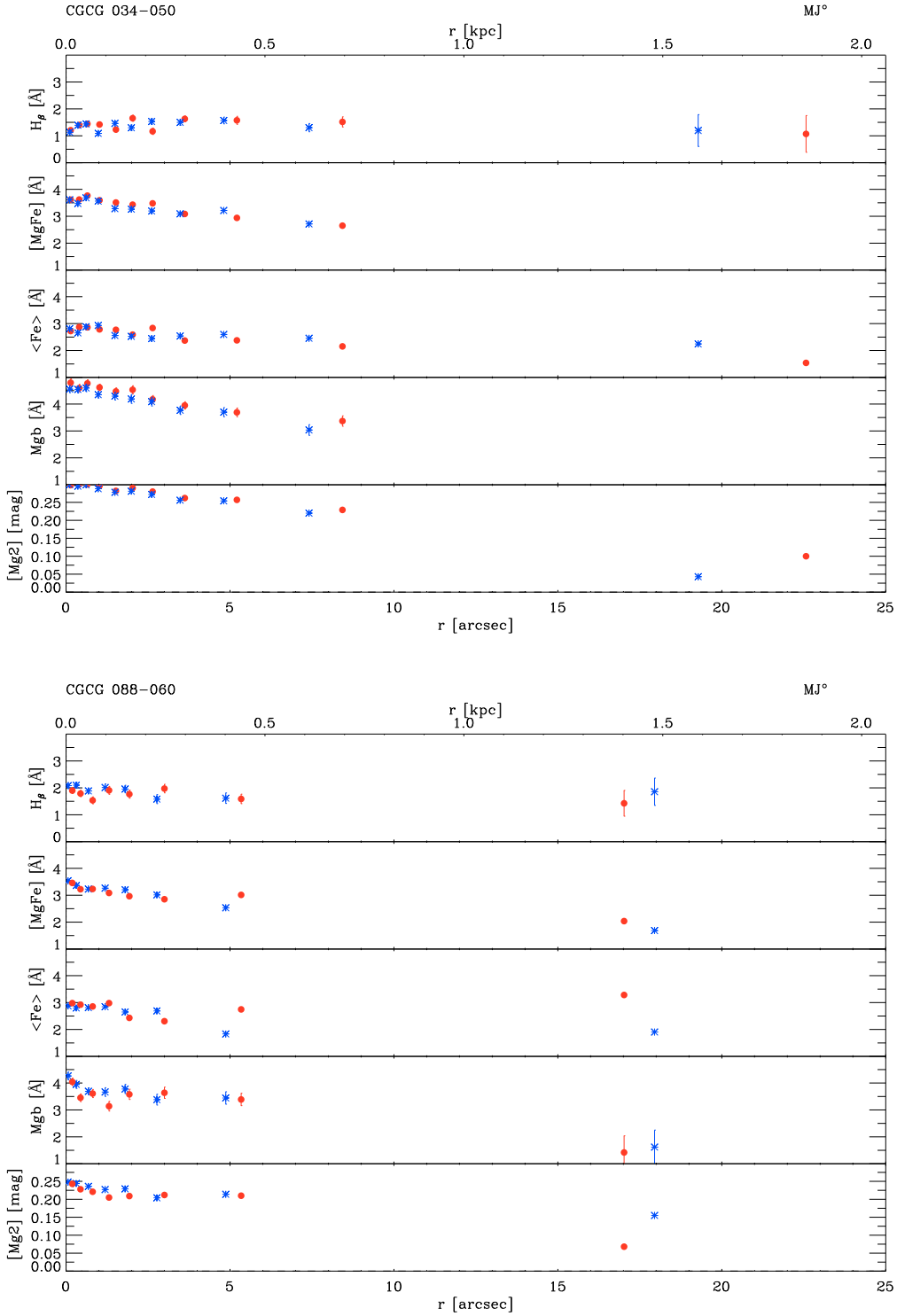

Figure 4.13: Lick index values on the major axis, plotted as a function of radius. Indices on the ordinates are, from top to bottom, Hβ, [MgFe]$'$, $\langle$Fe$\rangle$, Mgb and Mg$_2$. Symbols and colours are as in Figure 4.12.

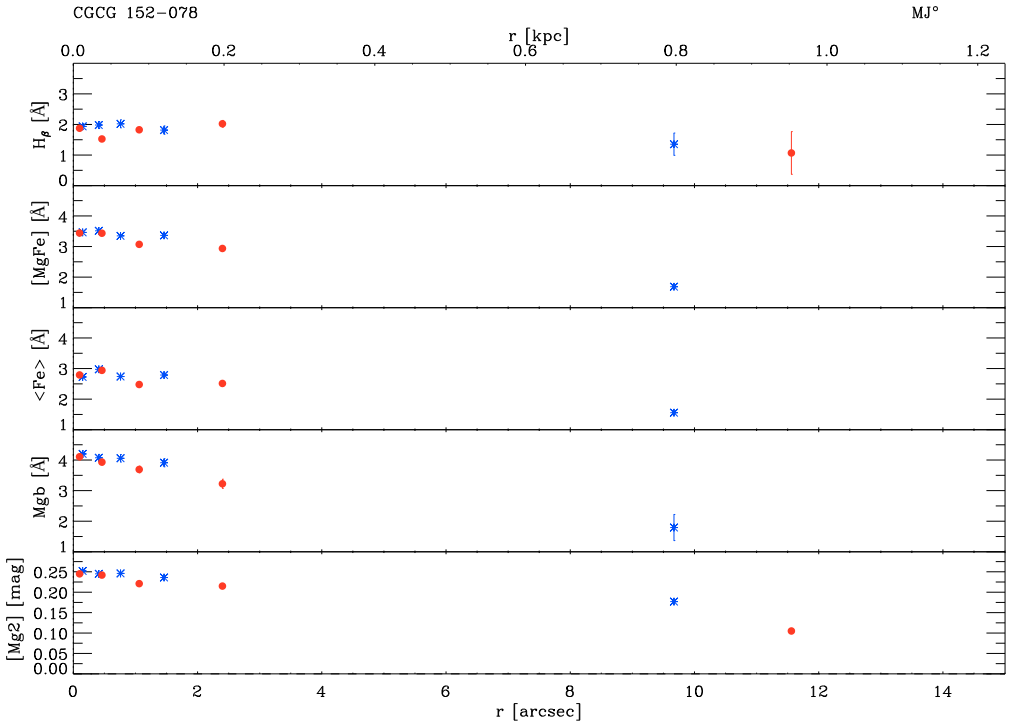

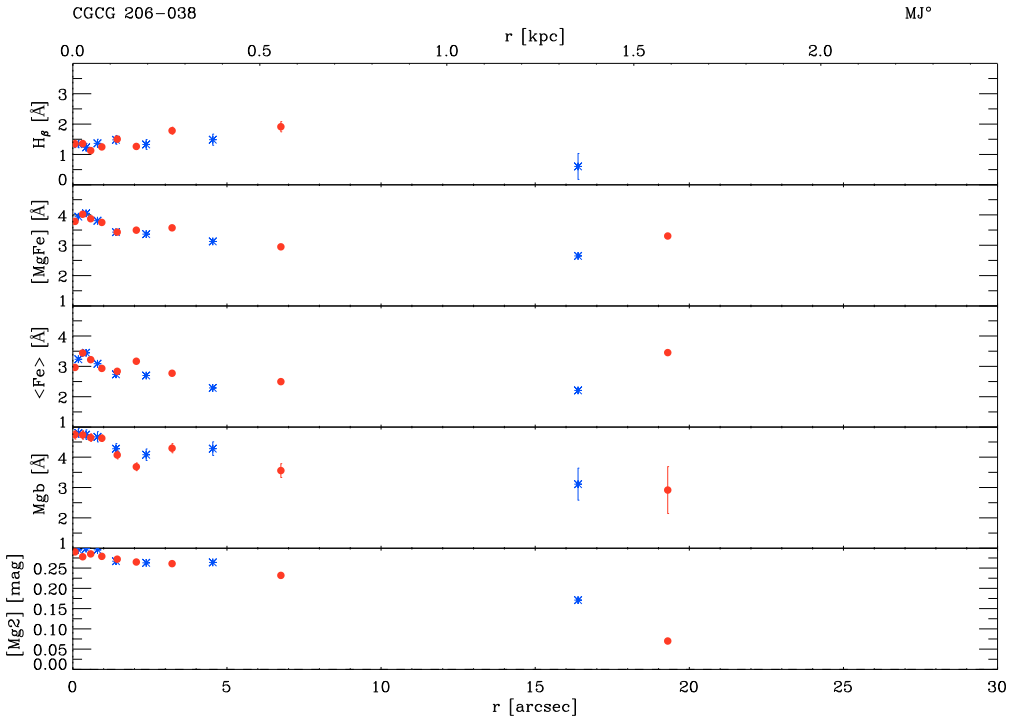

Figure 4.13: Continued.

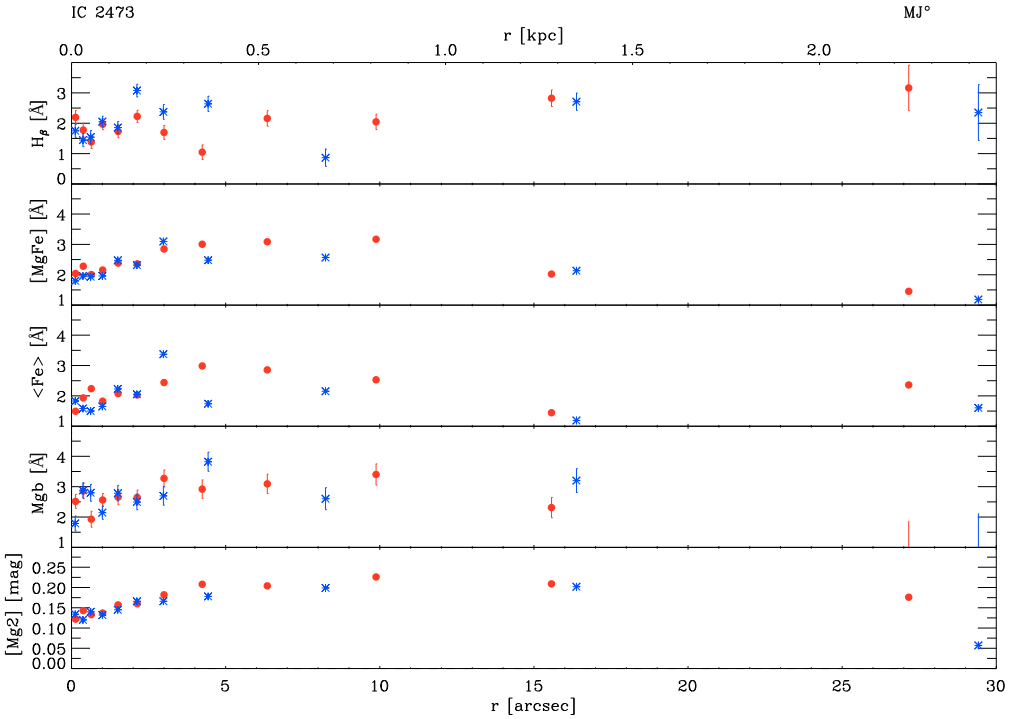

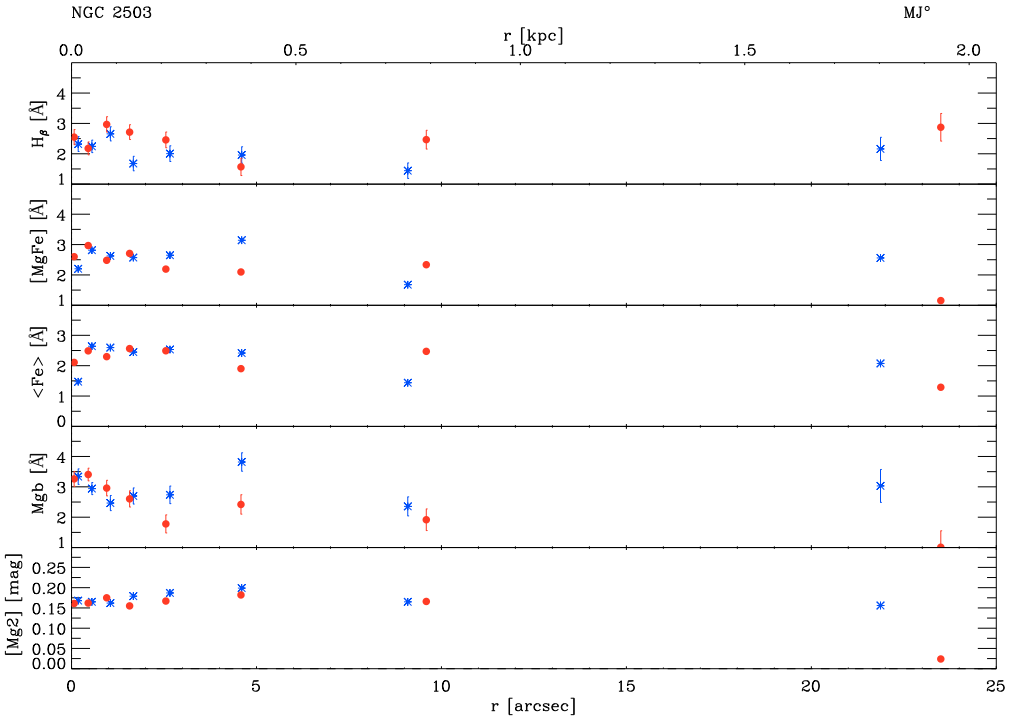

Figure 4.13: Continued.

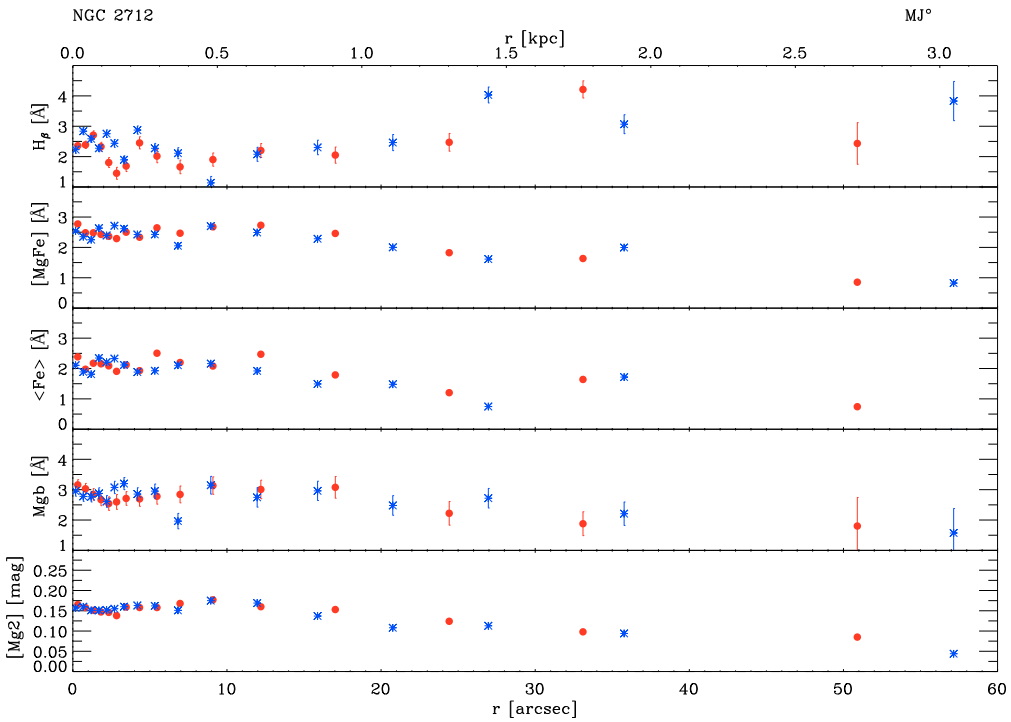

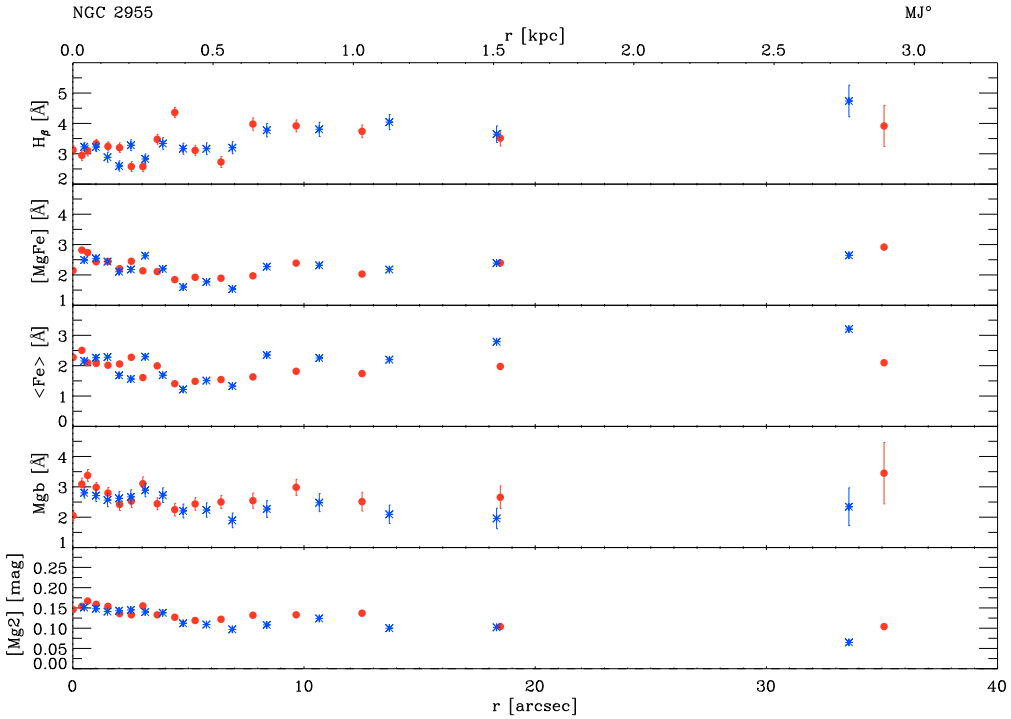

Figure 4.13: Continued.

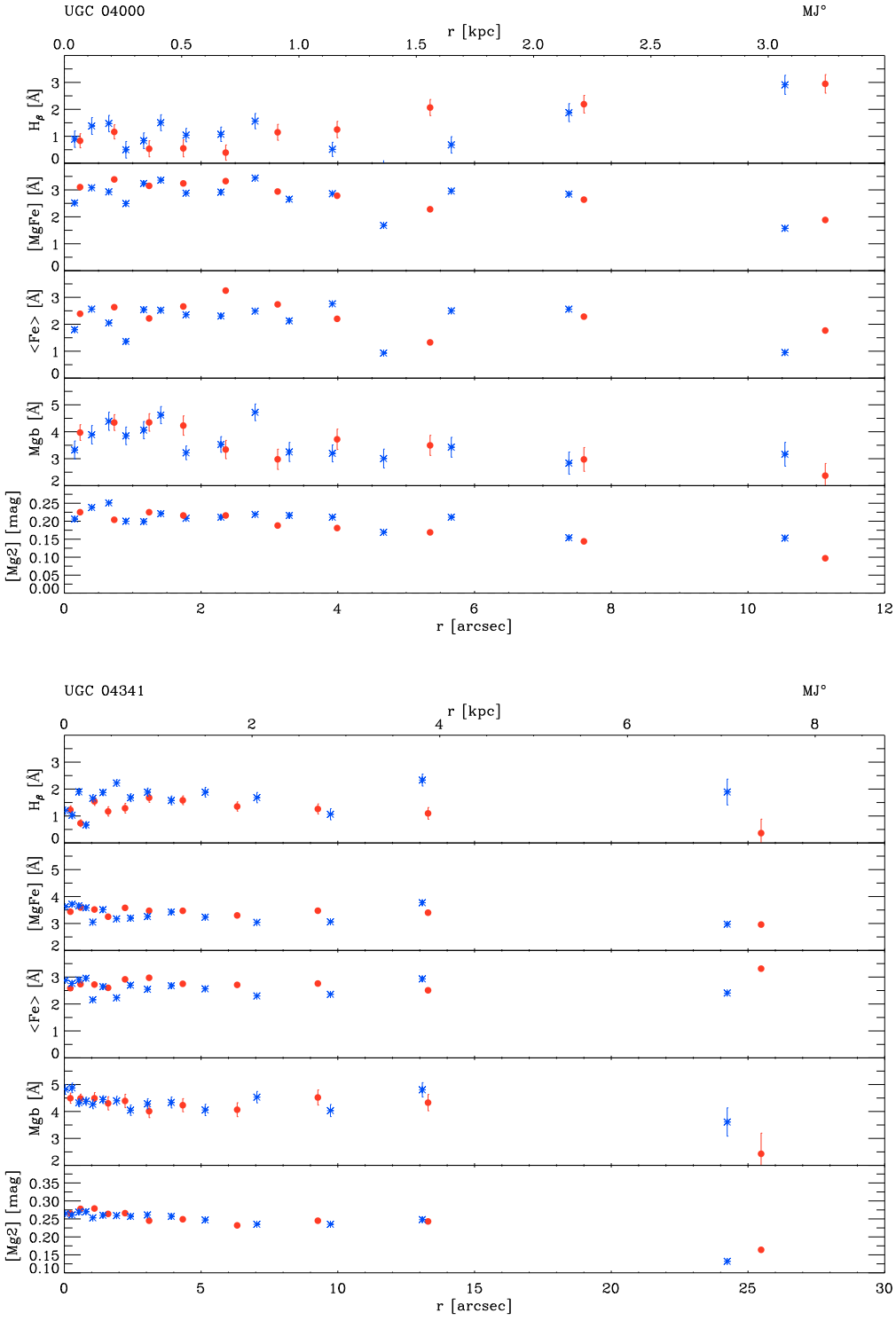

Figure 4.13: Continued.

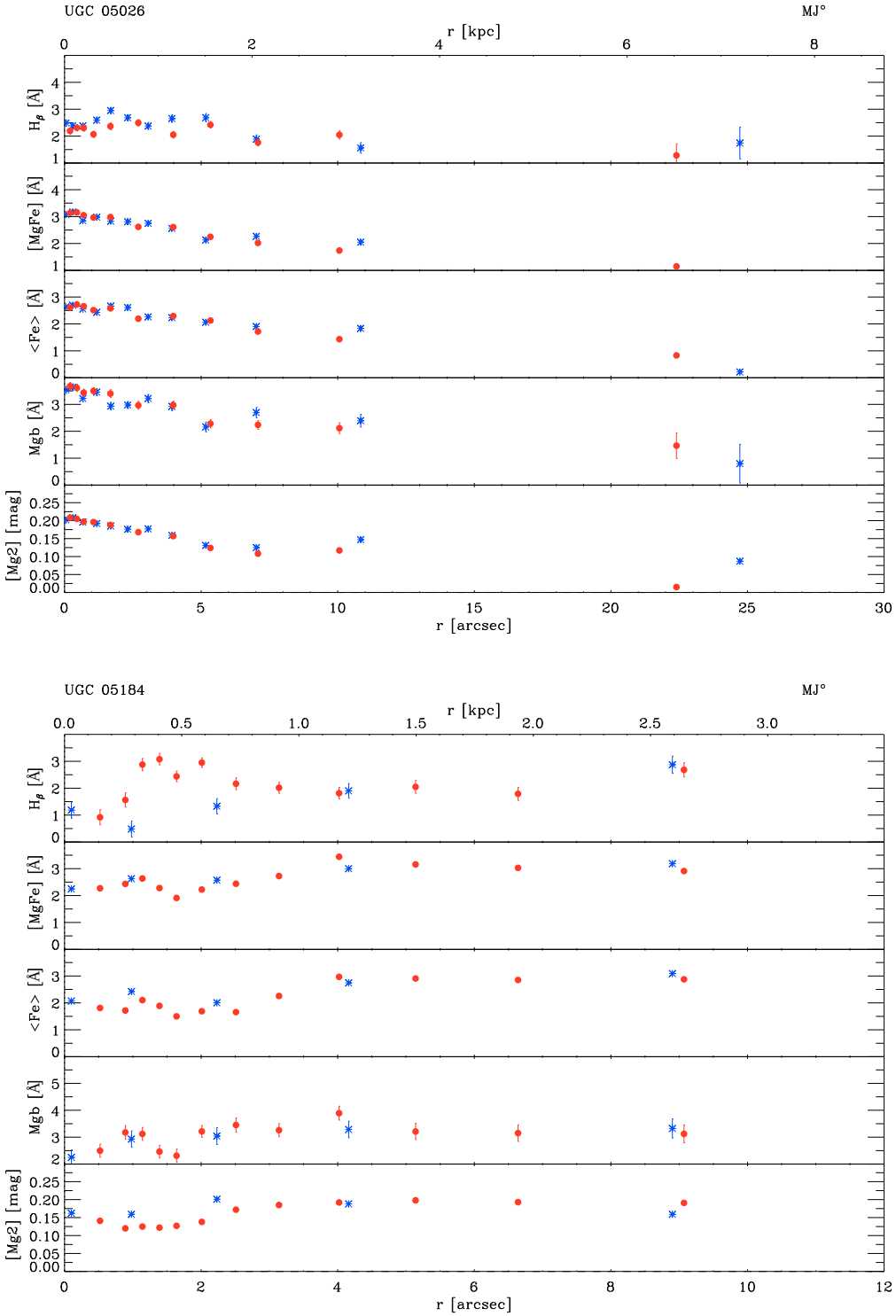

Figure 4.13: Continued.

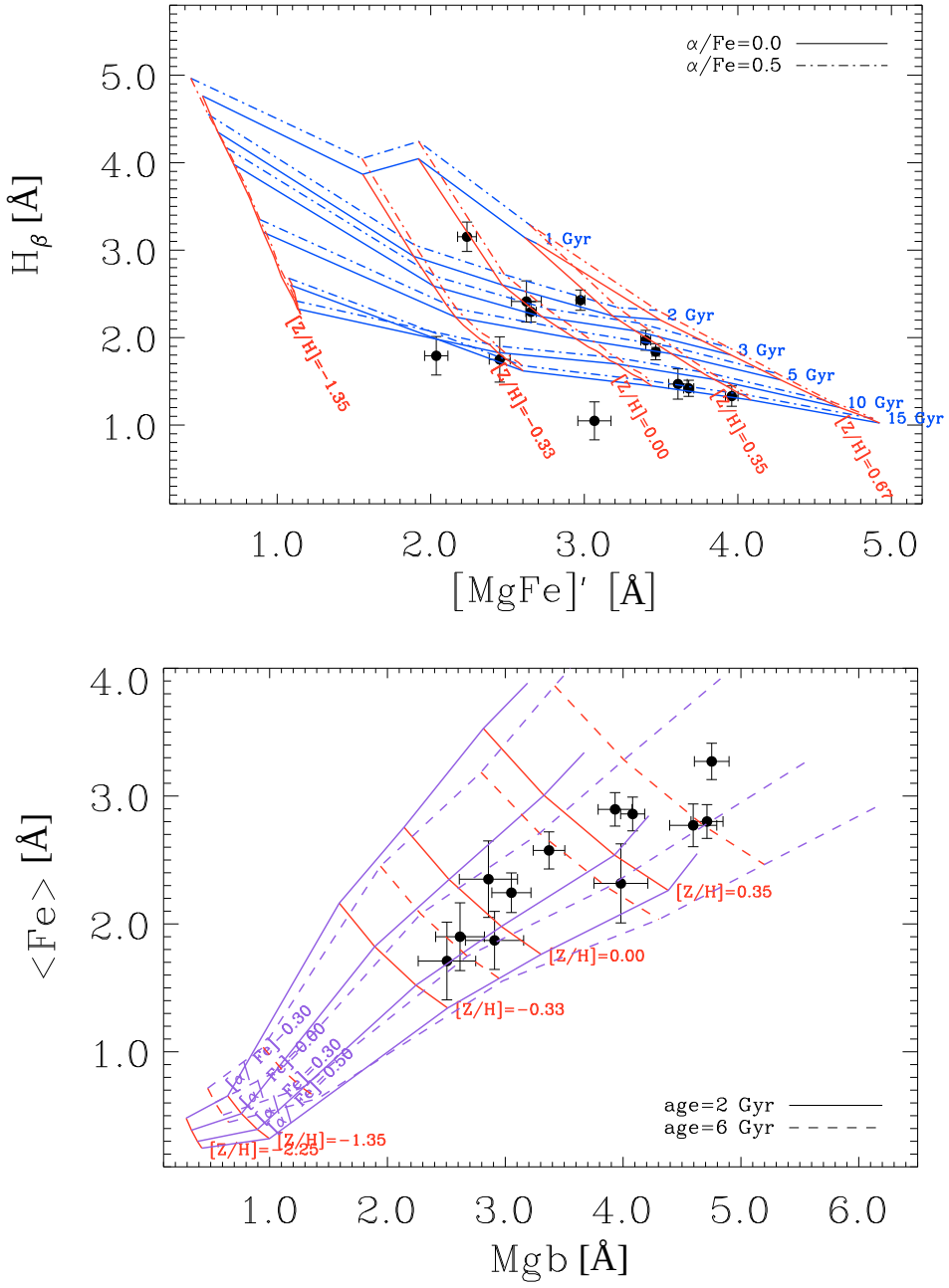

Figure 4.14: The distribution of the central values of Hβ and [MgFe]$'$ indices (top panel) and $\langle$Fe$\rangle$ and Mgb indices (bottom panel) measured over an aperture of $0.3r_{\rm e}$ for the sample galaxies. The lines indicate the models by Thomas et al. (2003). In the top panel the age-metallicity grids are plotted with two different α/Fe enhancements: [α/Fe]$=$ 0.0 dex (continuous lines) and [α/Fe]$=$ 0.5 dex (dashed lines). In the bottom panel the [α/Fe] ratio-metallicity grids are plotted with two different ages: 2 Gyr (continuous lines) and 6 Gyr (dashed lines).

Table 4.6: Central values for σ and Lick line-strength indices for the sample of isolated disc galaxies.

Galaxy	σ [km s^{-1}]	$\langle$Fe$\rangle$ [Å]	[MgFe]$'$ [Å]	Mg$_2$ [mag]	Mgb [Å]	Hβ [Å]	Fe5270 [Å]	Fe5335 [Å]
CGCG 034-050	112.6 ± 28.8	2.801 ± 0.132	3.680 ± 0.033	0.299 ± 0.012	4.712 ± 0.136	1.420 ± 0.092	2.925 ± 0.140	2.747 ± 0.124
CGCG 088-060	65.4 ± 7.5	2.896 ± 0.131	3.400 ± 0.032	0.241 ± 0.004	3.932 ± 0.144	1.969 ± 0.114	2.997 ± 0.138	2.794 ± 0.124
CGCG 152-078	108.6 ± 4.4	2.860 ± 0.132	3.465 ± 0.023	0.246 ± 0.003	4.081 ± 0.102	1.838 ± 0.092	3.046 ± 0.143	2.673 ± 0.121
CGCG 206-038	147.2 ± 6.1	3.271 ± 0.142	3.960 ± 0.041	0.290 ± 0.009	4.752 ± 0.147	1.331 ± 0.116	3.299 ± 0.131	3.243 ± 0.152
IC 2473	136.2 ± 11.9	1.710 ± 0.304	2.036 ± 0.076	0.130 ± 0.010	2.505 ± 0.244	1.792 ± 0.220	1.585 ± 0.304	1.835 ± 0.305
NGC 2503	77.6 ± 9.7	2.350 ± 0.299	2.623 ± 0.097	0.166 ± 0.007	2.857 ± 0.247	2.413 ± 0.236	2.482 ± 0.307	2.219 ± 0.291
NGC 2712	108.2 ± 8.6	2.244 ± 0.155	2.653 ± 0.034	0.161 ± 0.005	3.052 ± 0.166	2.294 ± 0.116	2.386 ± 0.143	2.102 ± 0.166
NGC 2955	128.2 ± 10.7	1.900 ± 0.265	2.236 ± 0.061	0.139 ± 0.008	2.616 ± 0.207	3.153 ± 0.168	1.928 ± 0.245	1.872 ± 0.285
UGC 4000	147.4 ± 10.6	2.317 ± 0.309	3.066 ± 0.108	0.218 ± 0.003	3.981 ± 0.229	1.048 ± 0.217	2.418 ± 0.281	2.215 ± 0.338
UGC 4341	192.5 ± 6.2	2.771 ± 0.167	3.610 ± 0.060	0.268 ± 0.010	4.595 ± 0.200	1.469 ± 0.173	2.917 ± 0.165	2.625 ± 0.169
UGC 5026	121.9 ± 3.1	2.575 ± 0.145	2.975 ± 0.029	0.194 ± 0.009	3.371 ± 0.134	2.428 ± 0.116	2.687 ± 0.140	2.463 ± 0.151
UGC 5184	130.9 ± 8.4	1.871 ± 0.227	2.449 ± 0.068	0.130 ± 0.007	2.909 ± 0.247	1.750 ± 0.259	2.289 ± 0.264	1.478 ± 0.189

Table 4.7: Central values of age, metallicity, and [α/Fe] ratio for the bulges in the sample of isolated disc galaxies.

Galaxy	Age [Gyr]	[Z/H] [dex]	[α/Fe] [dex]
CGCG 034-050	14.7 ± 2.7	0.14 ± 0.06	0.22 ± 0.05
CGCG 088-060	4.0 ± 1.4	0.30 ± 0.09	0.12 ± 0.06
CGCG 152-078	5.4 ± 1.7	0.27 ± 0.07	0.15 ± 0.06
CGCG 206-038	14.9 ± 3.8	0.28 ± 0.09	0.11 ± 0.05
IC 2473	15.0 ± 2.0	-0.65 ± 0.10	0.21 ± 0.15
NGC 2503	2.6 ± 1.3	0.00 ± 0.12	0.08 ± 0.14
NGC 2712	3.2 ± 0.8	-0.05 ± 0.06	0.16 ± 0.07
NGC 2955	1.7 ± 0.2	-0.04 ± 0.07	0.24 ± 0.13
UGC 4000	15.0 ± 5.9	-0.14 ± 0.08	0.29 ± 0.11
UGC 4341	13.8 ± 4.8	0.12 ± 0.11	0.22 ± 0.06
UGC 5026	1.9 ± 0.4	0.26 ± 0.06	0.16 ± 0.05
UGC 5184	14.7 ± 4.4	-0.43 ± 0.09	0.26 ± 0.14

The ages of the sample bulges have a bimodal distribution (Figure 4.15, left-hand panel) with about half of them being old (14-15 Gyr) and the remaining ones characterised by a young-to-intermediate age (1-5 Gyr). Such a large range of ages for the bulges of isolated galaxies is consistent with the results obtained by Katkov et al. (2015). We measured prominent emission lines, which are indicative of on-going star formation, only in the centre of sample galaxies with younger bulges and found no correlation between the bulge age and the presence of a bar (Table 4.4. The metallicity of the sample bulges spans a large range of values (Figure 4.15, middle panel) from high ($[Z/\mathrm{H}] = 0.3$ dex) to sub-solar metallicity ($[Z/\mathrm{H}] = -0.7$ dex). On the contrary, the $[\alpha/\mathrm{Fe}]$ enhancement of the sample bulges is characterised by a narrow distribution of super-solar values ($[\alpha/\mathrm{Fe}] = 0.1 - 0.3$ dex) peaked at $[\alpha/\mathrm{Fe}] = 0.2$ dex (Figure 4.15, right-hand panel).

In Figure 4.15 the number distributions of the age, metallicity, and α/Fe enhancement of the bulges of our sample of isolated galaxies are compared to those found by Morelli et al. (2008), who carried out a similar analysis on the bulge stellar populations of galaxies in groups and clusters. The isolated galaxies show a large fraction of very old bulges, which are not observed in group and cluster galaxies. There is no difference in the bulge metallicity distribution for most of the isolated galaxies with respect to the group and cluster galaxies, except for a couple of bulges with a very low metallicity. The most significant difference between the bulges of isolated galaxies and those of group and cluster galaxies is represented by the very different distributions of their $[\alpha/\mathrm{Fe}]$ ratios. The bulges of isolated galaxies have systematically higher values of α/Fe enhancement. This implies a difference in the star-formation timescale with the inner regions of isolated bulges being formed more rapidly with respect to bulges in high density environments.

The metallicity and α/Fe enhancement are well correlated with the central velocity dispersion in early-type galaxies (Mehlert et al. 2003; Spolaor et al. 2010) and in bulges of high (Ganda et al. 2007; Morelli et al. 2008) and low surface-brightness galaxies (Morelli et al. 2012). Cosmological hydrodynamic simulations (De Lucia et al. 2004; Tassis et al. 2008) and chemodinamycal models (Matteucci 1994; Kawata & Gibson 2003; Kobayashi 2004) demonstrated that these relations are the result of a mass-dependent star formation efficiency. High mass galaxies have a higher efficiency in converting gas-phase metals into new stars, giving rise to less prolonged star formation events and higher α/Fe enhancements. Our findings suggest that this is also true for the bulges of isolated galaxies. We conclude that the most massive bulges of our sample are more metal rich and characterised by a shorter star-formation timescale.

Finally, we looked for a possible correlation between the stellar population properties of the sample bulges and the morphology of their host galaxies. Indeed, very shallow correlations were found by Ganda et al. (2007) and Morelli et al. (2008) whereas Thomas & Davies (2006) and Morelli et al. (2012) did not observe any trend. However, we did not find any correlation between the galaxy morphological type and age, metallicity, or

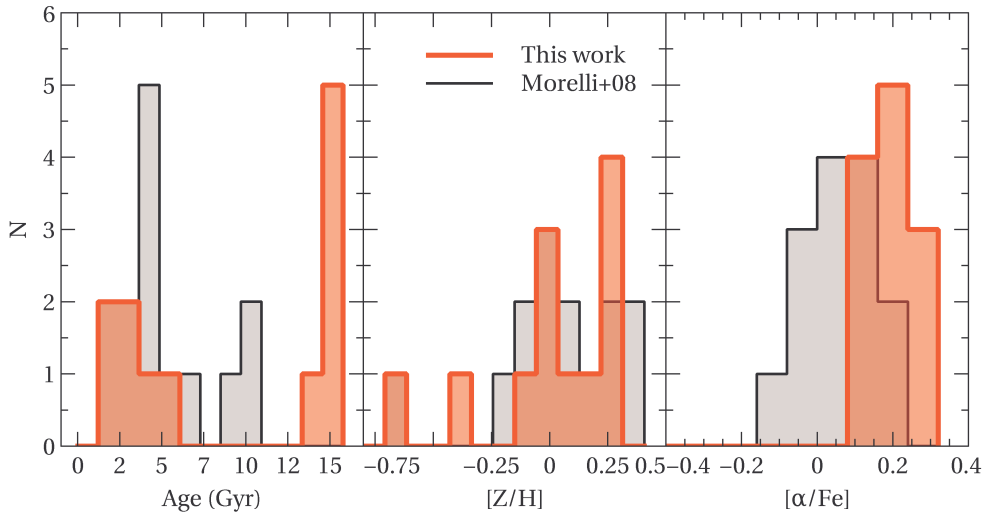

Figure 4.15: Distribution of age (left-hand panel), metallicity (central panel), and α/Fe enhancement (right-hand panel) for the stellar population of the bulges of the sample galaxies (red histograms). The distribution of the same quantities for the bulges of group and cluster galaxies studied by Morelli et al. (2008) is plotted for a comparison (grey histograms).

α/Fe enhancement of bulges in isolated galaxies (Figure 4.16). The absence of these correlations could be an indication that the stellar populations of the bulges and discs in isolated galaxies had an independent evolution.

4.5.3 Radial gradients of age, metallicity, and [α/Fe] enhancement

Different formation scenarios predict different radial trends of age, metallicity, and α/Fe enhancement. Therefore, the gradients of the stellar population properties within bulges are one of the most important diagnostics to understand the processes regulating their assembly.

From the theoretical point of view a steep metallicity gradient is expected in bulges forming through pure monolithic collapse scenarios (Eggen et al. 1962; Larson 1974; Arimoto & Yoshii 1987) and their modern versions (Kawata 2001; Kobayashi 2004). Gas dissipation toward the galaxy centre with subsequent occurrence of star formation and blowing of galactic winds produce the metallicity gradient. A relation between the steepening of the gradient and mass is also expected (Pipino et al. 2010). A strong gradient in the α/Fe enhancement is expected too (Ferreras & Silk 2002). However, Pipino et al. (2008) suggested that together with the outside-in scenario, other important processes need to be considered to explain the origin of the abundance ratios. The interplay between the star formation timescale and the gas flows is very important, since

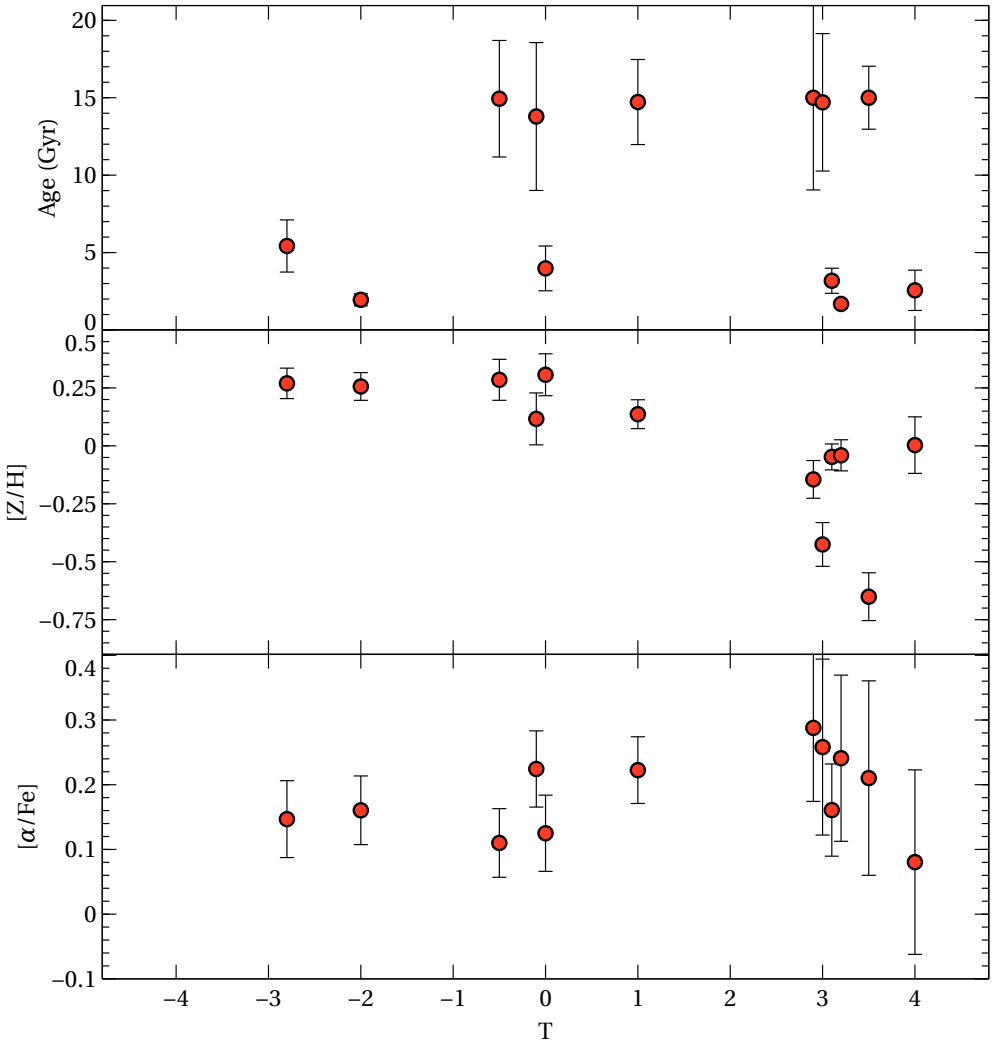

Figure 4.16: Correlation between the central values of age, metallicity, and α enhancement with morphological type of the sample galaxies.

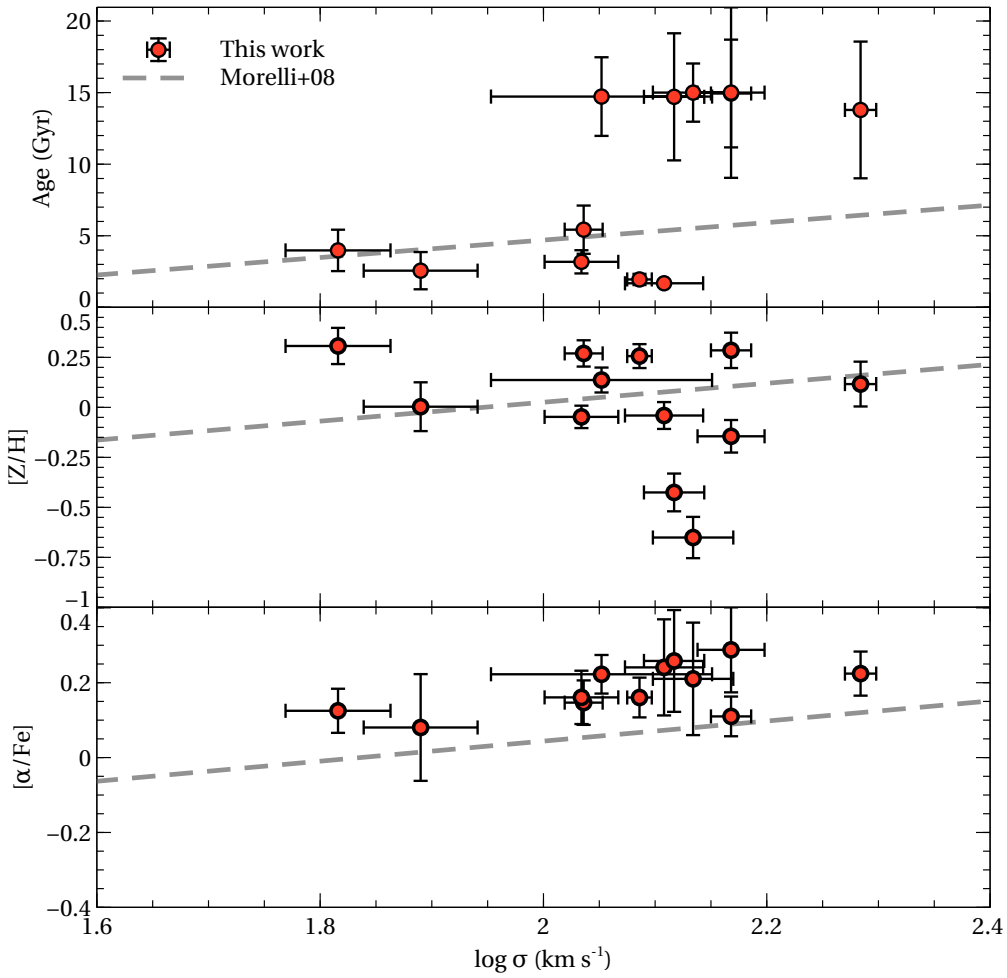

Figure 4.17: Age (upper panel), metallicity (middle panel), and α/Fe enhancement (lower panel) of the stellar populations of the bulges of the sample galaxies as a function of galaxy morphological type. In each panel the dashed line represents the correlation found by Morelli et al. (2008) for the bulges of group and cluster galaxies.

it acts both in flattening the α/Fe gradient and in enabling the galaxy to harbour a metallicity gradient (Pipino et al. 2008).

On the contrary, the metallicity gradient is expected to be very shallow or absent when it is investigated in merger-based models (Bekki & Shioya 1999). This is due to the fact that a mergers mix up all the stars in the galaxy removing the gradients. Secondary star formation, eventually happening during a wet merger, only rarely steepens the gradient (Kobayashi 2004). If this happens, a clear trace should remain in the age profile for several Gyr (Hopkins et al. 2009a) whereas dry mergers flatten all the pre-existing gradients (Pipino et al. 2010).

The predictions for bulges forming through a long timescale process, such as the dissipationless secular evolution of the disc component, are more contradictory. In this scenario the bulge is formed by the redistribution of disc stars. The gradients eventually present in the progenitor disc could be either amplified, since the resulting bulge has a smaller scalelength than the progenitor, or erased, as a consequence of disc heating (Moorthy & Holtzman 2006).

An issue in measuring the gradients of the age, metallicity, and α/Fe enhancement in bulges could be the contamination of their stellar population by the light coming from the underlying disc stellar component. To account for the light contamination from the disc component, we mapped the radial gradients up to the radius $r_{\rm bd}$ where the surface brightness contribution of the bulge component is equal to the contribution from the other components (see Section 4.3.4). Although it was not possible to completely remove the contribution from the disc, limiting the analysis to the radius $r_{\rm bd}$ ensured us that the degree of contamination is the same across all the sample of galaxies. For each galaxy, we derived the values of the Hβ, [MgFe]$'$, $\langle$Fe$\rangle$, and Mgb line-strength indices at $r_{\rm bd}$ and computed the corresponding age, metallicity, and α/Fe enhancement of the stellar population using the models by Thomas et al. (2003), as described in the previous section. The gradient of each stellar population property was derived as the difference between the value derived at $r_{\rm bd}$ and the central value obtained within $0.1R_{\rm e}$. The uncertainties on the resulting gradients were calculated using Monte Carlo simulations, taking into account the errors on the line-strength indices out to $r_{\rm bd}$. The gradients of age, metallicity, and α/Fe enhancement of the sample bulges are listed in Table 4.8 and their number distributions are shown in Figure 4.18.

Almost all the sample bulges show a null or very shallow age gradients with a distribution peaked at Δ(age)$=$ 0. The only exception is the bulge of CGCG 034-050 (Δ(age)$=$ -5.1 ± 4.7 Gyr) because the bulges of both CGCG 088-060 and NGC 4341 are consistent within the errors with Δ(age)$=$ 0 in spite of their large age gradients. Our findings are in agreement with previous results for early-type galaxies (Mehlert et al. 2003; Sánchez-Blázquez et al. 2006; Spolaor et al. 2010) and late-type bulges Jablonka et al. (2007). The number distribution of the age gradients of the bulges in isolated galax-

Table 4.8: Gradients of age, metallicity, and α/Fe enhancement of the stellar populations of the sample bulges derived from the central values and values at the radius $r_{\rm bd}$ where the surface-brightness contributions of the bulge and remaining components are equal

Galaxy	$r_{\rm bd}$ [arcsec]	Δ(Age) [Gyr]	$\Delta([Z/H]$)	$\Delta([\alpha/Fe])$
CGCG 034-050	5.7	-5.11 ± 4.7	-0.10 ± 0.07	-0.04 ± 0.10
CGCG 088-060	2.4	4.60 ± 5.7	-0.37 ± 0.11	-0.12 ± 0.11
CGCG 152-078	3.8	0.99 ± 2.1	-0.21 ± 0.10	-0.10 ± 0.09
CGCG 206-038	2.8	2.25 ± 4.2	-0.29 ± 0.08	-0.08 ± 0.07
IC 2473	3.7	–	–	–
NGC 2503	1.8	-0.12 ± 4.2	0.02 ± 0.18	-0.10 ± 0.17
NGC 2712	3.8	1.00 ± 2.3	-0.11 ± 0.08	-0.09 ± 0.14
NGC 2955	4.1	0.01 ± 0.5	-0.00 ± 0.09	0.02 ± 0.17
UGC 4000	4.2	–	–	–
UGC 4341	2.3	4.03 ± 4.2	-0.34 ± 0.19	-0.06 ± 0.12
UGC 5026	6.1	0.14 ± 0.9	-0.14 ± 0.07	-0.04 ± 0.10
UGC 5184	1.2	-1.81 ± 2.1	0.17 ± 0.13	-0.07 ± 0.19

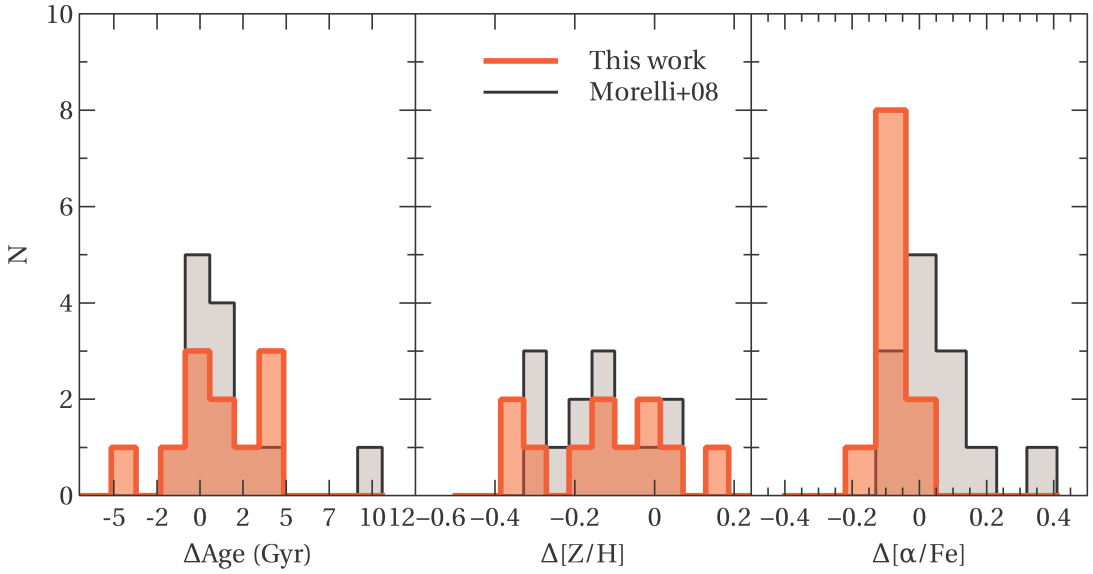

Figure 4.18: Distribution of the gradients of age (left-hand panel), metallicity (central panel) and α/Fe enhancement (right-hand panel) for the sample bulges (red histograms). The distribution of the same quantities for the bulges of group and cluster galaxies studied by Morelli et al. (2008) is plotted for a comparison (grey histograms).

ies is remarkably similar to that of bulges in group and cluster galaxies (Figure 4.18, left-hand panel) suggesting that the age distribution inside bulges is almost insensitive to environment.

The metallicity gradients of all the sample bulges are negative or null, with the exception of UGC 5184 that has a slightly positive gradient ($\Delta([Z/\mathrm{H}]) = 0.17$ dex). Negative metallicity gradients were also measured in early-type galaxies (Proctor & Sansom 2002; Mehlert et al. 2003; Sánchez-Blázquez et al. 2006; Rawle et al. 2010) and in bulges of spiral galaxies Jablonka et al. (2007); Morelli et al. (2015a). They are expected for bulges assembled through a process of dissipative collapse (Kobayashi 2004). As for the age gradients, the number distributions of the metallicity gradients of the bulges hosted in isolated or in group and cluster galaxies are very similar to each other (Figure 4.18, central panel) suggesting the same formation scenario for bulges in different environments.

The gradients of α/Fe enhancement are negative or null for all the sample bulges and display a number distribution with a remarkable peak at $\Delta([\alpha/\mathrm{Fe}]) = -0.1$ dex (Figure 4.18, right-hand panel). This is a particularly interesting finding since it is in contrast with previous results obtained for early-type galaxies (Mehlert et al. 2003; Sánchez-Blázquez et al. 2006; Spolaor et al. 2010) bulges of unbarred (Jablonka et al. 2007) and barred galaxies (Sánchez-Blázquez et al. 2011; de Lorenzo-Cáceres et al. 2012), and bulges of group and cluster galaxies (Morelli et al. 2008). The [α/Fe] ratio is commonly used as a proxy of the star formation timescale in galaxies (Thomas et al. 2005) because it is regulated by the different contributions to the enrichment of the interstellar medium caused by Type II and Type I supernovae (Matteucci & Greggio 1986). Therefore, we conclude that the star formation process was more prolonged in the outer parts of the sample bulges than in their central regions. Numerical simulations predict for dissipative collapse a strong inside-out formation process for bulges which gives rise to a negative gradient in the α/Fe enhancement (Ferreras & Silk 2002). Therefore, the negative gradients of α/Fe enhancement found in the bulges of isolated galaxies is consistent with the predictions of a dissipative collapse formation scenario.

The central values and gradients of metallicity and α/Fe enhancement of the sample bulges are plotted in Figure 4.19.

As Morelli et al. (2008) and Rawle et al. (2010), we found a tight linear correlation between the central values and gradients of metallicity (Figure 4.19, left-hand panel) with a slope consistent with that given by Morelli et al. (2008). If confirmed with a more firm statistics, this correlation is a further indication of the importance of dissipative collapse in the assembly of bulges (Arimoto & Yoshii 1987; Pipino et al. 2010). We did not find any correlation between the central values and gradients of α/Fe enhancement (Figure 4.19, right-hand panel) as also pointed out by Morelli et al. (2008) and Rawle et al. (2010).

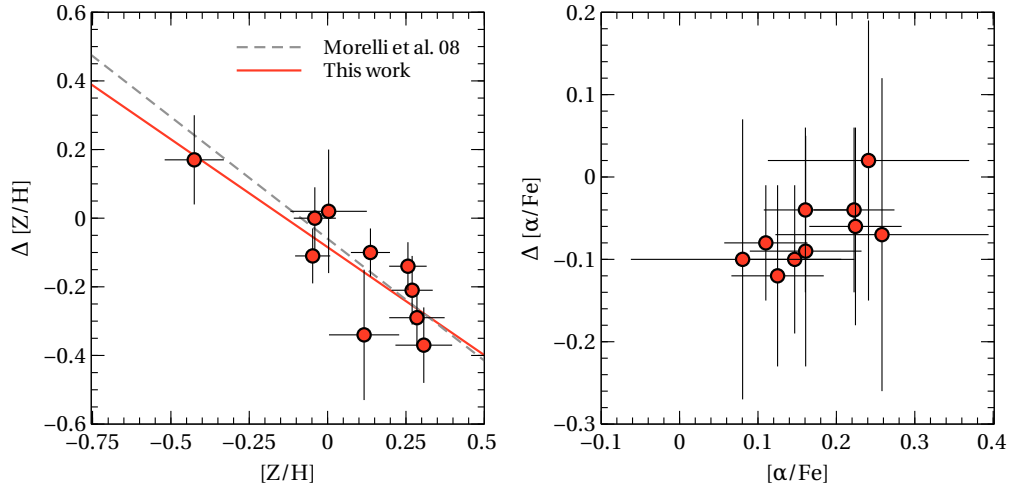

Figure 4.19: Stellar population propery gradients as function of the central value for metallicity (*left panel*) and [α/Fe] (*right panel*). The solid red line in the left diagram represents the linear least-squares fit to the data, while the dashed gray line is the linear relation found by Morelli et al. (2008) for bulges of galaxies in groups and clusters.

4.6 Conclusions

We derived the photometric structural parameters, stellar kinematics, and stellar population properties of a sample of 12 isolated galaxies to constrain the dominant mechanism in the assembly of their bulges. To this aim the properties of the sample bulges were compared with those of bulges in galaxies residing in groups and clusters.

- The bulge and disc parameters of the sample galaxies were derived performing a 2D photometric decomposition of their SDSS $i-$band images. The surface-brightness distribution of each galaxy was assumed to be the sum of the contribution of a Sérsic bulge and an exponential disc. Three sample galaxies host a bar and we included a Ferrers bar component in the fit procedure. The model parameters from the 2D decomposition were used to identify the bulge-dominated radial range by measuring the radius $r_{\rm bd}$, where the bulge contribution to the integrated light starts to dominate over the light from the remaining components.

- The stellar kinematics and radial profiles of the line-strength indices Mgb, Mg$_2$, H$_\beta$, $\langle$Fe$\rangle$ were measured from the major-axis spectra obtained at TNG. The kinematics of all the galaxies is very regular giving further support to the idea that these objects are not suffering interactions with the neighbour galaxies. The correlations between Mg$_2$, $\langle$Fe$\rangle$, and σ were found to be consistent with those for bulges of group and cluster galaxies (Idiart et al. 1996; Prugniel et al. 2001; Proctor &

Sansom 2002).

- The age, metallicity, and α/Fe enhancement were derived for all the sample bulges. They are characterized by a bimodal age distribution with intermediate-age ($\sim$ 3 Gyr) and old systems ($\sim$ 15 Gyr), a large spread in metallicities ranging from sub- to super-solar values, and α/Fe enhancements peaked at [α/Fe] = 0.2. The higher [α/Fe] ratios found for bulges of isolated galaxies indicate a shorter star-formation timescale with respect their counterparts in high density environment. The metallicity distribution is very similar for bulges in different environments.

- The absence of a correlation between the bulge stellar populations and galaxy morphology excludes a strong interplay between bulges and discs during their evolution. This conclusion is also supported by the findings of Sil'chenko et al. (2012) and Katkov et al. (2015) who formulated the hypothesis that the morphological type of a field galaxy is determined by the outer-gas accretion.

- The gradients of the stellar population properties were measured within the sample bulges. Most of them have a null age gradient and a negative metallicity gradient. This is in agreement with earlier findings for bulges in cluster (Jablonka et al. 2007; Morelli et al. 2008) and high surface-brightness galaxies (Morelli et al. 2012). All the sample bulges show a negative gradient for the α/Fe enhancement. This is a prediction of the dissipative collapse model of bulge formation and it was never been observed before. The stellar population gradients are believed to be flattened or even erased by merging and acquisition events. Therefore, we suggest that the gradients imprinted during the inside-out formation process are preserved in the bulges of isolated galaxies, which suffered a limited number of interactions and mergers, whereas the gradients are cancelled in the bulges of group and cluster galaxies as a consequence of phenomena driven by environment.

Chapter 5

Stellar populations of the bulges of four spiral galaxies

Abstract

Key information to understand the formation and evolution of disc galaxies are imprinted in the stellar populations of their bulges. In this chapter we present new measurements of the stellar population properties of the bulges of four spiral galaxies. Both the central values and radial profiles of the line strength of some of the most common Lick indices are measured along the major- and minor- axis of the bulge-dominated region of the sample galaxies. The corresponding age, metallicity, and α/Fe ratio are derived by using the simple stellar population synthesis model predictions. The central values and the gradients of the stellar population properties of ESO-LV 1890070, ESO-LV 4460170, and ESO-LV 5140100 are consistent with previous findings for bulges of spiral galaxies. On the contrary, the bulge of ESO-LV 4500200 shows peculiar chemical properties possibly due to the presence of a central kinematically-decoupled component. The negative metallicity gradient found in our bulges sample indicates a relevant role for the dissipative collapse in bulge formation. However, the shallow gradients found for the age and α/Fe ratio suggests that merging can not be completely ruled out for the sample bulges. This is confirmed by the properties of ESO-LV 4500200 which can hardly be explained without invoking the capture of external material.

5.1 Introduction

Due to their privileged position at the bottom of the galactic potential well, bulges are a key player in the process of the assembly of disc galaxies. In the current picture, the mechanisms of bulge formation include dissipative collapse (Gilmore & Wyse 1998), merging and acquisition events (Cole et al. 2000), and secular evolution (Kormendy &

Kennicutt 2004). Crucial information to understand the processes of formation and evolution of galaxies is imprinted in their stellar populations and even more in their radial gradients, since different formation scenarios predict different radial trends of age, metallicity, and α/Fe ratio.

In the last years the stellar populations of classical bulges have been spectroscopically studied in detail and compared among different morphological types and different environments in both lenticular (Rampazzo et al. 2005; Sánchez-Blázquez et al. 2006; Collobert et al. 2006; Annibali et al. 2007; Rawle et al. 2010; Kuntschner et al. 2010; Spolaor et al. 2010) and spiral galaxies (Moorthy & Holtzman 2006; Jablonka et al. 2007; Morelli et al. 2008; MacArthur et al. 2009; Morelli et al. 2012, 2013). The central values and radial gradients of age, metallicity, and α/Fe ratio have been derived for a large number of galaxies. The variety of the results testifies the complexity of the topic. The bulk of the stellar population can have a range of ages among different bulges and this is generally related with the morphological type (Ganda et al. 2007). The values of the α/Fe ratio, ranging from solar to super-solar, give a time-scale for star formation from 4-5 Gyr to less than 1 Gyr (Thomas & Davies 2006). The only common feature for all the bulges (independently from their morphological type and environment) is the negative radial gradient of metallicity. All these properties support formation scenarios related to an early formation through violent relaxation or dissipative collapse are favoured over those of secular evolution.

To further investigate this topic, Morelli et al. (2012) analyzed a sample of bulges embedded in low surface-brightness discs. Low surface-brightness galaxies are believed to not have experienced major merging events during their lifetime. The radial profiles of their age, metallicity, and α/Fe ratio confirm also for these bulges the violent relaxation as possible formation mechanism. Furthermore, the comparison between ordinary high and low surface-brightness galaxies shows that their bulges share many structural and chemical properties. Such similarity suggests that they possibly had common formation scenarios and evolution histories and indicates that there is not a relevant interplay between the bulge and disc components. All these results downsize the role of the secular evolution in the formation scenarios of the classical bulges, independently of the high or low surface-brightness of the host disc. However, secular evolution could still be the main mechanism responsible for the formation of pseudobulges (Kormendy et al. 2009).

In this chapter, we present new measurements of the central values and radial profiles of the line strength of some of the most common Lick indices for the bulges hosted by four spiral galaxies. These data are a valuable supplementary resource for the astronomical community. Indeed, the derived values of age, metallicity, and α/Fe ratio can be used for further comparison between the stellar populations of galactic components.

The sample of galaxies is described in the Section 5.2. In Section 5.3 we briefly

outline the photometric decomposition technique, in Section 5.4 we present the Lick index measurements and in Section 5.5 we employ the index measurements to derive the stellar population parameters of the bulges in the sample. We summarize and present our conclusions in Section 5.6.

5.2 Galaxy sample

The galaxy sample comprises four spiral galaxies whose basic properties are listed in Table 5.1. They belong to the sample of nearby galaxies studied by Pizzella et al. (2008) who analysed their stellar and ionized-gas kinematics and surface photometry. Pizzella et al. (2008) were interested in spiral galaxies with a low surface-brightness disc and we refer to their paper for the details about the selection criteria of the galaxy sample. ESO-LV 1890070, ESO-LV 4460170, ESO-LV 4500200, and ESO-LV 5140100 turned out to host a high surface-brightness disc and therefore were not considered in the subsequent analysis (Morelli et al. 2012). Since the long-slit spectra of the four neglected galaxies were available to us, we decided to derive the stellar population properties of their bulges.

5.3 Photometric decomposition

In their photometric analysis Pizzella et al. (2008) assumed the surface-brightness distribution of the sample galaxies to be the sum of the contributions of a bulge and a disc component only. We improved their photometric decomposition by including a bar component to precisely identify the bulge-dominated region of each galaxy. In this section we briefly outline the photometric decomposition procedure employed to derive the component parameters. Since the procedure closely follows the one described in Chapter 4, the reader is referred to Section 4.3.3.

The structural parameters of the bulge, disc, and bar components were derived by applying the GASP2D code (Méndez-Abreu et al. 2008, 2014) to the images obtained by Pizzella et al. (2008). Other components (e.g., lenses, ovals, or spiral arms) were not considered.

The surface brightness of the bulge was modelled using a Sérsic function (Sérsic 1968)

$$I_{\rm bulge}(r) = I_{\rm e} 10^{-b_n\left[(r/r_{\rm e})^{1/n}-1\right]}, \tag{5.1}$$

where $r_{\rm e}$ is the effective radius, $I_{\rm e}$ is the surface brightness at $r_{\rm e}$, n is a shape parameter that describes the curvature of the radial profile, and $b_n = 0.868\,n - 0.142$ (Caon et al. 1993). The bulge model was assumed to have elliptical isophotes centred on (x_0, y_0) with constant position angle $\mathrm{PA}_{\rm bulge}$ and constant axial ratio $q_{\rm bulge}$.

The surface brightness of the disc was modelled using an exponential function (Free-

man 1970)

$$I_{\rm disc}(r) = I_0 e^{-r/h}, \tag{5.2}$$

where I_0 is the central surface brightness and h is the scale length. The disc model was assumed to have elliptical isophotes centred on (x_0, y_0) with constant position angle $\mathrm{PA_{disc}}$ and constant axial ratio $q_{\rm disc}$.

The surface brightness of the bar was modelled with a Ferrers function (Ferrers 1877, but see Aguerri et al. 2009 for the choice of the shape parameter)

$$I_{\rm bar}(r) = I_{0,\rm bar}\left[1-\left(\frac{r_{\rm bar}}{a_{\rm bar}}\right)^2\right]^{2.5} \qquad r_{\rm bar} \leq a_{\rm bar}, \tag{5.3}$$

where $I_{0,bar}$ is the central surface brightness and $a_{\rm bar}$ is the bar length. The bar model was assumed to have isophotes described by generalized ellipses (Athanassoula et al. 1990) centred on (x_0, y_0) with constant position angle $\mathrm{PA_{bar}}$ and constant axial ratio $q_{\rm bar}$.

The GASP2D software yields the structural parameters for the bulge ($I_{\rm e}$, $r_{\rm e}$, n, $\mathrm{PA_{bulge}}$ and $q_{\rm bulge}$), disc (I_0, h, $\mathrm{PA_{disc}}$ and $q_{\rm disc}$), and bar ($I_{0,\rm bar}$, $a_{\rm bar}$, $\mathrm{PA_{bar}}$ and $q_{\rm bar}$) and the position of the galaxy centre (x_0, y_0) by iteratively fitting a model of the surface-brightness distribution to the pixels of the galaxy image. It was used a non-linear least-squares minimisation based on a robust Levenberg-Marquardt method (Moré 1978). The actual computation has been done using the MPFIT algorithm (Markwardt 2009) under the IDL. Each image pixel has been weighted according to the variance of its total observed photon counts due to the contribution of both the galaxy and sky, and determined assuming photon noise limitation and taking into account the detector readout noise. The seeing effects were taken into account by convolving the model image with a circular Moffat point spread function with the shape parameters measured directly from stars in the galaxy image.

The best-fitting solution was found by building surface-brightness models with and without the bar component. A bar was detected and modelled in ESO-LV 4460170 and ESO-LV 4500200, whereas no bar was needed to improve the surface-brightness models of ESO-LV 1890070 and ESO-LV 5140100. The bump in the surface-brightness profile associated to both a significant peak in the ellipticity and a roughly constant position angle is the photometric signature of the bar in ESO-LV 4460170 and ESO-LV 4500200 (see Aguerri et al. 2009 for a detailed discussion). The flat surface-brightness profile of ESO-LV 1890070 and the increase of ellipticity measured between 30 and 60 arcsec are due to the two prominent and symmetrical arms characterizing the galaxy spiral pattern. The multi-armed structure of ESO-LV 5140100 results in the increase and variation of the ellipticity between 20 and 40 arcsec.

Figure 5.1 shows the GASP2D fits for the sample galaxies. The best-fitting parameters derived for their structural components are collected in Table 5.2 together with the radius of the bulge-dominated region where half of the total surface brightness is due to the bulge only.

The errors on the best-fitting parameters of the barred galaxies were obtained through a series of Monte Carlo simulations. A set of 500 images of galaxies with a Sérsic bulge, an exponential disc, and a Ferrers bar was generated. The structural parameters of the artificial galaxies were randomly chosen among the ranges obtained for our galaxies. The adopted pixel scale, CCD gain, and read-out-noise were chosen to mimic the instrumental setup of the photometric observations by Pizzella et al. (2008). A background level and photon noise were added to the artificial images to yield a signal-to-noise ratio (S/N) similar to that of the observed ones. Finally, the images of artificial galaxies were analysed with GASP2D as if they were real and the errors on the fitted parameters were estimated by comparing the input and measured values assuming they were normally distributed. The mean and standard deviation of the relative errors of the artificial galaxies were adopted as the systematic and typical errors for the observed galaxies.

5.4 Measurement of the line-strength indices

Major- and minor-axis spectra were obtained for each sample galaxy by Pizzella et al. (2008). All the details about the acquisition and reduction of the galaxy spectra are available in Pizzella et al. (2008) and Morelli et al. (2008).

Mg, Fe, and H β line-strength indices as defined by Faber et al. (1985) and Worthey et al. (1994) were measured from the flux calibrated spectra of the four sample galaxies following Morelli et al. (2004, 2007). The average iron index $\langle \mathrm{Fe} \rangle = (\mathrm{Fe5270} + \mathrm{Fe5335})/2$ (Gorgas et al. 1990) and the combined magnesium-iron index (Thomas et al. 2003)

$$[\mathrm{MgFe}]' = \sqrt{\mathrm{Mg}\, b\, (0.72 \times \mathrm{Fe5270} + 0.28 \times \mathrm{Fe5335})}$$

were measured too.

The difference between the spectral resolution of the galaxy spectra and the Lick/IDS system (FWHM = 8.4 Å; Worthey & Ottaviani 1997) was taken into account by degrading our spectra through a Gaussian convolution to match the Lick/IDS resolution before measuring the line-strength indices. No focus correction was applied because the atmospheric seeing was the dominant effect during observations (see Mehlert et al. 1998, for details). The errors on the line-strength indices were derived from photon statistics and CCD read-out noise, and calibrated by means of Monte Carlo simulations.

The contamination of the H β line-strength index by the H β emission line due to the ionized gas present in the galaxy is a problem when deriving the properties of the stellar populations. Indeed, if the H β emission fills the absorption line and a proper

Table 5.1: Properties of the sample galaxies.

Name	Alt. Name	Type	T	$D_{25} \times d_{25}$ [arcmin]	B_T [mag]	$V_{\rm CMB}$ [km s^{-1}]	D [Mpc]	M_{B_T} [mag]
(1)	(2)	(3)	(4)	(5)	(6)	(7)	(8)	(9)
ESO-LV 1890070	NGC 7140	SABb	3.8	3.0×2.0	12.31	2981	37.5	-20.56
ESO-LV 4460170	...	SBb	3.3	2.2×1.5	13.55	4172	58.9	-20.30
ESO-LV 4500200	NGC 6000	SBbc	4.1	1.9×1.6	13.03	2118	31.6	-19.47
ESO-LV 5140100	IC 4538	SABc	5.1	2.5×1.9	12.88	2888	40.4	-20.13

NOTES: Col.(3): morphological classification from Lyon Extragalactic Database (LEDA). Col.(4): morphological type code from LEDA. Col.(5): apparent isophotal diameters measured at a surface-brightness level of $\mu_B = 25$ mag arcsec^{-2} from LEDA. Col.(6): total observed blue magnitude from LEDA. Col.(7): radial velocity with respect to the CMB radiation from LEDA. Col.(8): distance from Pizzella et al. (2008) adopting $H_0 = 75$ km s^{-1} Mpc^{-1}. Col.(9): absolute total blue magnitude from B_T corrected for extinction as in LEDA and adopting D.

Table 5.2: Structural parameters of the sample galaxies.

Parameter	ESO-LV 1890070	ESO-LV 4460170	ESO-LV 4500200	ESO-LV 5140100
(1)	(2)	(3)	(4)	(5)
$\mu_{\rm e}$ [mag arcsec^{-2}]	18.31 ± 0.13	18.03 ± 0.13	16.31 ± 0.13	19.2 ± 0.07
$r_{\rm e}$ [arcsec]	3.1 ± 0.3	2.6 ± 0.3	1.7 ± 0.2	1.9 ± 0.1
n	1.14 ± 0.17	1.28 ± 0.19	0.98 ± 0.15	1.00 ± 0.10
$q_{\rm bulge}$	0.69 ± 0.06	0.88 ± 0.08	0.72 ± 0.06	0.89 ± 0.04
PA$_{\rm bulge}$ [°]	16.4 ± 1.6	148.7 ± 14.9	134.9 ± 13.5	43.4 ± 4.3
μ_0 [mag arcsec^{-2}]	19.54 ± 0.11	19.70 ± 0.11	18.46 ± 0.12	19.64 ± 0.05
h [arcsec]	31.2 ± 3.1	20.1 ± 2.0	18.1 ± 1.8	25.2 ± 1.5
$q_{\rm disc}$	0.45 ± 0.04	0.58 ± 0.06	0.71 ± 0.07	0.81 ± 0.03
PA$_{\rm disc}$ [°]	21.2 ± 2.1	153.6 ± 15.4	155.4 ± 15.5	45.2 ± 4.5
$\mu_{0,\rm bar}$ [mag arcsec^{-2}]	...	20.68 ± 0.15	17.97 ± 0.15	...
$a_{\rm bar}$ [arcsec]	...	49.1 ± 7.4	25.4 ± 3.8	...
$q_{\rm bar}$	...	0.26 ± 0.03	0.32 ± 0.03	...
PA$_{\rm bar}$ [°]	...	160.6 ± 16.1	172.7 ± 17.3	...
$L_{\rm bulge}/L_{\rm T}$	0.01	0.18	0.09	0.02
$L_{\rm bar}/L_{\rm T}$	...	0.11	0.15	...
$r_{\rm bd}$ [arcsec]	5.60	4.65	2.60	2.50

NOTES. Surface-brightness values are given in R band according to the flux calibration by Pizzella et al. (2008). $L_{\rm bulge}/L_{\rm T}$ is the bulge-to-total luminosity ratio. $L_{\rm bar}/L_{\rm T}$ is the bar-to-total luminosity ratio. $r_{\rm bd}$ is radius of the bulge-dominated region where the bulge contributes the same surface brightness as the other components.

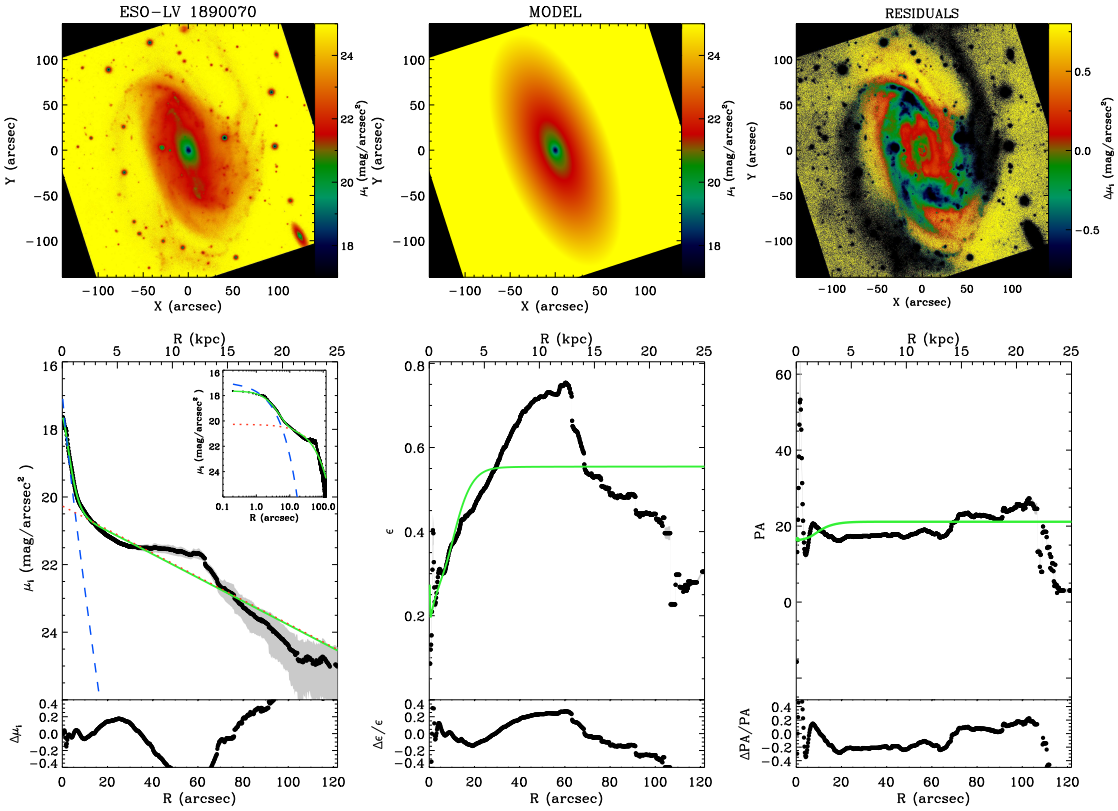

Figure 5.1: Photometric decomposition of the sample galaxies. Top left panel: galaxy image with North up and East left. Top middle panel: best-fitting model of the galaxy image obtained by summing a bulge, a disc, and a bar component. Top right panel: residual image obtained by subtracting the best-fitting model from the galaxy image. Bottom left panel: ellipse-averaged radial profile of surface brightness of the galaxy (black dots) and best-fitting model (green solid line). The light contributions of the bulge (dashed blue line), disc (dotted red line), and bar (dotted-dashed purple line) are shown. The upper inset plots a zoom of the surface-brightness data and fit with a logarithmic scale for the distance to the centre of the galaxy. Bottom middle panel: ellipse-averaged radial profile of ellipticity of the galaxy (black dots) and best-fitting model (green solid line). Bottom right panel: ellipse-averaged radial profile of position angle of the galaxy (black dots) and best-fitting model (green solid line).

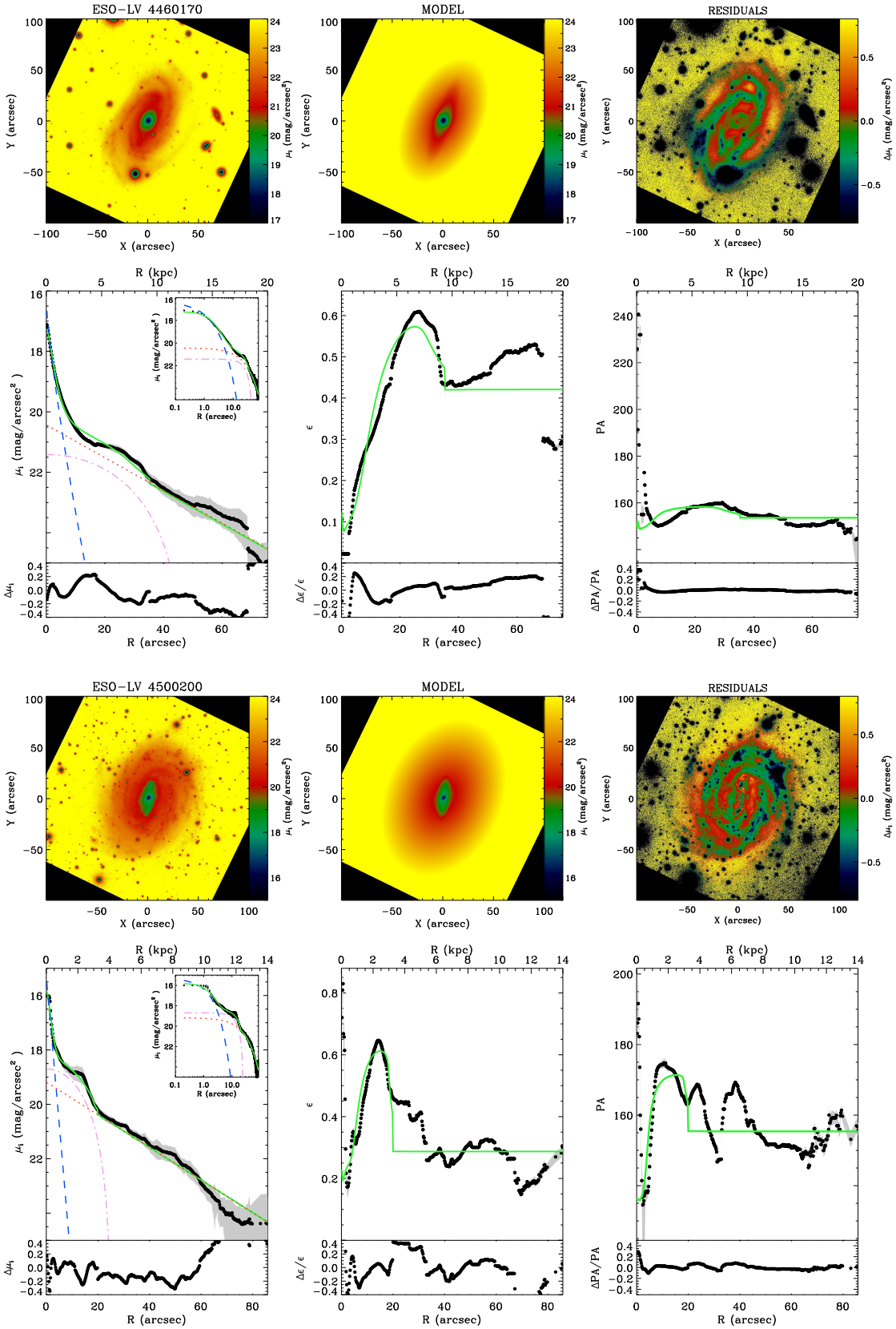

Figure 5.1: Continued.

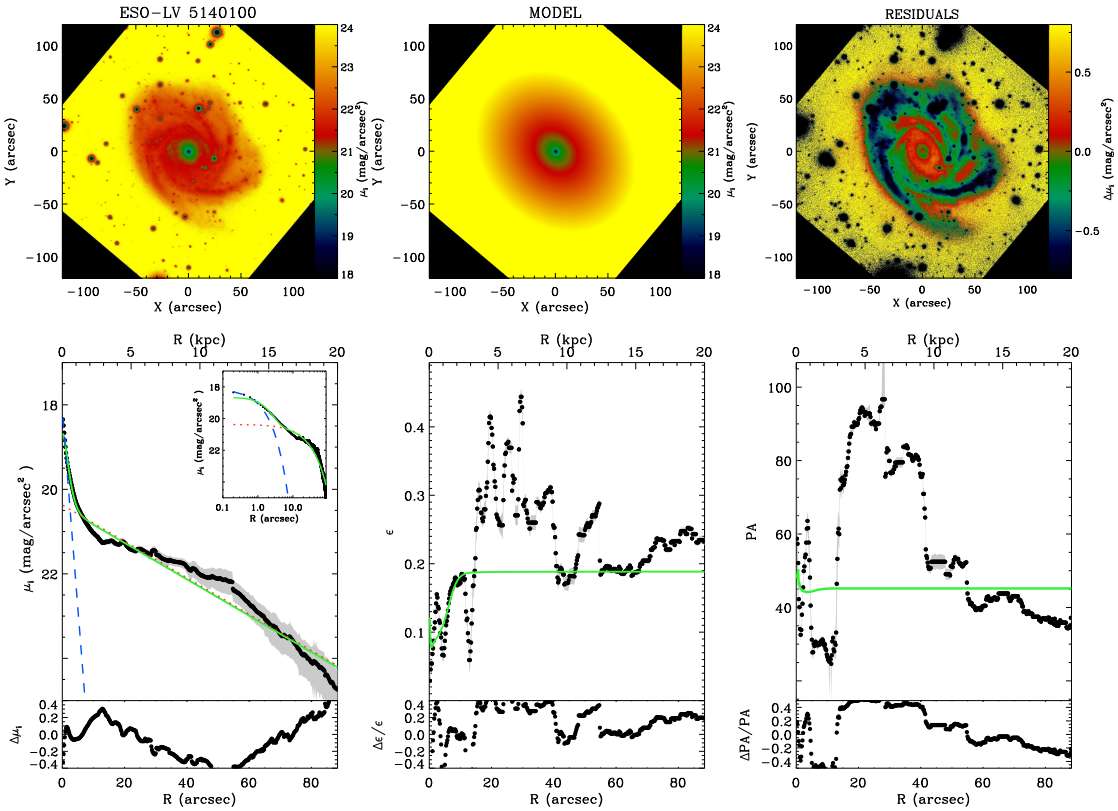

Figure 5.1: Continued.

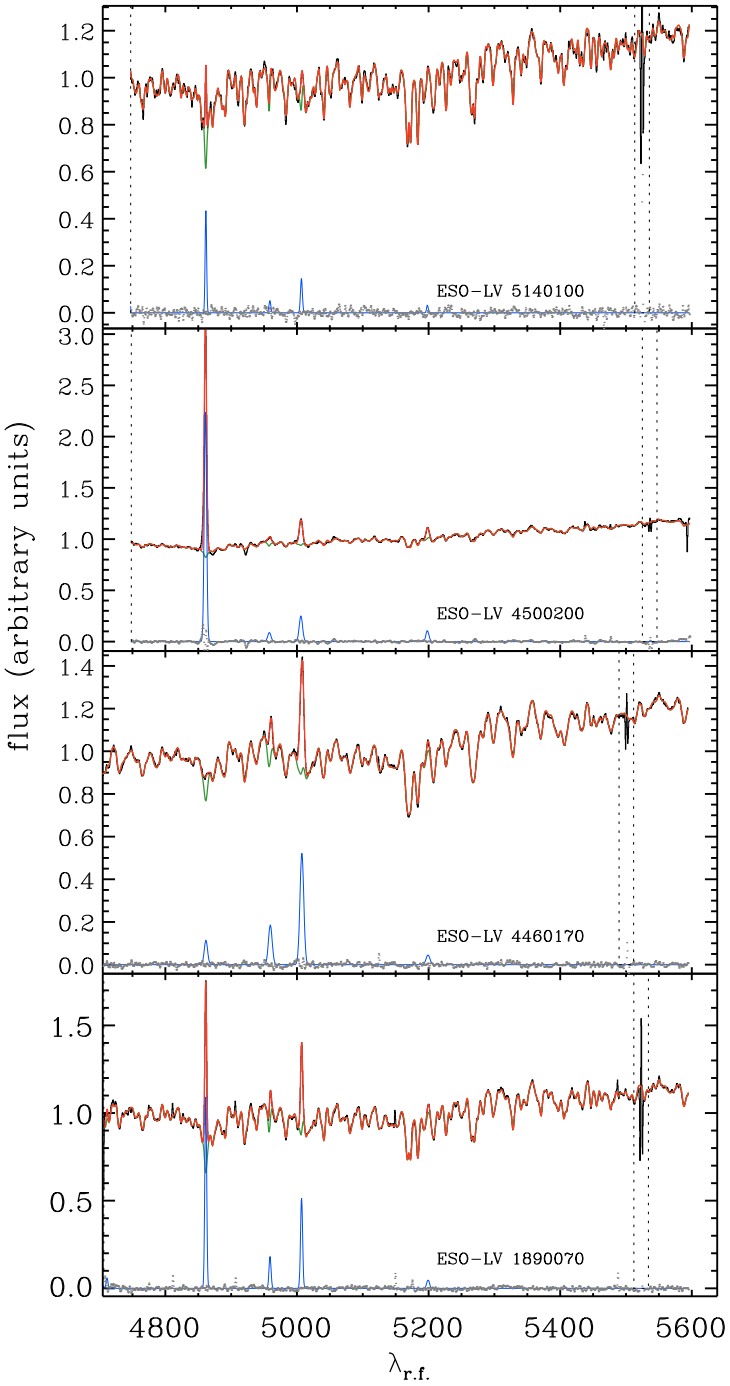

Figure 5.2: Example of central spectra. Relative fluxes have false zero points for viewing convenience. In each panel the best-fitting model (red line) is the sum of the spectra of the ionized-gas (blue line) and stellar component (green line). The latter is obtained convolving the synthetic templates with the best-fitting line-of-sight velocity distribution and multiplying them by the best-fitting Legendre polynomials. The residuals (grey dots) are obtained by subtracting the model from the spectrum. The vertical dashed line corresponds to region masked in fitting the spectra.

separation of both contributions is not performed before the analysis, the measured ages result to be artificially older. To address this issue we adopted the code Gas AND Absorption Line Fitting (GANDALF) to fit the galaxy spectra with synthetic population models as done by Sarzi et al. (2006) and Morelli et al. (2008). The models were built with different templates from the MILES stellar library by Vazdekis et al. (2010). For each spectrum, we fitted a linear combination of stellar population synthesis models to the observed galaxy spectrum by performing a χ^2 minimization in pixel space (Figure 5.2). We adopted the Salpeter initial mass function (Salpeter 1955), ages ranging from 1 to 15 Gyr, and metallicities from -1.31 to 0.22 dex. We simultaneously fitted the observed spectra using emission lines in addition to the stellar templates. Only H β emission lines detected with a $S/N > 3$ were subtracted from the observed spectra. To calibrate our measurements to the Lick/IDS system, the values of the line-strength indices measured for a sample of templates were compared to those obtained by Worthey et al. (1994) as done in Morelli et al. (2012). The offsets obtained were negligible when compared to the mean error of the differences between the tabulated and measured Lick indices. Therefore, no offset correction was applied to our line-strength measurements.

The measured values of H β, [MgFe]$'$, $\langle$Fe$\rangle$, Mgb, and Mg$_2$ for all the sample galaxies are plotted in Figure 5.3.

5.5 Properties of the stellar populations

5.5.1 Central values of age, metallicity, and α/Fe ratio

The central values of velocity dispersion σ and line-strength indices Mgb, Mg$_2$, H β, $\langle$Fe$\rangle$, and [MgFe]$'$ were derived from the major- and minor-axis radial profiles as done in Morelli et al. (2008, 2012). The data points inside an aperture of radius 0.3 r_e were averaged adopting a relative weight proportional to their S/N. The resulting values are listed in Table 5.3.

Figure 5.4 shows the central values of Mg$_2$, H β, and $\langle$Fe$\rangle$ as a function of the velocity dispersion for the sample galaxies. The values and correlations for the bulges of the sample of spiral galaxies with high surface-brightness discs by Morelli et al. (2008) are shown for comparison. The galaxy sample by Morelli et al. (2008) has similar properties to those of the galaxies studied in this chapter. Three galaxies in our sample follow the trends obtained by Morelli et al. (2008) whereas ESO-LV 4500200 has a lower abundance of $\alpha-$ and iron elements with respect to galaxies with similar central velocity dispersion, as shown by the lower values of Mg$_2$ and $\langle$Fe$\rangle$. ESO-LV 4500200 is also characterized by a lower value of H β. It is worth noticing that Pizzella et al. (2008) found a kinematically-decoupled and dynamically cold component in the nucleus ($r \simeq$ 2 arcsec) of this galaxy. Such a structure compromises the central stellar velocity dispersion and affects the values of the Lick indices. This is indirectly confirmed from the

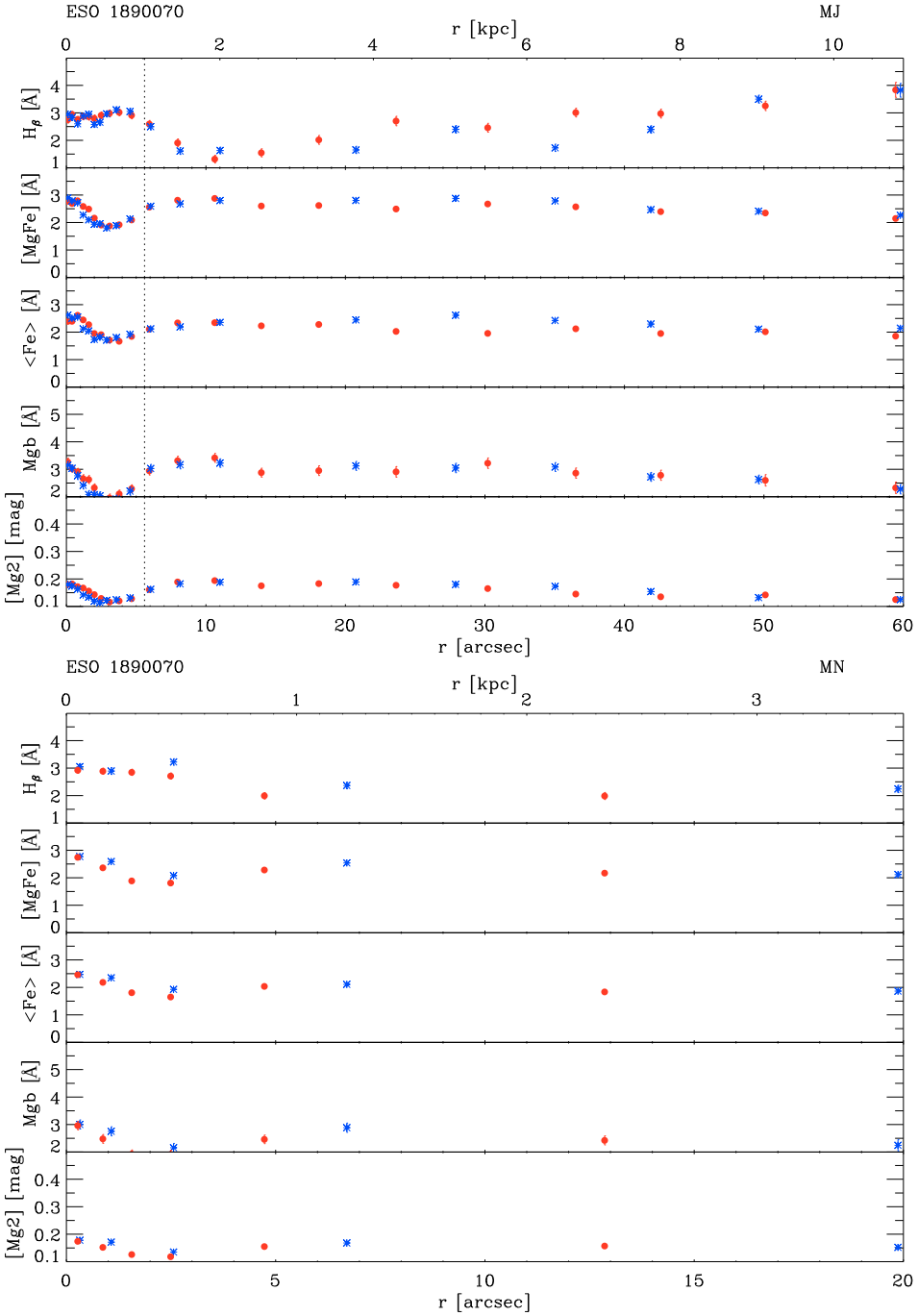

Figure 5.3: Line-strength indices measured along the available axes of the sample galaxies. For each axis, the curves are folded around the nucleus. Blue asterisks and red dots refer to data measured along the approaching and receding sides of the galaxy, respectively. The radial profiles of the line-strength indices H β, [MgFe]$'$, $\langle$Fe$\rangle$, Mgb, and Mg$_2$ are shown (panels from top to bottom). The vertical dotted line corresponds to the radius $r_{\rm bd}$ (Morelli et al. 2008) where the surface-brightness is dominated by the light of the bulge. For each data set, the name of the galaxy and the location of the slit position (MJ = major axis and MN = minor axis) are given.

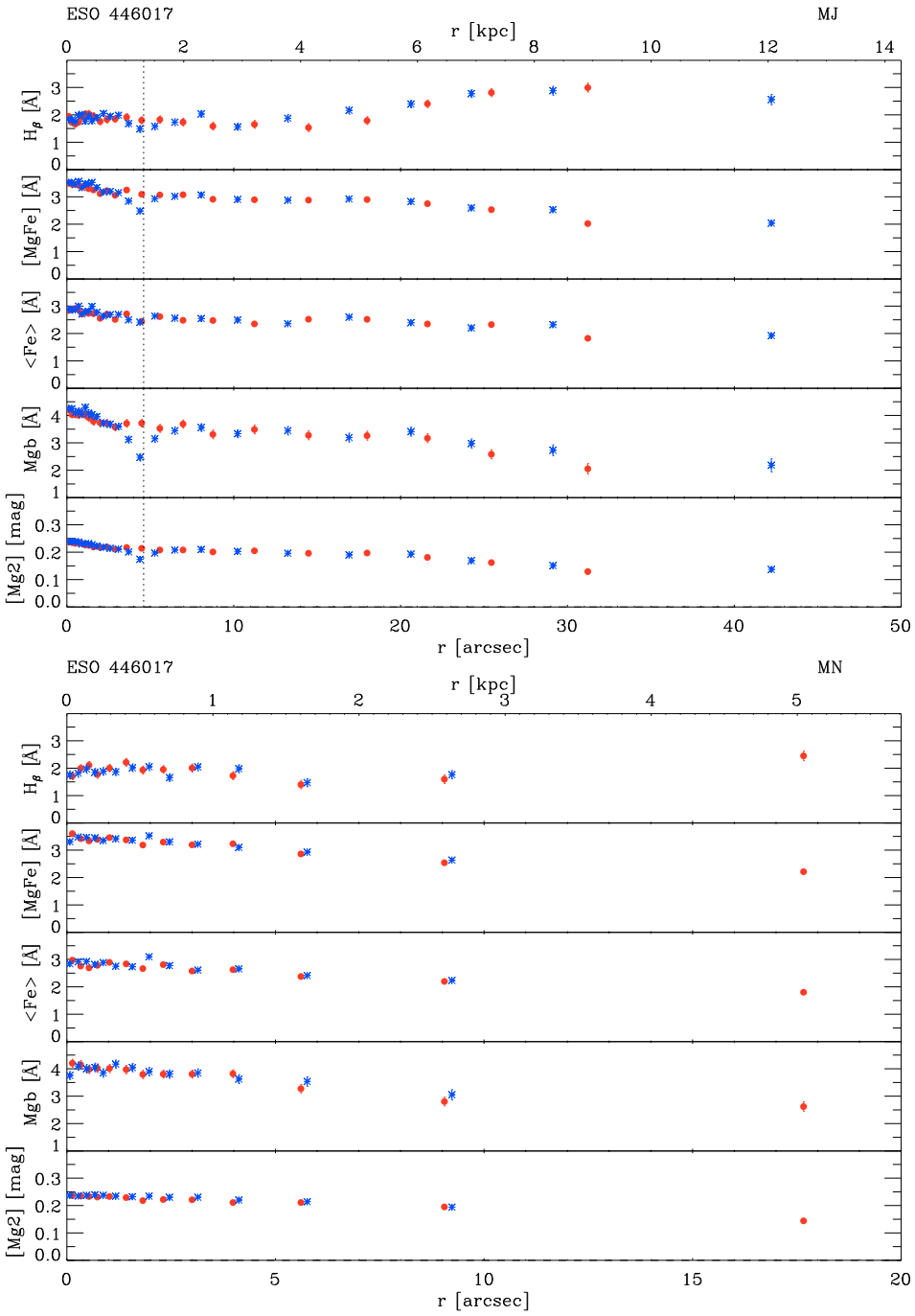

Figure 5.3: Continued.

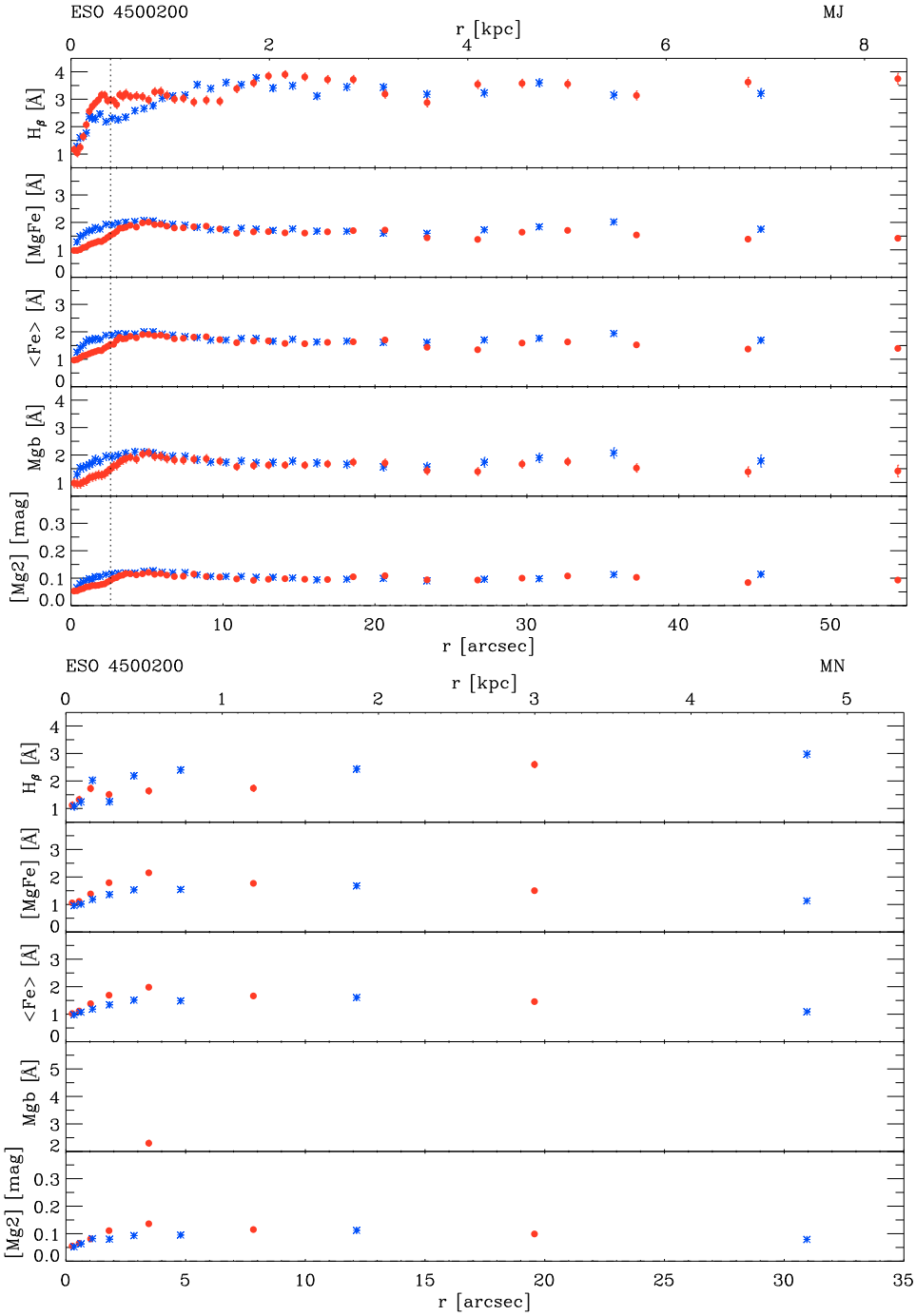

Figure 5.3: Continued.

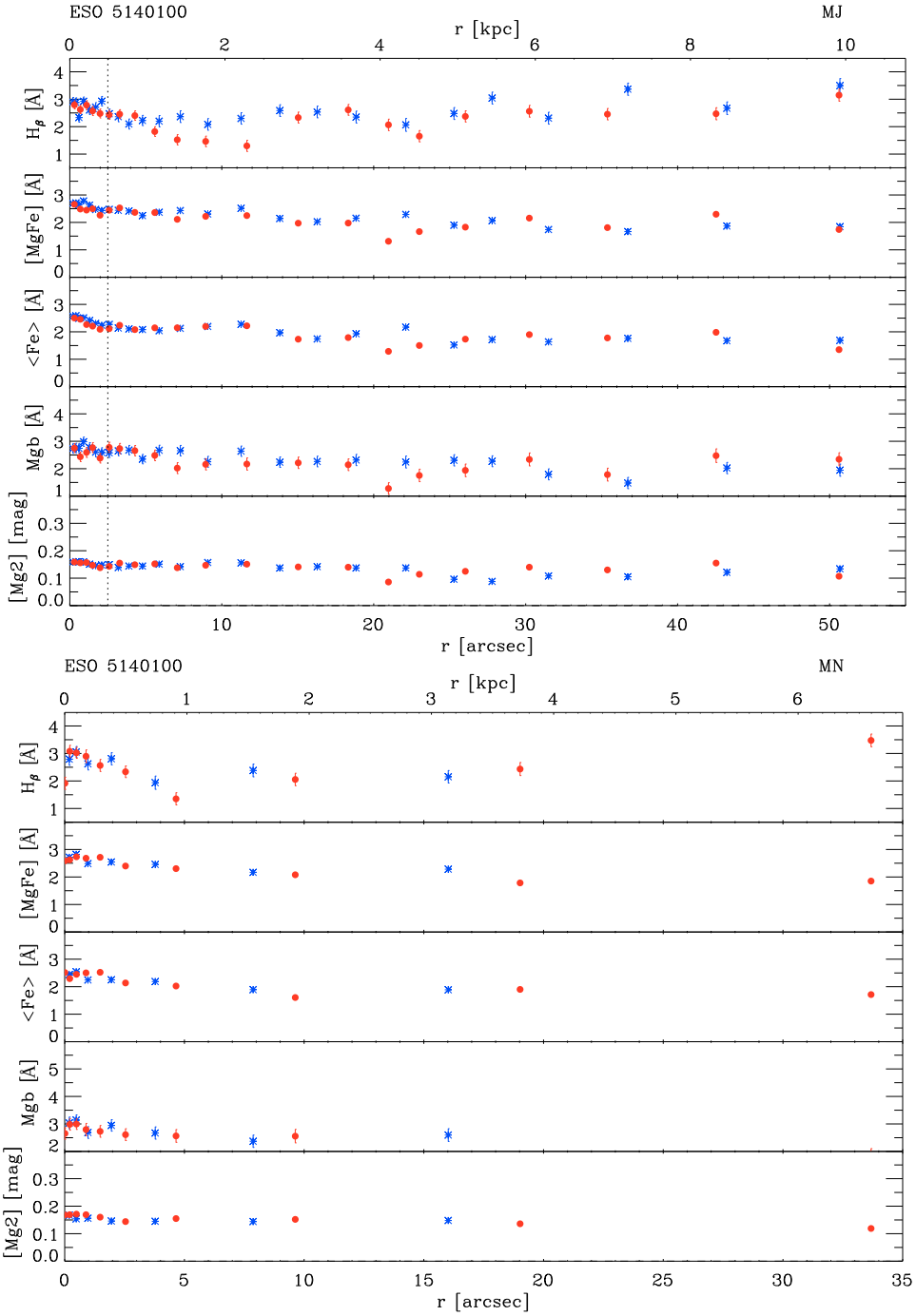

Figure 5.3: Continued.

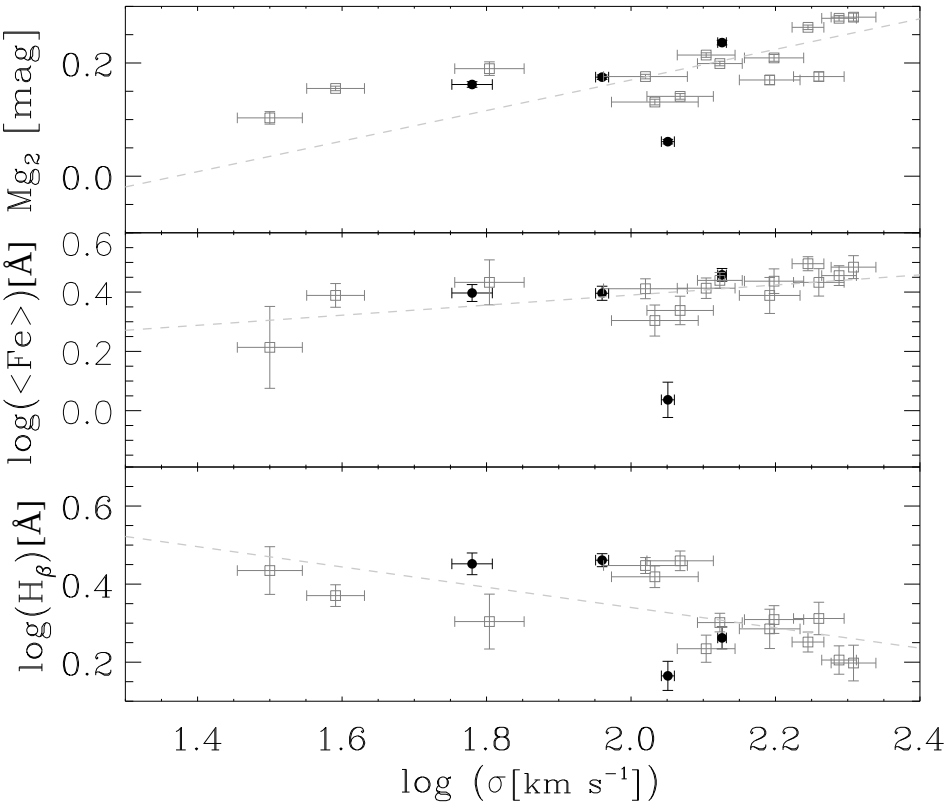

Figure 5.4: Central values of the line-strength indices Mg_2 (upper panel), $\langle\mathrm{Fe}\rangle$ (central panel), and $\mathrm{H}\beta$ (lower panel) as a function of the central velocity dispersion for the sample galaxies (filled black circles). Data for bulges in high surface brightness discs (open grey squares) and correlations (dashed lines) by Morelli et al. (2008) are reported for comparison.

outlier position of ESO-LV 4500200 in the relations of Figure 5.4

The models by Thomas et al. (2003) predict the values of the line-strength indices for a single stellar population as function of the age, metallicity, and [α/Fe]ratio.

Recent studies indicate the possibility of a multi-SP or extended star formation history nature for some bulges. These properties could be interpreted using mixed SSPs. However, in this chapter we decided to follow the SSP approach, since the sample bulges are the last ones of a series studied in Morelli et al. (2008) and Morelli et al. (2012). This approach allowed us to compare the results with the previous data. In the top panel of Figure 5.5 the central values of $\mathrm{H}\beta$ and [MgFe]$'$ are compared with the model predictions for two stellar populations with solar ([α/Fe] = 0 dex) and super-solar α/Fe ratio ([α/Fe] = 0.5 dex), respectively. In the bottom panel of Figure 5.5 the central values of Mgb and $\langle\mathrm{Fe}\rangle$ are compared with the model predictions for two stellar populations with an intermediate (2 Gyr) and old age (12 Gyr), respectively.

Table 5.3: Central values of the velocity dispersion, line-strength indices, and equivalent width of the H β emission line of the sample galaxies averaged within $0.3\,r_{\rm e}$.

Galaxy	σ	$\langle$Fe$\rangle$	[MgFe]$'$	Mg$_2$	Mgb	Hβ	H$\beta_{\rm em}$
	[km s^{-1}]	[Å]	[Å]	[mag]	[Å]	[Å]	[Å]
(1)	(2)	(3)	(4)	(5)	(6)	(7)	(8)
ESO-LV 1890070	91 ± 2.1	2.49 ± 0.14	2.76 ± 0.03	0.175 ± 0.004	3.00 ± 0.15	2.89 ± 0.11	3.9
ESO-LV 4460170	133 ± 2.2	2.87 ± 0.13	3.47 ± 0.04	0.234 ± 0.004	4.09 ± 0.13	1.83 ± 0.12	0.56
ESO-LV 4500200	112 ± 2.4	1.09 ± 0.15	1.08 ± 0.01	0.061 ± 0.003	1.06 ± 0.13	1.46 ± 0.13	10.3
ESO-LV 5140100	60 ± 4.0	2.50 ± 0.17	2.70 ± 0.04	0.163 ± 0.005	2.87 ± 0.19	2.83 ± 0.19	1.3

Table 5.4: Mean age, total metallicity, and total α/Fe ratio of the stellar populations of the bulges of the sample galaxies.

Galaxy	Age	$[Z/{\rm H}]$	$[\alpha/{\rm Fe}]$
	[Gyr]	[dex]	[dex]
(1)	(2)	(3)	(4)
ESO-LV 1890070	1.4 ± 0.2	0.29 ± 0.05	0.14 ± 0.07
ESO-LV 4460170	5.8 ± 2.0	0.26 ± 0.07	0.15 ± 0.06
ESO-LV 4500200	$\cdots$	$\cdot$	-0.25 ± 0.18
ESO-LV 5140100	1.6 ± 0.2	0.21 ± 0.06	0.07 ± 0.09

Table 5.5: Gradients of age, metallicity, and α/Fe ratio of the stellar populations of the sample bulges derived from the central values and values at the radius $r_{\rm bd}$.

Galaxy	Δ(Age)	$\Delta([Z/{\rm H}]$)	$\Delta([\alpha/{\rm Fe}])$
	[Gyr]		
(1)	(2)	(3)	(4)
ESO-LV 1890070	0.3 ± 0.4	-0.51 ± 0.08	-0.07 ± 0.10
ESO-LV 4460170	1.6 ± 3.3	-0.30 ± 0.09	-0.08 ± 0.11
ESO-LV 5140100	0.1 ± 0.7	-0.03 ± 0.12	0.00 ± 0.13

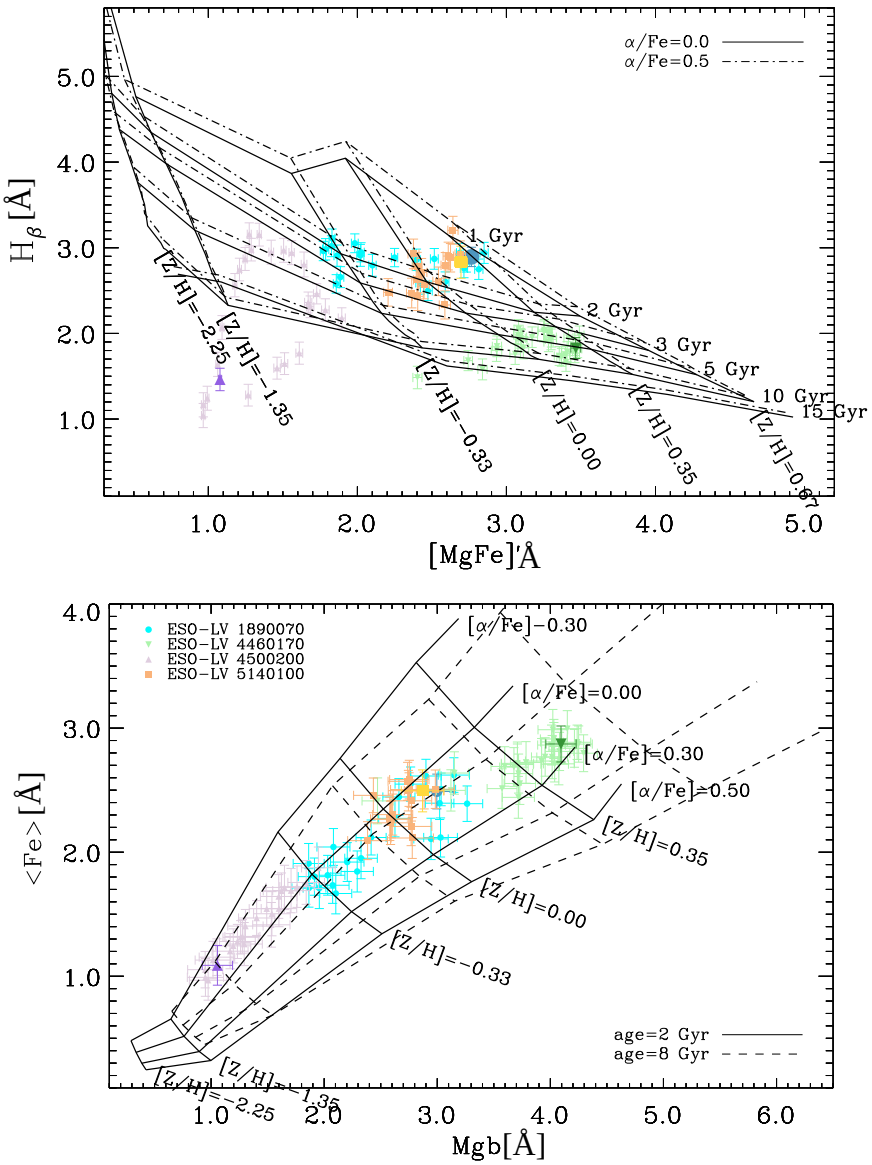

Figure 5.5: The distribution of the values of H β and [MgFe]′ indices (top panel) and $\langle$Fe$\rangle$ and Mgb indices (bottom panel) in the bulge dominated region (small symbols) and their averaged values inside an aperture of radius $0.3\,r_{\rm e}$ (big symbols) for the sample galaxies. The lines indicate the models by Thomas et al. (2003). In the top panel the age-metallicity grids are plotted with two different α/Fe enhancements: [α/Fe] = 0.0 dex (continuous lines) and [α/Fe] = 0.5 dex (dashed lines). In the bottom panel the [α/Fe] ratio-metallicity grids are plotted with two different ages: 2 Gyr (continuous lines) and 8 Gyr (dashed lines).

The central age, metallicity, and total α/Fe ratio of each bulge were derived by a linear interpolation between the model points using the iterative procedure described in Mehlert et al. (2003). The derived values and their corresponding errors are listed in Table 5.4 and were included in the histograms built by Morelli et al. (2008) (Figure 5.6).

The values of age, metallicity, and [α/Fe]ratio of ESO-LV 1890070, ESO-LV 4460170, and ESO-LV 5140100 are consistent with the distributions obtained by Morelli et al. (2008). On the contrary, the values of $\langle$Fe$\rangle$ and Mgb of ESO-LV 4500200 in the correspond to $[\alpha/\mathrm{Fe}] \simeq -0.25$, which is remarkably lower than the average α/Fe ratio found for similar galaxies (Figure 5.6). Furthermore, the kinematical and chemical properties of this galaxy place it in a region of the Hβ-[MgFe]$'$ diagram which is not covered by stellar population models. This does prevented us to derive the age and metallicity of the bulge of ESO-LV 4500200 and we did not considered it in the analysis of the gradients of the stellar population properties.

5.5.2 Radial gradients of the age, metallicity, and α/Fe ratio

The values of the Mg$_2$, Hβ, and $\langle$Fe$\rangle$ line-strength indices were measured along the bulge major axis at the radius r_{bd} (Morelli et al. 2008) where the surface-brightness contribution of the bulge is equal to that of the other components (Table 5.1). The corresponding ages, metallicities, and α/Fe ratio were derived by using the stellar population models by Thomas et al. (2003) as done for the central values.

An issue in measuring the gradients of age, metallicity and α/Fe ratio in bulge, could be the contamination of their stellar population by the light coming from the underlying disc or bar stellar component. This effect is negligible in the galaxy centre but it could increase going to the outer regions of the bulge, where the light starts to be dominated by the disc component. In order to reduce the impact of disc contamination and extend as much as possible the region in which deriving gradients, we map them inside r_{bd}, i.e. the radius where the bulge contributes half of the total surface brightness. This radius is slightly larger than the effective radius of the galaxy (Morelli et al. 2008) . Deriving gradients in the bulge-dominated region, will not remove completely the contamination by the disc or bar stellar population but it will assure always a similar degree of contamination in comparing the gradients of different galaxies.

The gradients were set as the difference between the values at centre and r_{bd} and their corresponding errors were calculated through Monte Carlo simulations taking into account the errors (Mehlert et al. 2003). The final gradients of the age, metallicity, and α/Fe ratio and their corresponding errors are listed in Table 5.5.

Shallow gradients in age and no gradient in α/Fe ratio were found for all the sample galaxies, whereas a negative shallow gradient in metallicity was observed for ESO-LV 1890070, ESO-LV 4460170, and ESO-LV 5140100. This was somehow expected for the bulges of spiral galaxies. Indeed, the measured gradients are consistent with the

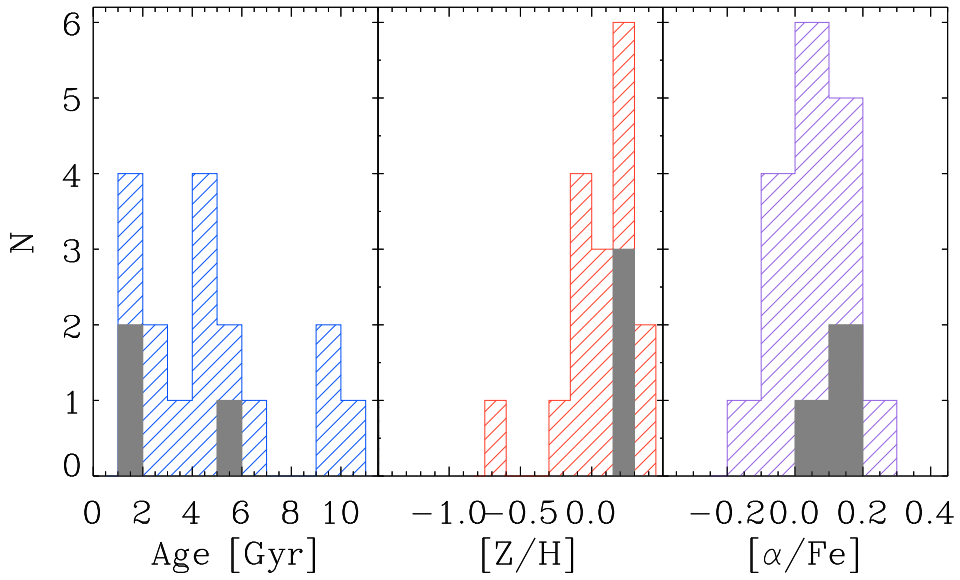

Figure 5.6: The distribution of the mean age (left-hand panel), total metallicity (central panel), and total α/Fe enhancement (right-hand panel) for the stellar populations of the bulges of the sample galaxies (grey histogram) and bulges studied by Morelli et al. (2008, hatched histogram). The properties of ESO-LV 4500200 are not reported in the figure.

distributions obtained by Morelli et al. (2008) (Figure 5.7).

Although we could not derive the age, metallicity, and [α/Fe], of ESO-LV 4500200, it is worth noticing that the radial trends of the line-strength indices are opposite with respect to the other sample galaxies (Figure 5.3). This is probably due to the presence of a decoupled component in the centre of the galaxy, as suggested by the kinematical properties discussed in Pizzella et al. (2008).

5.6 Conclusions

In this chapter we have presented the data and the results of the analysis of the stellar populations of the bulges hosted in four spiral galaxies with a high surface-brightness disc.

The central values of age, metallicity, and α/Fe ratio were derived for all the sample galaxies. The properties of the stellar populations of ESO-LV 1890070, ESO-LV 4460170, and ESO-LV 5140100 are consistent with the previous results obtained for the bulges of spiral galaxies (Jablonka et al. 2007; Ganda et al. 2007; Morelli et al. 2008).

The gradients of the stellar population properties along the major axis of all the galaxies were measured in their bulge-dominated regions. The results are consistent with previous findings for the bulges of spiral galaxies (Jablonka et al. 2007; Morelli

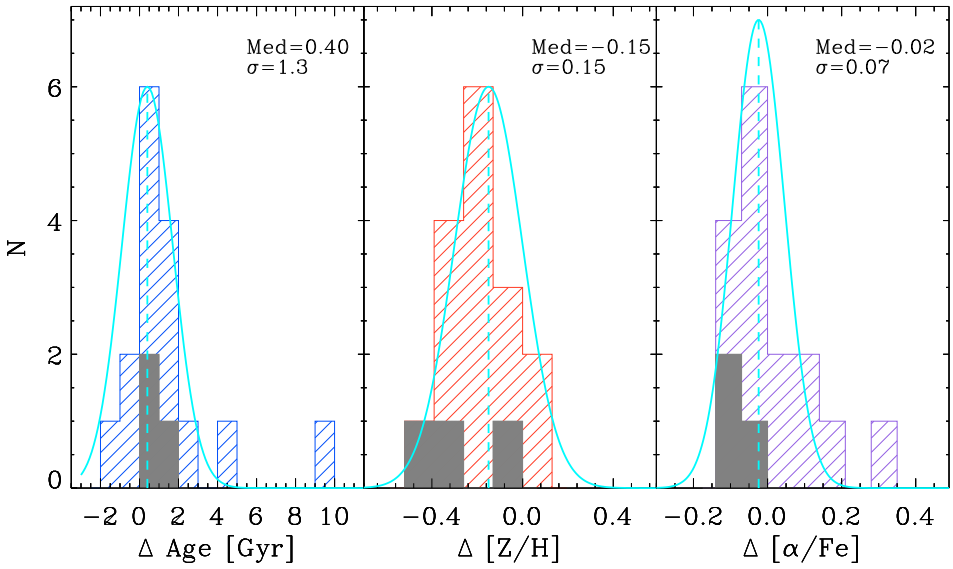

Figure 5.7: The distribution of the gradients of age (left-hand panel), metallicity (central panel) and α/Fe ratio (right-hand panel) for the bulges of the sample galaxies (grey histogram) and bulges studied by Morelli et al. (2008, hatched histogram). In each panel the dashed line represents the median of the distribution and its value is reported. Solid line represents a Gaussian centred in the median value of distribution. Its σ approximated by the value containing the 68% of the objects of the distribution is reported.

et al. 2008, 2012). The negative metallicity gradient suggests that dissipative collapse has an important role in the formation of these galaxies, but the absence of the gradients of α/Fe ratio and age indicates that hierarchical merging might be at work during the assembling process of these objects.

This is also confirmed by the peculiar properties of the bulge of ESO-LV 4500200 which can hardly be explained without invoking a recent merging or acquisition (Bertola & Corsini 1999; Coccato et al. 2011; Corsini 2014).

Chapter 6

Conclusions

In this thesis we presented an extensive observational work we have carried out to characterize the physical properties of galaxies across different environments. The goal was to determine how "nurture" by environment affects the evolutionary history of galaxies.

In Chapter 2, we presented the analysis of high- and medium-resolution optical spectra of a sample of 8 dwarf elliptical galaxies and 2 compact elliptical galaxies in the Centaurus Cluster. This study represents, together with the work by Penny et al. (2015), a first step in the construction of statistically significant samples of internal kinematics of dwarf galaxies across different environments. Such studies have usually been confined to the Virgo Cluster, because of its proximity. With our work, we increased the "environmental" parameter space to constrain how cluster environments affect the kinematics of dE galaxies. Using the high-resolution data in the visible band (6000–9800 Å), we were able to derive the internal velocity dispersion of the sample galaxies, and compute the first estimate of the Faber-Jackson relation for dEs in the Centaurus Cluster. We found that the dependence of the luminosity L on the galaxy velocity dispersion σ has a logarithmic slope ($L \propto \sigma^2$) which is smaller than that for giant elliptical galaxies. This finding is consistent with similar studies performed on other clusters (de Rijcke et al. 2005; Kourkchi et al. 2012), and is an important clue to the fact that dwarf and giant elliptical galaxies do not share the same evolutionary histories. We confirmed this result by studying the stellar population on the blue band (3900–5400 Å) spectra, which showed that dEs in the Centaurus Cluster usually have low metallicity and intermediate ages. Interestingly, we did not find faint dwarf galaxies with very old ages and metallicities close to solar, which were found in other cluster samples (Poggianti et al. 2001; Penny & Conselice 2008). While the number of sample galaxies of galaxies studied in this work is not sufficient to draw definitive conclusion, the paucity of old metal-rich dwarf may reflect the fact that the transformations driven by the cluster potential, gas halo, and galaxies is less effective in a relatively low-density environment such as Centaurus Cluster, while it is more effective in denser clusters such as Coma or Perseus.

In Chapter 3 we investigated the origin of the faint galaxy population in the Perseus Cluster. We constructed an updated database of radial velocities of the cluster members from our own fibre spectroscopy and from literature and archival data. We found an increasing velocity dispersion with decreasing galaxy luminosity, which we interpreted as an indication that a significant fraction of the dwarf galaxy population has become part of the cluster only in recent times (Penny & Conselice 2008). We verified that the cluster does not present significant substructure, and derived an updated estimate of the cluster dynamical mass, which was found in agreement with previous estimates (Girardi et al. 1998). We measured Lick line-strength line indices and luminosity-weighted ages and metallicities using full-spectrum fitting with state-of-the-art single stellar population models. These measurements will be used in a forthcoming study to derive radial trends in the stellar populations.

In Chapter 4 we derived the photometric structural parameters, stellar kinematics, and stellar population properties of a sample of bulges in 12 isolated galaxies. The analysis was performed using the same procedure employed in previous studies which analysed bulges in groups and clusters (Morelli et al. 2008, 2012) to provide a coherent framework in which to investigate the assembly history of the spheroidal component of disc galaxies. We performed a 2D decomposition of the galaxy surface brightness to identify the bulge-dominated radial range by measuring the radius $r_{\rm bd}$, where the bulge contribution to the integrated light starts to dominate over the light from the remaining components. The stellar kinematics and radial profiles of the Lick line-strength indices were measured from the major-axis spectra obtained at Telescopio Nazionale Galileo. We found correlations between Mg_2, $\langle\mathrm{Fe}\rangle$, and σ consistent with those for bulges of group and cluster galaxies (Idiart et al. 1996; Prugniel et al. 2001; Proctor & Sansom 2002). Using single stellar population model prediction for the absorption-line indices we derived age, metallicity, and α/Fe enhancement for all the sample bulges. They are characterised by a bimodal age distribution with intermediate-age and old systems, a large spread in metallicities ranging from sub- to super-solar values, and α/Fe enhancements peaked at $[\alpha/\mathrm{Fe}] = 0.2\,\mathrm{dex}$. The higher $[\alpha/\mathrm{Fe}]$ ratios found for bulges of isolated galaxies indicate a shorter star-formation timescale with respect their counterparts in high density environment. The absence of a correlation between the bulge stellar populations and galaxy morphology excludes a strong interplay between bulges and discs during their evolution. The gradients of the stellar population properties were measured within the sample bulges, finding null age gradients, negative metallicity gradients, and negative gradients for the α/Fe enhancement. Our findings are consistent with the predictions of the dissipative collapse model. Negative gradients in $[\alpha/\mathrm{Fe}]$ ratios are not observed in other bulge samples from higher density environments, where merging and acquisition event can flatten or even erase the features imprinted during the inside-out formation of the bulges. Using well controlled samples and homogeneous data analysis

methods, we were therefore able to derive evidence for the contribution of environmental effects on the evolution of bulges of disc galaxies.

In Chapter 5 we presented the data and the results of the analysis of the stellar populations of the bulges hosted in four spiral galaxies with a high surface-brightness disc. The central values of age, metallicity, and [α/Fe] ratio were derived for all the sample galaxies. The properties of the bulge stellar populations are consistent with the previous results obtained for the bulges of spiral galaxies (Ganda et al. 2007; Morelli et al. 2008). The gradients of the stellar population properties along the major axis of all the galaxies were measured in their bulge-dominated regions. The results are consistent with previous findings for the bulges of spiral galaxies (Jablonka et al. 2007; Morelli et al. 2012). The negative metallicity gradient suggests that dissipative collapse has an important role in the formation of these galaxies, but the absence of the gradients of α/Fe ratio and age indicates that hierarchical merging might be at work during the assembling process of these objects.

All the results presented in this thesis showed the importance of considering the effects the environment has on the evolution of galaxies. In the near future, we will improve our work in this thesis in several ways. The study of dE galaxies in the Centarus cluster will be improved with an accurate photometric study of the galaxies in the sample, with the analysis of the X-Shooter NIR spectroscopy and possibly with resolved kinematics from IFU observations. The study of the effects of environment on the assembly history of bulges will be improved with larger samples and a more controlled analysis of the local environment in which the disc galaxies evolved.

Acknowledgements

During the course of my Ph.D. I have benefited from the help and advice of many people and institutions.

I acknowledge financial support from Padova University, from INAF-Osservatorio Astronomico di Padova and from Ghent University.

I thank Dr. S. Covino and Dr. E. Palazzi for having carried out the observations which were analysed in Chapter 2 and Dr. G. Cupani for invaluable help in the data reduction process. I thank Dr. D. Bettoni for the help she has given me in the reduction of the fibre spectroscopic data presented in Chapter 3.

I warmly thank Prof. Sven de Rijcke for the ospitality during my stay in Ghent, and Dr. Mina Koleva for her patient guidance in the usage of the ULySS analysis software.

Luca Costantin and Dr. Jairo Méndez-Abreu have helped me in g(r)asping the GASP2D decomposition software.

I thank Enrico V., Enrico M. and Lorenzo for the patience they have shown in helping me reach the final goal, and for the wise advice they have given me in many (but probably not enough) occasions.

Finally, this work would not have been possible without the support I received from my family and all my friends.

References

Aguerri J. A. L., Méndez-Abreu J., Corsini E. M., 2009, A&A, 495, 491

van Albada T. S., 1982, MNRAS, 201, 939

Allen S. W., Fabian A. C., 1994, MNRAS, 269, 409

Annibali F., Bressan A., Rampazzo R., Zeilinger W. W., Danese L., 2007, A&A, 463, 455

Arimoto N., Yoshii Y., 1987, A&A, 173, 23

Athanassoula E., Morin S., Wozniak H., Puy D., Pierce M. J., Lombard J., Bosma A., 1990, MNRAS, 245, 130

Beers T. C., Flynn K., Gebhardt K., 1990, AJ, 100, 32

Bekki K., 2009, MNRAS, 399, 2221

Bekki K., Shioya Y., 1999, ApJ, 513, 108

Bell E. F., McIntosh D. H., Katz N., Weinberg M. D., 2003, ApJS, 149, 289

Bender R., 1990, A&A, 229, 441

Bender R., Burstein D., Faber S. M., 1992, ApJ, 399, 462

Bertelli G., Bressan A., Chiosi C., Fagotto F., Nasi E., 1994, A&AS, 106, 275

Bertin E., Arnouts S., 1996, A&AS, 117, 393

Bertin G., Ciotti L., Del Principe M., 2002, A&A, 386, 149

Bertola F., Corsini E. M., 1999, in Barnes J. E., Sanders D. B., eds, IAU Symposium Vol. 186, Galaxy Interactions at Low and High Redshift. Kluwer Ac. Pub., Dordrecht, p. 149

Bertone E., Buzzoni A., Chávez M., Rodríguez-Merino L. H., 2008, A&A, 485, 823

Binney J., Tremaine S., 1987, Galactic Dynamics. Princeton Univ. Press, Princeton, NJ

Blanton M. R., Moustakas J., 2009, ARA&A, 47, 159

Boggs P. T., Donaldson J. R., Byrd R. h., Schnabel R. B., 1989, ACM Trans. Math. Softw., 15, 348

Boselli A., Boissier S., Cortese L., Gavazzi G., 2008, ApJ, 674, 742

Bournaud F., Jog C. J., Combes F., 2007, A&A, 476, 1179

Bower R. G., Benson A. J., Malbon R., Helly J. C., Frenk C. S., Baugh C. M., Cole S., Lacey C. G., 2006, MNRAS, 370, 645

Brunzendorf J., Meusinger H., 1999, A&AS, 139, 141

Butcher H., Oemler Jr. A., 1984, ApJ, 285, 426

Byun Y. I., Freeman K. C., 1995, ApJ, 448, 563

Caon N., Capaccioli M., D'Onofrio M., 1993, MNRAS, 265, 1013

Cappellari M., Emsellem E., 2004, PASP, 116, 138

Cappellari M., et al., 2006, MNRAS, 366, 1126

Cardiel N., 2010, indexf: Line-strength Indices in Fully Calibrated FITS Spectra, Astrophysics Source Code Library (ascl:1010.046)

Cardiel N., Gorgas J., Cenarro J., Gonzalez J. J., 1998, A&AS, 127, 597

Cen R., Pop A. R., Bahcall N. A., 2014, Proc. Nat. Ac. Science, 111, 7914

Chen Y.-P., Trager S. C., Peletier R. F., Lançon A., Vazdekis A., Prugniel P., Silva D. R., Gonneau A., 2014, A&A, 565, A117

Chiboucas K., Mateo M., 2007, ApJS, 170, 95

Chilingarian I. V., 2009, MNRAS, 394, 1229

Chilingarian I., Zolotukhin I., 2015, Science, 348, 418

Chilingarian I., Prugniel P., Sil'Chenko O., Koleva M., 2007, in Vazdekis A., Peletier R., eds, IAU Symposium Vol. 241, IAU Symposium. CUP, Cambridge, pp 175–176

Chilingarian I. V., Cayatte V., Durret F., Adami C., Balkowski C., Chemin L., Laganá T. F., Prugniel P., 2008, A&A, 486, 85

Chilingarian I., Cayatte V., Revaz Y., Dodonov S., Durand D., Durret F., Micol A., Slezak E., 2009, Science, 326, 1379

Ciotti L., Bertin G., 1999, A&A, 352, 447

Cloet-Osselaer A., De Rijcke S., Vandenbroucke B., Schroyen J., Koleva M., Verbeke R., 2014, MNRAS, 442, 2909

Coccato L., Morelli L., Corsini E. M., Buson L., Pizzella A., Vergani D., Bertola F., 2011, MNRAS, 412, L113

Cody A. M., Carter D., Bridges T. J., Mobasher B., Poggianti B. M., 2009, MNRAS, 396, 1647

Cole S., Lacey C. G., Baugh C. M., Frenk C. S., 2000, MNRAS, 319, 168

Collobert M., Sarzi M., Davies R. L., Kuntschner H., Colless M., 2006, MNRAS, 370, 1213

Conselice C. J., Gallagher III J. S., Wyse R. F. G., 2001, ApJ, 559, 791

Conselice C. J., Gallagher III J. S., Wyse R. F. G., 2003, AJ, 125, 66

Corsini E. M., 2014, in Iodice E., Corsini E. M., eds, ASP Conf. Ser. Vol. 486, Multi-Spin Galaxies. Astron. Soc. Pac., San Francisco, CA, p. 51

Courteau S., et al., 2014, Reviews of Modern Physics, 86, 47

De Lucia G., Kauffmann G., White S. D. M., 2004, MNRAS, 349, 1101

De Lucia G., Springel V., White S. D. M., Croton D., Kauffmann G., 2006, MNRAS, 366, 499

Dekel A., Silk J., 1986, ApJ, 303, 39

Denicoló G., Terlevich R., Terlevich E., Forbes D. A., Terlevich A., 2005, MNRAS, 358, 813

Djorgovski S., Davis M., 1987, ApJ, 313, 59

van Dokkum P. G., 2001, PASP, 113, 1420

van Dokkum P. G., Conroy C., 2010, Nature, 468, 940

Dressler A., 1980, ApJ, 236, 351

Dressler A., Shectman S. A., 1988, AJ, 95, 985

Dressler A., et al., 1997, ApJ, 490, 577

Drinkwater M. J., Jones J. B., Gregg M. D., Phillipps S., 2000, PASA, 17, 227

Eggen O. J., Lynden-Bell D., Sandage A. R., 1962, ApJ, 136, 748

Faber S. M., Jackson R. E., 1976, ApJ, 204, 668

Faber S. M., Friel E. D., Burstein D., Gaskell C. M., 1985, ApJS, 57, 711

Fadda D., Girardi M., Giuricin G., Mardirossian F., Mezzetti M., 1996, ApJ, 473, 670

Ferguson H. C., Binggeli B., 1994, A&A Rev., 6, 67

Ferrarese L., et al., 2006, ApJS, 164, 334

Ferrarese L., et al., 2012, ApJS, 200, 4

Ferreras I., Silk J., 2002, MNRAS, 336, 1181

Ferrers N. M., 1877, Quart. J. Pure Appl. Math., 14, 1

Focardi P., Malavasi N., 2012, ApJ, 756, 117

Forbes D. A., Spitler L. R., Graham A. W., Foster C., Hau G. K. T., Benson A., 2011, MNRAS, 413, 2665

Forbes D. A., Norris M. A., Strader J., Romanowsky A. J., Pota V., Kannappan S. J., Brodie J. P., Huxor A., 2014, MNRAS, 444, 2993

Freeman K. C., 1970, ApJ, 160, 811

Ganda K., et al., 2007, MNRAS, 380, 506

Geha M., Guhathakurta P., van der Marel R. P., 2002, AJ, 124, 3073

Geha M., Guhathakurta P., van der Marel R. P., 2003, AJ, 126, 1794

Gilmore G., Wyse R. F. G., 1998, AJ, 116, 748

Girardi M., Giuricin G., Mardirossian F., Mezzetti M., Boschin W., 1998, ApJ, 505, 74

González Delgado R. M., et al., 2014, A&A, 562, A47

Gorgas J., Efstathiou G., Aragon Salamanca A., 1990, MNRAS, 245, 217

Graham A. W., Driver S. P., 2005, PASA, 22, 118

Graham A. W., Guzmán R., 2003, AJ, 125, 2936

Gunn J. E., Gott III J. R., 1972, ApJ, 176, 1

Guo Q., et al., 2011, MNRAS, 413, 101

Guth A. H., 1981, Phys. Rev. D, 23, 347

Held E. V., Mould J. R., 1994, AJ, 107, 1307

Held E. V., de Zeeuw T., Mould J., Picard A., 1992, AJ, 103, 851

Hopkins P. F., Cox T. J., Dutta S. N., Hernquist L., Kormendy J., Lauer T. R., 2009a, ApJS, 181, 135

Hopkins P. F., Cox T. J., Younger J. D., Hernquist L., 2009b, ApJ, 691, 1168

Horne K., 1986, PASP, 98, 609

Huchra J. P., Vogeley M. S., Geller M. J., 1999, ApJS, 121, 287

Humason M. L., Mayall N. U., Sandage A. R., 1956, AJ, 61, 97

Huxor A. P., Phillipps S., Price J., Harniman R., 2011, MNRAS, 414, 3557

Idiart T. P., de Freitas Pacheco J. A., Costa R. D. D., 1996, AJ, 112, 2541

Jablonka P., Gorgas J., Goudfrooij P., 2007, A&A, 474, 763

Janz J., et al., 2016, MNRAS, 456, 617

Jerjen H., Dressler A., 1997, A&AS, 124, 1

Kannan R., Macciò A. V., Fontanot F., Moster B. P., Karman W., Somerville R. S., 2015, MNRAS, 452, 4347

Karachentseva V. E., 1973, Soobshcheniya Spetsial'noj Astrofizicheskoj Observatorii, 8, 3

Katkov I. Y., Kniazev A. Y., Sil'chenko O. K., 2015, AJ, 150, 24

Kawata D., 2001, ApJ, 558, 598

Kawata D., Gibson B. K., 2003, MNRAS, 340, 908

Kenney J. D. P., van Gorkom J. H., Vollmer B., 2004, AJ, 127, 3361

Kenney J. D. P., Tal T., Crowl H. H., Feldmeier J., Jacoby G. H., 2008, ApJ, 687, L69

Kennicutt Jr. R. C., 1989, ApJ, 344, 685

Kent S. M., Sargent W. L. W., 1983, AJ, 88, 697

King D. L., 1985, RGO/La Palma Technical Note 31, Atmospheric Extinction at the Roque de los Muchachos Observatory, La Palma. Royal Greenwich Obs., Greenwich

Kobayashi C., 2004, MNRAS, 347, 740

Koda J., Yagi M., Yamanoi H., Komiyama Y., 2015, ApJ, 807, L2

Koleva M., Prugniel P., De Rijcke S., 2008a, AN, 329, 968

Koleva M., Prugniel P., Ocvirk P., Le Borgne D., Soubiran C., 2008b, MNRAS, 385, 1998

Koleva M., de Rijcke S., Prugniel P., Zeilinger W. W., Michielsen D., 2009a, MNRAS, 396, 2133

Koleva M., Prugniel P., Bouchard A., Wu Y., 2009b, A&A, 501, 1269

Kormendy J., 1977, ApJ, 217, 406

Kormendy J., Kennicutt Jr. R. C., 2004, ARA&A, 42, 603

Kormendy J., Fisher D. B., Cornell M. E., Bender R., 2009, ApJS, 182, 216

Kourkchi E., et al., 2012, MNRAS, 420, 2819

Kuntschner H., et al., 2010, MNRAS, 408, 97

Kurtz M. J., Mink D. J., 1998, PASP, 110, 934

La Barbera F., Pasquali A., Ferreras I., Gallazzi A., de Carvalho R. R., de la Rosa I. G., 2014, MNRAS, 445, 1977

Lacey C., Cole S., 1993, MNRAS, 262, 627

Larson R. B., 1974, MNRAS, 166, 585

Larson R. B., Tinsley B. M., Caldwell C. N., 1980, ApJ, 237, 692

Le Borgne D., Rocca-Volmerange B., Prugniel P., Lançon A., Fioc M., Soubiran C., 2004, A&A, 425, 881

Lisker T., Grebel E. K., Binggeli B., 2006, AJ, 132, 497

Lisker T., Grebel E. K., Binggeli B., Glatt K., 2007, ApJ, 660, 1186

de Lorenzo-Cáceres A., Vazdekis A., Aguerri J. A. L., Corsini E. M., Debattista V. P., 2012, MNRAS, 420, 1092

Lucey J. R., Currie M. J., Dickens R. J., 1986, MNRAS, 221, 453

Lupton R. H., et al., 2005, BAAS, 37, 1384

Lynden-Bell D., Lynden-Bell R. M., 1995, MNRAS, 275, 429

MacArthur L. A., González J. J., Courteau S., 2009, MNRAS, 395, 28

Makino N., Sasaki S., Suto Y., 1998, ApJ, 497, 555

Maraston C., 1998, MNRAS, 300, 872

van der Marel R. P., Franx M., 1993, ApJ, 407, 525

Marinoni S., Galleti S., Cocozza G., Pancino E., Altavilla G., 2013, Instrument Familiarization Plan for Ground Based Observations of SPSS. II. Calibration Frames Study and Recommendations, http://www.oabo.inaf.it/~pancino/docs/gaia_smr_002.pdf

Markwardt C. B., 2009, in Bohlender D. A., Durand D., Dowler P., eds, ASP Conf. Ser. Vol. 411, Astronomical Data Analysis Software and Systems XVIII. Astron. Soc. Pac., San Francisco, CA, p. 251

Mastropietro C., Moore B., Mayer L., Debattista V. P., Piffaretti R., Stadel J., 2005, MNRAS, 364, 607

Matteucci F., 1994, A&A, 288, 57

Matteucci F., Greggio L., 1986, A&A, 154, 279

McDermid R. M., et al., 2015, MNRAS, 448, 3484

McNaught-Roberts T., et al., 2014, MNRAS, 445, 2125

Mehlert D., Saglia R. P., Bender R., Wegner G., 1998, A&A, 332, 33

Mehlert D., Thomas D., Saglia R. P., Bender R., Wegner G., 2003, A&A, 407, 423

Méndez-Abreu J., Aguerri J. A. L., Corsini E. M., Simonneau E., 2008, A&A, 478, 353

Méndez-Abreu J., Debattista V. P., Corsini E. M., Aguerri J. A. L., 2014, A&A, 572, A25

Merritt D., 1987, ApJ, 313, 121

Mieske S., Infante L., Hilker M., Hertling G., Blakeslee J. P., Benítez N., Ford H., Zekser K., 2005a, A&A, 430, L25

Mieske S., Hilker M., Infante L., 2005b, A&A, 438, 103

Mieske S., Hilker M., Misgeld I., 2012, A&A, 537, A3

Misgeld I., Hilker M., Mieske S., 2009, A&A, 496, 683

Moffat A. F. J., 1969, A&A, 3, 455

Moore B., Katz N., Lake G., Dressler A., Oemler A., 1996, Nature, 379, 613

Moore B., Lake G., Katz N., 1998, ApJ, 495, 139

Moorthy B. K., Holtzman J. A., 2006, MNRAS, 371, 583

Moré J. J., 1978, in Watson G., ed., Lecture Notes in Mathematics, Vol. 630, Numerical Analysis. Springer, Berlin, p. 105

Morelli L., et al., 2004, MNRAS, 354, 753

Morelli L., et al., 2007, Nuovo Cimento B Serie, 122, 1281

Morelli L., et al., 2008, MNRAS, 389, 341

Morelli L., Corsini E. M., Pizzella A., Dalla Bontà E., Coccato L., Méndez-Abreu J., Cesetti M., 2012, MNRAS, 423, 962

Morelli L., Calvi V., Masetti N., Parisi P., Landi R., Maiorano E., Minniti D., Galaz G., 2013, A&A, 556, A135

Morelli L., Pizzella A., Corsini E. M., Dalla Bontà E., Coccato L., Méndez-Abreu J., Parmiggiani M., 2015a, AN, 336, 208

Morelli L., Corsini E. M., Pizzella A., Dalla Bontà E., Coccato L., Méndez-Abreu J., 2015b, MNRAS, 452, 1128

Noll S., Kausch W., Kimeswenger S., Barden M., Jones A. M., Modigliani A., Szyszka C., Taylor J., 2014, A&A, 567, A25

Norris M. A., et al., 2014, MNRAS, 443, 1151

Ocvirk P., Pichon C., Lançon A., Thiébaut E., 2006, MNRAS, 365, 46

Osterbrock D. E., Fulbright J. P., Martel A. R., Keane M. J., Trager S. C., Basri G., 1996, PASP, 108, 277

Peng C. Y., Ho L. C., Impey C. D., Rix H.-W., 2002, AJ, 124, 266

Peng Y., Maiolino R., Cochrane R., 2015, Nature, 521, 192

Penny S. J., Conselice C. J., 2008, MNRAS, 383, 247

Penny S. J., Conselice C. J., de Rijcke S., Held E. V., 2009, MNRAS, 393, 1054

Penny S. J., Forbes D. A., Pimbblet K. A., Floyd D. J. E., 2014, MNRAS, 443, 3381

Penny S. J., Janz J., Forbes D. A., Benson A. J., Mould J., 2015, MNRAS, 453, 3635

Perlmutter S., et al., 1999, ApJ, 517, 565

Pignatelli E., Fasano G., Cassata P., 2006, A&A, 446, 373

Pipino A., D'Ercole A., Matteucci F., 2008, A&A, 484, 679

Pipino A., D'Ercole A., Chiappini C., Matteucci F., 2010, MNRAS, 407, 1347

Pizzella A., Corsini E. M., Sarzi M., Magorrian J., Méndez-Abreu J., Coccato L., Morelli L., Bertola F., 2008, MNRAS, 387, 1099

Planck Collaboration et al., 2014, A&A, 571, A16

Poggianti B. M., et al., 2001, ApJ, 562, 689

Poggianti B. M., Bridges T. J., Komiyama Y., Yagi M., Carter D., Mobasher B., Okamura S., Kashikawa N., 2004, ApJ, 601, 197

Popesso P., Böhringer H., Romaniello M., Voges W., 2005, A&A, 433, 415

Popesso P., Biviano A., Böhringer H., Romaniello M., 2006, A&A, 445, 29

Press W. H., Schechter P., 1974, ApJ, 187, 425

Price J., et al., 2009, MNRAS, 397, 1816

Proctor R. N., Sansom A. E., 2002, MNRAS, 333, 517

Prugniel P., Soubiran C., 2001, A&A, 369, 1048

Prugniel P., Maubon G., Simien F., 2001, A&A, 366, 68

Prugniel P., Soubiran C., Koleva M., Le Borgne D., 2007 (arXiv:astro-ph/0703658)

Prugniel P., Vauglin I., Koleva M., 2011, A&A, 531, A165

Rampazzo R., Annibali F., Bressan A., Longhetti M., Padoan F., Zeilinger W. W., 2005, A&A, 433, 497

Rawle T. D., Smith R. J., Lucey J. R., 2010, MNRAS, 401, 852

Reda F. M., Proctor R. N., Forbes D. A., Hau G. K. T., Larsen S. S., 2007, MNRAS, 377, 1772

Riess A. G., et al., 1998, AJ, 116, 1009

de Rijcke S., Dejonghe H., Zeilinger W. W., Hau G. K. T., 2001, ApJ, 559, L21

de Rijcke S., Dejonghe H., Zeilinger W. W., Hau G. K. T., 2003, A&A, 400, 119

de Rijcke S., Michielsen D., Dejonghe H., Zeilinger W. W., Hau G. K. T., 2005, A&A, 438, 491

de Rijcke S., Penny S. J., Conselice C. J., Valcke S., Held E. V., 2009, MNRAS, 393, 798

Rix H.-W., White S. D. M., 1992, MNRAS, 254, 389

Robotham A., Phillipps S., de Propris R., 2010, MNRAS, 403, 1812

Roediger E., Hensler G., 2005, A&A, 433, 875

Ryś A., van de Ven G., Falcón-Barroso J., 2014, MNRAS, 439, 284

Ryś A., Koleva M., Falcón-Barroso J., Vazdekis A., Lisker T., Peletier R., van de Ven G., 2015, MNRAS, 452, 1888

Salpeter E. E., 1955, ApJ, 121, 161

Sánchez-Blázquez P., Gorgas J., Cardiel N., González J. J., 2006, A&A, 457, 809

Sánchez-Blázquez P., Ocvirk P., Gibson B. K., Pérez I., Peletier R. F., 2011, MNRAS, 415, 709

Sánchez-Blázquez P., et al., 2014, A&A, 570, A6

Sargent W. L. W., Schechter P. L., Boksenberg A., Shortridge K., 1977, ApJ, 212, 326

Sarzi M., et al., 2006, MNRAS, 366, 1151

Schechter P., 1976, ApJ, 203, 297

Schmidt M., 1959, ApJ, 129, 243

Schroyen J., De Rijcke S., Koleva M., Cloet-Osselaer A., Vandenbroucke B., 2013, MNRAS, 434, 888

Seidel M. K., Falcón-Barroso J., Martínez-Valpuesta I., Díaz-García S., Laurikainen E., Salo H., Knapen J. H., 2015, MNRAS, 451, 936

Sérsic J. L., 1968, Atlas de galaxias australes. Observatorio Astronómico, Córdoba

Sil'chenko O. K., Proshina I. S., Shulga A. P., Koposov S. E., 2012, MNRAS, 427, 790

Simard L., 1998, in Albrecht R., Hook R. N., Bushouse H. A., eds, ASP Conf. Ser. Vol. 145, Astronomical Data Analysis Software and Systems VII. Astron. Soc. Pac., San Francisco, CA, p. 108

Smith Castelli A. V., Faifer F. R., Richtler T., Bassino L. P., 2008, MNRAS, 391, 685

Smith R. J., Lucey J. R., Hudson M. J., Allanson S. P., Bridges T. J., Hornschemeier A. E., Marzke R. O., Miller N. A., 2009, MNRAS, 392, 1265

Smith R., Davies J. I., Nelson A. H., 2010, MNRAS, 405, 1723

Smith R. J., Lucey J. R., Price J., Hudson M. J., Phillipps S., 2012a, MNRAS, 419, 3167

Smith R., Fellhauer M., Assmann P., 2012b, MNRAS, 420, 1990

Smith R., et al., 2015, MNRAS, 454, 2502

Spolaor M., Kobayashi C., Forbes D. A., Couch W. J., Hau G. K. T., 2010, MNRAS, 408, 272

Springel V., Di Matteo T., Hernquist L., 2005, ApJ, 620, L79

Stein P., Jerjen H., Federspiel M., 1997, A&A, 327, 952

Stoehr F., et al., 2008, in Argyle R. W., Bunclark P. S., Lewis J. R., eds, ASP Conf. Ser. Vol. 394, Astronomical Data Analysis Software and Systems XVII. Astron. Soc. Pac., San Francisco, CA, p. 505

Tassis K., Kravtsov A. V., Gnedin N. Y. A., 2008, ApJ, 672, 888

Thomas D., Davies R. L., 2006, MNRAS, 366, 510

Thomas D., Maraston C., Bender R., 2003, MNRAS, 339, 897

Thomas D., Maraston C., Bender R., Mendes de Oliveira C., 2005, ApJ, 621, 673

Thomas D., Maraston C., Schawinski K., Sarzi M., Silk J., 2010, MNRAS, 404, 1775

Toloba E., Boselli A., Cenarro A. J., Peletier R. F., Gorgas J., Gil de Paz A., Muñoz-Mateos J. C., 2011, A&A, 526, A114

Toloba E., Boselli A., Peletier R. F., Falcón-Barroso J., van de Ven G., Gorgas J., 2012, A&A, 548, A78

Toloba E., et al., 2014, ApJS, 215, 17

Toloba E., et al., 2015, ApJ, 799, 172

Tonnesen S., Bryan G. L., 2009, ApJ, 694, 789

Tonnesen S., Bryan G. L., van Gorkom J. H., 2007, ApJ, 671, 1434

Tonry J., Davis M., 1979, AJ, 84, 1511

Tonry J., Schneider D. P., 1988, AJ, 96, 807

Tully R. B., Fisher J. R., 1977, A&A, 54, 661

Tully R. B., Somerville R. S., Trentham N., Verheijen M. A. W., 2002, ApJ, 569, 573

Valdes F., 1995, Guide to the Multifiber Reduction Task DOFIBERS. NOAO, `ftp://iraf.noao.edu/ftp/docs/dofibers.ps.Z`

de Vaucouleurs G., de Vaucouleurs A., Corwin Jr. H. G., Buta R. J., Paturel G., Fouqué P., 1991, Third Reference Catalogue of Bright Galaxies. Springer, Berlin

Vazdekis A., Sánchez-Blázquez P., Falcón-Barroso J., Cenarro A. J., Beasley M. A., Cardiel N., Gorgas J., Peletier R. F., 2010, MNRAS, 404, 1639

Vernet J., et al., 2011, A&A, 536, A105

Walker I. R., Mihos J. C., Hernquist L., 1996, ApJ, 460, 121

Weinmann S. M., Lisker T., Guo Q., Meyer H. T., Janz J., 2011, MNRAS, 416, 1197

White S. D. M., Rees M. J., 1978, MNRAS, 183, 341

Wilkinson D. M., et al., 2015, MNRAS, 449, 328

Worthey G., Ottaviani D. L., 1997, ApJS, 111, 377

Worthey G., Faber S. M., Gonzalez J. J., Burstein D., 1994, ApJS, 94, 687

Wu Y., Singh H. P., Prugniel P., Gupta R., Koleva M., 2011, A&A, 525, A71

York D. G., et al., 2000, AJ, 120, 1579

Yoshii Y., Arimoto N., 1987, A&A, 188, 13

Zandivarez A., Martínez H. J., 2011, MNRAS, 415, 2553

van Zee L., Skillman E. D., Haynes M. P., 2004, AJ, 128, 121

Zoccali M., Hill V., Lecureur A., Barbuy B., Renzini A., Minniti D., Gómez A., Ortolani S., 2008, A&A, 486, 177